Recent Progresses in Inflatable Robotics

Hugo Rodrigue, Jin-Gyu Lee, Namsoo Oh, Haneol Lee

어나더스쿨

산업통상자원부
Ministry of Trade, Industry and Energy

KAR 한국로봇산업협회
Korea Association of Robot industry

Robot SC
Human Resource Development

성균관대학교
SUNGKYUNKWAN UNIVERSITY

본 교재는 산업통상자원부의 재원으로 한국산업기술진흥원-로봇산업 인적자원개발협의체의
지원을 받아 발간된 교재임(RS-2024-00443410)

Recent Progresses in Inflatable Robotics

First eBook Edition Published on April 24, 205

Authors: Hugo Rodrigue, Jin-Gyu Lee, Namsoo Oh, Haneol Lee

Publisher: Kang Shinwon
Published by: AnotherSchool
Publication Registration: No. 2021-000014, January 28, 2021
Address: 15, Gwanggyohosu-ro 386beon-gil, Suji-gu, Yongin-si, Gyeonggi-do, Republic of Korea
Email: pub@anotherschool.kr

eBook ISBN 979-11-93673-09-6 (95550)

Copyright © 2025 by Hugo Rodrigue, Jin-Gyu Lee, Namsoo Oh, and Haneol Lee

All rights reserved. This eBook is protected by copyright laws and international treaties. No part of this publication may be copied, reproduced, stored in a retrieval system, or transmitted in any form or by any means—electronic, mechanical, digital, photocopying, recording, or otherwise—without the prior written permission of the publisher.
Unauthorized distribution or sharing of this eBook, including uploading to websites or file-sharing platforms, is strictly prohibited and may result in legal action.

Greeting

This book is an exploration of a rapidly evolving and fascinating field: inflatable soft robotics. In an era where the boundaries between engineering, biology, and material science are increasingly blurred. Soft robotics not only reflects this interdisciplinary spirit but also pushes the boundaries of what we traditionally define as robotics. This book introduces one particular area of this branch of robotics within this growing field, where smooth deformations and clever designs replace the brute force of motors and gears.

The origins of soft robotics can be traced back more than half a century, with early concepts such as the McKibben actuator laying the groundwork for a new paradigm in robotic actuation. The rise of elastomeric materials, additive manufacturing, and microfabrication techniques has sparked an explosion of innovation. Yet, despite the growing popularity of stretchable rubbers and polymers, there remains an underexplored opportunity in the use of thin and non-stretchable films which can deform in precise, controllable ways when pressurized. The use of these materials in the field of soft robotics is the principal theme of this book.

Here, we explore how these films, when thoughtfully designed and integrated, can give rise to soft robotic systems that are lightweight, cost-effective, and remarkably powerful. By leveraging pressure-based actuation and simple mechanical principles, it is possible to achieve sophisticated movement patterns, large deformations, and even lifelike behaviors without the complexity and fragility often associated with traditional rigid robots. From vacuum-based artificial muscles capable of dramatic contractions, to scalable inflatable joints and origami-inspired actuators, this book examines a spectrum of designs that challenge conventional approaches to motion, force generation, and robotic interaction.

More than just a technical manual, this book aims to be a source of inspiration and a foundation for further innovation. It brings together principles from physics, design, and engineering to demonstrate how inflatable systems can unlock new frontiers. Whether you are a researcher, student, engineer, or simply a curious mind, we hope this book inspires you to look beyond the rigid and into the soft, to explore not just how things move, but how they could move: with elegance, efficiency, and intention.

C/o/n/t/e/n/t/s

Chapter 05

Chapter 06

Chapter 07

Chapter 01

Introduction

The concept of using soft materials to build actuators and mechanical systems making use of the deformation of materials to produce a movement goes back to the 1950s with the development of the McKibben actuator [1, 2]. This actuator consists of a flexible pneumatic tube shielded by a braided mesh which, upon pressurization, balloons laterally and shrinks longitudinally to produce a linear force. This corresponds with the development of the first rigid robots such as Unimate in 1954. Subsequent decades saw significant developments of rigid robots which have become ubiquitous in industries due to their precision, speed and versatility. However, the next significant development in soft robotics came in the 1990s with the development of flexible rubber micro-actuators which could produce complex motions through the pressurization of multiple chambers within a single body [3]. The next significant milestone was through the use of soft lithography techniques used to mold structures made from polymers in the early 2010s, which has been used to build soft grippers [4], and crawling robots [5]. The rest of this decade saw an explosion of pneumatically actuated structures made these polymers ranging from actuators [6], soft robotic grippers [7], medical robots [8], and biomimetic robots [9].

The basic principle of creating motion through pneumatic actuation of a rubber or polymer is to design the structure such that an increase in pressure results in the selective stretching of the structure to cause an intended deformation. This selective stretching can be implemented through various methods such as by using different wall thicknesses throughout the structure or by embedding non-stretchable elements serving as strain limiting layers in the structure. The elasticity of the materials causes the structure to return to its original configuration upon depressurization and enables easy cyclic actuation of the structure. However, using pressures higher than intended results in ballooning of the structures due to the walls of the structure reducing in thickness as they are stretched. This induces unintended deformations, increases the amount of air required to increase the pressure, weakens the structure, and can lead to bursting of the structure. So, designing soft pneumatic robots from rubbers and polymers is a balancing act between optimizing for force or deformations.

An alternative to using rubbers or polymers is to use thin non-stretchable materials which can easily be deformed but aren't stretchable[10-13]. The non-stretchability of the material means that a pneumatic volume by itself would deform only minimally whether it is pressurized only slightly above the atmospheric pressure or whether it is pressurized significantly more. For this reason, they can be considered as a kind of inflatable structure, and their motion should be created through the equilibrium between the inflatable element and a passive structure or an active structure such as a second inflatable element. The design of inflatable elements for use in robotics is not yet a mature field. This book explores the design and modelling of different types of pneumatic actuators and robots making use of thin films.

Chapter 2 looks at the design of vacuum-based pneumatic artificial muscles using a combination of thin films and rigid 3D printed elements. It explores different design embodiments of this concept including basic linear actuators, linear actuators with constant force, and modular designs which can be combined to produce cooperative behaviors or multi-functional actuators, and numerical models are proposed for each design. The main advantage of this concept is that vacuum-based artificial muscles can produce very large deformations (>90% contraction ratio) while lifting heavy payloads over their entire range of deformation.

Chapter 3 introduces the concept of inflatable joints and bi-directional twisting elements for integration into soft inflatable robotic arms. The joints are capable of 2-DOFs bending and have a large range of motion while the twisting elements use antagonistic inflatable chambers to control their bidirectional motion. The bending joints were integrated into 6-DOFs robotic arms which can be controller antagonistically using a single pressure source and using one regulator per antagonistic pair of chambers, and its fabrication was scaled up to build an inflatable robotic arm with a length of 5 meters. A torsional wrist element was then added to this concept to form a 7-DOFs robotic arm with human-like capabilities.

Chapter 4 builds upon the concept introduced in chapter 3 by replacing the chambers of the inflatable joint by an origami chamber which can produce a steadier force throughout the deformation and uses a rigid structure to constrain the deformation of the joint. This makes the structure easier to control. Two joints are introduced where one uses a passive element to produce an antagonistic force and another uses two antagonistic chambers to control the position. These are then used in a 3-DOFs robotic arm capable of pick-and-place operations.

Chapter 5 focuses on the basic behavior of buckling inflatable tubes and their numerical modeling. These tubes exhibit several interesting behaviors such as having a bistable behavior within a certain range of length and producing a snapthrough motion when reaching certain breakpoint in length which differ depending on whether they are in the buckled or unbuckled state. The numerical model uses the principle of conservation of energy and assumes that inflatable tubes will follow the configuration with the highest local volume from their current state.

Chapter 6 focuses on harnessing the behavior of buckling and unbuckling multi-chamber inflatable tubes for soft robotic applications. A bi-stable structure using two chambered inflatable tubes was proposed capable of rapid triggerable motions, and bending actuators using multi-chamber tubes coupled to a flexible skeleton were adapted into a soft robotic hand capable of lifting objects 100 times heavier than the hand itself. These examples demonstrate how nonlinearities can be used to augment the capabilities of soft robots.

This book delves into the innovative use of inflatable elements as a transformative approach to creating lightweight structures with remarkable performance capabilities, particularly in the realm of actuation. By exploring the unique properties of inflatable materials—such as their flexibility, adaptability, and efficiency, it demonstrates how these elements can be harnessed to design and construct soft robotic systems. These systems are not only capable of performing complex tasks traditionally handled by rigid robots but also do so at significantly reduced costs. The text provides a comprehensive overview of the principles, design strategies, and applications of inflatable soft robotics, showcasing how this emerging technology has the potential to rival and even surpass conventional rigid robotics in certain scenarios, opening new possibilities in fields such as patient care and elderly care, for implementation as household robots, and to explore extreme environments.

Chapter 02

Vacuum-based soft actuators

2.1 Background

Soft actuators have several advantages over conventional rigid actuators. One of the advantages is that soft actuators cause minimal damage even when they collide with the environment, as they can conform to the environment with their soft bodies. Another advantage is that soft robots made of soft materials such as polymers and films can have many degrees of freedom that enable complex and continuous motions [14-18], and unconventional deformation, enhancing the versatility of the system [19-23].

Many soft linear actuators have been developed, and they show remarkable characteristics that have not been found in traditional rigid robots. There are soft actuators that make use of heat and explosion. The shape-memory alloy (SMA) offers high specific work (~2 kJ/kg) [24, 25], while SMA coils produce relatively large strain (~50%) [26]. Twisted and coiled can produce a good strain (~50%) similar to SMA coils, while being made of fibers [27]. Some actuators utilize a mixture of explosive gases that generate high pressure and thus flow through its pneumatic channels, enabling fast movement (~3 m/s) compared to other soft actuators. Some soft actuators use pneumatic pressure as their power source. Pouch motors and pneumatic artificial muscles (PAMs) have a simple structure, but they can produce various motions under positive pressure [10, 16, 28-33]. Series PAMs are composed of PAMs connected in series, and they can offer many degrees of freedom to drive continuum manipulators [34]. Other than those actuators, many origami-based and polymer-based actuators utilize pressure to generate diverse deformations and wide working range [35-39]. Also, there are many soft actuators such as dielectric elastomer actuators (DEAs) that can be used as a starfish-shaped gripper [40], phase-change material-based (PCM) actuators that alter their shape under an external trigger [41, 42].

However, previous soft actuators have limitations that prevent their wide adoption in the real world. One of common issues is the significant trade-offs between their force and displacement as most soft actuators have a force profile that becomes near zero at its maximum working range, which restricts their potential application [43-55]. Other than that, thermally driven actuator like SMA have low energy efficiency (~2%) [56], and high operating temperature (~100℃), which makes them dangerous in proximity [57]. Also, twisted-coiled artificial muscles (TCAs) require pre-tension to actuate [58]. Vacuum-based artificial muscles made from elastomers require thick vertical beams to obtain the desired deformation, which making it produce small useful work due to elastic energy stored during their actuation [59, 60]. Another actuator that utilizes the expansion of vertical axis under horizontal compression, and its force output is affected by the softness of the horizontal beams like the previous vacuum actuator [61]. Other than that, DEAs require a high operating voltage (>1 kV) and corresponding circuit [62, 63], PCM actuators are slow and take several minutes to complete one actuation cycles [42, 64, 65].

As mentioned in the previous paragraph, most soft actuators show the trade-offs between their force and displacement, which means they exert a large force when they are at one end of their working range, while they exert a small force when they are at the other end of the range. This characteristic can be problematic when they drive a gripper that is supposed to handle various sizes of objects as they may damage large objects or fail to grasp small objects due to the characteristic. Advanced modeling and vision-based sensing have been proposed to remedy this issue, but those approaches require a sophisticated sensor system and cannot be applied when force output is insufficient to grasp objects. To resolve this issue, several constant force mechanisms (CFMs) have been developed, including a gravity-balancing mechanism [66], a spring-based [67], and link-based mechanism [68, 69]. However, gravity-balancing mechanisms and spring-based CFMs are rigid and cannot directly produce a linear motion, and link-based CFMS cannot change their output force easily. A DEA-based soft constant force actuator is also proposed, but its force output is too small (~1N) [70].

Although previously developed soft actuators have remarkable characteristics, their functionalities are limited to a certain degree as their behaviors are determined in the manufacturing process and cannot be modified on-the-fly. One of the solutions for such an issue would be to apply modular design concepts where simple structures are easily and reversibly combined to build complex systems[71]. Several modular systems that exploit application-specific standardized connectors[72], push-fittings and screw threads [73, 74], magnets[75], and mechanical fasteners[76] have been proposed to allow basic modification of their behavior, but further research is required as the functionality of the modules is generally limited to one or two modes of deformation and their performance is often insufficient for real-world applications.

To resolve these issues, origami-based vacuum pneumatic artificial muscles (OV-PAMs) and three variants that each add extra functionality to the OV-PAMs are presented. In chapter 2.2, the OV-PAMs that utilize vacuum pressure to generate both large force and high contraction ratio are introduced. An analytical model is presented to provide insight of their force and speed, and experiment results follow to verify the proposed model. With the unique characteristics of the OV-PAMs, they can achieve extreme performance, lifting tens of kilograms over the entire working range and reaching a contraction ratio of 99.7%. Also, these actuators can convert the pressure-volume work into mechanical work to maximize their efficiency and operate when a power source is limited in an off-grid environment.

In chapter 2.3, armor-based stable force pneumatic artificial muscles (AS-PAMs) are introduced. The AS-PAMs implement 3D-printed parts named armor and film-based constraints that alter the volumetric profile and thus force output of the actuators so that their force profile becomes slightly concave while increasing along with the contraction ratio. By exploiting this characteristic, the AS-PAMs can make use of a new actuation strategy named pre-vacuuming to boost their power and speed and ensure a wider effective working range with their consistent force.

In chapter 2.4, reconfigurable origami-based vacuum pneumatic artificial muscles (ROV-PAMs) are introduced to expand the functionality and versatility of the actuator by implementing components named assisting plates and magnetic connectors. The ROV-PAMs consist of six actuating modules and three supporting modules which can be assembled in arbitrary order. With those modules, the ROV-PAMs can expand their working range, create complex geometries, and enhance their performance.

2.2 Origami-based vacuum PAMs

2.2.1 Introduction

Future robots that maneuver near humans will require actuators that can offer a high contraction ratio, large force, and acceptable efficiency so that they can overcome any challenges they might encounter in real-world scenarios. Although previous soft linear actuators have proved that they can achieve some of the requirements, no actuator can meet all the requirements at the same time as discussed in the previous chapter.

In this chapter, we present origami-based vacuum pneumatic artificial muscles (OV-PAMs), the new linear actuators that utilize negative pressure to produce linear contraction. Unlike other pneumatic soft actuators that have a limited contraction ratio and force diminishing to zero throughout the contraction, OV-PAMs can offer both a high contraction ratio (>80%) and a large force (>100 N). Also, as the OV-PAMs are made of a thin film that does not store elastic energy during deformation, they can directly convert pressure-volume work into mechanical work to achieve actuator efficiency of near 100%, and system efficiency of 16% with the optimized dimensions.

In the next section, the manufacturing process and modeling of the performance and efficiency of OV-PAMs will be presented, followed by experiments and demonstrations that verify the model and show the potential of the OV-PAMs.

2.2.2 Manufacturing and modeling

OV-PAMs consist of two plates and a chamber connecting the two plates. The chamber is made of thin film, and contains transversal reinforcements evenly spaced to prevent collapse of the chamber and keep the cross-sectional area of the chamber relatively consistent, which results in a large contractile force throughout the actuation. To maximize the contraction ratio, the chamber is folded in a modified Yoshimura pattern to allow the chamber to fold in an even and ordered manner until the actuator is fully contracted. Throughout the following sections, the 3D-printed triangular polylactic acid (PLA) plates and polyvinyl chloride (PVC) film with a thickness of 70um are used to build the actuators, although the use of any materials will produce the same result if they have similar properties.

To build the OV-PAMs, a PVC film is taped on each side of the edge to create a cylinder (Fig. 2-1), and the reinforcements are positioned in the cylinder using tape. Then, each end of the cylinder is cut to form flaps that are folded onto the top and bottom plates and taped onto the plates. Finally, the side sections of the cylindrical chamber are pushed manually to define the pattern of deformation of the film during actuation.

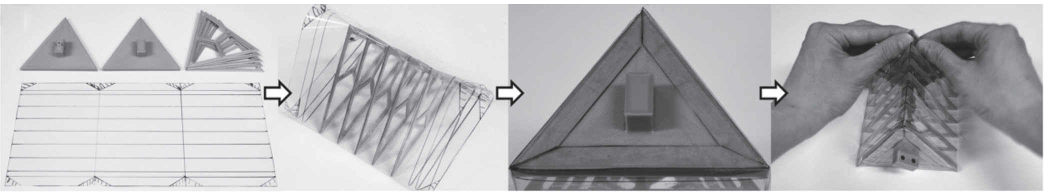

Figure 2-1. Manufacturing process of OV-PAMs.

The performance and efficiency of the actuator can be predicted using a quasistatic model derived from the law of conservation of energy. To do so, we first derive the two volume equations of the actuator at low $(< \left(1 - \frac{2}{\pi}\right) \approx 36.3\%)$, and high $(> 36.3\%)$ contraction ratio. The volume in the former case can be approximated by a triangular prism where each side folds inward to shape a cylinder (Fig. 2-2). Based on the volume of the cylindrical shape as a function of θ derived for the previously developed pouch motors, the overall volume becomes:

$$V_1(\theta) = \frac{\sqrt{3}}{4} D^2 h \frac{\sin\theta}{\theta} - \frac{3h_0^2 D}{4}\left(\frac{\theta - \cos\theta\sin\theta}{\theta^2}\right) \tag{2-1}$$

where V_1 is the volume of the chamber at a low contraction ratio, D is the side length of triangular plates, h is the height of each section between two neighboring reinforcements, h_0 is the initial height of each section between two neighboring reinforcements, θ is the central angle of the circular segment of the cylindrical sides.

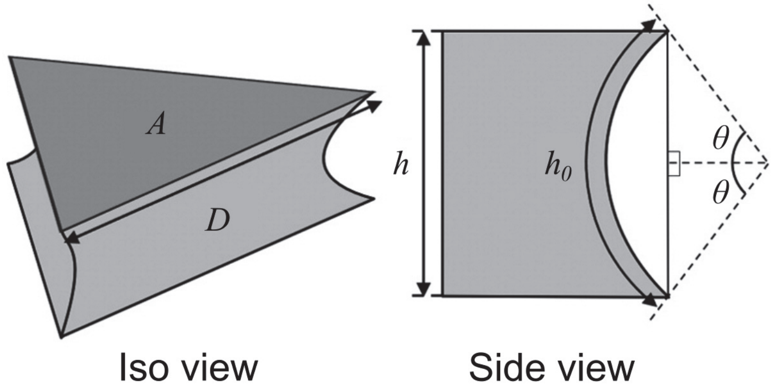

Figure 2-2. The shape of the actuator in the isometric and side views.

When the contraction ratio is higher than 36.3%, θ becomes 90° and the film starts to stick to the reinforcements, top and bottom plates, reducing the effective dimensions and the cross-sectional area of the chamber to some extent. Unless the initial height between reinforcements h exceeds $\frac{D}{\sqrt{3}}$, the cross-sectional area remains nonnegative, and the volume of the chamber can be derived by replacing D with $D-\frac{\sqrt{3}}{2}(2h_0-\pi h)$ and θ with 90°, which results in:

$$V_2(h)=\frac{\sqrt{3}}{4}\left(D-\frac{\sqrt{3}}{2}(2h_0-\pi h)\right)^2 h-\frac{3\pi}{8}h^2\left(D-\frac{\sqrt{3}}{2}(2h_0-\pi h)\right) \tag{2-2}$$

where V_2 is the volume of the chamber at a high contraction ratio. Then, the law of conservation of energy can be written as follows:

$$F_1(\theta)=P\frac{dV}{dh}=P=\frac{\frac{dV}{d\theta}}{\frac{dh}{d\theta}}=P\left(\frac{\sqrt{3}}{4}D^2+\frac{3}{2}h_0D\frac{\cos\theta}{\theta}\right) \tag{2-3}$$

$$F_2(h)=P\left(\frac{\sqrt{3}}{4}\left(D-\sqrt{3}\,h_0+\frac{\sqrt{3}\,\pi h}{2}\right)\left(D-\sqrt{3}\,h_0+\frac{3\sqrt{3}\,\pi h}{2}\right)-\left(\frac{(D-\sqrt{3}\,h_0)\pi}{4}h+\frac{3\sqrt{3}\,\pi^2}{16}h^2-\frac{\sqrt{3}}{2}h^2\right)\right) \tag{2-4}$$

where F_1 and F_2 are the forces of the chamber at the low and high contraction ratio, respectively, P is the negative pressure applied to the chamber. By assuming the payload and flow rate of the system is constant over a short time, the time to actuate the actuator between two states based on the volume differences between the two states becomes:

$$\triangle t = \frac{1}{Q}| V_i - V_{i+1}| \rightarrow t_{total} = \sum_{i=0} \frac{1}{Q}| V_i - V_{i+1}| \tag{2-5}$$

where t_{total} is the time required to actuate the actuator, Q is the flow rate of the pump and V is the volume of the actuator. Similarly, the energy consumed to actuate the actuator between two states becomes:

$$\triangle E = P_i \triangle t \rightarrow E_{total} = \sum_{i=0} \frac{P_i}{Q}| V_i - V_{i+1}| \tag{2-7}$$

where E_{total} is the overall system energy consumption, and P_i is the average power input of the pump during actuation.

2.2.3 Basic characteristics of OV-PAMs

In this section, the basic characteristics and effects of each dimension of OV-PAMs on their performance are presented through a set of experiments. In the first experiment, payloads ranging from 1 to 14 kg were attached to the end of an actuator with a side length of 90 mm, a reinforcement thickness of 1 mm, and a total active length of 90mm. Then, a vacuum pump was connected directly to the actuator to measure its maximum contraction ratio depending on payloads (Fig. 2-3). In the experiment, the actuator could reach a contraction ratio of nearly 90% with a payload up to 12 kg while the actuator weights only 53.0 g, which means it was capable of producing a full contraction even with a payload more than 200 times greater than its own weight. There is a slight increase in contraction ratio for payloads less than 7 kg, which may result from stretching of the film. Meanwhile, the contraction ratio started to decrease for payloads of 13 kg or higher, and further experiment was limited due to actuator failure. This experiment demonstrated that the OV-PAMs can produce both a large force and a high contraction ratio, which is one of the unique characteristics of this actuator that cannot be found in other actuators.

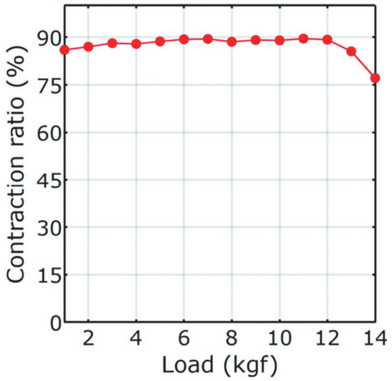

Figure 2-3. Contraction ratio versus load at maximum pump pressure.

In the second experiment, the blocked force as a function of contraction ratio and vacuum pressure was measured (Fig. 2-4). During the experiment, the free end of the actuator from the previous experiment was attached to a fixed element whose position was varied, and the vacuum pressure ranging from 10 to 50 kPa in increments of 5 kPa was applied to the actuator until a force exceeded 120 N to prevent actuator failure. The blocked force increased linearly with an increase in pressure throughout most of the deformation and corresponds very well with our proposed model. Plotting the data as isobaric curves shows that for a fixed pressure the force produced by the actuator drops sharply in the initial actuation phase but stabilizes in the later phase, producing a large contractile force (Fig. 2-5), which explains how the OV-PAMs can produce both large force and high contraction ratio unlike other actuators.

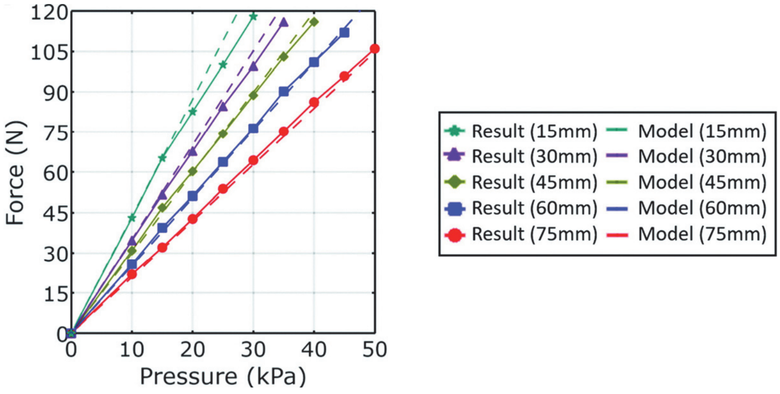

Figure 2-4. Blocked force at different contraction lengths.

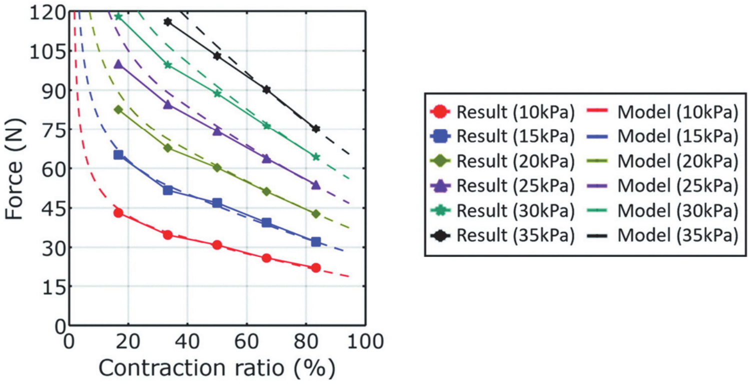

Figure 2-5. Isobaric curves at different pressures.

In the third experiment, the effect of the payload on the contraction ratio as a function of the vacuum was verified by applying payloads ranging from 2 to 8 kg and vacuum pressures ranging from 10 to 60 kPa to the same actuator from the previous experiment (Fig. 2-6). For the 2 kg payload, the actuator reaches its maximum contraction ratio at the smallest pressure and applying higher pressure has not much effect on the contraction ratio. However, a transition region appears for the 4 kg payload, and the region becomes wider along with the payload. This is because the pressure for the actuation force at the highest contraction ratio to reach the payload becomes higher as the payload increases, and it causes the behavior of the OV-PAMs largely depends on the payload as predicted by the model. Although some visible errors can be found in the high contraction ratio region that are possibly caused by manufacturing errors or inaccuracies in experiment parameters, the result shows that the model can predict the effect of the payload on the contraction ratio and pressure of the actuator.

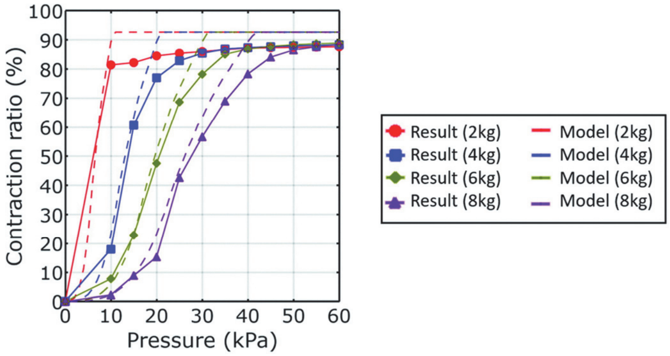

Figure 2-6. Contraction ratio at different pressures with different payloads.

In the fourth experiment, the effect of the number of reinforcements with the same initial layer height on linear displacement was verified by applying the payload ranging from 2 to 8 kg and vacuum pressure ranging from 10 to 60 kPa to actuators with the same initial layer height, but different numbers of reinforcements ranging from zero to five and total lengths ranging from 15 to 90 mm (Fig. 2-7). The results showed that the behavior of the actuators is quite similar in terms of force versus contraction ratio regardless of the total length of the actuator, as long as the initial layer height is the same, which allows us to select the displacement and force of the actuator independently and gives us more freedom when designing the actuator. It can also be seen that there is a weak negative correlation between the maximum contraction ratio and the length of the actuator. This is because of the space occupied by the reinforcements and can be resolved by using thinner reinforcements if needed.

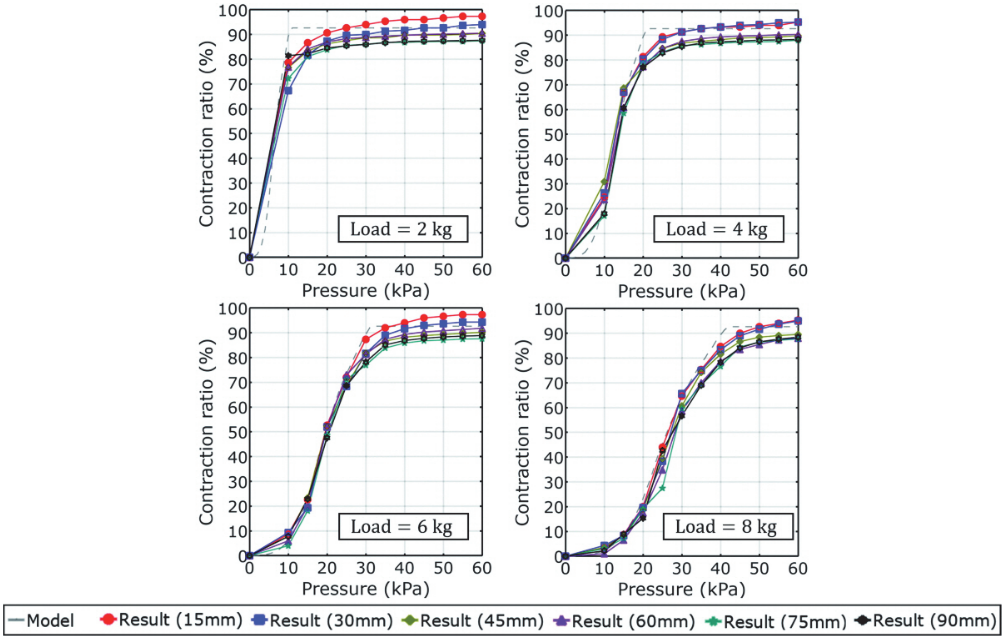

Figure 2-7. Contraction ratios for actuators with different lengths.

The fifth experiment is about the effect of the initial layer height on the contraction ratio. In this experiment, the same payloads and vacuum pressures from previous experiment were applied to actuators with the same total length of 90 mm but different initial layer heights of 10, 15, and 30 mm (Fig. 2-8). As shown in the figure, the actuator with longer initial layer height shows higher maximum contraction ratios as it contains less reinforcement. However, the actuator with a longer initial layer height required higher vacuum pressure to produce the same contraction ratio under the same conditions, and the actuator with an initial layer height of 30 mm and a payload of 8 kg failed once the vacuum pressure reached 30 kPa, possibly because of the large stress on only two reinforcements. These results show the relationship between the initial layer height and the contraction ratio, and that it is vital to select the right dimensions when designing the actuator.

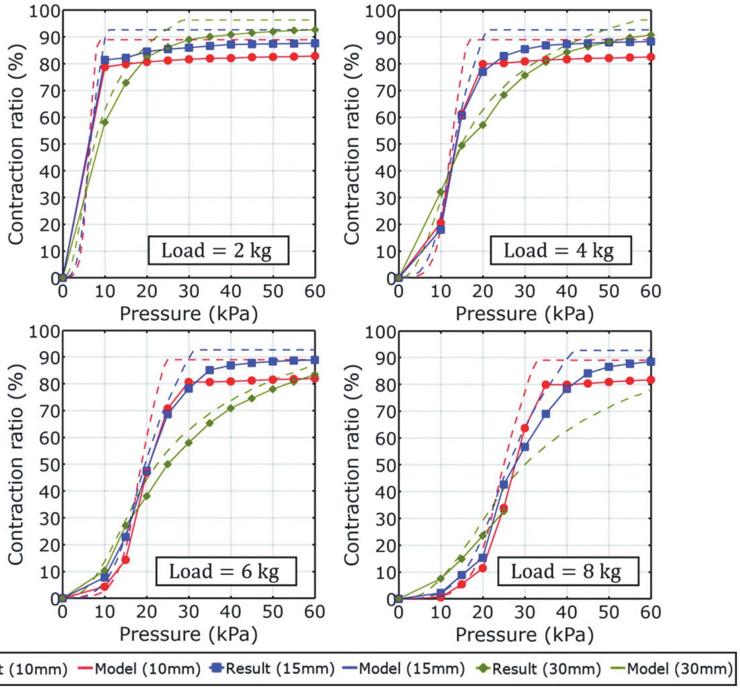

Figure 2-8. Contraction ratios for actuators with different initial layer heights.

In the sixth experiment, the effect of side length on contraction ratio was verified. As shown in the force model, the actuation force equation has two terms. Since the second term diminishes rapidly in the initial phase of actuation while the first term, which is proportional to the square of the side length, remains throughout the entire phase, it is possible to scale the actuation force by altering the side length. To show that, the same payloads and vacuum pressures were applied to actuators with the same dimensions but different side lengths of 90, 120, and 150mm (Fig. 2-9). As predicted by the model, all actuators behave similarly when the payload is light, but actuators with short side length show a wider transition region than those with long side length as a payload becomes heavier. The largest actuator could reach a contraction ratio of 85% with an 8 kg payload at only 10 kPa of vacuum pressure, which shows the high potential of OV-PAMs for producing large force with a portable pump and low vacuum pressure. These are highly valuable characteristics for soft actuators that operate near humans as a portable pump enables a light and versatile actuation system and low-pressure actuation reduces the chance of injury in the case of an unexpected accident.

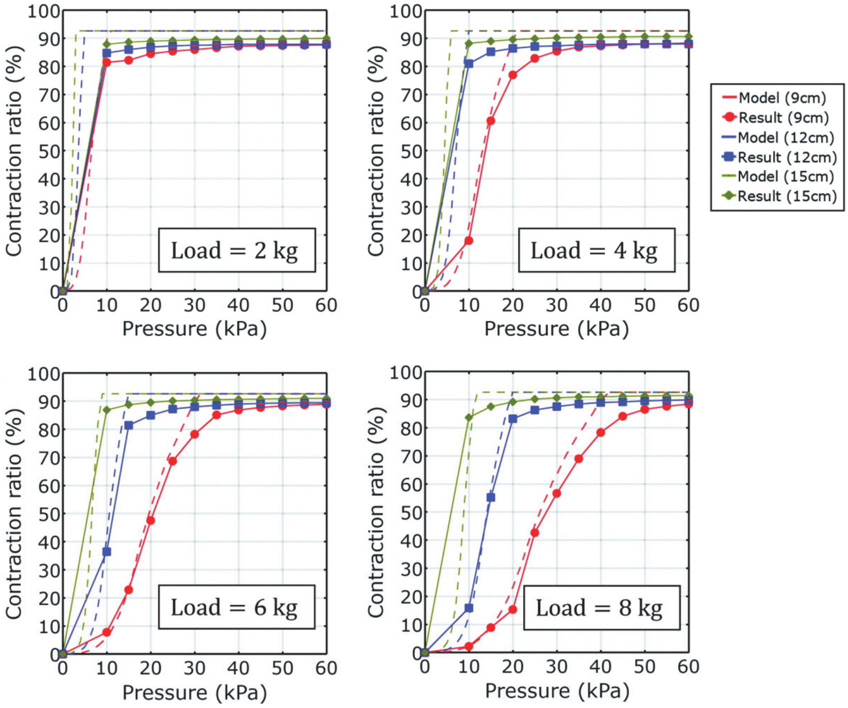

Figure 2-9. Contraction ratios for actuators with different side lengths.

2.2.4 Speed and energy efficiency of OV-PAMs

In this section, the actuation speed and effects of each parameter of the actuation system on the efficiency of OV-PAMs are presented. In the first experiment, payloads ranging from 2 to 10 kg were attached to the end of an actuator with an initial layer height of 30 mm, a side length of 90 mm, and a total length of 60 mm. Then, a small vacuum pump was connected directly to the actuator to observe the actuation speed (Fig. 2-10). On the one hand, the results showed that the actuator with a heavy payload moved slightly slower than predicted in the later phase of the actuation. This is because the heavy payload requires high vacuum pressure to actuate, which lowers the flow rate of the pump and amplifies the effect of any leaks or manufacturing errors. On the other hand, the results showed that the actuator with a light payload moved faster than predicted. This is possibly caused by the difference in actuator position at rest, which caused the increased contraction ratio for heavy payloads in the previous experiment for contraction ratio at maximum pump pressure. Overall, the results closely followed the model's prediction indicating that the actuators can convert pressure-volume work directly into mechanical work without any significant loss, allowing us to predict their efficiency and optimize their dimensions.

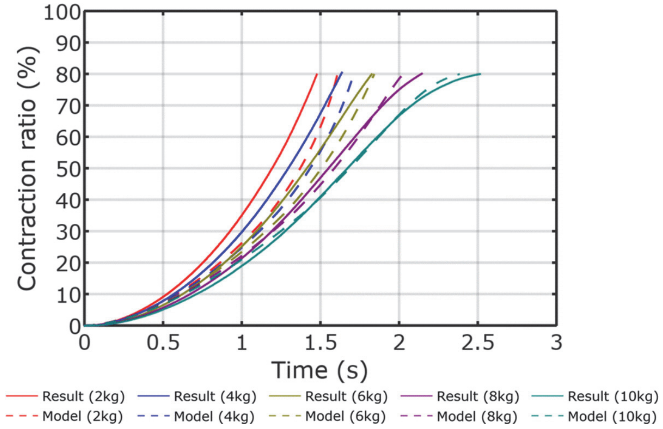

Figure 2-10. Contraction ratio versus time for an actuator with payloads of 2, 4, 6, 8, and 10 kg

In the second experiment, the effect of initial layer height on efficiency as a function of payload was verified (Fig. 2-11). In this experiment, actuators with the same edge length of 90 mm, but different initial layer heights of 20, 30, and 40 mm were built and tested with a payload of 2 kg. Then the payload increased up to 14 kg in increments of 2 kg until the actuator could not lift the payload. The results showed that increasing the initial layer height has a negative effect on both the maximum payload and efficiency, such that increasing the initial layer height does not have any tangible advantages for efficiency. This is because the actuator with a higher initial layer height requires larger vacuum pressure, which results in a low flow rate. However, it is to be noted that reducing the height too much would limit the maximum contraction ratio significantly, so selecting the right initial layer height is crucial to balancing performance and efficiency.

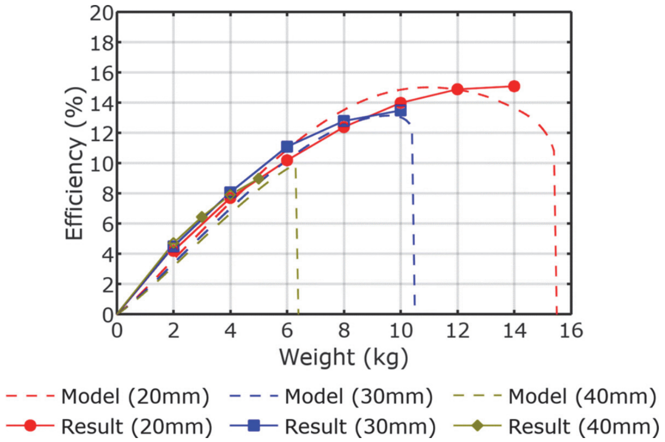

Figure 2-11. Effect of the initial layer height on the efficiency of the system

In the third experiment, the effect of side length on efficiency as a function of payload was verified (Fig. 2-12). Similar to the previous experiment, actuators with edge lengths of 80, 90, and 100 mm were built and tested starting from a payload of 2 kg, until the actuator failed. From the result, it can be seen that all actuators have their optimal efficiency at different payloads, and that their optimal payloads are near their maximum payload. Both their maximum payloads and optimal payloads scale with their side length, which indicates that an actuator with a short side length is optimized for a lighter payload, while an actuator with a long side length is optimized for a heavier payload. Using this result, the OV-PAMs can be optimized so that the actuators operate near their maximum payload with optimal efficiency.

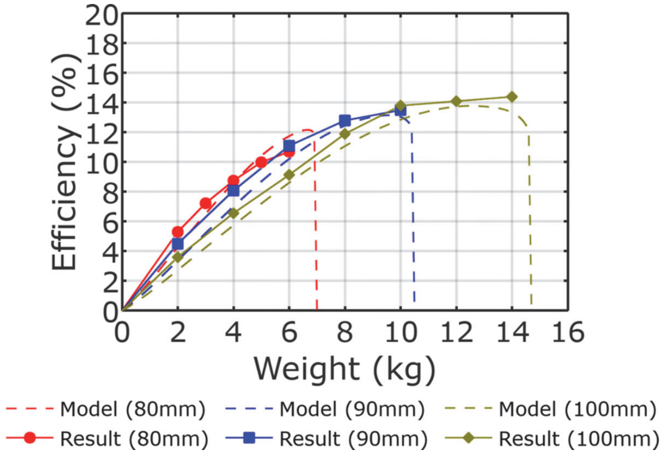

Figure 2-12. Effect of the edge length on the efficiency of the system

In the fourth experiment, the effect of pumps on efficiency as a function of payload was verified (Fig. 2-13). To illustrate how the pump affects the efficiency of the actuator, three pumps were tested with an actuator from the actuation speed experiment. During the experiment, the same payload conditions from the previous experiments were applied to the first two pumps, while payloads of 0.5, 1, 1.5 and 2 kg were applied to the third pump as the maximum vacuum pressure of the pump is much lower than the other pumps. The results show that the use of different pumps results in different efficiencies as each pump has different flow characteristics. Although they have different efficiency profiles, each of them has an optimal payload where its efficiency becomes the highest among the three, which indicates that choosing the right pump is also crucial when designing an optimal actuation system.

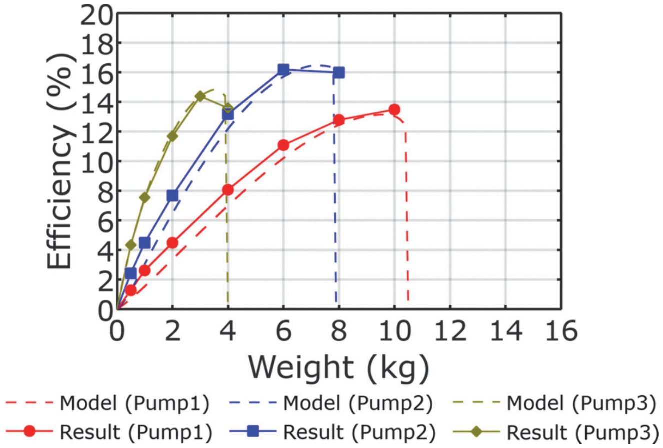

Figure 2-13. Effect of the pump on the efficiency of the system.

2.2.5 Testing of OV-PAMs

In this section, the two actuation systems using an OV-PAM are presented to show the potential of the OV-PAMs to be a driving element for off-grid system. The first actuation system consists of a single solar panel, a portable pump and an OV-PAM (Fig. 2-14). The solar panel generates a voltage up to 17.7V which is directly supplied to the pump to generate vacuum pressure. With this simple configuration, the actuator successfully lifted a payload of 10 kg in 4 seconds. The second system consists of a single lithium-ion battery, a miniature pump, and an OV-PAM. The battery supplied a voltage of 3.7V to the pump to generate a vacuum pressure, and the actuator achieved a full contraction with a payload of 1 kg in 140 seconds (Fig. 2-15). These simple actuating systems could be made as the OV-PAMs can provide both large force and high performance even when a power source is limited. With the OV-PAMs, it is possible to build an off-grid system with a significant payload using minimal equipment, which shows the potential of OV-PAM to be used in a wide range of applications where compact system is desired.

Figure 2-14. The actuator with a payload of 10 kg driven using a 17.7 V solar panel.

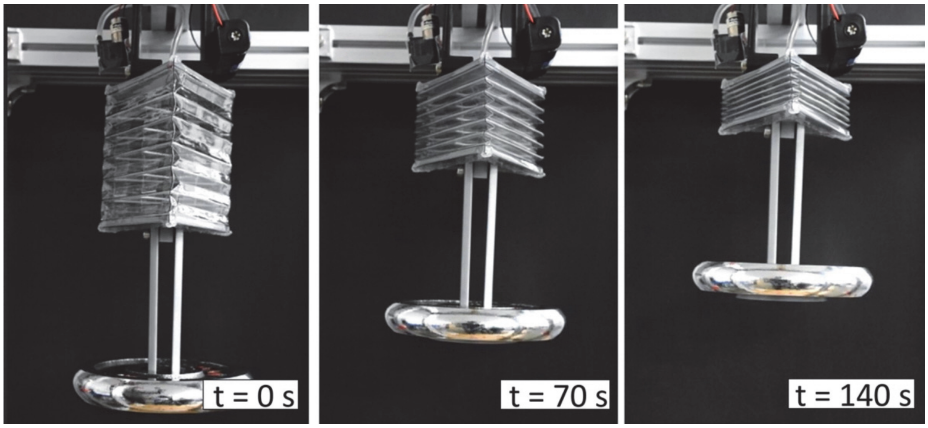

Figure 2-15. The actuator with a payload of 1 kg driven by a miniature pump using a 3.7 V lithium-ion battery.

The dimensions of the OV-PAMs can be tailored to push their performance to an extreme level. To show that, two OV-PAMs with unique dimensions were built for extreme contraction ratio and force, respectively. In the previous experiment, the OV-PAMs showed a maximum contraction ratio of about 90% because their contraction ratios were limited by the thickness of the reinforcements. This limitation can be overcome by using flexible top and bottom plates that bend toward each other under vacuum pressure, allowing the actuator to reach the 100% contraction ratio in theory.

To verify that, an actuator with a top and bottom plate thickness of 1 mm, an edge length of 90 mm, and a reinforcement thickness of 1 mm was built and tested with a payload of 2 kg (Fig. 2-16). Under vacuum pressure of 10 kPa, the actuator was able to produce a contraction ratio of 90%, and the ratio kept increasing along with the applied vacuum pressure until it reached 99.7% (Fig. 2-17). This contraction ratio is the largest achieved among all surveyed soft linear actuators, which shows that the OV-PAMs can produce an extremely high contraction ratio.

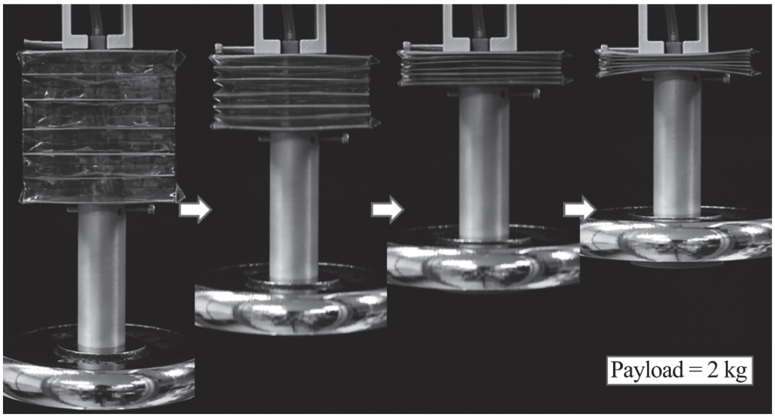

Figure 2-16. Actuation of OV-PAM reaching a contraction ratio of 99.7% with a payload of 2 kg,

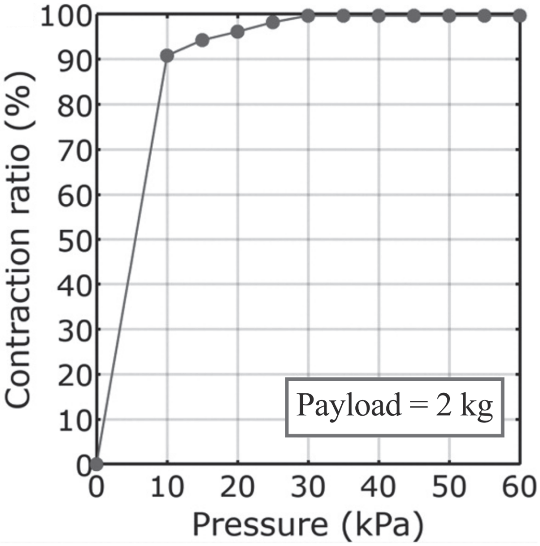

Figure 2-17. Contraction ratio versus pressure of an actuator with flexible top and bottom plates.

The actuation force of the OV-PAMs can be scaled without sacrificing their contraction ratio simply by enlarging their side length. To demonstrate how much force the OV-PAMs can produce, an actuator with a side length of 150 mm was fabricated and tested how much payload it can lift using a portable pump (Fig. 2-18). In the experiment, the actuator could lift a payload of 40 kg for its full contraction length, although its own weight was only 160 g. From this result, a graph of the relationship between the payload and contraction ratio of the soft pneumatic actuators can be derived (Fig. 2-19). Here, the distance from the origin means the performance of the actuator, and the

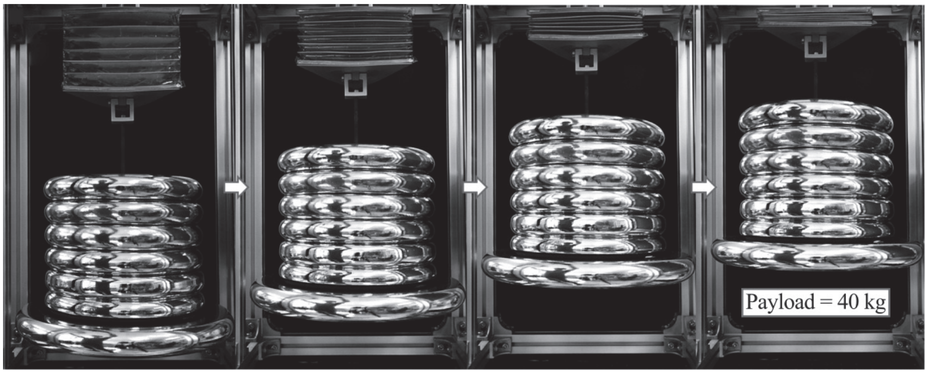

Figure 2-18. Actuation of an actuator with a side length of 150mm and a payload of 40 kg.

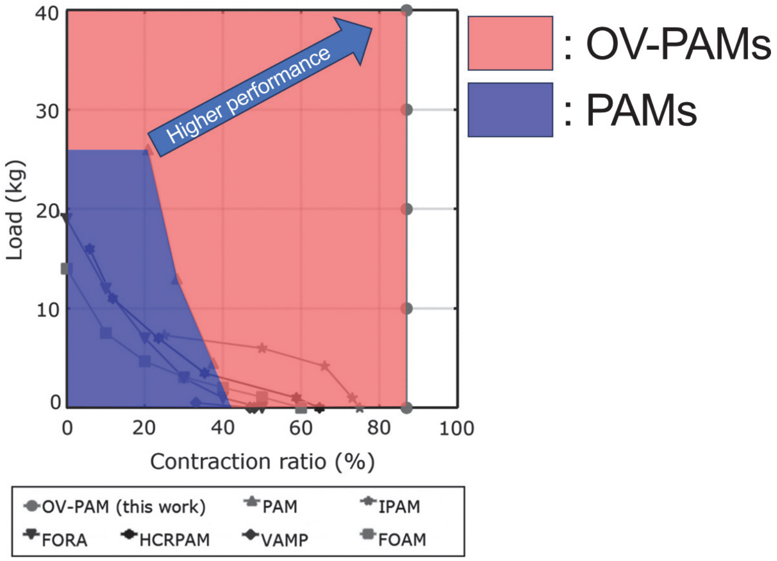

Figure 2-19. Comparison of OV-PAM with existing pneumatic linear actuators.

area of each actuator surrounded by the corresponding points means the combination of payload and contraction ratio that the actuator can offer. The OV-PAMs and PAMs are highlighted to show the differences between the two, and the two examples clearly show that the OV-PAMs can offer an extreme performance and are suitable for a wider range of applications than other actuators, including PAMs.

2.3 Armor-based stable force PAMs

2.3.1 Introduction

In the previous chapter, the characteristics and performance of the OV-PAMs were presented. Although the OV-PAMs can produce large force over the whole actuation range as proved by experiments, they still share one common point with other soft pneumatic actuators: their isobaric force diminishes throughout the actuation. Adding additional components such as constant force mechanisms could change the overall force profile, but it makes the system bulky and complex, which is not an ideal solution, especially when compactness is required.

In this chapter, an actuator named armor-based stable force pneumatic artificial muscles (AS-PAMs), which implement 3D-printed plates named armor, and film-based constraints that guide the deformation pattern are presented. The model of the AS-PAMs shows that the force profile of these actuators remains almost straight throughout their entire actuation range unlike other soft pneumatic actuators, and the experiments verify that the actuators indeed have distinctive characteristics that can make the actuators ideal solutions for constant force generation.

2.3.2 Manufacturing and modeling

The force produced by a pneumatic linear actuator is proportional to the rate of volume change over the rate of length change. In the previous chapter, the OV-PAMs consist of a chamber made of thin film that deforms freely inward under vacuum pressure, which results in a large force early in a low contraction ratio region and a relatively small force in a high contraction ratio region. To change this behavior, 3D-printed components named armor are printed and attached on the side wall of the actuators. These armors prevent the chamber from deforming inward completely, thus the actuators fold outward, resulting in an increasing rate of volume change over its contraction. When the actuators are almost straight, the side walls folding outward causes the volume profiles to increase to create negative contractile force in that region, so film-based constraints are added so that the actuators become slightly folded.

The AS-PAMs consist of top and bottom plates, a chamber made of thin film, reinforcements, rigid armor, and constraints (Fig. 2-20). To manufacture the actuators, the thin film creates a cylinder chamber using tape (Fig. 2-21). Then, the reinforcements and the rigid armor are placed inside the chamber using tape. Afterward, the faces of the armor are pushed outward, and the constraints are placed at the center of each side and are connected to the reinforcements. Finally, the edges of the top and bottom plates are coated with a thin layer of hot glue and sealed to the chamber. The basic structure of the AS-PAMs remains free from any rigid connector despite the rigid armor, and this makes the actuators flexible and compliant, allowing them to deform under external force unlike conventional rigid actuators (Fig. 2-22).

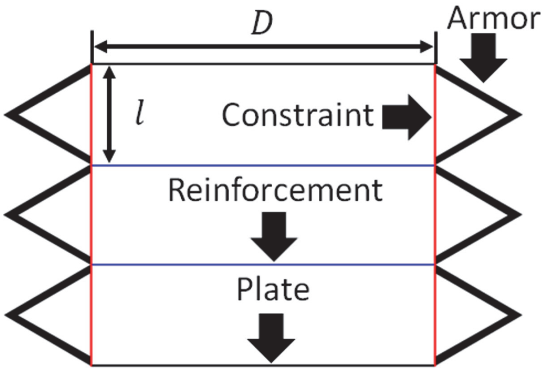

Figure 2-20. Conceptual cross-sectional view of the AS-PAM.

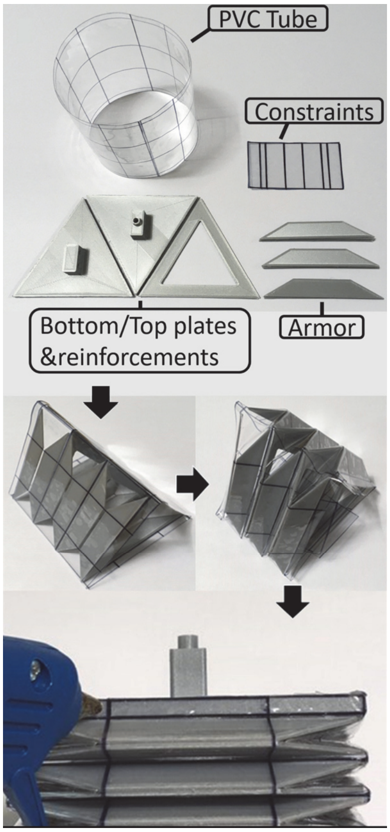

Figure 2-21. Manufacturing steps of the AS-PAM.

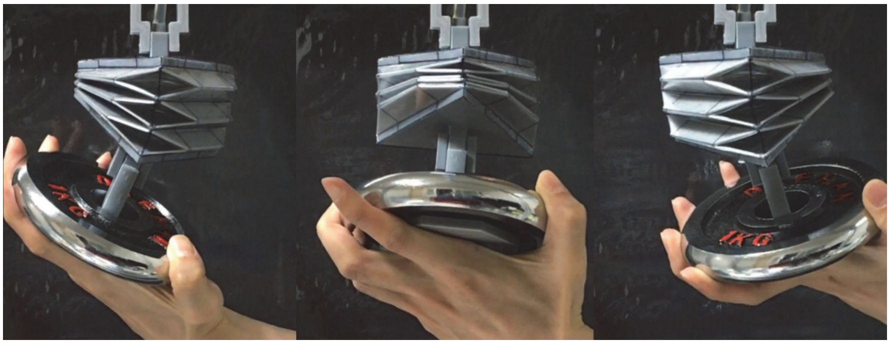

Figure 2-22. An AS-PAM with low stiffness to allow the actuator to deform in response to the environment

The analytical model of the AS-PAMs can be derived using the law of conservation of energy. To do so, the volume of one chamber of the actuators is approximated by the two triangular prism sections, each denoted by a number (Fig. 2-23). Here, the other two sections denoted with the letters "A" and "B" can be ignored as their sizes are similar while their effects on the volume are opposite. With the two sections, the volume of the chamber can be obtained as follows:

$$V = \frac{\sqrt{3}}{4} D^2 h + \frac{3}{4} h\left(D - \sqrt{3}\, h_0\right)\sqrt{h_0^2 - h^2} \tag{2-8}$$

where V is the volume, D is the side length of the triangular plates, h is the height of the chamber, h_0 is the initial layer height of the chamber.

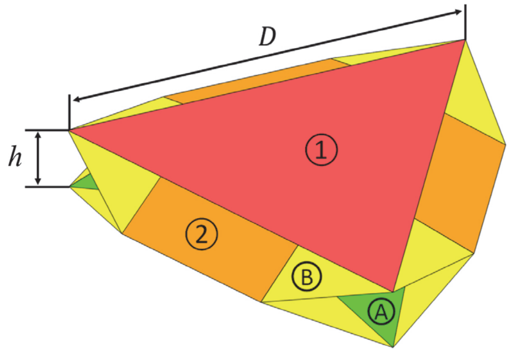

Figure 2-23. Four volume sections of the AS-PAM.

Then, the law of conservation of energy can be written as follows:

$$Fdh = PdV \rightarrow F = P\frac{dV}{dh} = P\left(\frac{\sqrt{3}}{4} D^2 + \frac{3}{4}\left(D - \sqrt{3}\, h_0\right)\left(\sqrt{h_0^2 - h^2} - \frac{h^2}{\sqrt{h_0^2 - h^2}}\right)\right) \tag{2-9}$$

where F is the force produced by the actuators. The volume and force as a function of the contraction ratio was calculated for an actuator with a side length of 90 mm, and an initial layer height of 30 mm (Fig. 2-24). The result shows that the volume profile increases slightly in a low contraction ratio region due to section 2. Because of this, the actuation force of the AS-PAMs in that region becomes negative, which makes the actuators expand under vacuum pressure (Fig. 2-25). To avoid this behavior, a constraint with a length of half of the initial layer height is implemented to limit the actuation region and produce a stable force throughout the chosen region.

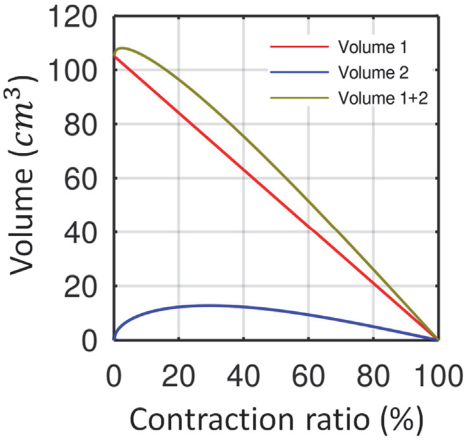

Figure 2-24. Volume profile of the actuator with side length of 90 mm and initial layer height of 30 mm.

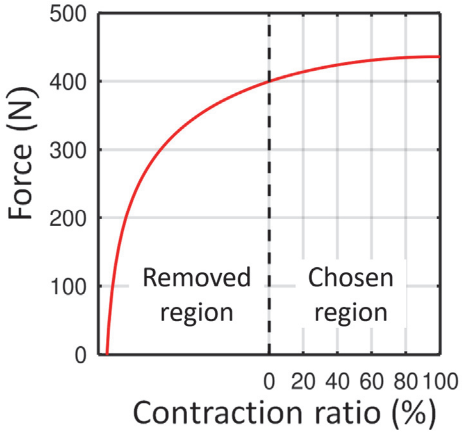

Figure 2-25. Force profile as a function of contraction ratio.

As the actuation force of the AS-PAMs is increasing along with the contraction ratio, the actuation time can be calculated using two terms by assuming that the payload is fixed and that the pressure remains constant throughout the actuation as follows:

$$t_{total} = t_1 + t_2 \tag{2-10}$$

$$t_1 = \sum_{i=a}^{b} \frac{\triangle P}{P_i Q_i} V_i \tag{2-10}$$

$$t_2 = \frac{V_c - V_f}{Q_c} \tag{2-11}$$

$$P_c = P_{atm}\left(1 - \frac{mg}{F_{max}}\right) \tag{2-12}$$

where t_{total} is the total actuation time, t_1 is the duration of the stationary phase, which is the time required for the actuators to reach a critical pressure to actuate, $\triangle P$ is the small pressure range at which the flow rate and volume remain constant, a is the initial pressure divided by $\triangle P$, b is the critical pressure divided by $\triangle P$, P_i is the $\triangle P$ times i, Q is the flow rate at P_i, V is the volume, t_2 is the duration of the moving phase, which is the time required for the actuators to reach the target displacement after the stationary phase, V_c is the volume at critical pressure, V_f is the final volume, Q_c is the flow rate at critical pressure, P_c is the critical pressure, P_{atm} is the atmospheric pressure, m is the mass of the payload, g is the gravitational constant, and F_{max} is the maximum force that the actuators can produce under maximum vacuum pressure.

2.3.3 Results

2.3.3.1 Blocked force

In this section, the effect of contraction ratios and pressures on the blocked forces of the AS-PAMs are presented. For this experiment, an actuator with a side length of 90 mm, and a constraint length of 15 mm was connected to an adjustable displacement constraint to which the force sensor is connected, then tested by applying pressures ranging from 5 to 25 kPa and contraction ratios ranging from 0 to 60% (Fig. 2-26). The blocked force as a function of the pressure shows that the actuator can produce roughly 40 N of linear force per 10 kPa of vacuum pressure regardless of the contraction ratio, which indicates the actuator produces a stable force throughout its entire working range as expected by the proposed model. The largest absolute error of 7.09N, which corresponds to a percentage error of 6.86%, occurred at a pressure of 25 kPa, which is the highest vacuum pressure applied in the experiment. This is because the flexible portions of the actuator, such as the vertices, allow the actuator to produce unexpected deformations.

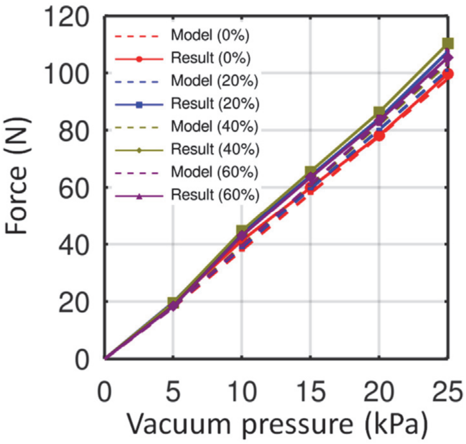

Figure 2-26. Blocked force versus pressure at different contraction ratios.

Using the previous data, the blocked forces as a function of contraction ratio was derived to obtain further insights about the AS-PAMs (Fig. 2-27). The forces show that the actuation force increases slightly for all tested pressures with an increase in the contraction ratio up to 40%, and this increase in force reaches 7.78% for a pressure of 15 kPa and a contraction ratio of 40%. This behavior is a distinctive characteristic of the AS-PAMs as previous soft pneumatic linear actuators all have a force that diminishes throughout the actuation. This could make the actuator uniquely well suited for specific situations such as for maintaining a certain force over the whole actuation range.

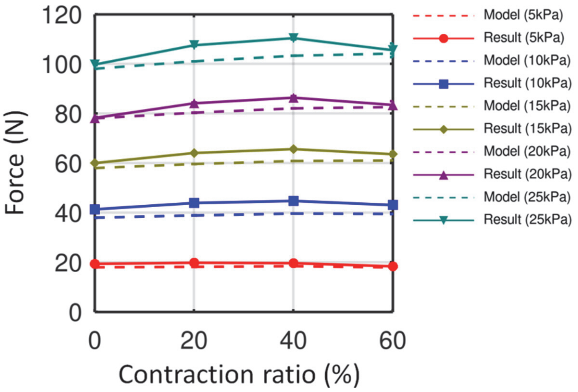

Figure 2-27. Isobaric curves at different pressures.

2.3.3.2 Contraction ratio

In this section, the effect of payloads on contraction ratios of AS-PAMs is presented. For this experiment, the contraction ratio of the actuator was measured with payloads ranging from 5 to 20 kg and vacuum pressures ranging from 5 to 60 kPa (Fig. 2-28). The results show that the contraction ratio of the actuator remains small until sufficient vacuum pressure is applied, then it shows a sharp increase in contraction ratio to roughly 70% at vacuum pressures of 15, 30, 40, and 55 kPa. After the transition, the contraction ratio continues to increase slowly up to 85%, which is the maximum feasible contraction ratio considering the thickness of the armor. Before the actuator shows the sharp transition, the contraction ratio increases slightly, especially for the 20 kg payload. This is because the actuator deforms under high vacuum pressure that is needed to enter the moving phase and is undesirable behavior as it makes the actuators behave in unexpected ways. To resolve this, a material that offers higher strength than PLA to prevent deformation from high vacuum pressure or a larger actuator to lower the critical pressure for a given payload must be used.

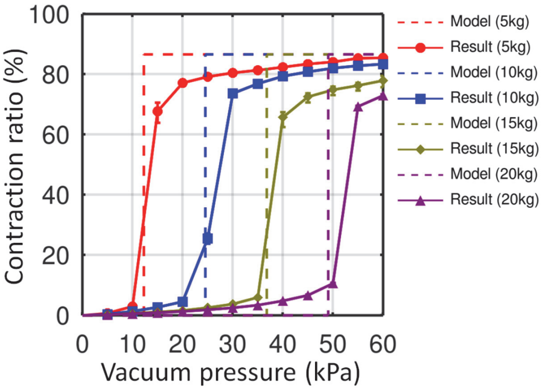

Figure 2-28. Contraction ratio as a function of pressure with various payloads.

Overall, these results agree with the model as the model predicts that there would be a sharp transition at the critical pressures of 12.3, 24.5, 36.8, and 49.1 kPa. It is worth noting that 65% out of 85% of the contraction ratio change happens over a small pressure change from 10 to 15 kPa for a payload of 5 kg, and similar tendencies are observed for other payloads. This shows that the actuator will have a high potential to transit between two fixed points within an extremely narrow pressure range, which allows us to optimize the actuation performance. At the same time, the change in narrow pressure range means that pressure-based position control would be difficult due to the sharp transition of the actuator near the critical pressure point, and flow-based control using a solenoid valve and flow regulator is required if precise position control is necessary.

2.3.3.3 Pre-vacuuming experiment

In this section, the effect of pre-vacuuming on actuation speed and power of AS-PAMs is presented. As shown in the model, the actuation process of the AS-PAMs can be divided into two phases: a stationary and a moving phase. During the stationary phase, the actuator does not move even with an increase in vacuum pressure, and its duration can be calculated as shown in Eq. 2-10. Once the vacuum pressure reaches the critical point, the actuators enter the moving phase and undergo large deformation with little change in its pressure and its duration can be calculated as shown in Eq. 2-11. The total actuation time at normal condition simply becomes the sum of the durations of two phases as shown in Eq. 2-9, but the length of the first phase can be reduced or even eliminated by setting the vacuum pressure inside the actuator to just below the critical pressure and operating only around the pressure, which is called pre-vacuuming.

To demonstrate the effect of the pre-vacuuming strategy, the contraction ratio as a function of time with payloads ranging from 5 to 20 kg was derived with and without pre-vacuuming and then compared with the model. Without pre-vacuuming, the model predicts that the total actuation time would be 0.618, 0.922, 1.44, and 2.50 s for each payload, respectively, while the experiment results show that the actual actuation time was 0.66, 0.94, 1.38, and 2.67 s, respectively (Fig. 2-29). Then, the pre-vacuuming was applied with the vacuum pressures of 10, 20, 35, and 45 kPa for each payload, respectively (Fig. 2-30). The model predicts that the total actuation time would be 0.528, 0.702, 0.918, and 1.59s for each payload, respectively, while the experiment results show that the actual actuation time was 0.41, 0.55, 0.63, and 1.42 s, respectively. These results confirm that pre-vacuuming significantly reduces the duration of the stationary phase and the total actuation time to reach the target position as predicted by the model.

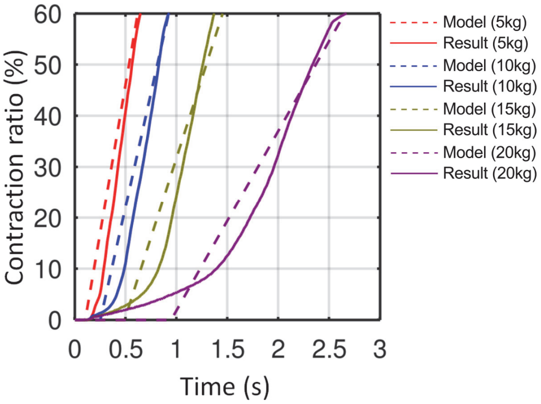

Figure 2-29. Contraction ratio as a function of time without pre-vacuuming.

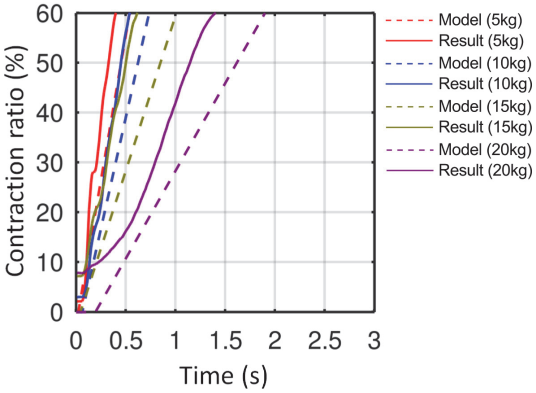

Figure 2-30. Contraction ratio as a function of time with pre-vacuuming.

The previous pre-vacuuming experiment showed that the actuator can produce the same amount of contraction in less time, which means that it enhances the power of the actuator. To illustrate the effect of pre-vacuuming on actuation power, the power as a function of payloads with and without pre-vacuuming is compared (Fig. 2-31). Without pre-vacuuming, the power was 0.668, 0.939, 0.960, and 0.661 W for each payload, while the corresponding power with the pre-vacuuming was 1.04, 1.53, 1.95, and 1.08 W, respectively. For payloads from 5 to 15 kg, the power boost effect becomes larger with increasing payloads, so that the actuator produces twice as much power as before. This trend stopped for the 20 kg case, possibly by unintended deformation of the armor, and deformation below the critical pressure due to high vacuum pressure. Further improvements to the armor will enable the trend to continue for even higher payloads, which allows the actuator to achieve an even faster response time and high-power actuation.

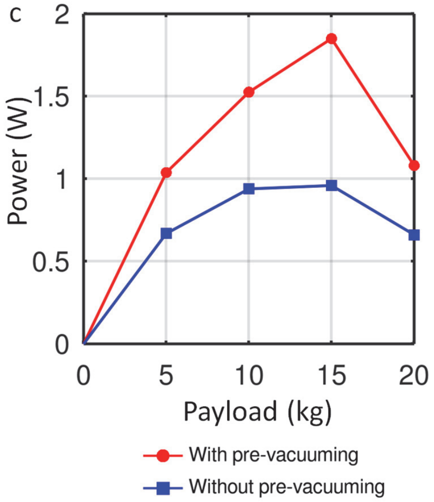

Figure 2-31. Power versus payload of the actuator with and without pre-vacuuming.

2.3.3.4 AS-PAM-based gripper

In this section, two grippers, which are referred to as “normal gripper” and “armored gripper”, are presented to show that the actuation properties of the proposed AS-PAM are significantly different from other soft pneumatic actuators and how this can be helpful for real applications. The normal gripper is made of two OV-PAMs without reinforcements, where one OV-PAM is used to close the jaw of the gripper and produce the gripping force, while another OV-PAM is used to lift the payload. The absence of reinforcements accentuates the behavior through which the force will reduce throughout the contraction, which approximates the surveyed soft pneumatic actuators. The armored gripper is made of two AS-PAMs where each of them is used to produce the gripping and the lifting force, respectively.

A testing jig with a payload of 2 kg and widths of 4 and 2 cm at the contact point with the gripper was built to approximate the different object widths such that the grippers are at different contraction ratios when gripping each jig. In the case of a jig with a 4 cm gripping width, the two grippers were able to lift the payload without any problem (Fig. 2-32). However, in the case of a jig with a 2 cm gripping width, the normal gripper failed, while the armored gripper succeeded (Fig. 2-33).

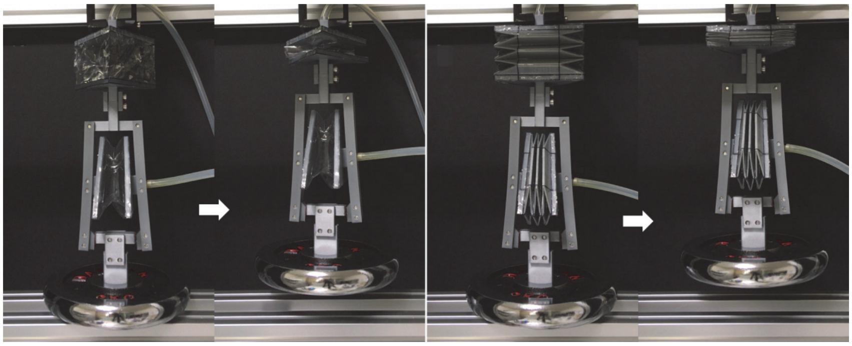

Figure 2-32. Normal and armored gripper lifting a payload with a jig with gripping width of 4 cm.

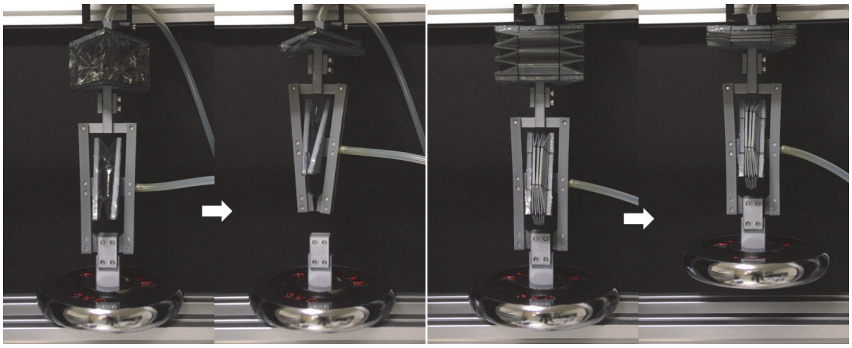

Figure 2-33. Normal and armored grippers lifting a payload with a jig with gripping width of 2 cm.

This difference in the two results comes from the differences in the force profiles of actuation used in each gripper. In the case of the normal gripper, the force produced by the actuator decreases, while in the case of the AS-PAM, the force remains large throughout its actuation range (Fig. 2-34). Because of this, the effective actuation range of the normal gripper is limited to the point where it cannot produce the force required to lift the payload, which results in a smaller actuation range compared to that of the armored gripper.

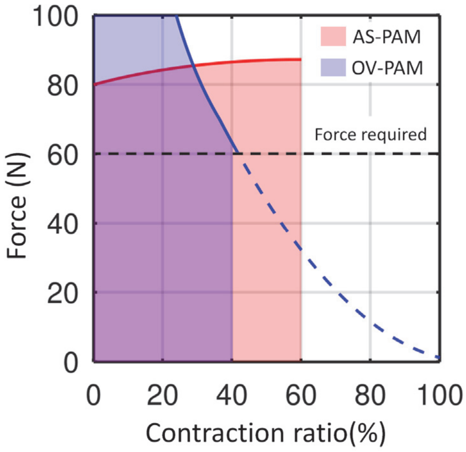

Figure 2-34. Effective contraction ratio of the two grippers with force requirement

Also, as shown in the pre-vacuuming experiment, the AS-PAMs move at a stable speed during the moving phase regardless of payload, unlike OV-PAMs. This is due to the actuator moving mainly around a fixed critical pressure where the pump generates a constant flow rate for a given pressure, which means the AS-PAMs can make constant speed inherently. To show this more clearly, the vacuum pressures were released without any control for the two grippers holding 2 kg of payload under vacuum pressure of 20 kPa (Fig. 2-35). The position of the payload was recorded every 0.2 s highlighted with red lines, and the results show that while the speed of the normal gripper changes drastically from fast to slow, that of the armored gripper remains stable throughout the motion. This result can be further explained by deriving the relaxation ratio versus volume relationship for each gripper. In the case of the normal gripper, a small change in volume makes a large change in the relaxation ratio in the early stage of deformation and the opposite happens at the final stage of deformation, resulting in a drastic speed change (Fig. 2-35a). In the case of the armored gripper, the change in the relaxation ratio remains stable at any point and thus the gripper moves at a stable speed (Fig. 2-35b).

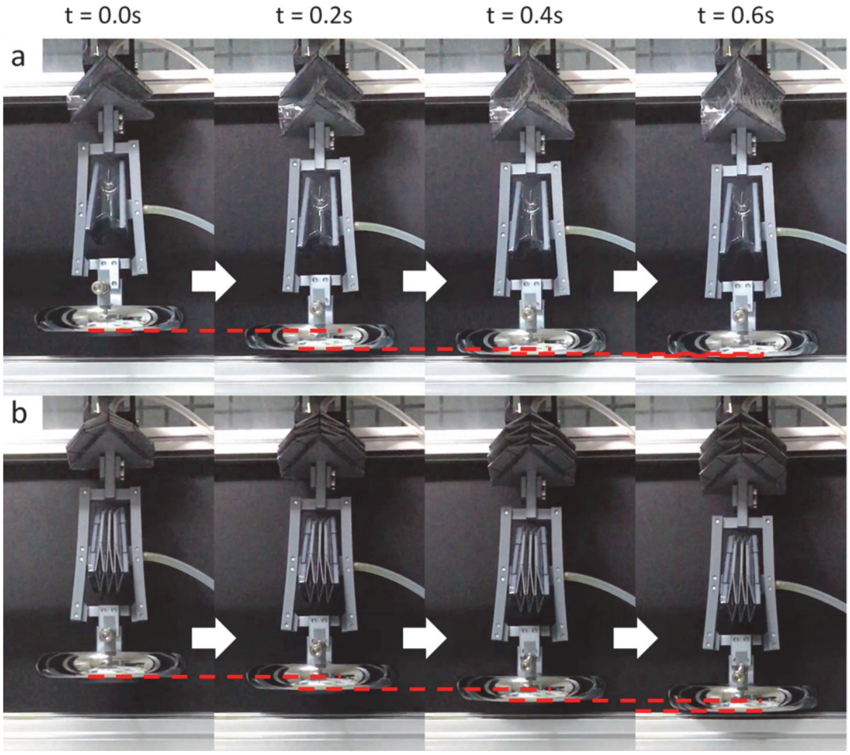

Figure 2-35. Normal and armored gripper releasing a payload at (a) a drastic speed change and (b) a stable speed.

Having a stable speed can significantly increase safety in the case of unexpected events by decreasing the maximum speed, which also minimizes the maximum impact force. In such events, the normal gripper can cause large impact, while the armored gripper only causes minimal impact by regulating its speed when it collides with the environment.

2.4 Reconfigurable origami-based PAMs

2.4.1 Introduction

In the previous chapters, the capability of the vacuum-based actuator to achieve superior performance in terms of force and contraction ratio is presented. However, the functionality of those actuators is limited to producing contractile deformation which might be inapplicable in some cases.

One of the solutions for such an issue would be applying modular design where simple structures are easily and reversibly combined to build complex systems. Although there have been a number of modular soft pneumatic actuators implementing application-specific standardized connectors, magnets, and mechanical fasteners, their functionality is still limited to one or two modes of deformation and their performance is often insufficient for many applications.

Thus, the actuator modular reconfigurable origami-based vacuum pneumatic artificial muscles (ROV-PAM) is presented in this chapter. The ROV-PAMs consist of actuating modules that use assisting plates to define their actuation mode and supporting modules that are used as fluidic elements. Magnet-based connectors are positioned at each end of the modules, which allow us to adjust the characteristics of the ROV-PAM-based system easily by using the proposed modular design. The modules can be assembled not only in series but also in parallel, altering both their functionality and performance. This versatility of the ROV-PAMs illustrates the potential of the proposed modules and shows that the ROV-PAMs can expand the range of applications of soft robots.

2.4.2 Manufacturing and modeling

The basic structure of the ROV-PAM consists of 3D-printed parts and a thin film. The 3D-printed parts are used as reinforcement that guides the deformation of the module, and the film is used to create the sealed flexible chamber of the module. Six types of actuating modules (contractile, channeling, two bending, and two twisting modules) and three types of supporting modules (head, spine, and tail modules) were developed in this work (Fig. 2-36).

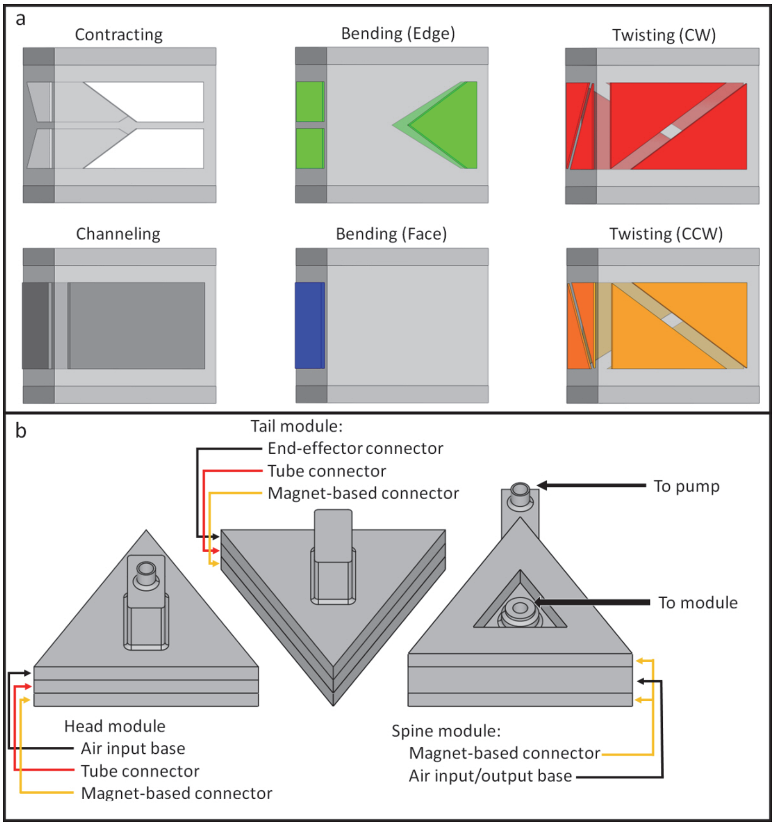

Figure 2-36. (a) Side view of the six types of actuating modules with their supporting plates, and (b) isometric view of the three basic supporting modules.

All modules have a magnet-based connector at both ends in an alternating configuration, such that the modules can be assembled in an arbitrary orientation, and the actuating modules have additional assisting plates that define the actuation characteristics and mode of deformation of the modules (Fig. 2-37).

The shapes of the bending and twisting assisting plates are designed based on the primary geometry of side walls at maximum possible deformation (Fig. 2-38). In the figure, an area enclosed with dashed lines represents the primary geometry, and it is worth noting that a bending module can operate as long as one of its columns remains straight, but the whole surface around the column is covered with a plate to ensure its integrity under high vacuum pressure. Also, it should be noticed that the shape of the assisting plates of the contractile module can be chosen arbitrary as long as the plates do not prevent the module from contracting, and the contractile module in this work has a modified Yoshimura pattern like OV-PAMs for convenience.

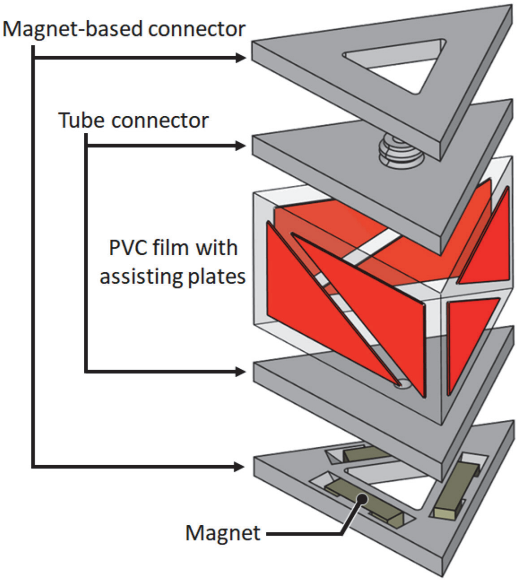

Figure 2-37. An exploded view of a twisting module.

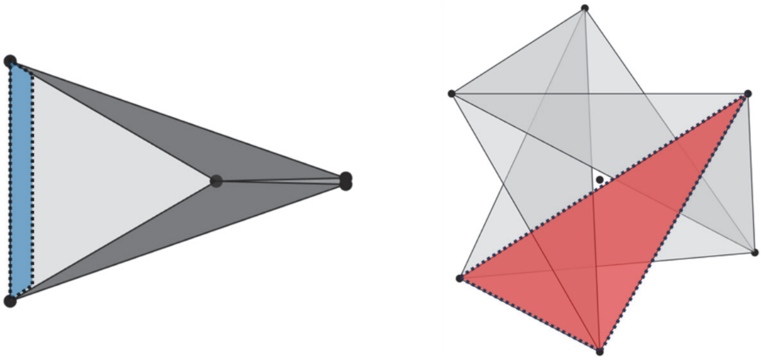

Figure 2-38. Primary geometry of bending and twisting modules.

The contractile modules have two trapezoidal plates on each side to produce a linear contraction, and the channeling modules have a rectangular plate on each side to limit the motion and act as a channel for air flow. The edge bending modules have two triangular plates attached on both sides of one edge, which makes the actuator bend around this edge, while the face bending modules have a rectangular plate on one of their faces, which makes the actuator bend around this face. The clockwise (CW) and counterclockwise (CCW) twisting modules have two triangular plates on each of their faces to produce twisting motions in the intended direction. The head module is the main input channel for the modules and serves as a connection to the mechanical ground, while the spine module blocks the air flow from the previous module and offers an additional input channel for subsequent modules. This allows for the ROV-PAM-based system to have several sections that can be controlled separately. The tail module closes the last actuating module and provides a connection to an external component, such as an end-effector.

Although most ROV-PAM-based systems presented in this chapter have modules with the same area connected in series, it is possible to build a system with larger supporting modules to attach multiple actuating modules in parallel for higher performance (Fig. 2-39) as will be demonstrated later in the application section. Notice that the assisting plates do not cover the whole surface to prevent possible overlapping between them during actuation.

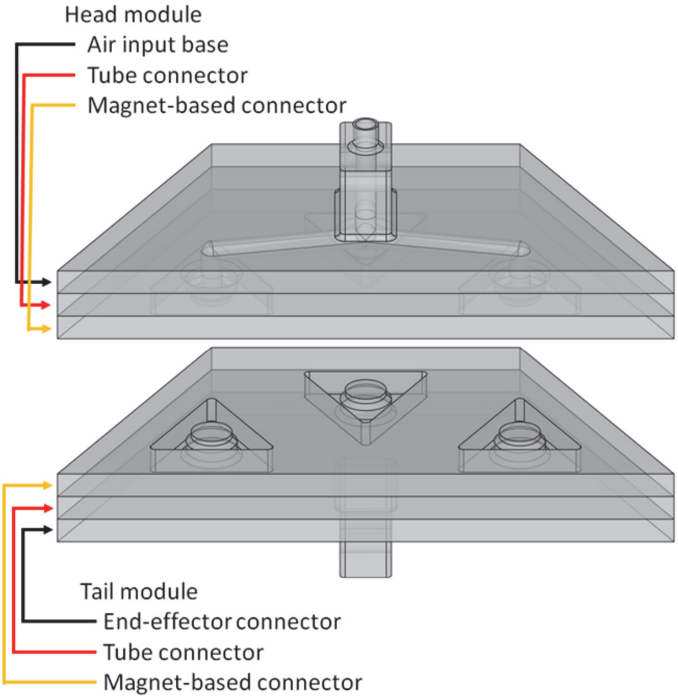

Figure 2-39. Two large supporting modules accommodating three actuators in parallel

The performance of the ROV-PAM modules can be predicted by an analytical model derived based on the law of conservation of energy. To do so, representative points are extracted that can illustrate how the volume of the module changes during actuation: six vertices from the top and bottom plates, three points from the middle of the module for the contractile modules, two points from the center of each side without rectangular assisting plates for the bending modules, two points from the center of top and bottom plates and one point at the center of the module for twisting modules (Fig. 2-40).

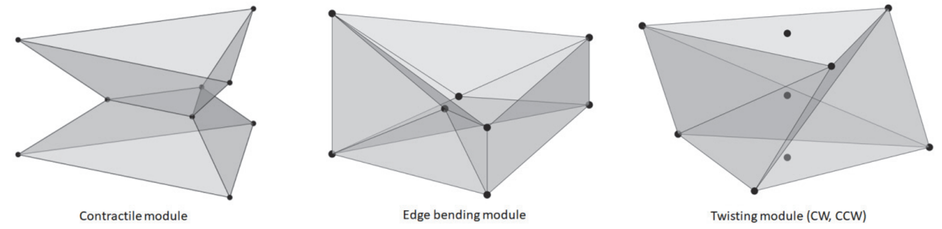

Figure 2-40. Representative points for contractile, bending, and twisting modules.

From the volume bound by these points, the volume change due to deformation can be calculated assuming that the faces that connect the representative points remain flat, and the module does not store any elastic energy during the actuation, which results in:

$$V_C = \frac{\sqrt{3}}{4} h\left(D^2 - D\sqrt{3(h_0^2 - h^2)} + (h_0^2 - h^2)\right) \tag{2-13}$$

$$V_B = \left(\frac{1 - a\sin\frac{\theta}{2}}{4}\cos\frac{\theta}{2} - \frac{2 - 3\sin\frac{\theta}{2}}{6\sqrt{3}}\sqrt{\sin\frac{\theta}{2} - \sin^2\frac{\theta}{2}}\right) D^3 \tag{2-14}$$

$$V_T = \frac{\sqrt{1 - 4\sin^2\frac{\varphi}{2}}}{12}\left(3 - 4\sin\frac{\varphi}{2}\right) L^3 \tag{2-15}$$

where V_C, V_B, and V_T are the volumes of the contractile, bending, and twisting modules, respectively, D is the side length of top and bottom plates, h is the current height of the module, h_0 is the initial height of the module, a is a geometrical constant which corresponds to 1 for a face bending module and 2 for an edge bending module, θ is the bending angle of the module, φ is the twisting angle of the module (Fig. 2-41).

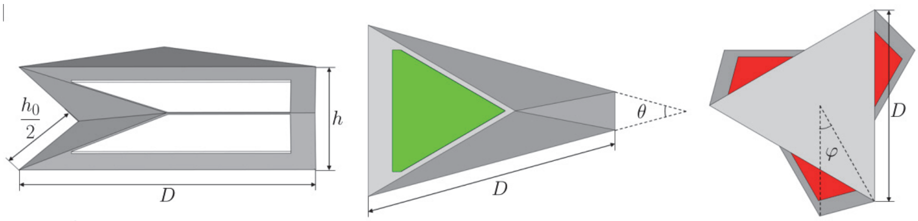

Figure 2-41. Key deformation parameters for contractile, bending, and twisting modules.

Then, the performance of the actuating modules can be expressed using the law of conservation of energy. For contractile and bending modules, this becomes:

$$P_d V_C = Fdh \rightarrow F = P\frac{dV}{dh} = \frac{\sqrt{3}}{4}\left(D^2 + h_0^2 - 3h^2 + L\frac{6h^2 - 3h_0^2}{\sqrt{3(h_0^2 - h^2)}}\right) \tag{2-16}$$

$$\rightarrow M = P\frac{dV_B}{d\theta} = \left(b\sin^2\frac{\theta}{2} - 3\sin\frac{\theta}{2} - c - \frac{12\sin^2\frac{\theta}{2} - 13\sin\frac{\theta}{2} + 2}{\sqrt{3\left(\sin\frac{\theta}{2} - \sin^2\frac{\theta}{2}\right)}}\cos\frac{\theta}{2}\right)\frac{D^3}{24} \tag{2-17}$$

where P is the negative pressure applied to the module, b and c are geometrical constants which are 6 and 3 for face bending modules, and 12 and 6 for edge bending modules. For the twisting modules, we can write:

$$P_d V_T = RFdh + (1 - R)Td\varphi \tag{2-18}$$

where F and T are the contracting force and twisting torque the module produces, respectively, R is the ratio between the energy produced from the contractile and twisting motions. From the experiments, it is shown that the ratio R can be any value between 0 and 1 due to the free deformation of the thin film and modeling this behavior for all values of R would requires a complex analysis outside the scope of this chapter. Thus, the ratio is set to be 1 in this model, which happens when the payload acts only in the longitudinal direction, which results in:

$$Pd_T = Fdh \rightarrow F = P\frac{dV_T}{dh} = \frac{1 + 3\sin\frac{\varphi}{2} - 8\sin^2\frac{\varphi}{2}}{4\sqrt{3}\sin\frac{\varphi}{2}}D^2 \tag{2-19}$$

Although the ROV-PAM modules were designed to operate with vacuum pressure, the same analysis can be applied to the modules under positive pressure, and they can become a bidirectional actuator with the help of a dedicated pressure supplying system, allowing us to build a cooperative actuation mechanism where two actuators both exert force to enhance overall system performance.

2.4.3 Model validation

In this section, the proposed analytical models are verified by experiment results for each actuating module. During the experiments, the modules were fixed to the testing jig using bolts as the maximum holding force of the magnetic connector was approximately 10 N, which is insufficient to fix the module under large vacuum pressure.

In the case of the contractile ROV-PAM module, the results follow the model well for the contraction ratio range from 20 to 60% but departs from the model at a contraction ratio of 80% (Fig. 2-42a). This is due to the side films and assisting plates being fully folded inward and starting to hinder the actuation as available space becomes scarce.

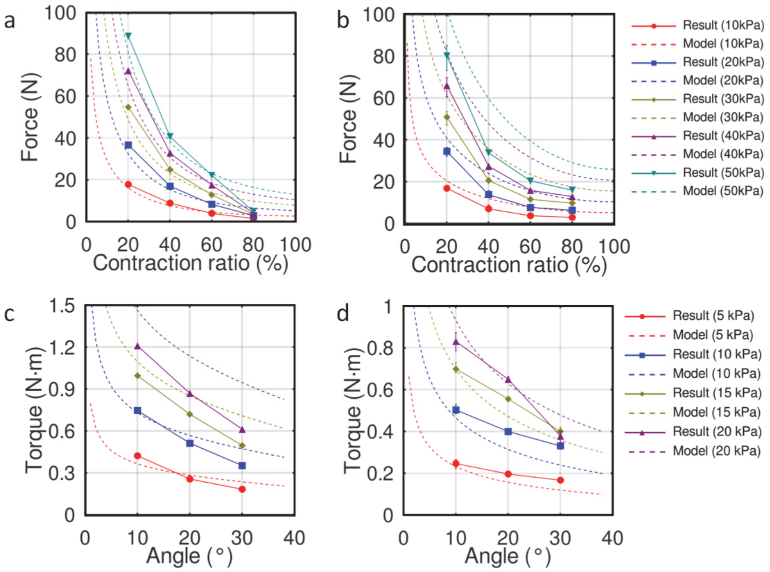

Figure 2-42. Blocked force and torque of the ROV-PAM (a) contractile, (b) twisting, (c) edge bending, and (d) face bending modules.

In the case of the twisting module, the result follows the analytical model with reasonable error at lower pressures or when the contraction ratio is small (Fig. 2-42b).

As the vacuum pressure and the contraction ratio increase, the error becomes larger due to the unintended deformation of the film, which is not considered by the analytical model. As discussed in the modeling section, the twisting module can undergo large changes in shape due to the compliance of the film. This results in an error in the predicted volume of the module, and implementing strong materials could help the module maintain its shape under high pressure, suppressing the error.

In the case of the face and edge bending modules, the results follow the model with reasonable accuracy under small pressure (Fig. 2-42c, 2-42d). However, the torques produced by the modules are not proportional to the pressure as expected by the model, and a snapshot of the assisting plates and film indicates that the modules suffer from undesired deformation as pressure increases (Fig. 2-43). Due to the deformation, the volume of modules and models become different, and the assisting plate starts to store elastic energy which results in smaller output. An improved manufacturing process would reinforce the module, making it perform better at higher pressures. Overall, the result shows that the proposed simple analytical model can predict the behavior of the different modules at low pressure and their maximum performance, which could be obtained by using better materials and assembly processes.

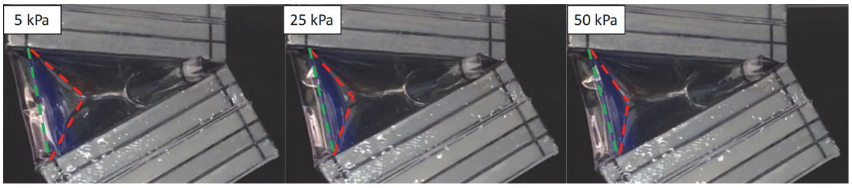

Figure 2-43. The deformation of an assisting plate and film under different pressures.

2.4.4 Modularity

The modular capabilities of the ROV-PAM can be utilized in many ways and one of them is for extending the working range of its basic modules by connecting the same types of modules to build a homogeneous system. Contractile, bending, and twisting homogenous systems containing 1, 2, and 3 contractile, bending and twisting modules in series were built, and vacuum pressure was applied to each to verify the scaling effect of adding modules in series (Fig. 2-44, 2-45, 2-46). All systems show that the deformation scales proportionally to the number of connected modules, and it confirms that the working range of ROV-PAMs can be easily extended by adding more modules in series to execute a given task.

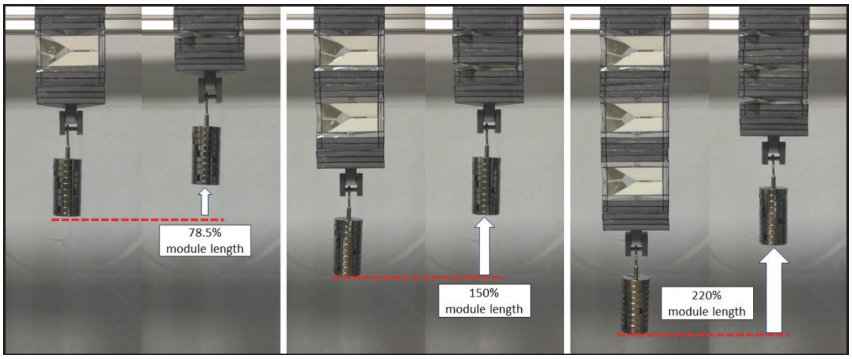

Figure 2-44. Contractile modules connected in series to extend working range.

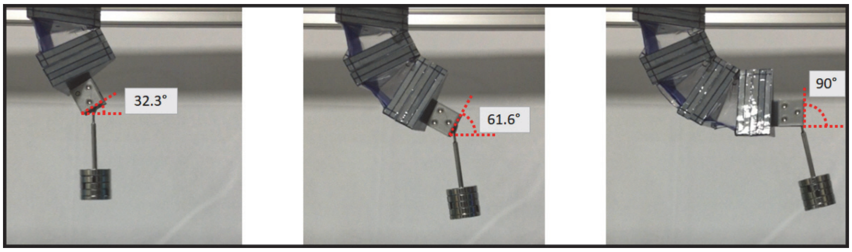

Figure 2-45. Bending modules connected in series to extend working range.

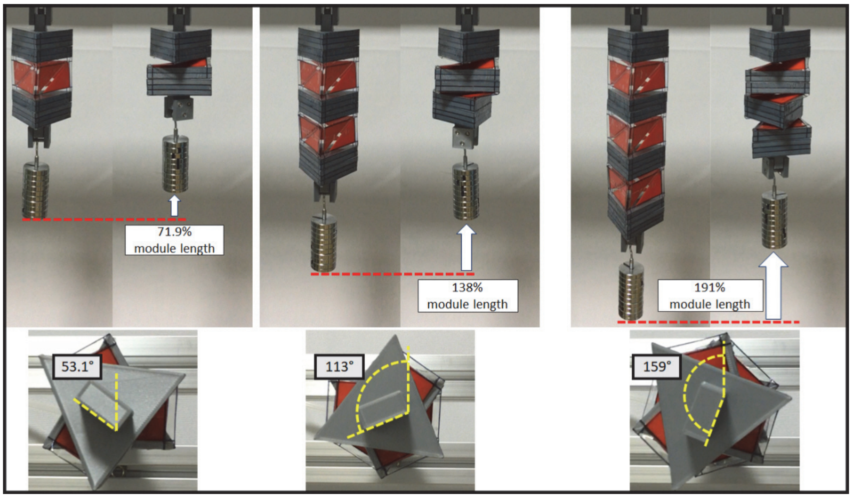

Figure 2-46. Twisting modules connected in series to extend working range.

ROV-PAM modules can also be connected in series to build a heterogenous system by connecting different types of modules to produce more complex deformations which may be required for certain types of complex tasks. Three types of heterogenous systems making use of a combination of bending and channeling modules were built. The first system produces a “J” shaped deformation where a channeling module stands straight providing air flow to the subsequent face bending modules (Fig. 2-47). The second

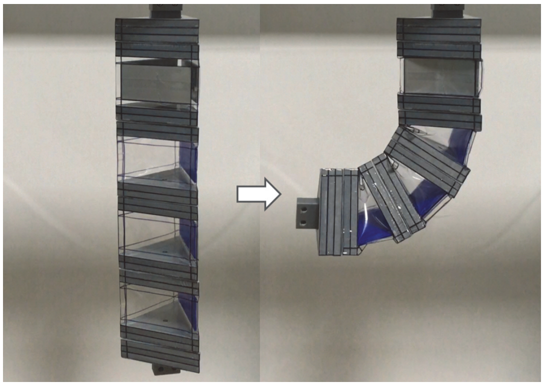

Figure 2-47. ROV-PAM modules forming a “J” shape.

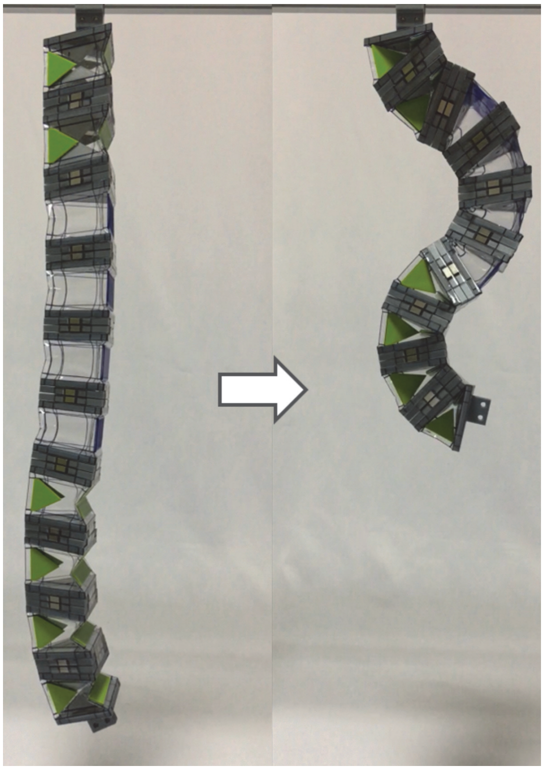

Figure 2-48. ROV-PAM modules forming a wave shape.

produces a wave-shaped deformation, with the two edge bending modules starting a wave, followed by four consecutive edge and face bending modules responsible for creating each half of the wave (Fig. 2-48). Then a helix-shaped deformation was produced with two edge bending modules creating the tilted base for the subsequent modules and three consecutive edge and face bending modules assembled with the orientation rotated by 120° that form the main helix shape (Fig. 2-49). This shows that ROV-PAM modules can be easily reconfigured to produce complex deformation by changing the type and orientation of the modules.

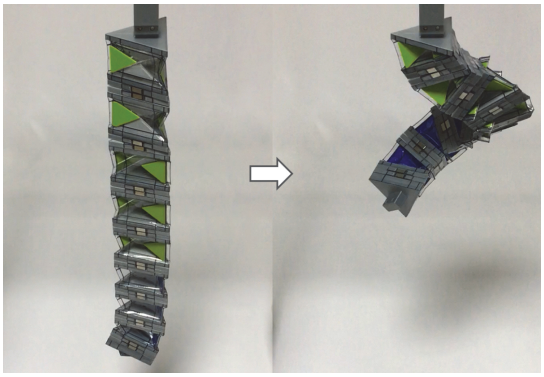

Figure 2-49. ROV-PAM forming a helix shape.

Since all ROV-PAMs share the same basic structure, it is possible to connect the modules in parallel to make the modules cooperate and increase the performance of the system. To demonstrate this, two types of cooperating system were built (Fig. 2-50), then compared with a corresponding single module system. The first system consists of three contractile modules which were vacuumed to lift a payload of 500 g. The single module counterpart with a single contractile module required 25 kPa of vacuum pressure to lift the payload while the cooperating contractile ROV-PAM-based system required only 15 kPa of pressure, which means that it needs 40% less pressure to produce the same force (Fig. 2-51a). Then, a vacuum pressure of 20 kPa was applied to the cooperating contractile ROV-PAM-based system and its single module counterpart with a payload of 1,000 g. The single module produced a contraction ratio of 47.1% while the cooperating system produced a contraction ratio of 75.7%, corresponding to an increase of 61% (Fig. 2-51b).

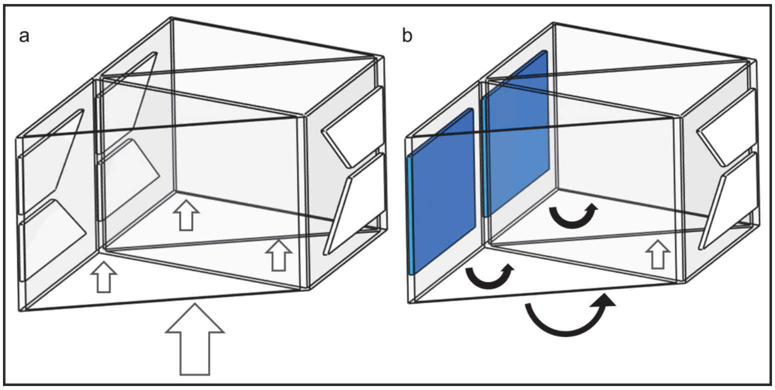

Figure 2-50. Two cooperating ROV-PAM-based system configurations for producing (a) contractile, and (b) bending deformations.

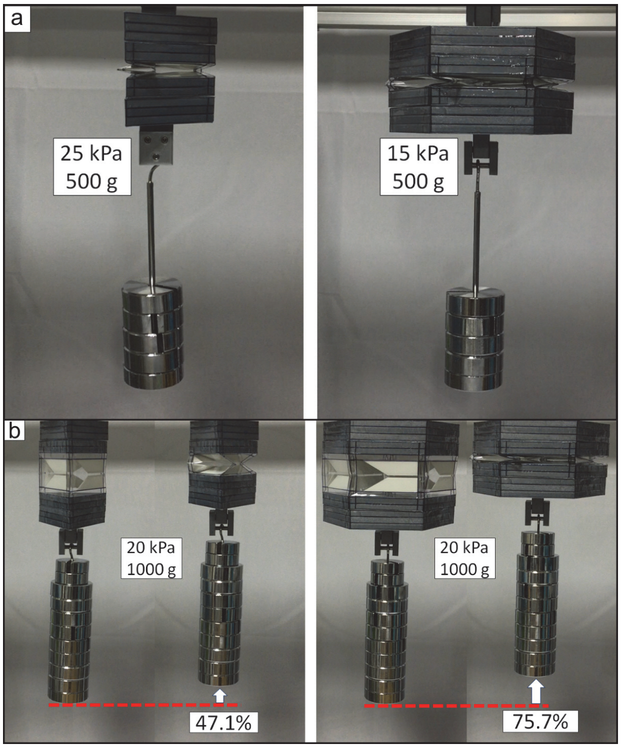

Figure 2-51. Single module (left) and cooperating modules (right) systems lifting payloads of (a) 500 g, and (b) 1000 g.

The second system consists of two edge bending modules and one contractile module. This cooperating bending system and its single module counterpart with a single face bending module were vacuumed to produce a bending deformation with a payload of 500 g. This time, the single module counterpart required 30 kPa of pressure while the cooperating bending system required only 15 kPa of pressure, which corresponds to a reduction of 50% in the required pressure (Fig. 2-52a). Then, a vacuum pressure of 20 kPa was applied to the cooperating bending system and the single module counterpart with a payload of 1,000 g. The single module produced a bending angle of 18.8° while the cooperating bending system produced a bending angle of 26.1°, resulting in an increase of 39% at the same pressure (Fig. 2-52b). These results showed that the cooperating system reduces the pressure required to achieve a target performance and increases the maximum performance with modules working cooperatively.

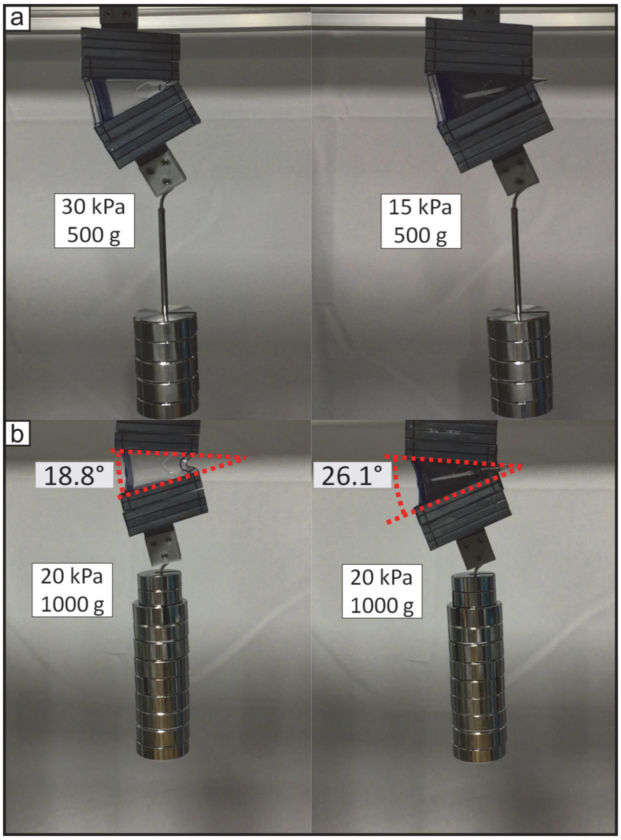

Figure 2-52. Single module (left) and cooperating modules (right) systems producing bending deformation with payloads of (a) 500 g, and (b) 1000 g.

As ROV-PAM modules can produce a wide range of types of deformation, it is possible to build a service robot capable of targeted tasks. To demonstrate this, a block sorting robot that consists of one clockwise twisting module, one counterclockwise twisting module, and two contractile modules were built with two spine modules that separate each module segment, and a gripper attached at the bottom of the robot. The two spine modules allow for separate control of clockwise, counterclockwise, and contractile motions of the robot, and there were two types of blocks, red and yellow, with three different vertical positions while their corresponding bins were placed on the left and right sides of the robot. By applying vacuum pressure to a specific module segment in the right order, the contractile modules adjusted the length of the robot, and the twisting modules changed the orientation of the gripper so that the robot could pick up and place the blocks into the right bin regardless of their position (Fig. 2-53). This shows the potential of ROV-PAM modules to build a system capable of completing tasks by utilizing combinations of different modules.

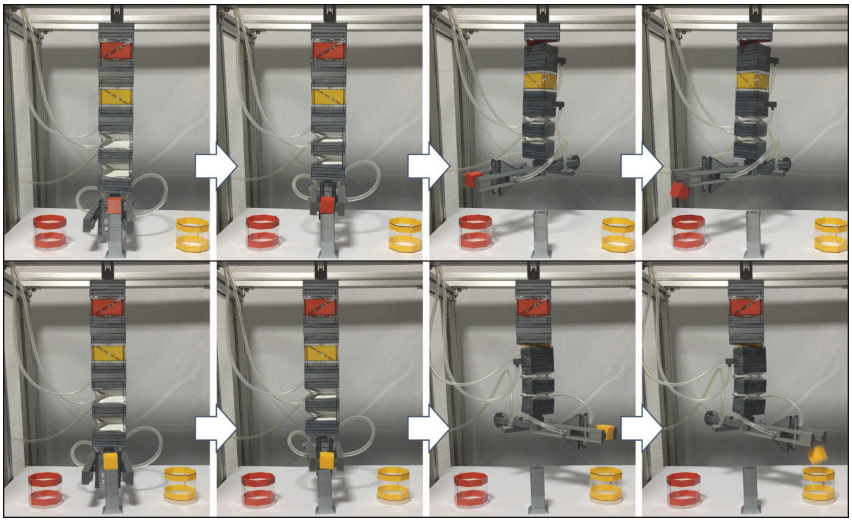

Figure 2-53. An ROV-PAM-based block sorting system placing each block in the right bin based on their colors

Chapter 03

Inflatable robotic manipulators

3.1 Introduction

Soft robots mostly have various shapes ranging in size from millimeters to centimeters, but there are also micro or meter scale. A robot manipulator is a type of robot with high utility, as is common in industry. However, it is difficult to say that soft pneumatic manipulators have performance comparable to those of rigid robots or human arms[77, 78]. It is necessary to develop a soft pneumatic manipulator that can perform tasks around humans and safely collaborate with humans.

Continuum manipulators create infinite degrees of freedom (DOF), replicating the fluid deformations of octopus tentacles or elephant trunks[79, 80]. Two main approaches are employed to construct these manipulators using soft pneumatic structures. The first approach involves longitudinal actuators that shrink or extend as the trunk of the continuum structure[81-83], or deform the manipulator's trunk directly[34]. The second approach utilizes repeated pneumatic cells along the manipulator's length[84-86].

Robotic manipulators with jointed discrete motions mimic human arm motions better by using linear soft actuators, such as McKibben actuators[87, 88] or pouch motors[89], to drive the joints such as shoulder, elbow, and wrist. These actuators offer variable stiffness through antagonistic usage[36, 90], but their length presents design constraints. Alternatively, inflatable pouches or bellows enable the assembly of simple manipulators with single DOF joints[91, 92] and even complex manipulators with multiple DOFs[12, 93]. Multiple sets of pouches or bellows arranged around a joint allow for two bending DOFs[94], and for soft robotic manipulators to reach up to six DOFs[95]. However, neither continuum-based nor discrete-motion-based soft pneumatic manipulators surveyed can produce torsional motions of the human forearm, limiting their ability to fully behave like human arms.

For the soft manipulator to have motion and modalities similar to those of the human arm, a forearm that generates a torsional motion is required. Various unidirectional twisting actuators have been developed including small-scale twisting actuators using antisymmetric air channels[96], anisotropic 3D printed blocks[74], McKibben actuators with asymmetric fiber angles[22, 97], fluidic-powered auxetic cylinders[98], asymmetric vacuum chambers[99, 100], pressurized chambers with various anisotropic features[101, 102], and inflatable pouches with antisymmetric pleats[103]. However, it should be noted that humans have the ability to generate bidirectional twisting motion of their forearm, which remains elusive for current soft robotic manipulators with these actuators.

Various approaches have been proposed to achieve bidirectional motion in actuators. Helical inflatable actuators offer potential, although their torque remains unverified experimentally[104]. Asymmetric chambers enable bidirectional motion based on pressurization or vacuuming[105], while timing patterns with longitudinal constraints[106], and antagonistic bidirectional bending actuators have also been explored[107]. However, the aforementioned approaches fail to incorporate torsional actuators possessing wide range of motion, high torque, controllable stiffness, or the actuators are not applied to manipulators.

Most existing pneumatic joints which use positive pressure use expanding elements coupled with a rigid frame such that their expansion causes a rotational motion of the joint. Several types of expanding elements have been used including film-based folded tubes[92], rubber bellows[93], stacked pouch motors[91], and pouch motor patterns[12]. In the case of 2DOFs joints, there are actuators that generate bending by using stacked pouch bellows or inflatable chambers in parallel fixed between rigid plates[94, 95, 108]. Several examples of negative pressure bending actuators have been presented using rigid plates and a flexible constraint layer[109, 110], 3D printed structures[111], paper-elastomer composites[35], technical textile with tessellated rigid faces[112], or hydrogels[113]. Most of these negative pressure actuators required the implementation of rigid components to constrain their deformation and prevent the collapse of the actuator's chamber. The collapse of the structure corresponds to buckling of the walls of the structure such that it does not produce mechanical work. Repeating units consisting of parallel chambers with foam cores have been used as a manipulator[114], but it lacks precise sensors for position feedback. Negative pressure actuators have yet to be used in hybrid hard-soft robotic joints as they would have to replace positive pressure actuators.

Linear pneumatic artificial muscles (PAMs) can be attached to a rigid joint with an angular encoder to build a pneumatically actuated robotic joint. The most commonly used pneumatic linear actuator is the McKibben muscle[22, 54, 115], and they have been applied to robot manipulators since the early stages of research into PAMs[81, 82]. Other forms of linear PAMs have been used such as film-based pouch motors[116], paired pouch motors[11] and series PAMs[34]. PAMs harnessing a drop in pressure have been used as actuators for wearable applications[117], and negative pressure-driven linear actuators have been used as external actuators for robotic joints and for wearable applications[52, 118-120]. The use of an origami structure to guide the deformation of the structure and modulate its actuation properties was also proposed[121], and coupled with tendons for controlling the extension or inducing bending of a module[122]. However, this approach entails that the length of the links determines the maximum length of the linear actuator and thus the performance of the joints, and it also poses significant design challenges for the implementation of 2DOFs joints.

There are cases where both positive and negative pressures are used to drive a single actuator. Bellows capable of extending using positive pressure and contracting using negative pressures have been developed[86, 123, 124], and used in platforms using multiple such bellows in parallel[106]. Such bellows avoid collapse of the structure under a negative pressure at the cost of actuation performance. Actuators using simultaneous positive and negative pressures have been developed including an actuator using negative pressure for actuation and positive pressure into an antagonistic chamber for stiffening[125], and an actuator has used an hyperbaric chamber for combined positive and negative pressure-based linear actuation[126]. However, most of these actuators could not utilize a wide range of both positive and negative pressures for bidirectional actuation of origami chambers due to structural collapse under vacuum pressure[127, 128]. They were primarily employed in simpler robotic systems and have not been demonstrated for human-scale robotic arms[129]. There is a need for a larger actuator joint concept that can be implemented for robotic arm applications that can harness both negative and positive pressures without collapsing under negative pressures to increase their actuation performance.

In this chapter, a manufacturing method of a technical textile-based pneumatic chamber using hot air welding technique which makes a lap seal over the textile is introduced. Lap seals withstand large tensile forces generated by various types of pneumatic structures without fatigue or destruction, and direct comparison of the bonding strength between fin and lap seals shows that lap seals are suitable fabrication methods for scaled-up pneumatic actuators.

This manufacturing method is then used to build a 2DOFs bending joint actuator and design of bending actuator and torsional actuator with hybrid hard-soft structures that can be used in soft pneumatic manipulators. The bending actuator produces a wide range of motion, high torque, and superior repeatability. Furthermore, the bending actuator offers the advantage of scalability, enabling straightforward adaptation to different sizes. This versatility allows for easy upscaling of the actuator when high torque output is necessary, while also downsizing in scenarios that require minimal torque to conserve volume. The torsional actuator uses a pretwisted pneumatic chamber to generate bidirectional, high-torque twisting motion, variable stiffness, and closed-loop position and torque control. Its range of motion and blocked torque are similar to those of humans, which makes the proposed design ideally suited for a human-like pneumatic soft robotic manipulator.

A multi-DOF inflatable manipulator was built by integration of the proposed bending actuators and torsional actuator. By using bending actuator only, a dual-arm inflatable robot featuring large meter-scale robotic manipulators, each with 6DOFs is constructed. These arms provide a wide range of motion and can lift payloads weighing up to 3 kg. The robot demonstrated its ability to handle misaligned boxes by capitalizing on the inherent compliance of its inflatable arms. A torsional actuator can be replaced by a forearm of the 6DOFs manipulator resulting in human-like 7DOFs manipulator. Furthermore, an inflatable robotic manipulator, measuring nearly 5 meters in length, accurately placed a basketball into a hoop from several meters away.

Hybrid hard-soft robotic joints were developed to enable position control of joints that are difficult to control, while maintaining both structural stability and rotational compliance. An origami-based pneumatic robotic joint where both positive and negative pressures can be used as the origami structure guides the motion through both expansion and contraction of the chamber, and a joint actuator that can be used for hybrid hard-soft robotic systems was developed. Two types of joints were developed using this concept. A single chamber joint was developed that can generate torque bidirectionally through switching between positive and negative pressures. A dual chamber joint was then developed where antagonistic chambers can also cooperate to generate a larger torque. Finally, a 3DOFs manipulator was developed by integrating single and dual chamber joints with a robotic link and a pneumatic gripper. The range of motion, torque performance and position control performance of both types of joints were evaluated through experiments and the manipulator demonstrated its ability to perform pick-and-place operations even with payloads exceeding 1 kg. The controllability of both types of joints was demonstrated, and multi-DOFs structure were easily controlled using decoupled controllers.

3.2 Concept and design of bending joint actuator

The basic element of the joints of the proposed dual-arm inflatable robot is shaped as a rounded triangular prism with slanted ends. Three of these elements are then fixed using bolts at each end to rigid plates such that the length at the external side of the joint is longer than that on the inside. This creates a length constraint at the center of the actuator where the external portion of each element tries to unfold to increase its volume and causes a decrease in volume of the other elements (Fig. 3-1). Each element is made from a single piece of tarpaulin sealed into an airtight chamber using two tabs that are folded and sealed (Fig. 3-2a). The balance in pressure between the elements can then be used to the 2DOFs orientation of the joint (Fig. 3-2b).

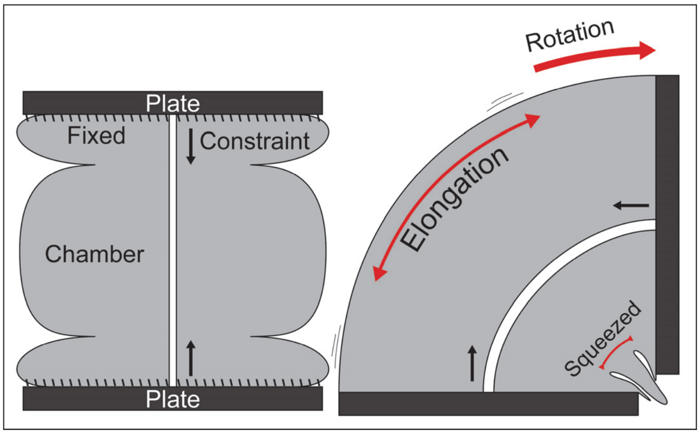

Figure 3-1. Principle of the inflatable 2DOFs bending joint.

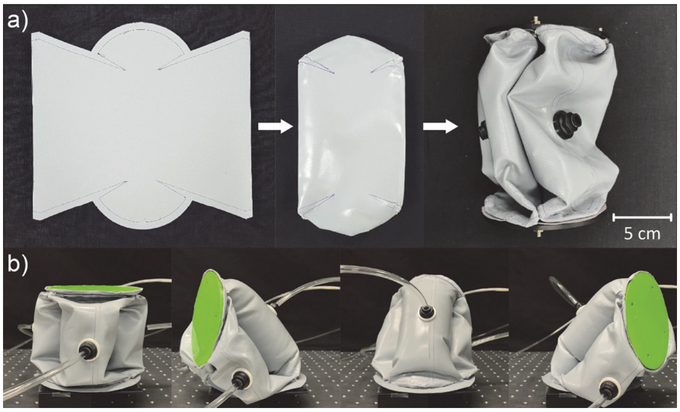

Figure 3-2. Assembly and movement of the 2DOFs bending joint.

3.3 Performance of bending joint actuator

3.3.1 Maximum bending angle and angular velocity

Three 2DOFs joints with diameters of 10 cm, 15 cm and 20 cm were built with heights of 10.8 cm, 14.7 cm, and 18.7 cm, respectively, to measure their performance and to determine the effect of their dimensions on performance.

First, the maximum angle of each joint was measured in two directions; the first being with a single actuated chamber at a pressure of 30 kPa such that it bends towards the gap between the opposite two chambers, and the second being with two actuators chambers at a pressure of 30 kPa such that it bends towards the center of the third chamber. The joint with a diameter of 15 cm has very similar maximum angle for both directions while the 20 cm joint has slightly less range with two actuators chambers and the 10 cm joint has a maximum bending angle approximately 40% smaller when using two chambers using one chamber (Fig. 3-3a). This could be a limitation of using a shorter actuator which results in the actuator not being able to sufficiently deform to reach a similar maximum angle in both directions.

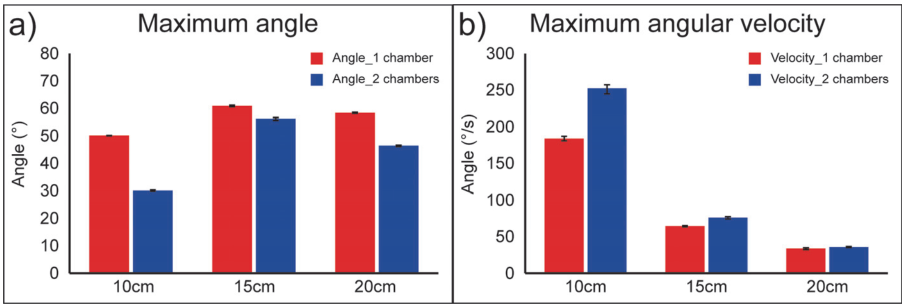

Figure 3-3. Comparison of (a) the maximum joint angle and (b) the maximum angular velocity in two directions for 2DOFs joints with diameters of 10 cm, 15 cm, and 20 cm.

Next, the maximum joint velocity was measured by placing an IMU (E2BOX, EBMotion V4) on top of the joint and actuating the joint in the same two directions as the previous experiment for the same three joint dimensions. The actuated chambers were connected directly to a pneumatic pump (Bambi Air Compressors Ltd., MD 75/250), and the target pressure of the pneumatic regulator was set to 50 kPa. The maximum measured angular velocity of the joint during the motion was then measured (Fig. 3-3b). The smaller joint produced the largest angular acceleration when the two chambers were simultaneously inflated despite having the smallest maximum angle due to having the smallest chambers and being able to use the airflow from two regulators to produce the motion. Larger joints had lower maximum angular velocities with the direction using two chambers producing slightly larger angular velocities.

3.3.2 Blocked torque

The next experiment is for the blocked torque of the joint. A load cell (Dacell, CB1) was connected to the top of the joint when in the upright vertical position to measure the lateral force produced as when bending the joint (Fig. 3-4a). The pressure within the joint is then increased from 0 to 60 kPa with the force measured in the position where a single chamber is pressurized. Each measurement was done for three cycles of pressurization and depressurization and there is very little hysteresis between the results as there is no displacement of the joints (Fig. 3-4b). The force also increases linearly with an increase in pressure due to the joint not relying on stretching of the materials to produce a change in volume. At 60 kPa, the 10 cm joint produces a blocked torque of 2.80 Nm while the 15 cm and 20 cm joints produce a blocked torque of 8.72

Nm and 22.56 Nm, respectively. This increase in blocked force is close to being proportional to the change in cross-sectional area of the joint, which demonstrates the scalability of the concept.

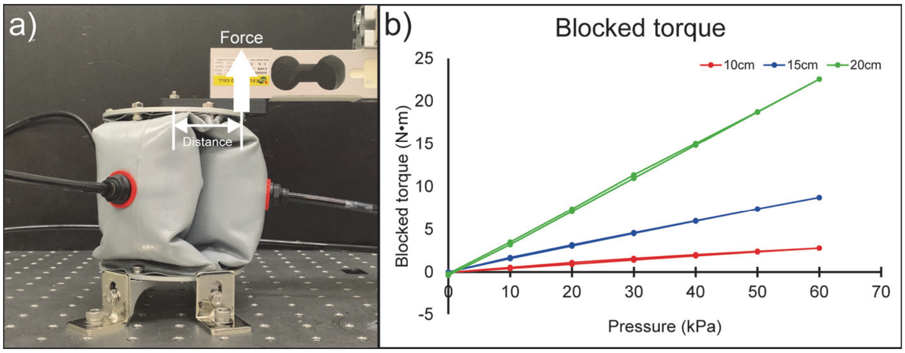

Figure 3-4. (a) Setup for measuring the blocked force and (b) comparison of the blocked force in the upright position for 2DOFs joints with diameters of 10 cm, 15 cm, and 20 cm.

3.3.3 Pressure response

The response of the joints was tested by alternating inflation between antagonistic single and double chambers to produce a back-and-forth motion. The target pressure on the regulator was set at 30 kPa on the actuated size and at zero on the uninflated side. An approximate cycle time was found that allows for full or near full actuation in both directions for each joint size; 2s for the 10 cm joint, 6s for the 15 cm joint, and 10s for the 20 cm joint (Fig. 3-5a-c). The cycle time was then reduced successively to 60%, 30% and 10% of the initial cycle and the corresponding actuation range as a proportion of the initial actuation range was measured. The 10 cm joint produced 88% of its maximum range at 0.5 Hz, 67% of its maximum range at 0.833 Hz, 31% of its maximum range at 1.67 Hz, and 13% of its maximum range at 5 Hz. The 15 cm joint produced 82% of its maximum range at 0.167 Hz, 77% of its maximum range at 0.278 Hz, 39% of its maximum range at 0.556 Hz, and 8.2% of its maximum range at 1.67 Hz. Finally, the 20 cm joint produced 100% of its maximum range at 0.1 Hz, 68% of its maximum range at 0.167 Hz, 34% of its maximum range at 0.333 Hz, and 8.3% of its maximum range at 1 Hz. This shows that the speed of the actuator for a given pneumatic system reduces as its volume is increased and that increase in actuation frequency decreases the range of motion it can achieve between actuation cycle.

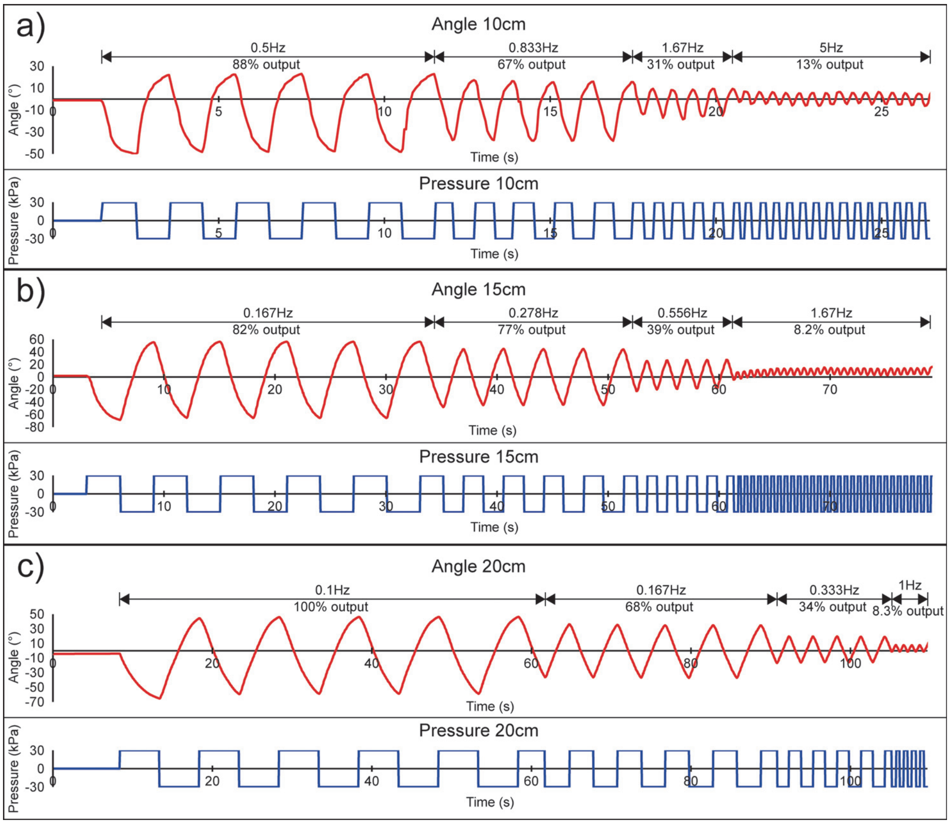

Figure 3-5. Comparison of the response of the (a) 10 cm, (b) 15 cm and (c) 20 cm joint for actuation cycles allowing full actuation range and cycles with durations of 60%, 30% and 10% of the initial cycle time.

3.3.4 Durability

Last, the 10 cm joint was tested for 5000 cycles of 2 seconds each in the same method as the previous experiment. The results show that the performance of the actuator did not degrade over this extended duration of operation (Fig. 3-6). A slight transient behavior can be seen in the early deformations which is due to starting from the unpressurized state and the joint's motion stabilizing as the pressure changes stabilize through repeated motions.

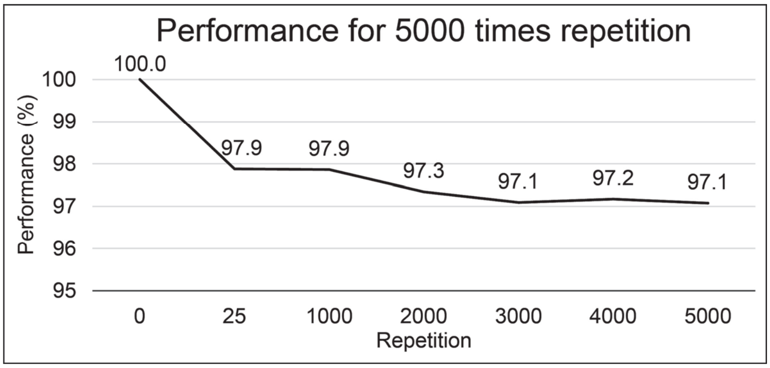

Figure 3-6. Cyclic results for the 10 cm diameter joint for 5000 cycles of 2 seconds each for a total of 10000 seconds.

The maximum pressure of the 10 cm, 15 cm and 20 cm joints was tested by increasing the pressure in a single chamber of each joint in steps of 10 kPa until leaks or ruptures prevented further inflation of the joint. The results of this experiment show that the 10 cm joint ruptured at 320 kPa, the 15 cm joint ruptured at 270 kPa, and the 20 cm joint at 230 kPa (Fig. 3-7).

Ruptures of the seal in the 10 cm and 15 cm joints occurred near the top plate of the joint (Fig. 3-8a-b). In the case of the 20 cm joint, the chamber exploded with most seals failing simultaneously (Fig. 3-8c). The rupture of the 10 cm and 15 joints was a few centimeters in length (Fig. 3-8d-e) while the rupture of the 20 cm joint was throughout the entire joint (Fig. 3-8f).

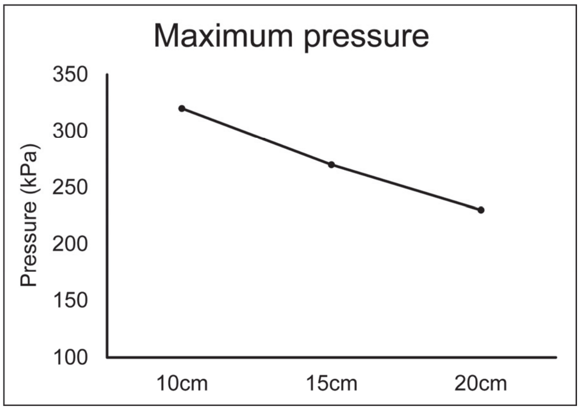

Figure 3-7. Maximum pressure before failure of the 10 cm, 15 cm, and 20 cm joints.

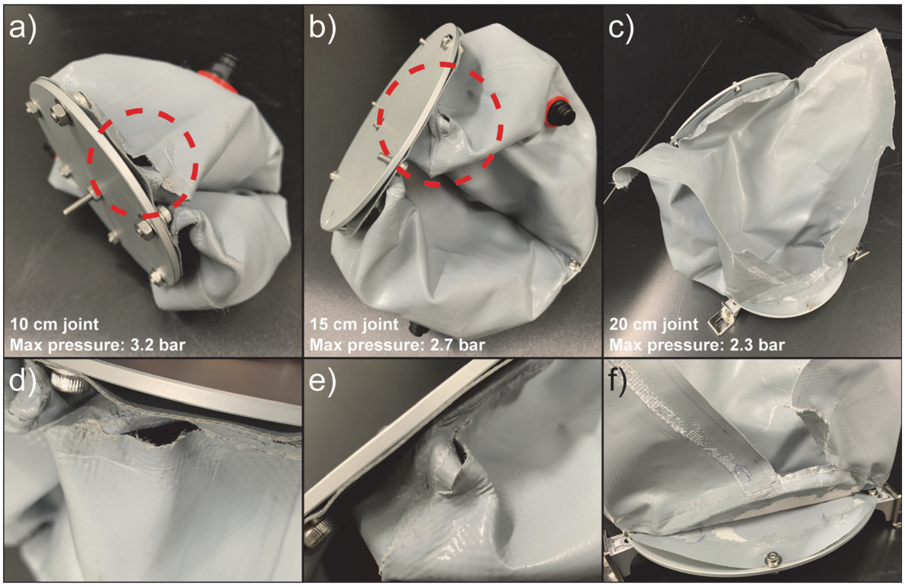

Figure 3-8. Failure of the (a) 10 cm, (b) 15 cm, and (c) 20 cm joint. Close-up of the failure point of the (d) 10 cm, (e) 15 cm, and (f) 20 cm joint.

3.4 Concept, design and manufacturing of torsional actuator

The torsion mechanism of the human forearm is done by a rotation of the ulna and radius bones to produce both the pronation and supination of the forearm (Fig. 3-9a)[130]. The pronator teres, pronator quadratus, and brachioradialis muscles are used to produce the pronation of the forearm, and the supinator and biceps brachii muscles are used for its supination. Inspired by the rotation mechanism of the human forearm, this article introduces the concept of inversely pretwisted pneumatic tubes for generating the bidirectional torsional motion of the forearm of a soft robotic manipulator. These pretwisted pneumatic tubes untwist in order to maximize their volume upon pressurization (Fig. 3-9b).

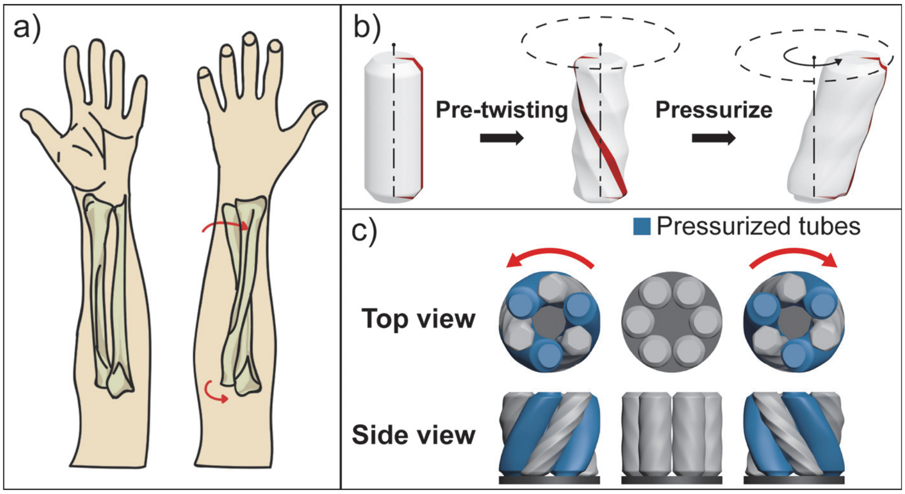

Figure 3-9. (a) Schematic of the torsion of the human forearm. (b) Deformation of a pretwisted pneumatic tube and (c) implementation in a bidirectional joint using antagonistic configuration.

The direction of the pretwisting of the pneumatic tube decides the direction of the twisting motion such that antagonistic clockwise (CW) and counterclockwise (CCW) pretwisted pneumatic tubes can be used to produce a bidirectional motion (Fig 3-9c). These tubes are arranged around a central shaft which is free to extend or contract while the top plate is free to rotate. As will be shown later in this article, these tubes do not need to be placed at the rotational axis and placing them at an offset of the central axis causes their untwisting to tilt and to produce torque. This positioning also allows the actuator to contain multiple pretwisted pneumatic tubes which can be combined to produce both CW and CCW torsional motions. Thus, pretwisted pneumatic tubes with opposite untwisting directions were selected to fabricate a wrist-like actuator with a bidirectional twisting motion and antagonistic actuation which enables the actuator to have an adjustable stiffness. The bidirectional actuator proposed in this article uses a total of six pneumatic tubes where three tubes are pretwisted CW and three are pretwisted CCW.

The chamber of the pretwisted pneumatic tube is designed as a simple cylindrical shape and consists of three parts: the chamber; the upper cap; and the lower cap (Fig. 3-10). Both the upper and lower caps are rigid while the chamber is made from a soft material. The chamber is made by rolling a tarpaulin piece into a cylindrical shape and sealing it in the longitudinal direction using a plastic bond (Loctite 401, Henkel)

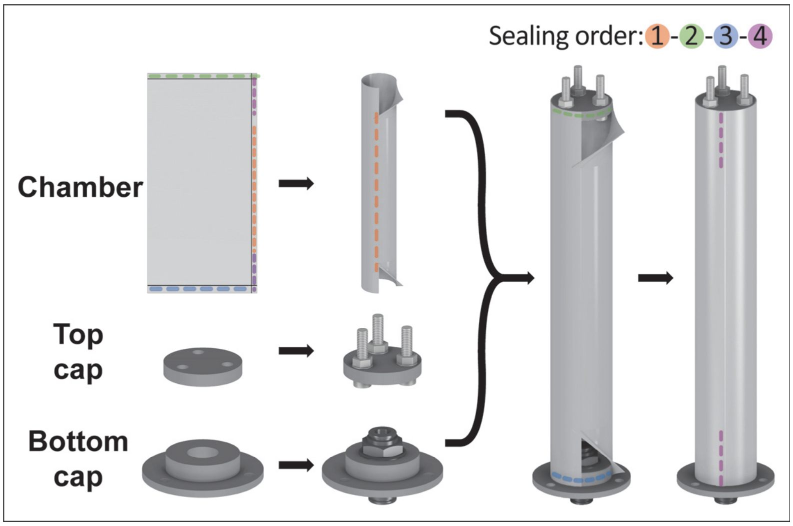

Figure 3-10. Assembly of a pneumatic tube.

with unsealed ends. Both the upper and lower caps have a cylindrical surface which is bonded to the inner side of the pneumatic chamber using plastic bond. Both caps have holes for connecting them to external parts using bolts, and the lower cap contains a pneumatic connector (32PLPBH-4, Parker Hannifin) to connect the tube to the pneumatic system. The developed bidirectional torsional actuator contains six such pretwisted pneumatic tubes with lengths of 20 cm which are pretwisted and fixed between rigid frames (Fig. 3-11). Their length was selected to be similar to that of the human forearm.

The assembly needs to be able to deform along its length and to produce a relative rotation between the rigid frames. It consists of a top plate, a bottom plate, a shaft, a sensor cover, and a sensor case. Both the top and bottom plates are 3D printed solid disks with holes for assembly. The bottom plate has a larger diameter than the top plate and has a protruding shaft with a square hole throughout its length. A rectangular shaft with a circular base is inserted into a circular hole in the top plate and into the rectangular hole of the shaft of the bottom plate. This allows for longitudinal motions of the shaft with respect to the bottom plate while restricting rotational motions. A sensor case is fixed to the top plate that prevents longitudinal deformations of the rectangular shaft with respect to the top plate. A potentiometer (3382, Boruns, Inc.) and a sensor cover are fixed to and rotate with respect to the top plate and are used to measure the rotation angle of the top plate with respect to the shaft. The six pneumatic

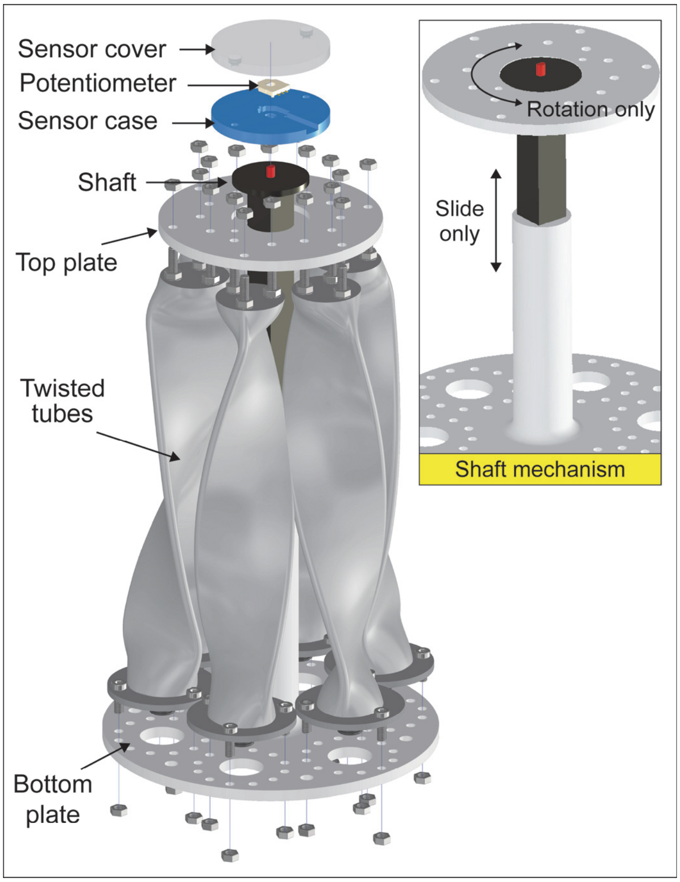

Figure 3-11. Assembly of the pneumatic torsional actuator making use of pretwisted pneumatic tubes.

tubes were fixed to the top plate using bolts and nuts, pretwisted to a desired angle, and then fixed to the bottom plate using bolts and nuts. There is no relative change in angle between the tubes and the plates; however, the plate rotates due to the flexibility of the pretwisted tube, resulting in the generation of torque.

3.5 Theoretical model of pretwisted tubes

A theoretical model was developed that relies on an estimation of the change of volume of the pretwisted pneumatic tube when pressurized and deformed. When twisted, the pressurized pneumatic tubes deform and exhibit wrinkles only towards the middle portion of the tube while the other portions of the tubes remain cylindrical in order to maximize its volume (Fig. 3-12a).

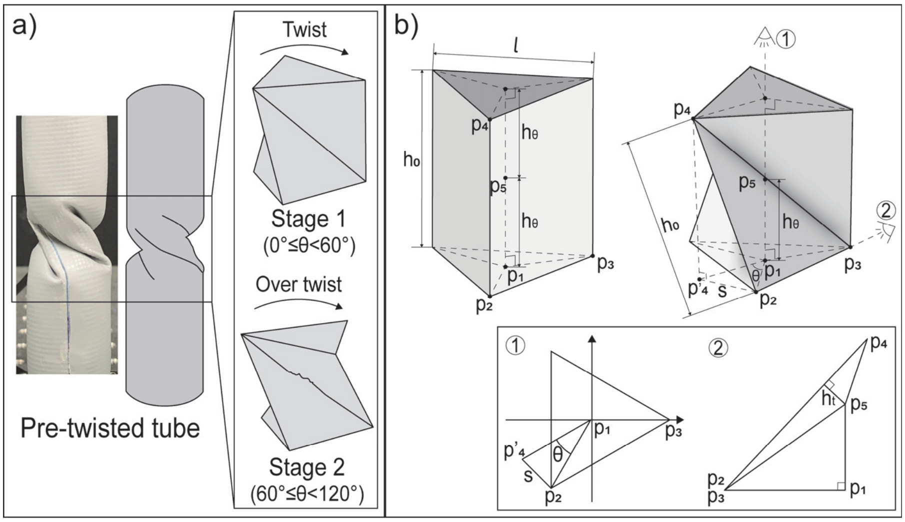

Figure 3-12. (a) Schematic diagram of the twisting of a pretwisted tube and the two stages of twisting of a triangular prism and (b) dimension and vertices of a triangular prism during twisting.

The twisting deformation of the portion of the tube which twists can be observed to occur in the shape of a triangular prism of height h_0 being twisted where the bottom area of the prism is the same as that of the cylindrical tube. A triangular prism being twisted will start to have interferences between the faces and the edges at a twisting angle of 60° regardless of its dimensions. Thus, the deformation of a triangular prism during twisting can be divided into a first stage which occurs at twisting angles between 0° and 60° and a second stage which occurs at twisting angles between 60° and 120° such that the faces and the edges do not intersect in the first stage and start intersecting in the second stage (Fig. 3-12a). In the first stage, the volume can be calculated by summing the volumes of two triangular pyramids (Fig. 3-12b). One is the pyramid with vertices $\{p_1, p_2, p_3, p_5\}$ and the other with vertices $\{p_2, p_3, p_4, p_5\}$ where p_1 is the center point of the bottom triangle and p_5 is point between the center points of the top and bottom triangles. The perpendicular distances h_θ and h_t, from p_5 to area $\{p_1, p_2, p_3\}$ and $\{p_2, p_3, p_4\}$, respectively, can be calculated as

$$h_0 = \frac{2}{\sqrt{3}} l \tag{3-1}$$

$$s = \frac{2}{\sqrt{3}} l \sin\frac{\theta}{2} \tag{3-2}$$

$$h_\theta = \frac{1}{2}\sqrt{h_0^2 - s^2} = \frac{1}{\sqrt{3}} l \cos\frac{\theta}{2} \tag{3-3}$$

$$h_t = \frac{1}{\sqrt{3}} l \cos\frac{\theta}{2}\left(\frac{1}{2} - \sin\frac{\theta}{2}\right) \tag{3-4}$$

where h_0 is the initial height of the triangular prism, s is the horizontal distance between the vertices p_2 and p_4 of the top and bottom triangles, l is the side length of the triangle, and θ is the twisting angle of the prism. Based on observations, h_0 is set to twice the theoretical height that allows the prism to twist by 60° before the edges meet. The volume V_1 of the first stage can be calculated as

$$V_1 = l^3\left(\frac{1}{2}\cos\frac{\theta}{2} - \frac{1}{3}\sin\theta\right) \tag{3-5}$$

In the second stage, the edges of the side wall meet at their center and thus a portion of their length reorients horizontally while the height of the prism diminishes. Therefore, it is assumed that the volume of the triangular pyramid with vertices $\{p_2, p_3, p_4, p_5\}$ is zero in the second stage. The configuration of the pyramid $\{p_1, p_2, p_3, p_5\}$ maintains the shape obtained at a twisting angle of 60°, and the effective length $h_{0,\,2}$ of the edges diminishes. The length $h_{0,\,2}$ of the side of the prism can be found as

$$h_{0,\,2} = \sqrt{4h_\theta^2 + s^2_{\theta = 60^\circ}} = \frac{2}{\sqrt{3}} l \sqrt{\cos^2\frac{\theta}{2} + \frac{1}{4}} \tag{3-6}$$

Then, s_2 and $h_{0,\,2}$ can be used to find the height $h_{\theta,\,2}$ of the pyramid as

$$h_{\theta,\,2} = \frac{1}{2}\sqrt{h_{0,\,2}^2 - s_2^2} = \frac{1}{\sqrt{3}} l \sqrt{\frac{1}{4} + \cos^2\frac{\theta}{2} - \sin^2\frac{\theta_2}{2}} \tag{3-7}$$

By using the same principle from the firest stage, V_2 can be calculated as

$$V_2 = l^3\sqrt{1 + 4\cos^2\frac{\theta}{2} - 4\sin^2\frac{\theta_2}{2}}\left(\frac{1}{4} - \frac{1}{3}\sin\frac{\theta_2}{2}\right) \tag{3-8}$$

The principle of conservation of energy where the input work of the fluid corresponds to the output mechanical work for this system can be written as

$$PdV = FdL + Md\theta \tag{3-9}$$

where P is the pressure of the tube, dV is the volume change of the prism, F is the longitudinal force, M is the angular torque, and L and θ are the longitudinal and angular displacements of a point mass, respectively. Assuming quasi-static conditions, the longitudinal terms can be represented as a function of the angular terms using a ratio of

$$\frac{F}{M} = \frac{dL}{r^2 d\theta} \tag{3-10}$$

where r is the horizontal distance to a point located on the perimeter of the prism from the center of the prism. By using this ratio, the angular torque M can be written as

$$M = P\frac{dV}{d\theta}\frac{1}{1+\left(\frac{1}{r}\frac{dL}{d\theta}\right)^2} \tag{3-11}$$

The average distance $\bar{r}$ from the center point for all points on a triangle is

$$\bar{r} = \sqrt{\frac{1}{12}}\,l \tag{3-12}$$

Equation (4.11) can be written by replacing L by h_θ and $h_{\theta,2}$ in stages 1 and 2, respectively, r by $\bar{r}$, and by deriving V_1 and V_2 with respect to θ as

$$M = \begin{cases} \dfrac{Pl^3\left(-\dfrac{1}{4}\sin\dfrac{\theta}{2} - \dfrac{1}{3}\cos\theta\right)}{1+\left(2\sin\dfrac{\theta}{2}\right)^2}, & 0 \le \theta < 60 \\ \dfrac{Pl^3\left(-\dfrac{1}{16\sqrt{3}\cos\dfrac{\theta}{2}} - \dfrac{1}{2\sqrt{3}}\cos\dfrac{\theta}{2}\right)}{1+\left(2\sin\dfrac{\theta}{2}\right)^2}, & 60 \le \theta < 120 \end{cases} \tag{3-13}$$

The calculated torque M versus the pretwisting angle of a single pneumatic tube with a length l of 40.4 mm is shown in Fig. 3-13.

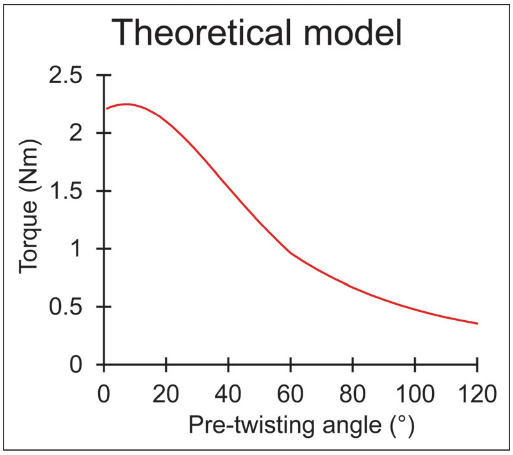

Figure 3-13. Theoretical model for the torque of a pretwisted tube.

3.6 Performance of torsional actuator

3.6.1 Effect of the pretwisting angle

If all pretwisted tubes are located at the center of the plates, then the twisting angle should be same as the pretwisting angle. But since the tubes are located at an offset from the center, the tubes lean while the plate rotates. Thus, due to the physical interference between materials and between the pneumatic tubes and the central shaft, the actuator is limited in how much it can rotate. The rotation of the actuator occurs due to the untwisting of the pretwisted pneumatic tubes and the amount of pretwisting can be adjusted during assembly. Thus, finding the pretwisting angle which produces the maximum twisting angle of the actuator is necessary. Pretwisting angles of 0° to 150° in increments of 30° were tested by pressurizing the tubes with the same pretwisting direction to a pressure of 150 kPa and measuring the twisting angle of the actuator (Fig. 3-14). The twisting angle can be observed to increase as the pretwisting angle increases up to a pretwisting angle of 120° but then decreases significantly at a pretwisting angle of 150° due to severe geometrical deformations in the pneumatic tubes which fail to loosen. However, the pretwisting angle that produces the largest deformations could change depending on the actuator's length, other dimensions, or material of the pneumatic tubes. This angle can be found for other configurations through a similar process of increasing gradually the pretwisting angle until a drop in maximum twisting angle is observed.

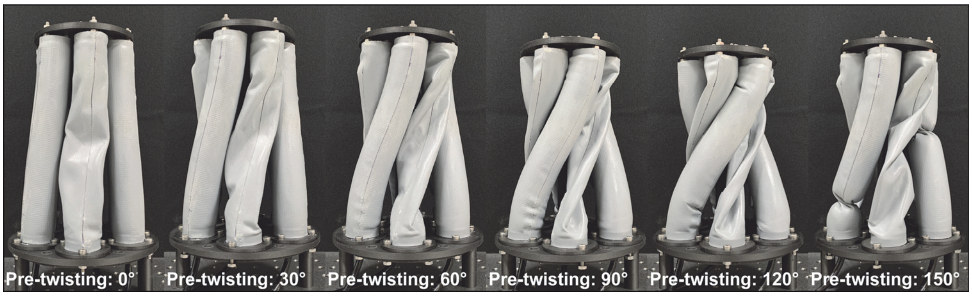

Figure 3-14. Maximum deformation of the actuator for different pretwisting angles.

The twisting angle was then measured visually for both CW and CCW rotations for pretwisting angles up to 120° and the twisting angle was shown to increase nearly linearly with an increase in pretwisting angle with both directions of twisting producing nearly equal twisting angles (Fig. 3-15a). Three measurements were taken for each of five samples and the variation in measured twisting angle between samples was less than 1.77° throughout all measurements. Therefore, the actuators used throughout all future experiments were made with a pretwisting angle of 120°. The twisting angle of the actuator was then measured for pressures varying from 0 to 150 kPa in increments of 10 kPa (Fig. 3-15b). The twisting angle was shown to increase slightly up to a pressure of 30 kPa, then increase rapidly at a pressure of 40 kPa, and then increase very slightly up to a pressure of 150 kPa. Its maximum twisting was 107.7° in the CW direction and 107.0° in the CCW direction (Fig. 3-16). This rapid increase in angle at 40 kPa is because

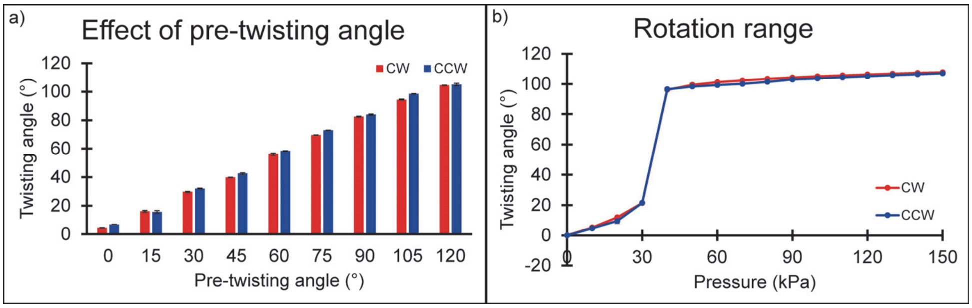

Figure 3-15. (a) Comparison of the range of motion of the actuator for different pretwisting angles and (b) results of the effect of pressure on twisting angle.

the change of volume of the twisted tube is small in the early stage of untwisting but significantly larger once the twisted angle of the tube reaches 60°. This causes a decrease in the required pressure to increase the angle and thus the actuation to produce a full deformation upon reaching this pressure.

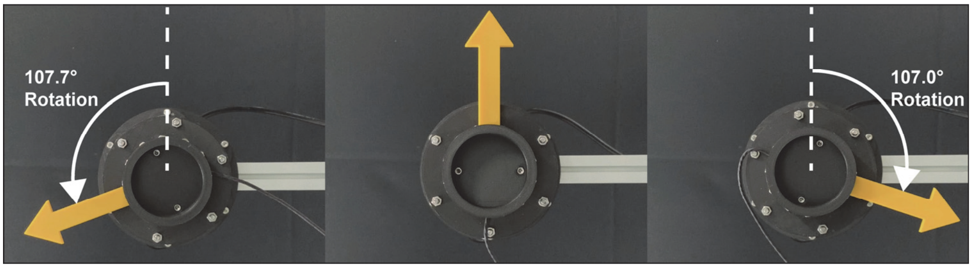

Figure 3-16. Maximum bidirectional deformations of the actuator.

3.6.2 Theoretical model for the height of the actuator

When a twisting motion occurs, the height of the actuator changes. Therefore, a theoretical model was developed to explain the change in height of the actuator due to rotation. As the actuator rotates, the pretwisted tube leans, and this inclination increases with further rotation of the actuator (Fig. 3-17). When a pneumatic tube with an initial length L_0 is pretwisted by an angle theta, the length L of the tube can be calculated as follows.

$$L = L_0 + 2h_\theta \tag{3-14}$$

Where h_θ represents the height of the triangular prism shown in Fig. 3-17a and is the same as equations (3-3) and (3-7) from the previous section.

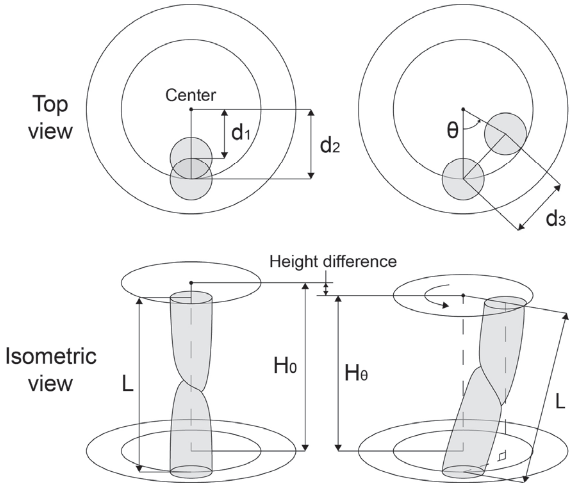

Figure 3-17. Schematic diagram of the twisting of a torsional actuator and change of height during twisting.

By projecting the upper end of the tube onto the bottom plate, the distance d_3 between the centers of both ends is

$$d_3 = \sqrt{d_1^2 + d_2^2 - 2d_1 d_2 \cos\theta} \tag{3-15}$$

where d_1 and d_2 represent the distances from the rotation center of the actuator to the centers of the tube ends fixed to the upper and lower plates, respectively. The height of the actuator H_θ as it rotates by theta is as follows.

$$H_\theta = \sqrt{L^2 - d_3^2} \tag{3-16}$$

Combining (3-3), (3-7), (3-14), (3-15), and (3-16), we obtain the following.

$$H_\theta = \begin{cases} \sqrt{L_0^2 + \frac{4}{3}l^2\cos^2\frac{\theta}{2} - d_1^2 + d_2^2 + 2d_1 d_2\cos\theta}, & 0 \le \theta < 60 \\ \sqrt{L_0^2 + \frac{4}{3}l^2\left(\frac{1}{4}\cos^2\frac{\theta}{2} - \sin^2\frac{\theta_2}{2}\right)} - d_1^2 + d_2^2 + 2d_1 d_2\cos\theta, & 60 \le \theta < 120 \end{cases} \tag{3-17}$$

Here, l represents the side length of the triangular prism as described in the previous section. The theoretical height of the actuator was compared with its actual height (Fig. 3-18). The actual height change of the actuator was measured using a laser distance sensor (LK-G150, Keyence), and the height of the actuator was determined by subtracting this value from its initial height.

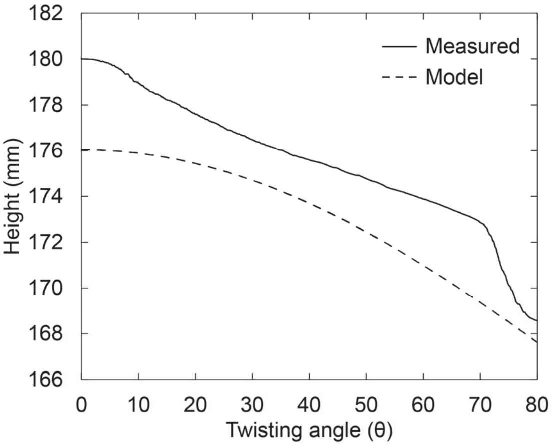

Figure 3-18. Theoretical model for the height of a torsional actuator and comparison with measured height.

3.6.3 Torque experiments

The pretwisted pneumatic tubes produce a torque through their untwisting which should be independent of the axis where they are placed between two rigid plates. This is important as it is necessary to place these actuators at an offset from the center axis in order to have both CW and CCW pretwisted pneumatic tubes. But as the offset pneumatic tubes need to tilt through the twisting motion, it should be verified whether pretwisted pneumatic tubes placed at the center axis and offset to the side produce a similar blocked torque (Fig. 3-19a). Theoretically, the reaction torque should be the same regardless of the position of an applied torque if it is in the same plane. The blocked torque was measured using a force-torque sensor connected to the top plate (RFT60, Robotous). The maximum blocked torque was measured as 0.806 Nm when the tube is placed at the center and 0.794 Nm when it is placed offset to the side.

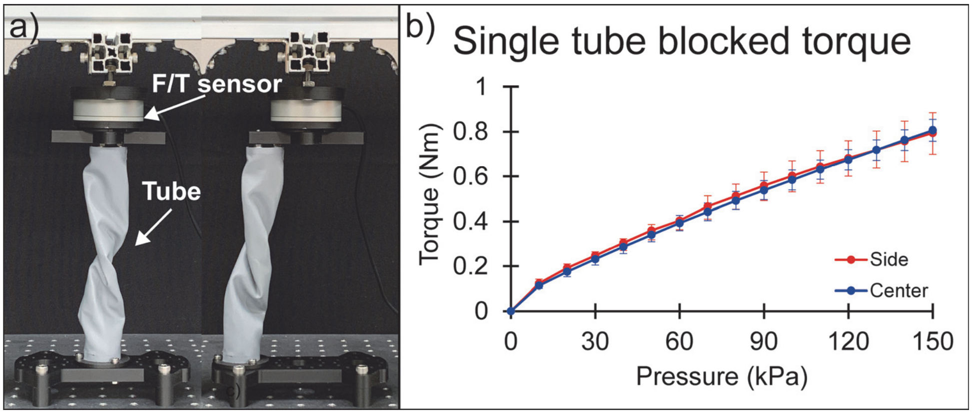

Figure 3-19. (a) Testing setup and (b) torque results for the comparison of central versus side offset pretwisted pneumatic tubes.

The blocked torque as a function of pressure showed a similar rate of increase which is relatively linear, but the offset tube showed a slightly larger error range possibly due to the additional nonlinearities caused by the tilting of the tube (Fig. 3-19b). The measurement deviation for three measurements for three samples each was within 0.095 Nm. The blocked torque of a single tube was measured at 50, 100, and 150 kPa by varying the pretwisting angle in increments of 5° and was compared with the results from the theoretical model (Fig. 3-20). The measurement deviation for three measurements for three samples each was within 0.14 Nm. In the early portion of the deformation, the torque is negative due to the fiber angle of the tarpaulin which makes the tube behave similarly to a fiber reinforced PAM with asymmetric fiber orientation[96].

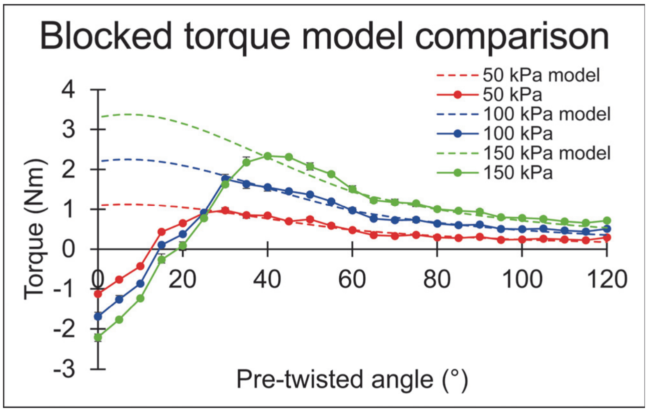

Figure 3-20. Blocked torque of a single tube and comparison with the model.

Measurements at higher pretwisting angles showed a good agreement between the model and the experimental results.

The blocked torque of the actuator containing three CW and three CCW pretwisted pneumatic tubes was then tested using a similar setup by increasing the pressure from 0 to 150 kPa in increments of 10 kPa and then decreasing it back to 0 kPa in decrements of 10 kPa (Fig. 3-21a). Results show that the actuator could generate a maximum blocked torque of 2.44 Nm in the CW direction and a maximum of 2.40 Nm in the CCW direction (Fig. 3-21b). The measurement deviation for three measurements for three samples each was within 0.12 Nm, which is comparable to that measured with a single tube. The increase in blocked torque versus pressure is nearly linear and a slight hysteresis can be seen due to the nonlinearities inherent in soft pneumatic actuators. This torque trend is also similar to that produced by the values produced by a single pretwisted pneumatic tube multiplied by three showing that there is no significant difference in performance even though the number of tubes is increased and with the presence of antagonistic pneumatic tubes (Fig. 3-22). Slightly more hysteresis can be observed due to the larger amount of deformation of the material and interaction between adjacent tubes.

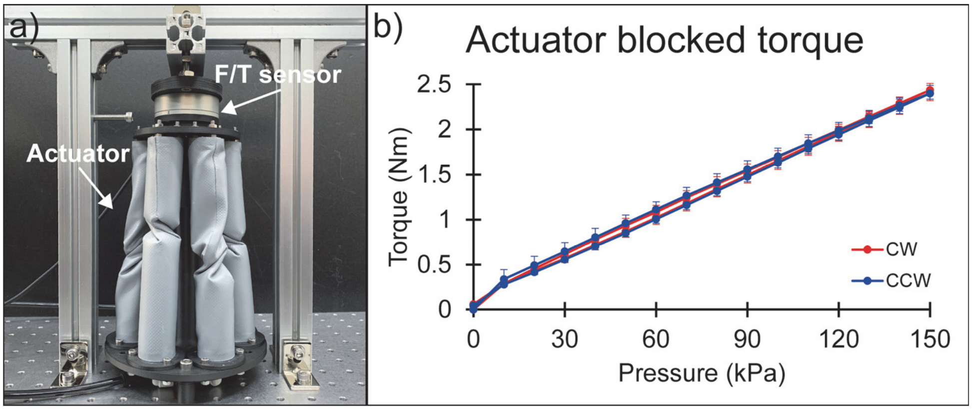

Figure 3-21. (a) Testing jig for measuring the (b) blocked torque of the actuator.

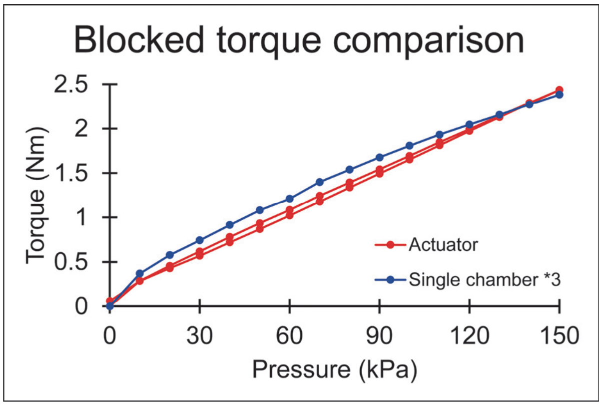

Figure 3-22. Comparison of the blocked torque of actuator versus three individual tubes.

To be useful as part of a robotic system, the actuator should produce sufficient torque over a large ROM. The operation range of the actuator under constant external torques was measured by hanging a payload using a thread to a cylindrical structure at the end of the actuator (Fig. 3-23a). This cylindrical structure has a diameter of 6.5 cm, and payloads of 1, 2, and 3 kg were used to simulate the effect of external torques. The results were then compared to the behavior without payloads shown in Fig. 3-14b. The actuator was pressurized to lift the payload vertically by applying pressures ranging from 0 to 150 kPa in increments of 10 kPa (Fig. 3-23b). For payloads of 1 and 2 kg, the behavior was similar to that observed without payloads in that a large increase in twisting angle occurs at a specific pressure, but this pressure increases as the payload increases. This large increase in twisting angle was not observed within the tested pressure range for the payload of 3 kg but would likely occur with a larger pressure input. The maximum twisting angle was 107.7° without payload, 103.1° for the 1 kg payload, and 100.3° for the 2 kg payload. However, the maximum twisting angle was only 15.87° with the 3 kg payload because the pressure was insufficient to reach the high torque portion of the deformation of the actuator where the pressure required to produce further deformation decreases. These results show that the behavior of the actuator does not change significantly under different payloads, but that more pressure is required for heavier payloads. This also means that further increasing the pressure range allowable by the pretwisted pneumatic tubes should increase the range of external torques which the actuator can operate at.

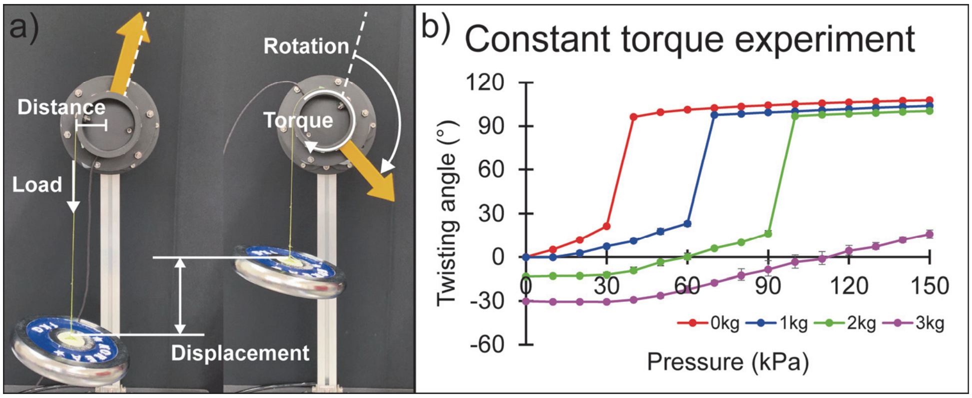

Figure 3-23. (a) Testing setup and (b) results for the twisting actuator at a constant external torque based on input pressure.

Next, the blocked torque of the actuator at different twisting angles and at different pressure was measured (Fig. 3-24). The blocked torque first decreases until a twisting angle of 20° then rapidly increases until 70° and then drops when it reaches near the maximum twisting angle. The low torque up to 20° is the reason the actuator produces a small twisting deformation between 0 to 30 kPa. After this point, the torque increases at a fixed pressure such that the actuator only needs to overcome the low torque region to be able to produce large twisting deformations.

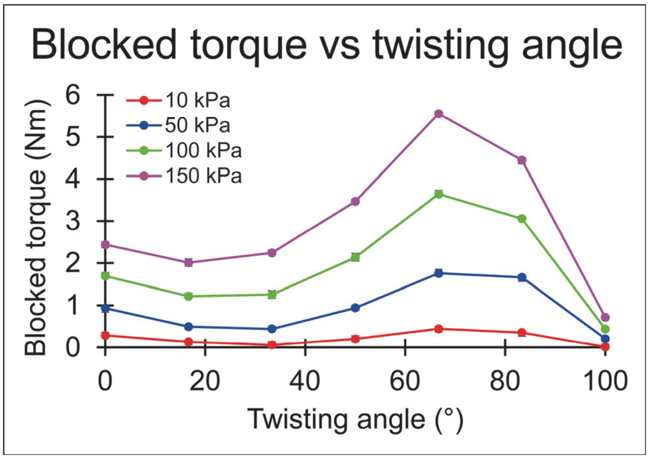

Figure 3-24. Blocked torque at different twisting angles.

3.6.4 Variable stiffness properties

A unidirectional or bidirectional actuator without antagonistic actuation can vary the force it produces if resisted against and its position when not resisted against, but it cannot vary its stiffness at a given position. The proposed actuator can make use of its antagonistic actuation capabilities for varying its stiffness at a given position. The deformation of the actuator originally at its center position under different magnitudes of external torques was measured while equal pressures were applied to both the CW and CCW pretwisted pneumatic tubes. The stiffness was varied by supplying the actuator with pressures of 10, 50, and 80 kPa, and applying external torques of 0.32, 0.64, 0.96, 1.28, and 1.59 Nm by using a payload at a moment arm of 3.25 cm and measuring the twisting angle caused by the applied torque (Fig. 3-25). At 10 kPa, the actuator remained fairly impervious under small external torques due to the intrinsic rigidity of the pneumatic tubes, but it complied with the external torque and reached a maximum twisting angle 31.50° at an external torque of 1.59 Nm, which corresponds to a stiffness of 0.0491 Nm/° (Fig. 3-26a). However, increasing the pressure within the actuator significantly increases the stiffness of the actuator and the maximum twisting angle at an external torque of 1.59 Nm decreased to 6.15° and the stiffness increased to 0.2218 Nm/° at 80 kPa. The stiffness at off-centered positions of 30°, 60°, and 90° was evaluated by finding pressure sets that allowed them to reach these positions with sum of pressures of the CW and CCW tubes of 50, 100, and 150 kPa and applying CW and CCW external torques (Fig. 3-26b). The stiffness at any position increased as the pressure increased. Maximum stiffness values of 0.1417, 0.0901, and 0.7345 Nm/° were achieved at 30°, 60°, and 90° at 150 kPa. These results show that the stiffness of the torsional actuator can be controlled through adjusting the pressure equilibrium

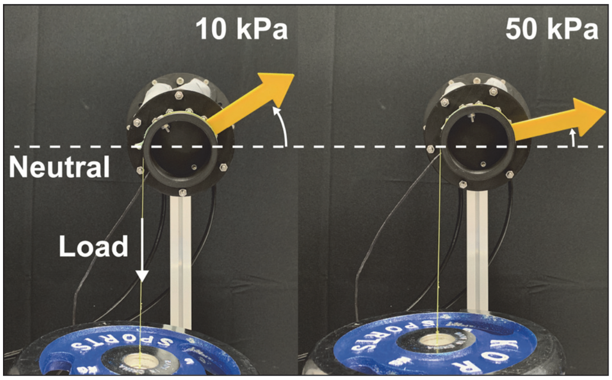

Figure 3-25. Testing setup for variable stiffness.

in the antagonistic tubes.

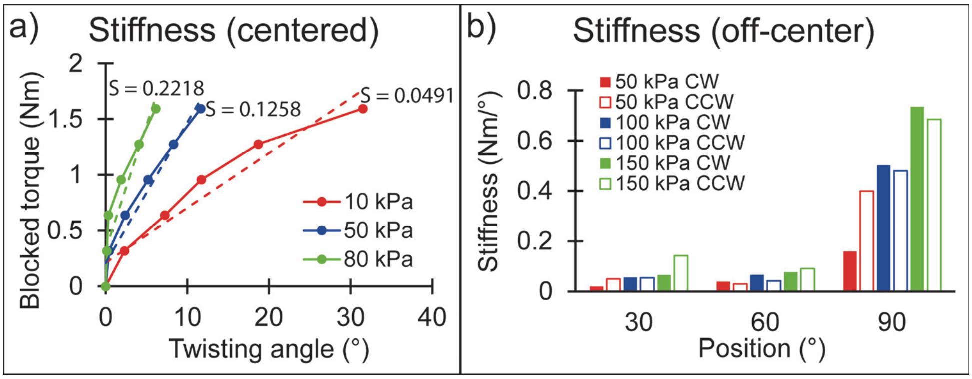

Figure 3-26. (a) Results for the variable stiffness test when the actuator is centered and (b) off-center.

3.6.5 Position control

The angular position control of the actuator was implemented by using proportional-integral-derivative (PID) control (P: 2.500; I: 0.020; D: 0.005). A sum of the pressure of the antagonistic CW and CCW pretwisted tubes of 170 kPa was used. This was done to allow the PID controller to have a single output (Fig. 3-27). This means that if the CW pretwisted pneumatic tubes are pressurized at 100 kPa, then the CCW pretwisted pneumatic tubes are all pressurized at 70 kPa. The actuator was made to follow a square wave pattern with a period of 40 seconds and amplitudes of 30°, 60°, and 90° without any payload (Fig. 3-28a). Results show that the actuator can follow the desired trajectory but that there is a delay in reaching the desired setpoint after each position changes potentially due to the time to inflate and deflate the tubes. The experiment was repeated with a sine wave pattern with a similar period and amplitudes (Fig. 3-28b). Results show that there is a delay between the setpoint and the present twisting angle value which is due to the delay generated by the time required for the airflow exchange within the pneumatic system.

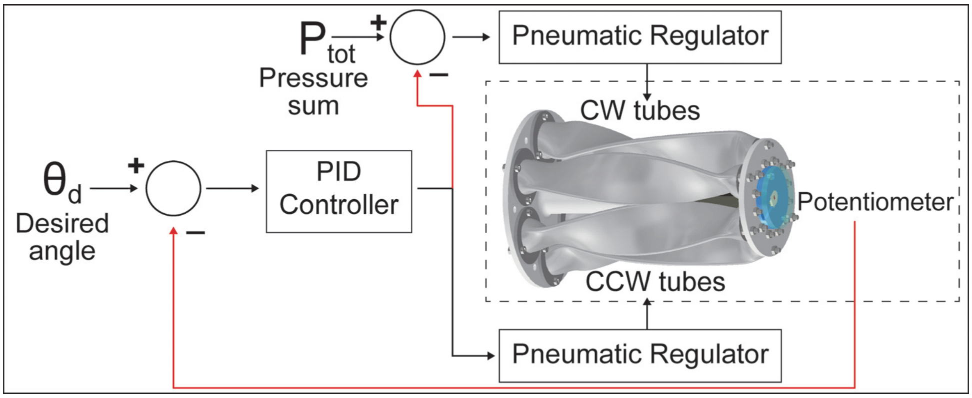

Figure 3-27. PID control diagram for torsional actuator.

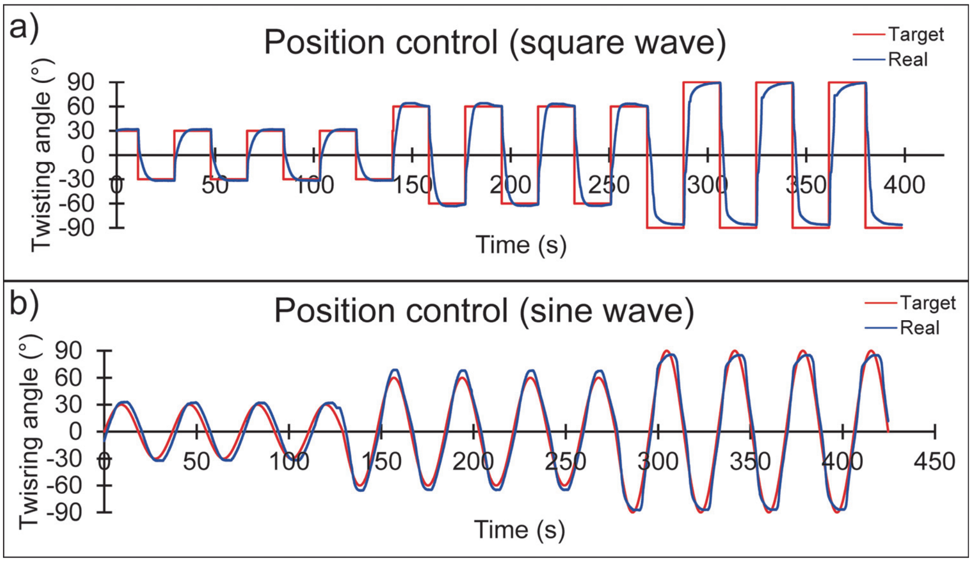

Figure 3-28. Twisting angle control results for a (a) square wave, (b) sine wave.

The position control of the actuator was evaluated for small angle changes over a range of 20° to 40°, which is when the system goes from a lower to a higher torque, with step increments of 2° (Fig. 3-29). Results show that the PID controller with antagonistic actuation produced a good control performance within this region.

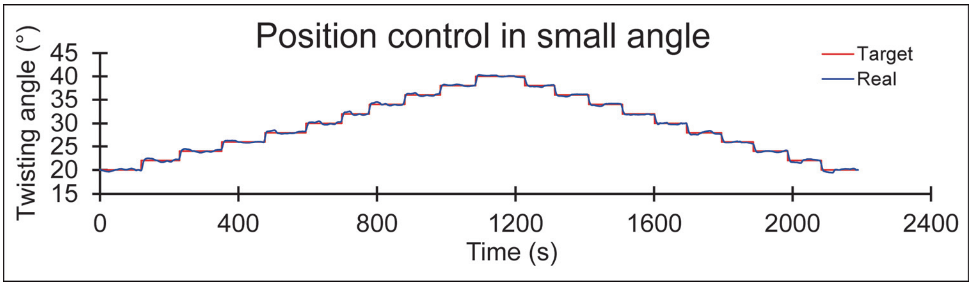

Figure 3-29. Twisting angle control results for small angular step changes.

The actuator was then tested using stepwise inputs with step increases and decreases of 30° within a range of -90° to +90° (Fig. 3-30a). Although the actuator follows the target without much difficulty, there is a delay in reaching the target at low angles due to the high pressure in the antagonistic tubes. This performance could be improved with a more advanced control strategy. The same experiment was then repeated with a payload of 2 kg at a moment arm of 3.25 cm (Fig. 3-30b). A similar behavior could be observed when no external payloads are applied. This shows that the actuator simply changes its pressure equilibrium without affecting its general behavior.

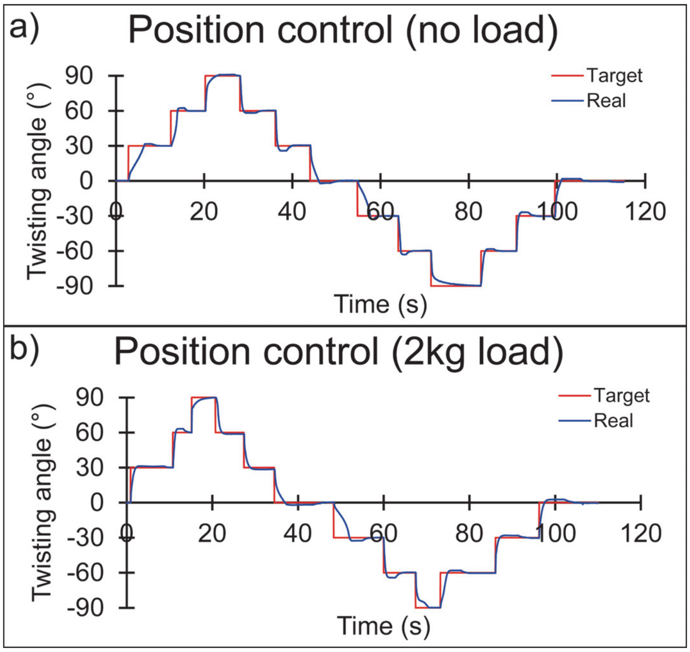

Figure 3-30. Twisting angle control results for (a) step inputs without load, and (b) with an external torque of 0.64 Nm.

3.6.6 Torque control

The blocked torque control of the actuator was implemented using PID control with the parameters (P: 10.000, I: 0.050, D: 0.010), employing the same controller for the pressure sum of 150 kPa of the antagonistic pretwisted tubes as in angular position control. The actuator was tested using stepwise inputs, with an increment and decrement of 0.2 Nm within a range of -1 Nm to +1 Nm (Fig. 3-31). The result shows that the actuator can follow blocked torque input with less delay compared to angular position control. Torque control required significantly higher proportional gains compared to position control, resulting in quicker response times and shorter settling times across all target ranges.

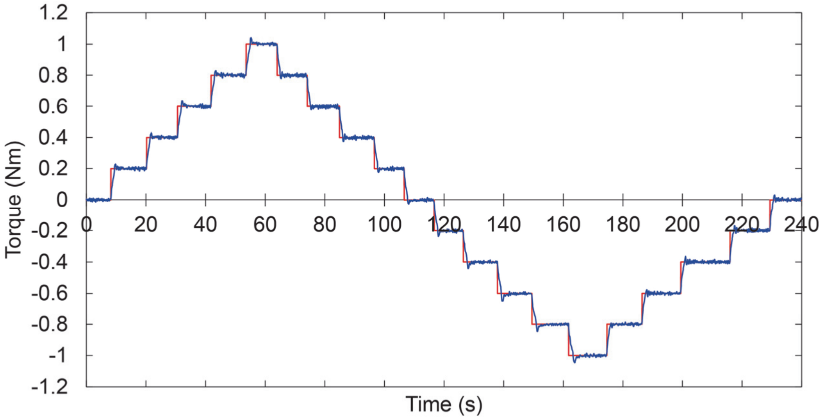

Figure 3-31. Blocked torque control results for torque step changes.

One of the purposes of force or torque control of the actuator is to facilitate smooth interaction with external situations. For a torsional actuator, a free-rotation mode was demonstrated (Fig. 3-32). This mode sets the actuator's target torque to zero and rotates it in the same direction as the external torque when applied. As a result, the actuator was able to rotate freely in compliance with the external torque even when the actuator was inflated with high pressure and maintained its position when the force was removed.

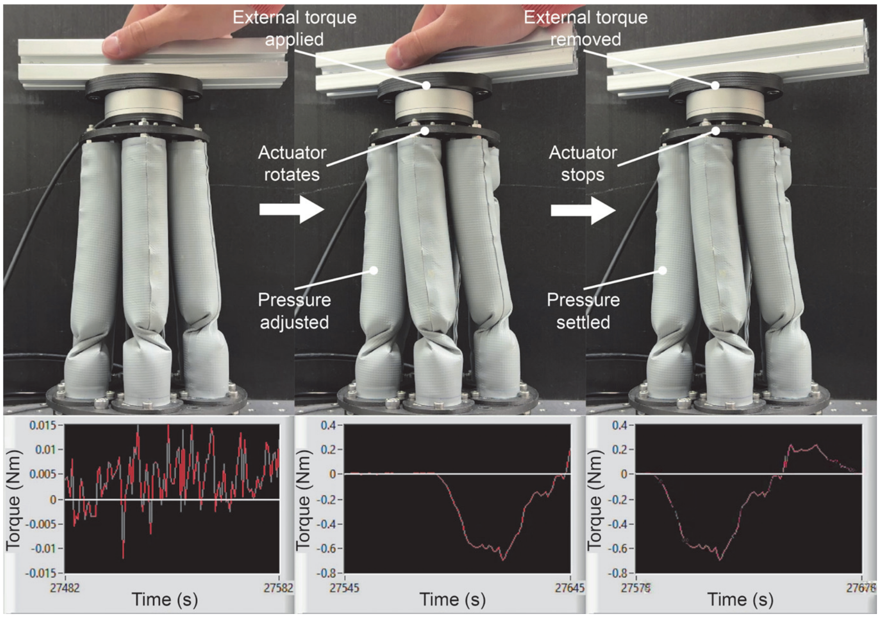

Figure 3-32. Zero targeted torque control for rotational compliance and free rotation mode of torsional actuator.

3.7 Integration into multi-DOF manipulators

3.7.1 6DOFs soft manipulator

A 6DOFs inflatable robotic manipulator with a length of 85 cm was then built by connecting three 2DOFs joints with cylindrical upper arm and lower arm elements (Fig. 3-33). The joint is capable of a maximum bending angle of 85° which gives the arm a large range of motion (Fig. 3-32a), and the arm was tested for handling payloads up to 3 kg (Fig. 3-34b). An inflatable torso with an internal rigid support was built, and two arms were attached at opposite ends of this torso onto the rigid support (Fig. 3-34c).

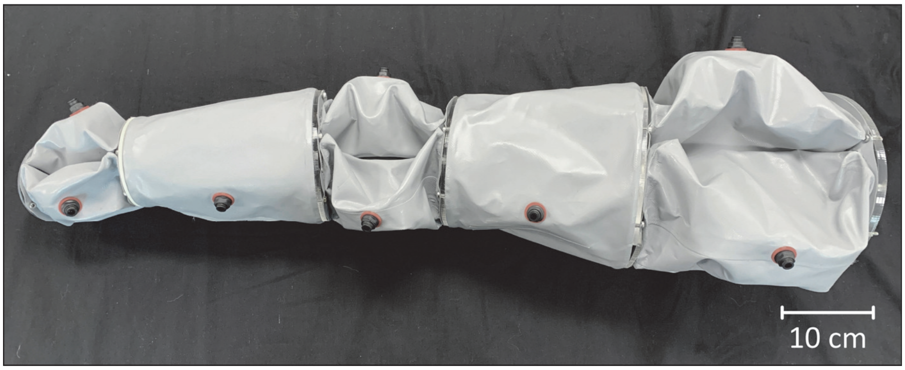

Figure 3-33. Inflatable robotic arm with 6DOFs.

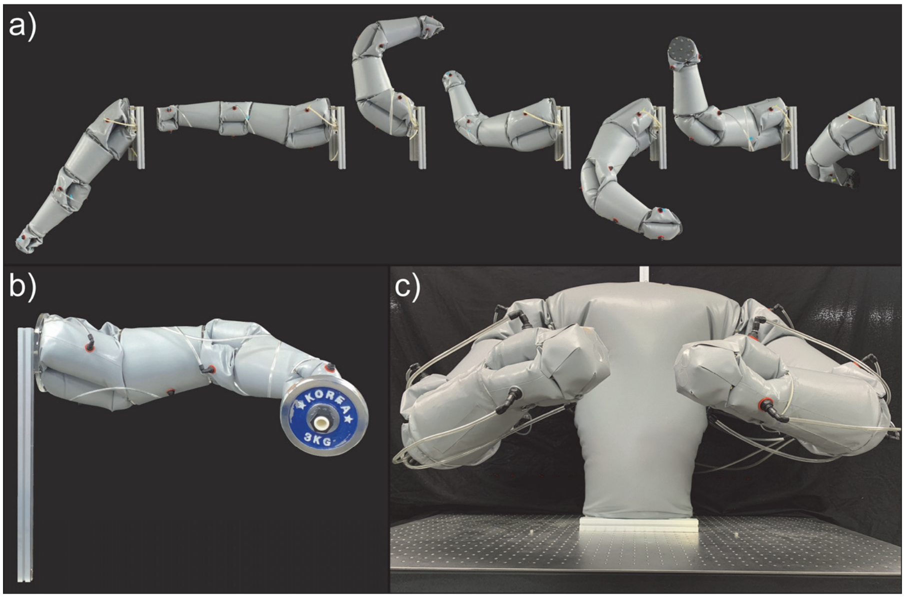

Figure 3-34. (a) Range of motion, (b) the arm handling a payload of 3kg, (c) and its implementation in a dual-arm inflatable robot.

The dual-arm inflatable robot contains a total of 23 individual inflatable elements where each of the three joints of each arm contains three inflatable elements each, and the remaining five elements correspond to the torso of the robot and the upper and lower arms of each arm. The robot is intended for lifting boxes by pushing the tips of both arms onto the box and to utilize the friction force generated from the normal force applied onto the box by each arm. Thus, the arms should move in a mirrored manner to realize this motion.

The 18 inflatable elements of the six joints were connected to nine pneumatic regulators such that each element is connected to the same regulator as the opposite element on the opposite arm to produce this mirrored motion. The remaining five elements were connected to a single regulator. The non-actuating inflatable elements were all set at a pressure of 5 kPa, and a sequence of inflation was set such that the arm began far from the body, moved toward the center of the body as to push on any object in front of the body, and then lifting both arms from the shoulder to produce a lifting motion (Fig. 3-35).

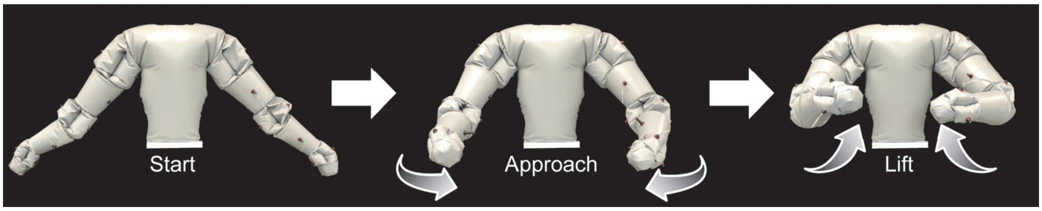

Figure 3-35. Motion of the dual-arm inflatable robot used to lift a box.

This strategy can be used to lift objects such as a box without any specialized lifting end-effectors or without grabbing the box from the bottom (Fig. 3-36a). This motion can also be used to lift objects whose location is unknown since the compliance of the arm making contact before the other will simply push it until contact is made by the other arm. This was tested by positioning boxes with a weight of 160 g and dimensions of 28 cm in height, 41 cm in width, and 31 cm in depth at different positions in front of the arms. The origin of the grid was set as the middle point between the arms in the x-direction and as the line through which the ends of the arms meet in the y-axis.

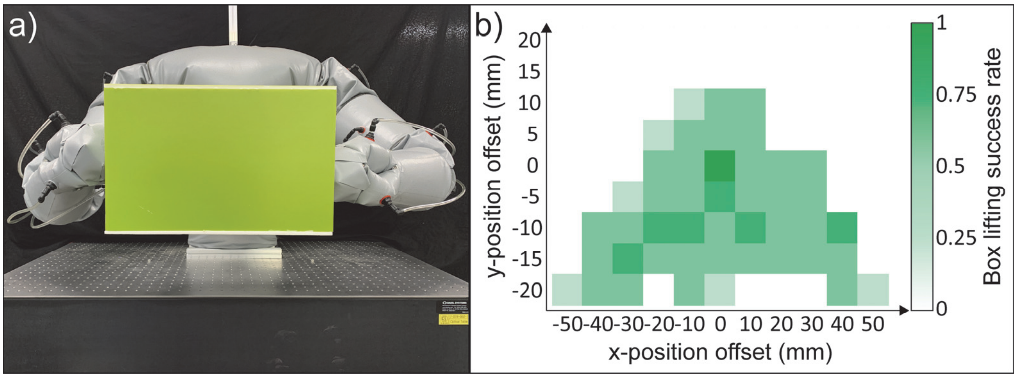

Figure 3-36. (a) Dual-arm inflatable robot lifting a box, (b) lifting success rate depending on the position of the box.

The success rate for lifting boxes for four different trials with position offsets in increments of 10 mm in the x-direction and 5 mm in the y-direction was measured (Fig. 3-36b). The result of this experiment shows that the dual-arm robot can lift boxes with moderate success of 0.5 to 1.0 if the box is located within a triangle from the base of the robot to the origin of the grid. This is because the arm pushes on the box such that it rotates out of the way without being pushed toward the other arm. So, the robot would need to move sufficiently close to the box such that its center of mass remains within this triangle.

Next, the success rate for five trials for boxes of different sizes was measured where the box sizes are based on standard Korean post office box sizes (Fig. 3-37). The dimensions of each box are given in the legend of the figure. Results show that the dual-arm robot has the highest success rate when boxes are sufficient size for the arm to position themselves correctly and stay within the range where the arms can produce a sufficient lateral force. Large boxes resulted in the arms being unable to position themselves adequately while smaller box sizes were outside of the range of the arms. Next, the box of size 4 (width: 41 cm, depth: 31 cm, height: 28 cm, weight: 160.3 g) was tested for five trials for different boxes with weights ranging from 160 to 560 g (Fig. 3-38).

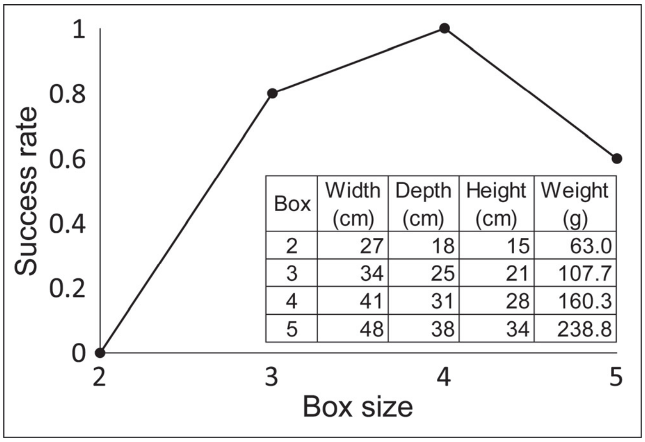

Box	Width (cm)	Depth (cm)	Height (cm)	Weight (g)
2	27	18	15	63.0
3	34	25	21	107.7
4	41	31	28	160.3
5	48	38	34	238.8

Figure 3-37. Lifting success rate depending on the box size.

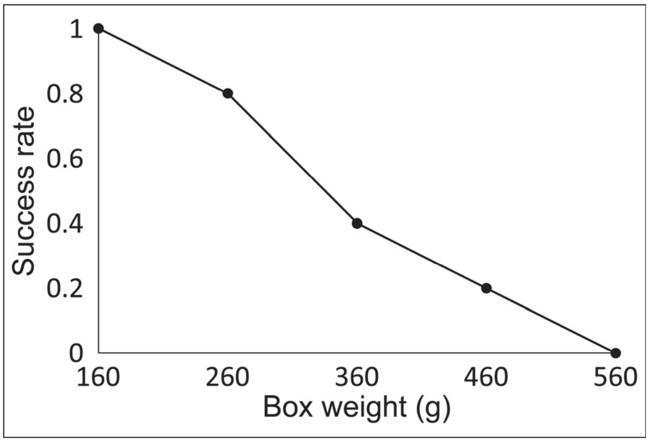

Figure 3-38. Lifting success rate depending on the box weight.

The dual-arm robot's success rate decreased almost linearly until failing every trial at 560 g. It is to be noted that the lifting capability could be increased by using more specialized grippers that produce higher friction forces such as gecko-inspired grippers or ones that do not rely as much on friction such as suction cups.

3.7.2 DOFs soft manipulator

The proposed torsional actuator was used as the forearm of a soft robotic manipulator which has a shoulder joint, an elbow joint, a wrist joint, an upper arm, and a forearm (Fig. 3-39). By adding torsional actuator's one DOF, the soft robotic manipulator has a total of 7DOFs, weighs 3.32 kg, and has a length of 90 cm. The twisting forearm by itself weighs 0.405 kg. Compared to a human arm, the shoulder is missing a torsional DOF, and the elbow has an additional bending DOF. A 3D printed hanger was used

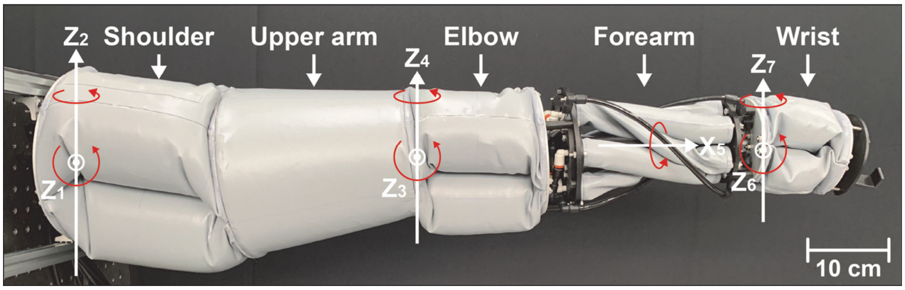

Figure 3-39. Implementation of the 7DOFs soft robotic manipulator with the proposed torsional actuator as the forearm and its rotational axes.

as the end-effector of the soft robotic manipulator (Fig. 3-40). This hanger could easily be replaced by a soft or rigid robotic gripper.

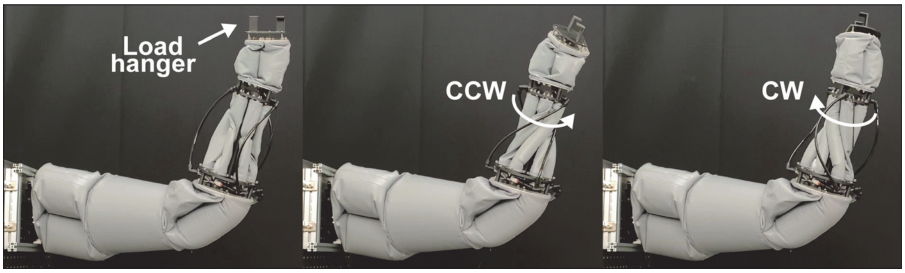

Figure 3-40. Torsional range of motion of the forearm.

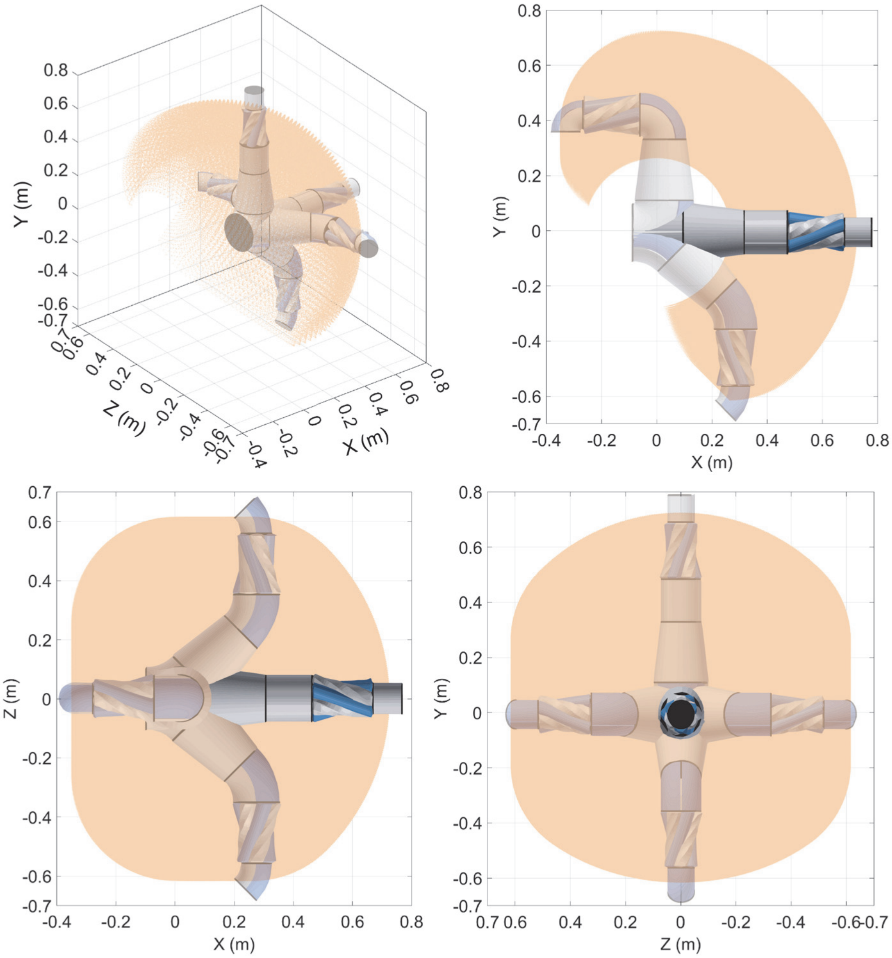

Figure 3-41. Workspace of the 7DOFs manipulator.

The robotic manipulator was installed horizontally on a vertical surface, and a watering can and a flower basket were placed in front of the arm, inside the manipulator's workspace (Fig. 3-41). This workspace is where the robot can reach in at least one orientation. In open-loop control, the robotic manipulator was made to approach the watering can, pick it up using the hanger through a CW motion of the

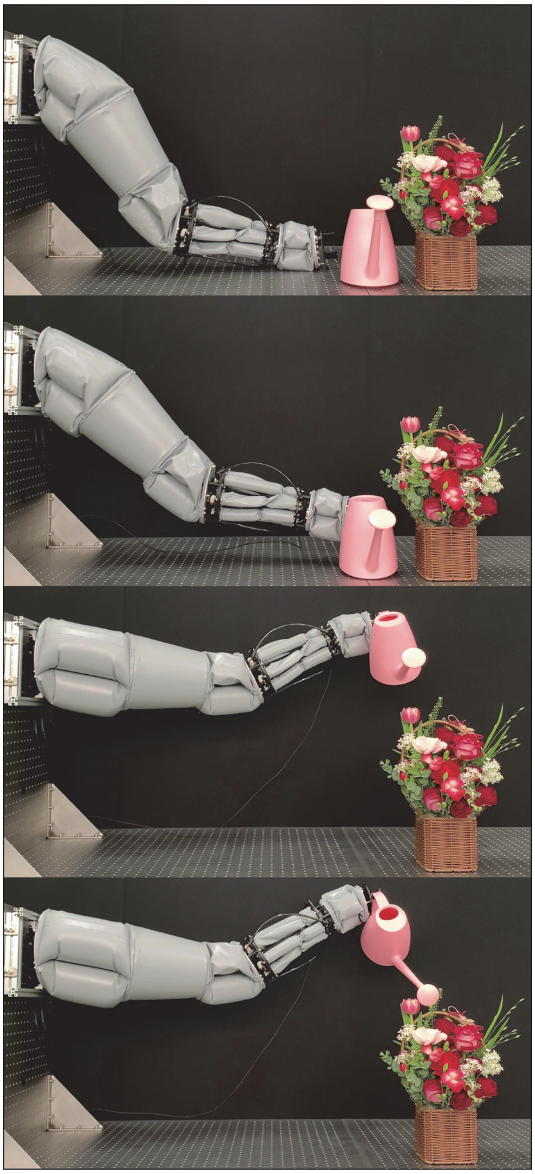

Figure 3-42. The soft robotic manipulator approaching, picking up and using a watering can for watering flowers.

forearm, lift it up, and water the flowers by tipping the watering can using a CCW motion of the forearm (Fig. 3-42). This is an example of a daily life task which requires bidirectional motion of the forearm and would be hard to achieve without this additional DOF. The robustness and compliance of the soft robotic manipulator and twisting forearm under external disturbances was validated. First, a payload of 3 kg was fixed at the end of the wrist joint, and the robot arm was made to move to the horizontal position followed by twisting of the forearm. The forearm could fully twist when pressurized to 180 kPa. The robot arm was made to follow a repeated motion pattern while several impacts were applied to it. It was confirmed that all joints and the forearm could perform the given motion without being significantly affected by these disturbances.

3.7.3 Large-scale inflatable robotic arm

The concept of the proposed inflatable robotic arm can be scaled in size if the inflatable chambers can withstand the tension forces that they transmit and if the rigid parts can withstand the mechanical forces that they are subject to. A large-scale inflatable robotic arm was built to test the upper limit of the proposed concept in terms of size. To this end, the rigid plates used in the joints were replaced with 5 mm thick aluminum plates, and additional plates were added on the inside of the inflatable chambers of the shoulder joint.

The inflatable chamber of the shoulder joint was scaled such that the dimensions of the shoulder joint are 40 cm in diameter and 40 cm in height, which are approximately twice the dimensions of the inflatable shoulder joint used in the 7DOFs soft robotic arm and four times that of its wrist (Fig. 3-43). The total length of the large-scale inflatable robotic arm is 4.95 m with the shoulder and elbow joints having a length of 0.4 m each, the upper and lower arms having a length of 2 m each, and the wrist joint having a length of 0.15 m (Fig. 3-44). The total weight of this arm is 16.85 kg with the shoulder joint having a weight of 7.75 kg, the upper arm having a weight of 2.02 kg, the elbow joint weighing 4.53 kg, and the forearm weighing 2.55 kg. An inflatable gripper made from paired pouch motor patterns was attached at the end of the large-scale inflatable robotic arm such that the length from the base of the arm to the palm of the gripper is 5 meters.

Figure 3-43. Inflatable joint element with a diameter of 40 cm and a height of 40 cm.

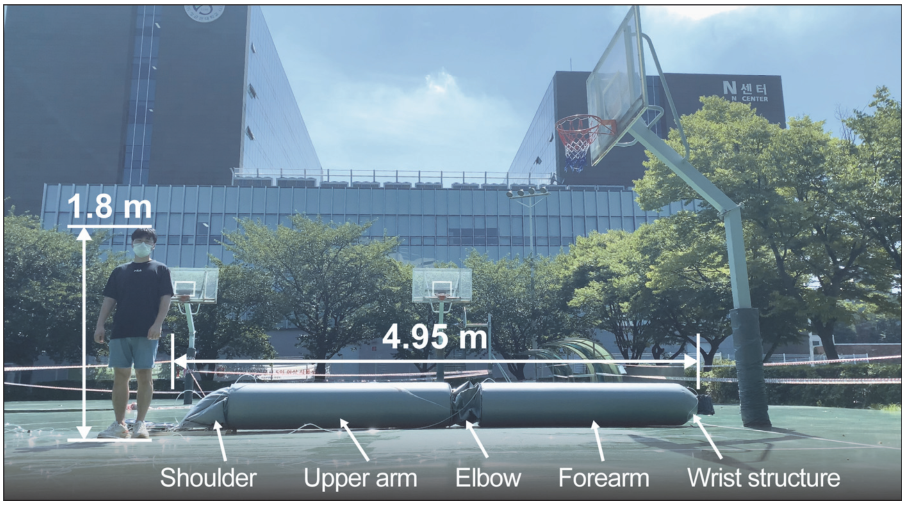

Figure 3-44. Comparison of the large-scale inflatable robotic arm with a human.

The large-scale inflatable robotic arm was installed on an outside basketball court at the free-throw line 4.60 m from the board with the hoop being 3.05 m off the ground, and a basketball was positioned in diagonal in front of the inflatable arm (Fig. 3-45). In open-loop control, the inflatable robotic arm was made to reach for the basketball, grab it, lift it, the arm was extended in a nearly straight position to place the basketball over the hoop, and the basketball was then released through the hoop. The basketball weighs 624 g and was able to be lifted off the ground and the arm fully extended while holding the basketball.

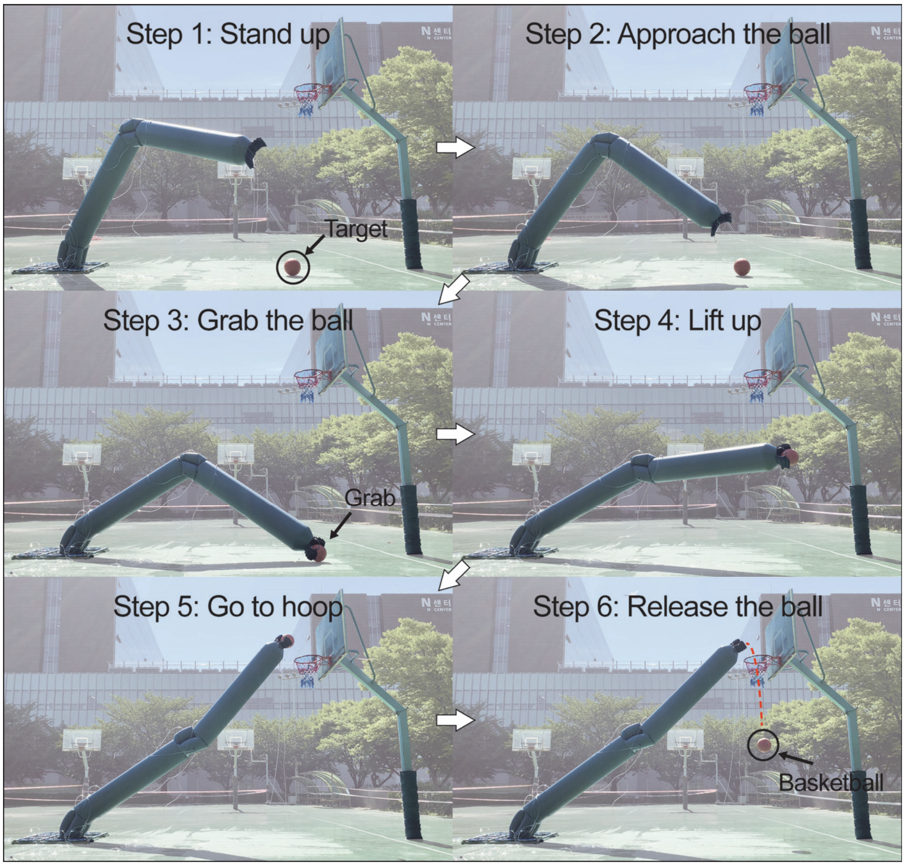

Figure 3-45. Large-scale inflatable robotic arm scoring a 2-point from the free-throw line on a basketball court.

Some of the largest issues encountered while doing this experiment were related to oscillation of the arm during the regulation motion. This occurred due to the large momentum generated during its motion against the high compliance in the joints and the increased external torque produced by the wind forces acting on the large structure itself. The length of this arm is comparable with the largest industrial robotic arms yet weighs and costs multiple orders of magnitude less, and it can be safely handled by and around humans.

Chapter 04

Hybrid hard-soft robotic joints and manipulators

4.1 Introduction

The bending actuators in the previous chapter have shown that they can be used in a variety of applications based on their high compliance and wide range of motion. However, due to structural complexity and a high degree of freedom, non-conventional sensors such as soft sensors are required to measure joint angles, making position control difficult. Therefore, in this chapter, a hybrid soft robotic joint that complements the shortcomings of the previous bending actuator without losing its advantages is introduced. This soft robot joint has a hybrid hard-soft structure by combining an origami-structured pneumatic chamber with a rigid frame, which has a fixed rotational axis. Additionally, rotational compliance is maintained while preventing unintended deformations, and a general rotary sensor such as an encoder or potentiometer can be used, enabling simpler joint angle measurement and control.

Two designs of hybrid joints were developed, consisting of a single chamber and a dual chamber. The manufacturing process, torque modeling, torque and range of motion, and position control are explored. A 3DOFs soft robotic manipulator was constructed by integrating one single chamber joint and two dual chamber joints, and its kinematics were analyzed. A pick-and-place operation of fruit was then performed.

4.2 Design and manufacturing of origami joint

The main purpose of this work is to develop an origami-based inflatable robotic joint that can be used to produce high actuation torques with a volume efficient design such that a high range of motion can be used (Fig. 4-1a). One advantage of using an origami structure is that the semi-rigid origami structure constrains the excessive DOFs that entirely soft structures have and forces the deformation of the structure to deform according to the pattern of the origami. This allows positive pressure to be used for expansion of the joint and negative pressure for the folding of the joint without causing a collapse of the structure (Fig. 4-1b). Each joint is composed of multiple unit origami chambers, each containing a base chamber to which reinforcements of the same material as the base chamber are fixed to stiffen the facets more than the folding lines that define its deformation (Fig. 4-1c). The portion of the unit chamber to which facet reinforcements are not attached have lower rigidity than the reinforced portion which allows for the natural formation of valley and mountain folds of the structure.

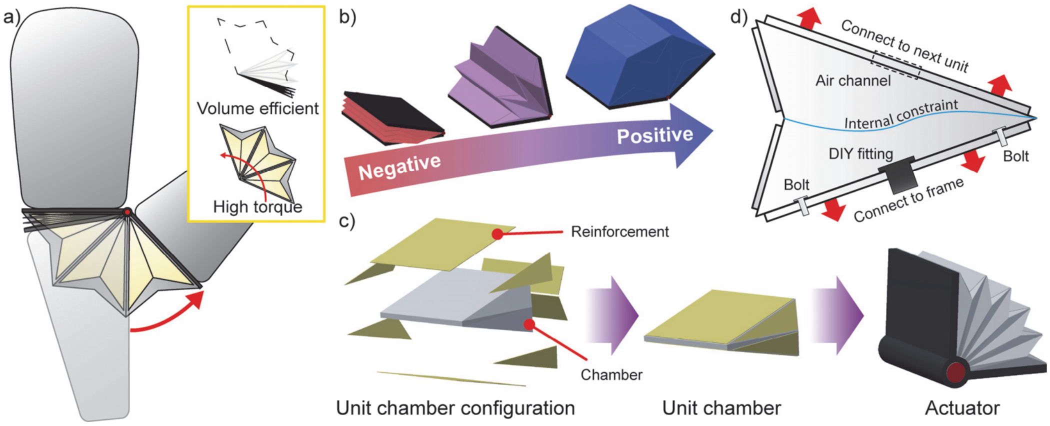

Figure 4-1. (a) Schematic of the origami inflatable robotic joint, and (b) behavior of joint when positive and negative pressures are applied. (c) Configuration of the unit chamber with reinforcement and of the inflatable joint, and (d) internal constraint that prevents unintended wall deformations and connection between chamber and frame.

The higher rigidity of the reinforcements also allows them to not significantly deform under applied pressure and thus not to collapse or buckle whether subjected to positive or negative pressures. The facet reinforcements are the same shape as each chamber pattern piece but are about 1 mm smaller in size and are attached to the chamber facets. In addition to using stiff facets, the individual origami chambers also contain internal constraints that prevent the outside wall from folding outward and thus maintain the joint in the range of deformation where a positive volume change results in a positive change in chamber angle. A detailed internal diagram of a chamber connected to the frame is shown in Fig. 4-1d. A tarpaulin strip serves as an internal constraint, limiting the distance between both ends of the unit chamber while withstanding tension during high-pressure actuation without any loss in torque.

The origami chambers in this chapter are made from tarpaulin, which is a type of fiber-reinforced material consisting of polyester fabric coated on both sides with polyvinyl chloride (PVC). First, mask layer pieces, chamber pattern pieces and facet reinforcements are laser cut (Fig. 4-2). The mask layer pieces are used to draw marks on the chamber pattern pieces to help with its assembly process. The facet reinforcements are attached to the chamber pattern pieces using an adhesive (Loctite 401, Henkel). The assembly of all elements produces a three-dimensional unit chamber. Multiple unit origami chambers can then be stacked to form a complete origami joint through connections between the air passages among nearby unit chambers. The actuator is then combined with a 3D printed hinged rigid frame to prevent off-plane deformation and enable the use of a potentiometer to measure the deformation of the joint.

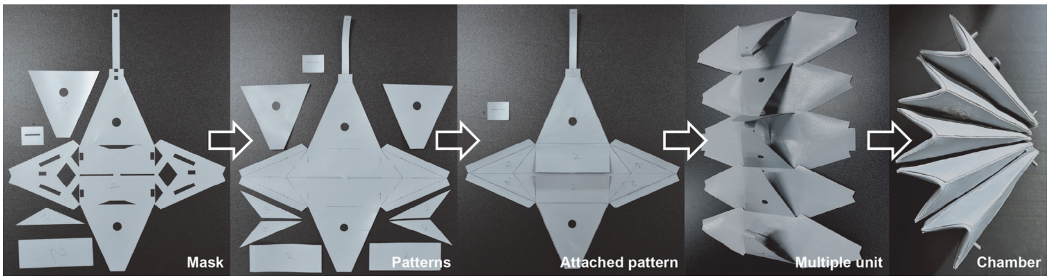

Figure 4-2. Manufacturing process of the joint chamber.

Two designs of origami joints will be investigated in this work and all origami joints tested in this work will contain five unit origami chambers. The first is a single chamber origami joint where a single actuator is used for actuation such that positive pressure creates the expansion of the joint and negative pressure the folding of the joint. This can be done without an active antagonistic force such that it may require a bias such as a spring to maintain its folded configuration in the absence of an applied pressure. The second is a dual chamber origami joint where antagonistic actuators can use the same type of pressure, positive or negative, to change the stiffness of the joint or have opposite types of pressures such that both chambers can be used cooperatively to produce a torque in the desired direction.

4.3 Theoretical model of unit chamber

The unit chamber of this actuator is in the shape of a triangular prism when fully expanded, and folds according to the designed origami pattern during contraction. Taking one of the unit chambers used in this work as an example, the length of two sides of the triangle side is l, the length of the surface with the folding line is $2b$, and the distance between the sides is l (Fig. 4-3a). The initial angle between the top and bottom surfaces is θ_0, and during the process of folding the chamber, the angle between the top and bottom surfaces is θ. During folding, the folding line on the back moves inward by a distance s, and the side protrudes outward with a distance x (Fig. 4-3b). According to the geometry, the relationship between l, b, α and s can be written as

$$l^2 = \left(l\cos\frac{\theta}{2} - s\right)^2 + b^2 - 2\left(l\cos\frac{\theta}{2} - s\right)b\cos\alpha \tag{4-1}$$

where α represents the back angle, which increases as the folding line in the back moves forward.

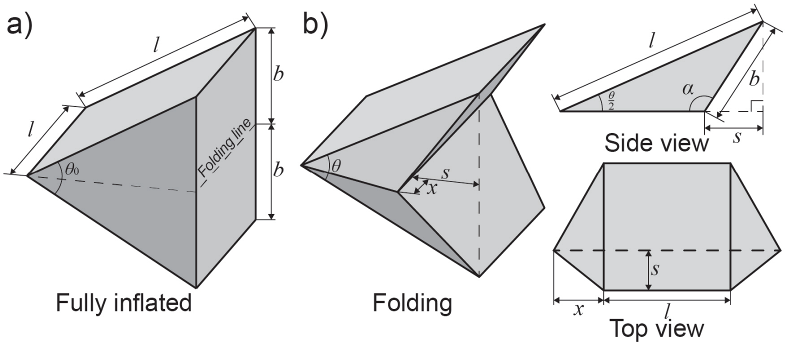

Figure 4-3. (a) Schematic diagram of a unit chamber and its dimensions in the fully inflated state and (b) during folding.

It can be calculated from the following relation.

$$\cos\alpha = -\cos(\pi - \alpha) = -\frac{s}{b} \tag{4-2}$$

Where s can be calculated as follows.

$$s = \sqrt{l^2\left(\cos^2\frac{\theta}{2} - 1\right) + b^2} \tag{4-3}$$

The projection from the top view shows the following relationship between l, s, and x.

$$x^2 + \left(l\cos\frac{\theta}{2} - s\right)^2 = \left(l\cos\frac{\theta_0}{2} - x\right)^2 \tag{4-4}$$

Substituting s into (6.4) and rearranging for ,x

$$x = \frac{l}{2}\cos\frac{\theta_0}{2} - \frac{2l^2\cos^2\frac{\theta}{2} - 2l\cos\frac{\theta}{2}\sqrt{l^2\left(\cos^2\frac{\theta}{2} - 1\right) + b^2} + b^2 - l^2}{2l\cos\frac{\theta_0}{2}} \tag{4-5}$$

The area A of triangle in Fig. 6-3b can be written as

$$A = \frac{1}{2}l\sin\frac{\theta}{2}\left(l\cos\frac{\theta}{2} - s\right) \tag{4-6}$$

and the volume V of the unit chamber can be represented as a sum of the middle volume V_1 and side volume V_2.

$$V = V_1 + 2V_2 = 2Al + \frac{4}{3}Ax \tag{4-7}$$

Combining (4-2), (4-5), (4-6), and (4-7), we obtain the following.

$$\begin{aligned} V = {} & l\sin\frac{\theta}{2}\left(l\cos\frac{\theta}{2} - \sqrt{l^2\left(\cos^2\frac{\theta}{2} - 1\right) + b^2}\right) \\ & \left(l + \frac{l}{3}\cos\frac{\theta_0}{2} - \frac{2l^2\cos^2\frac{\theta}{2} - 2l\cos\frac{\theta}{2}\sqrt{l^2\left(\cos^2\frac{\theta}{2} - 1\right) + b^2} + b^2 - l^2}{3l\cos\frac{\theta_0}{2}}\right) \end{aligned} \tag{4-8}$$

By the principle of conservation of energy, the torque M that the unit chamber produces can be written as

$$M = P\frac{dV}{d\theta} \tag{4-9}$$

Where P is the internal pressure and $dV/d\theta$ is the change of volume with respect to the change of angle of the chamber. In order to calculate M, $dV/d\theta$ must be calculated but can also be approximated by numerical methods such as finite difference approximation. Since the actuation system have high resistive torques generated by the friction between the frame and the chambers, the net theoretical torque M_{net} can be represented as follows.

$$M_{net} = M - M_f \tag{4-10}$$

Where M_f is resistive torque which can be experimentally measured at the atmospheric pressure. Multiple chambers can cooperate to improve the torque of the actuator by using positive and negative pressure together, and the sum of the torque M_{tot} is as follows.

$$M_{tot} = \sum_{i=1}^{n} M_{net,\,i} \tag{4-11}$$

When l is 70 mm and b is 40 mm, the torque produced by the unit chamber at a pressure of 10, 30, and 50 kPa is as shown in Fig. 4-4. This curve only considers the geometric characteristics of the chamber, but it will also account for the material resistance and structural constraints of the actuator in later sections.

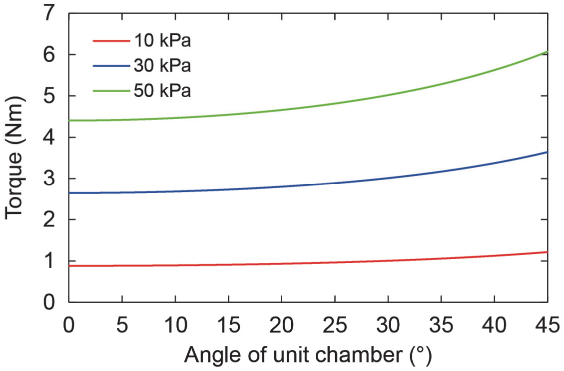

Figure 4-4. Theoretical model for the torque of a unit chamber.

4.4 Performance of origami joints

4.4.1 Single chamber origami joint

The single chamber origami joint contains five unit chambers that are connected in series and share the same pressure to simultaneously expand and contract. The chambers are connected to each other through air channels and are connected to a rigid frame using bolts. A 3D printed pneumatic connector is added to the first unit chamber to connect it to the pneumatic source. A potentiometer (3382, Bourns) is inserted on the rotation axis of the joint to measure its deformation (Fig. 4-5a). Eight elastic rubbers are used to provide an antagonistic force to the joint during expansion as to prevent the actuator from fully deforming at low pressures when unloaded. The main advantage of this single chamber origami joint design is its large fluidic chamber volume occupying the entirety of the cross-sectional area and its large range of motion even if it lacks a controllable antagonistic force. Its implementation with a rigid frame means that the overall joint is a hard-soft hybrid structure with a motion pattern determined entirely by the rigid structure. The rotational resistive torque of the single chamber joint was measured by fixing a force/torque sensor to the tip of a 35 cm aluminum profile attached to the joint (Fig. 4-5b).

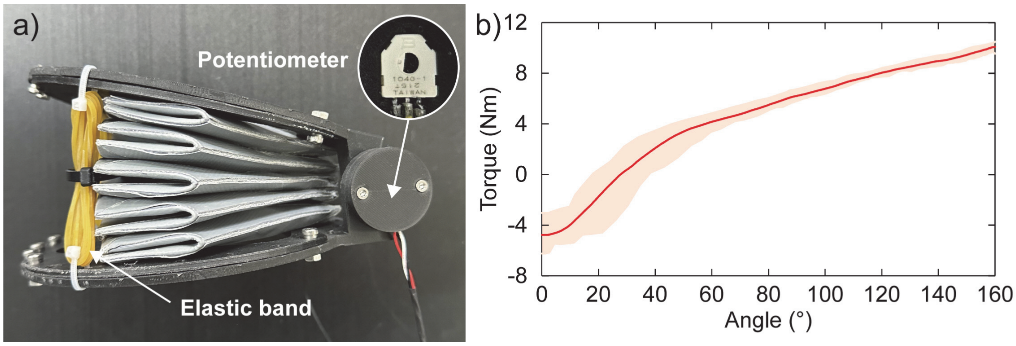

Figure 4-5. (a) Single chamber joint with potentiometer and elastic band and (b) connection between chamber and frame.

The single chamber origami joint was then tested by fixing it vertically and applying a positive pressure to the chamber which was increased from 0 to 50 kPa in increments of 10 kPa (Fig. 4-6a). The joint angle was measured by using the on-board potentiometer. The joint was tested with payloads of 1, 3, and 5 kg attached at the end of a 20 cm aluminum profile. With payloads of 1 and 3 kg, the joint easily reaches close to its maximum joint angle of 162° at pressures of 30 kPa and higher (Fig. 4-6b). However, the joint can only reach a joint angle of 130° at 50 kPa with a payload of 5 kg. Higher pressures would be necessary to reach higher angles with this payload or to operate with its full operational range with heavier payloads. Additionally, the tension of the elastic band increases as the actuator reaches a higher angle, requiring even higher pressure to overcome. A large hysteresis is found for all payloads. The reason is that the torque applied by the load is highest at an angle of 90° and decreases as the angle increases, so a large angle is maintained until the pressure falls below a certain threshold.

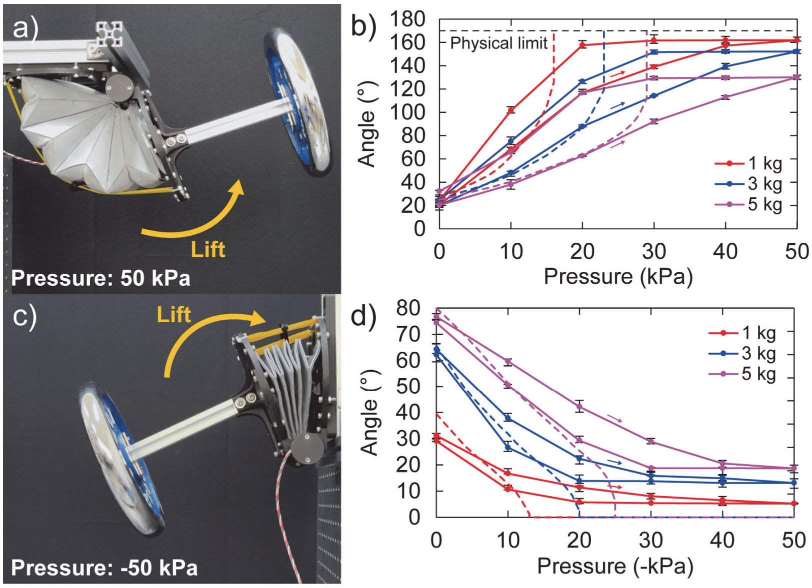

Figure 4-6. Single chamber joint lifting different payloads using (a) positive pressure and (b) its range of motion, and using (c) negative pressure, and (d) its range of motion.

The joint chamber was then fixed vertically such that the payload causes an increase in angle of the joint and a negative pressure ranging from 0 to 50 kPa was used joint to lift the payload (Fig. 4-6c). Results show that the joint could reach a joint angle of 5.3° at 50 kPa and started from a joint angle of 31° under 1 kg payload (Fig. 4-6d). The highest position that the joint lifted with a payload of 5 kg was 19° at 50 kPa. The data in Fig. 4-6b, and Fig. 4-6d were compared with the results from the theoretical model, which was built through the same process but customized for a single chamber joint. The theoretical value of the angle for each type of pressure and payload was calculated from the numerical model.

4.4.2 Dual chamber origami joint

The dual chamber origami joint contains two antagonistic origami chambers which can both sustain positive and negative pressures connected to a rigid structure (Fig. 4-7). Although the two chambers can act antagonistically by using the same type of pressure, they can also be used cooperatively by using positive pressure in one chamber and negative pressure in the other chamber. Compared to the single chamber origami joint, the range of motion in a single bending direction is much smaller, but it is possible to bend bidirectionally. A potentiometer is connected to this shaft to measure the deformation of the joint.

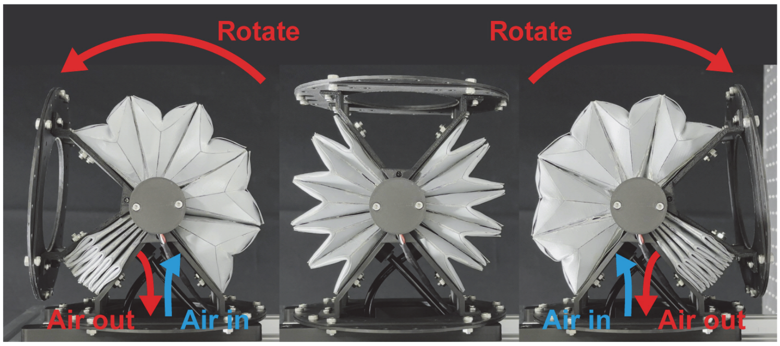

Figure 4-7. Dual chamber joint using positive and negative pressures and actual rotation.

The rotational resistive torque of the dual chamber joint was measured using the same procedure as the single chamber joint (Fig. 4-8). Since most of the resistance is caused by material deformation and frame friction, it can be observed that the resistance increases with the angle and is smaller than the single chamber joint.

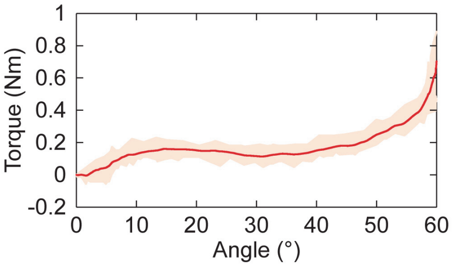

Figure 4-8. Resistive torque of dual chamber joint.

The dual chamber origami joint was tested by hanging the joint vertically, attaching a payload, and applying pressure in one chamber (Fig. 4-9). The joint was first tested by applying positive pressure ranging from 0 to 50 kPa in one chamber with payloads of 1, 3 and 5 kg attached at the end of an aluminum profile with a length of 20 cm. With a payload of 1 kg, the joint could reach a bending angle of 65° at a pressure of 50 kPa (Fig. 4-10a). However, the joint could only achieve a bending angle of 21° with a payload of 5 kg. Hysteresis could also be observed between inflation and deflation due to the bending stress and nonlinear behavior of the origami chamber material resulting from material deformation. Applying a negative pressure ranging from 0 to 50 kPa in the same chamber with similar payloads results in a similar behavior (Fig. 4-10b). A small difference in performance with the positive pressure experiment can be observed, but this difference could be due to differences in chamber geometry resulting from manufacturing errors.

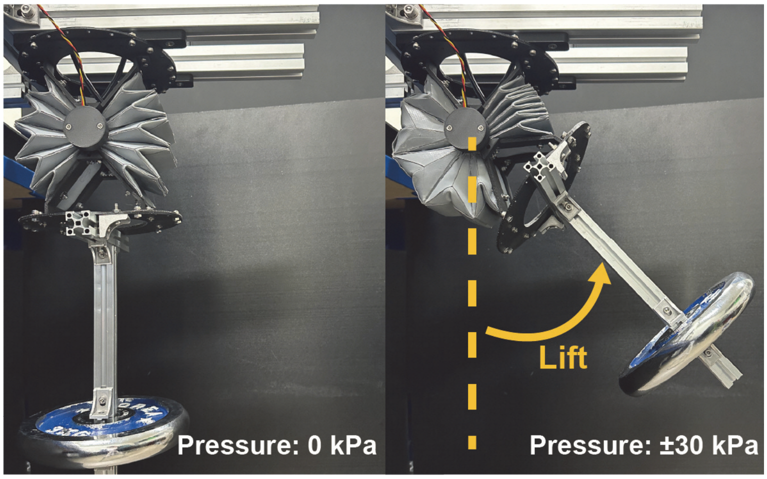

Figure 4-9. Load lifting experiment using the dual chamber joint and its range of motion under different payloads.

The data in Fig. 4-10a and Fig. 4-10b were compared with the results from the theoretical model. The theoretical value of the angle for each type of pressure and payload was calculated from the numerical model. However, there is a point where the rotation of the actuator is blocked due to physical limitations, which is at an actuator angle of 65°. The difference between theoretical and experimental data is largest with a payload of 1 kg and relatively small at higher loads. The reason is that the resistive torque, mainly made by the non-actuating chamber, blocks the actuator from rotating even when the pressure is sufficient to lift the load. In the case of 1 kg, the error is significant because the interruption is severe at the higher range of rotation. In the case of 3 kg and 5 kg, the actuator remains in the range of deformation where the resistive torque is small.

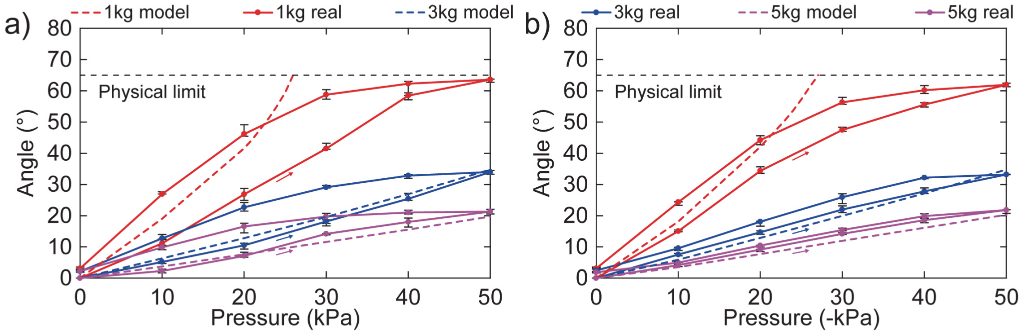

Figure 4-10. Load lifting experiment results when (a) positive pressure and (b) negative pressure are applied.

Next, the dual chamber origami joint was tested while using the two chambers in cooperative mode by applying positive pressure in one chamber and negative pressure in the antagonistic chamber (Fig. 4-11). This mode was tested for opposite negative and positive pressures up to 50 kPa with payloads ranging from 1 to 5 kg (Fig. 4-12a). Results show that the actuator can achieve a similar performance to when using a single type of pressure with approximately half the pressure in each chamber. However, when positive and negative pressures of 50 kPa were applied to the two chambers, joint angles of 74°, 62°, and 42° were generated at payloads of 1, 3, and 5 kg, respectively. In the case of a 1 kg load, the angle surpasses the physical limit due to the deformation of the 3D printed frame caused by the high force exerted by the chamber. The result is a larger angle than when using pressure in only one chamber (Fig. 4-12b). Another advantage is that a larger joint angle is reached at a similar total pressure differential such that the joint using negative and positive pressures of 20 kPa in each joint in Fig. 6-12a produces a larger joint angle than the same joint using a single chamber for actuation with 40 kPa of either positive (Fig. 4-10a) or negative (Fig. 4-10b) pressure. A possible explanation for this is that the actuation of each chamber causes their structure to deform actively rather than passively and reduces their resistance to being deformed.

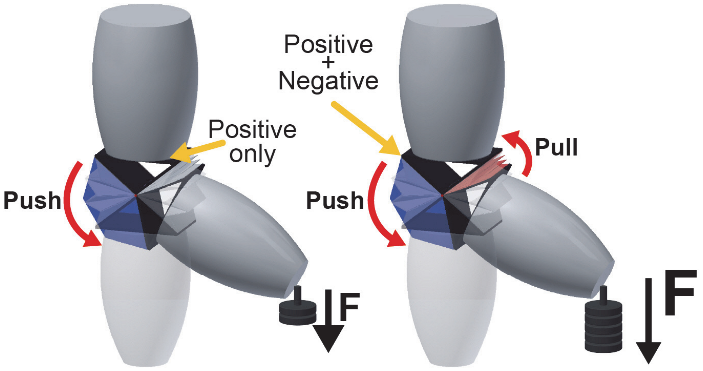

Figure 4-11. Concept of cooperative actuation of the antagonistic chambers.

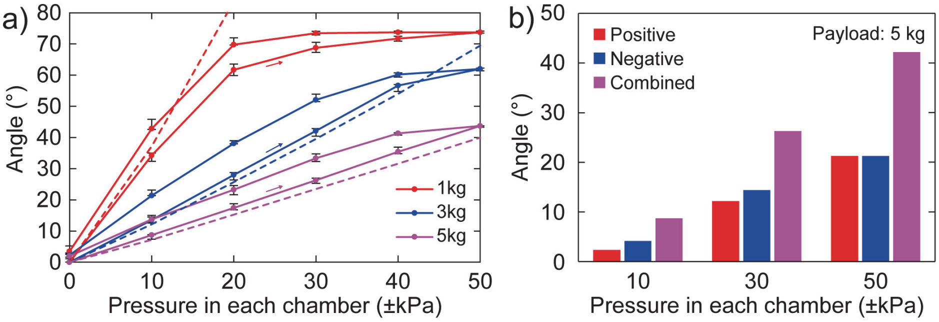

Figure 4-12. (a) Range of motion and (b) comparison between driving pressures of cooperative actuation.

4.4.3 Origami joint position control

The joints implemented in the robot arm must be able to perform position control for all joint orientations. In the case of the single chamber joint, there can be situations where the payload acts to open the joint and cannot be overcome by passive antagonistic characteristics. Therefore, negative pressure is needed to be able to control the joint in such situations. There is also a neutral position with respect to the vertical axis where the net torque from the payload on the joint is zero. For example, in the case of a single chamber joint with a 5 kg payload as shown in Fig. 4-6c, the neutral orientation is approximately 70° from the base of the joint. If the target position of the joint is near this neutral position, position control must be performed with low pressures. The use of high pressures for control near this neutral position is likely to result in oscillation. However, the neutral position, which is directly related to the orientation of the joint and of the payload, cannot be determined without external sensors. Therefore, in this work, rapid pressure switching between positive and negative pressure was used and position control was performed through this strategy.

Pulse width modulation (PWM) with a proportional-integral-derivative (PID) controller (Kc: 1.0, Ti: 0.15, Td: 0.0001) is used to determine when to switch pressure and individual PID controllers (Kc: 1.5, Ti: 0.025, Td: 0.01) are used to regulate the input positive and negative pressures (Fig. 4-13a). Pressure was controlled by electropneumatic regulators (ITV2030, ITV2090, SMC) connected to a pneumatic pump (GSAL-300, ACOM) and the switching frequency was determined experimentally. The joint was fixed vertically and a 20 cm aluminum profile with a 2 kg payload attached at its end such that the load pulls down the joint until a joint angle of 45°. The joint was made to follow a stepwise input from 20° to 80° with step sizes of 20° (Fig. 4-13b). The neutral position of the joint at the start of the experiment is 45° such that negative pressure is required when the target angle is smaller than 45° and positive pressure is required above 45°. The joint was able to follow the target signal while switching between positive and negative pressure as required.

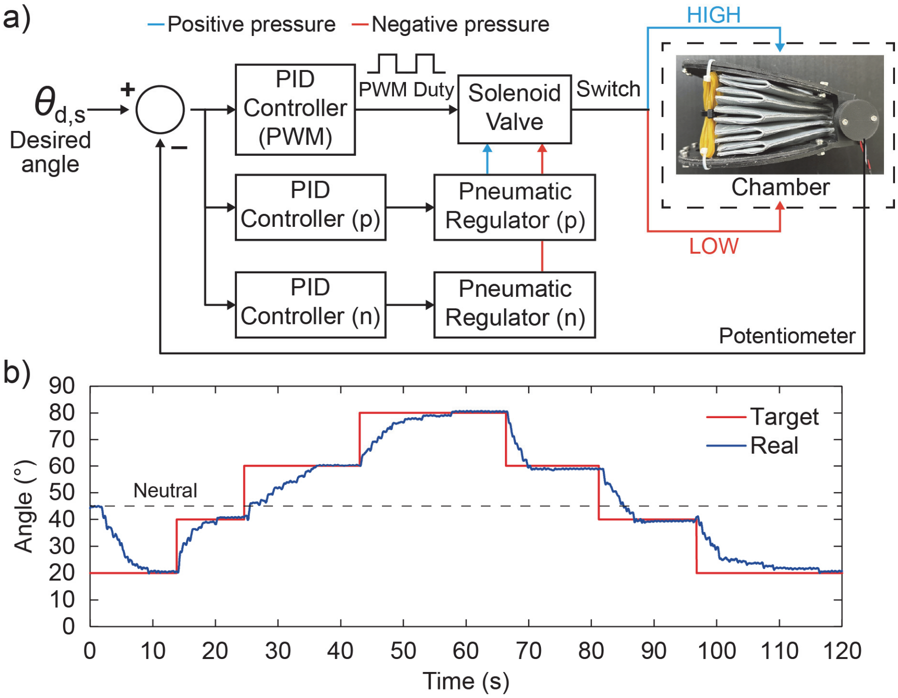

Figure 4-13. (a) PID control diagram of the single chamber joint and (b) position control result for step inputs.

This experiment confirms that the pressure switching-based position control can be used even in the absence of a controllable antagonistic element. This control strategy has the following advantages: avoid failure to reach the target position due to low pressure and minimize the risk of oscillation due to high pressure.

With the dual chamber origami joint, a simple PID controller (Kc: 0.5, Ti: 0.02, Td: 0.001) can be used where the sum of pressures is constant for both chambers to simplify the control solution (Fig. 4-14a). Unlike single chamber joints that do not have an antagonistic element, the pressure difference between antagonistic set of chambers will define the direction of the joint. Two positive pressure electropneumatic regulators are used to regulate the pressure in each chamber. The joint followed a step input signal with increments and decrements of 20° followed by sine wave input signals with amplitude of 20°, 40°, and 60° (Fig. 4-14b). The results show that the dual chamber joint, with an average speed of 20.6°/s, is faster than the single chamber joint, which has an average speed of 3.2°/s. Additionally, the dual chamber joint could follow wave inputs that are difficult for a single chamber to track. Since the dual chamber joint is not subject to strong oscillations when switching pressures, it is thus simpler to control.

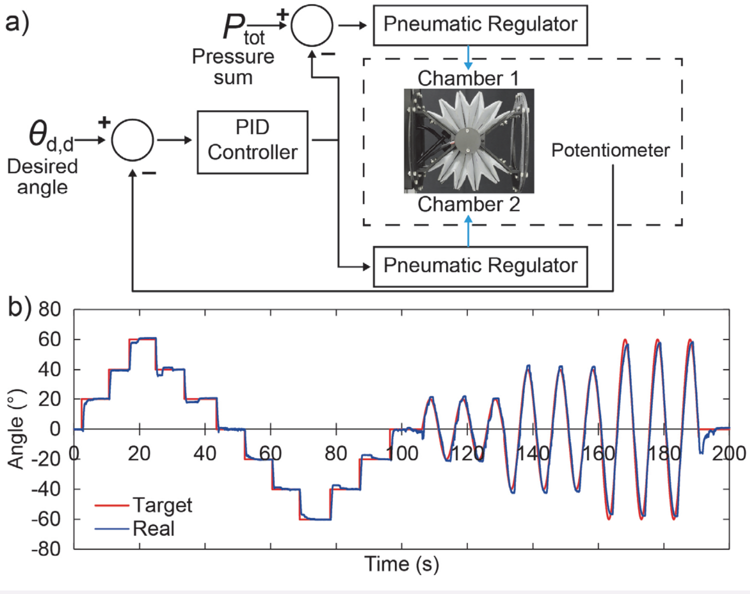

Figure 4-14. (a) PID control diagram of the dual chamber joint and (b) result for step and sine inputs.

The main advantage of using this kind of hybrid hard-soft system is that the influence of each joint on the other joint can be easily compensated through the feedback signal provided by the potentiometers. Here, a single chamber origami joint was fixed horizontally to the wall and a double chamber origami joint was fixed at the other end to produce a 2DOFs motion (Fig. 4-15a). Control was implemented separately for both chambers by using positive pressure only. The device was then made to move between four positions alternating between positions of 30° and 60° for the single chamber origami joint and -30° and +30° for the double chamber origami joint (Fig. 4-15b). Results show that both the single chamber joint (Fig. 4-16a) and the dual chamber joint (Fig. 4-16b) are not affected significantly by the operation of the other joint such that control of more complex robotic devices can be highly simplified.

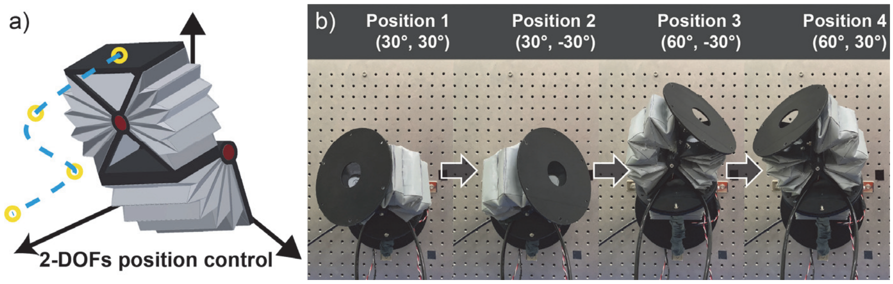

Figure 4-15. (a) Schematic of the 2DOFs joint and (b) simultaneous position control of the single and dual chamber joints.

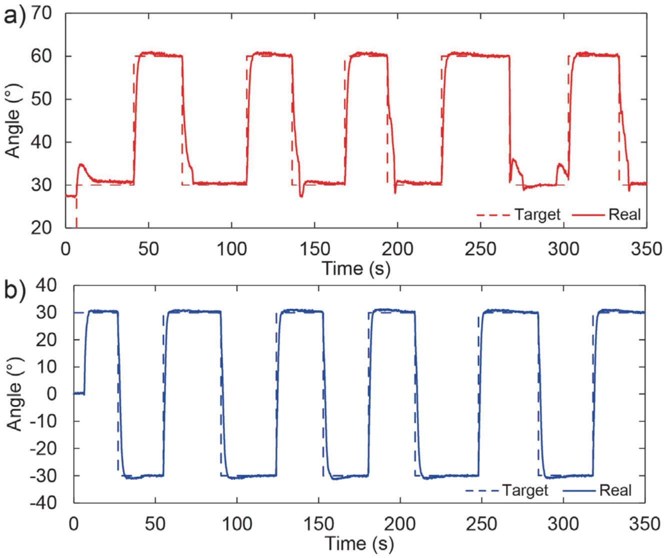

Figure 4-16. Control results of (a) single chamber and (b) dual chamber joint for four target combinations.

4.5 3DOFs hybrid robotic manipulator

4.5.1 Kinematics of hybrid robotic manipulator

A 3DOFs hybrid manipulator consisting of a single and a dual chamber joint placed at its elbow and a dual chamber joint on the wrist was built with two rigid links each with a length of 25 cm and a pouch-based soft robotic gripper. Through previous experiments, it was confirmed that a single chamber joint generates a wide range of motion and high torque but has relatively low position control performance. In contrast, a dual chamber joint generates a relatively narrow range of motion and low torque but demonstrates better position control performance. Based on the strengths and weaknesses of each joint, a single chamber joint was used as the elbow to lift heavy payloads, while two dual chamber joints were used as a 2DOFs wrist, respectively, to perform detailed manipulation of objects. The rigid links were covered by an inflatable plastic wrap. This robotic arm has a total length of 90 cm from the upper arm to the wrist joint and a weight of 2.67 kg including air supply tubes going through the inside of the arm (Fig. 4-17a).

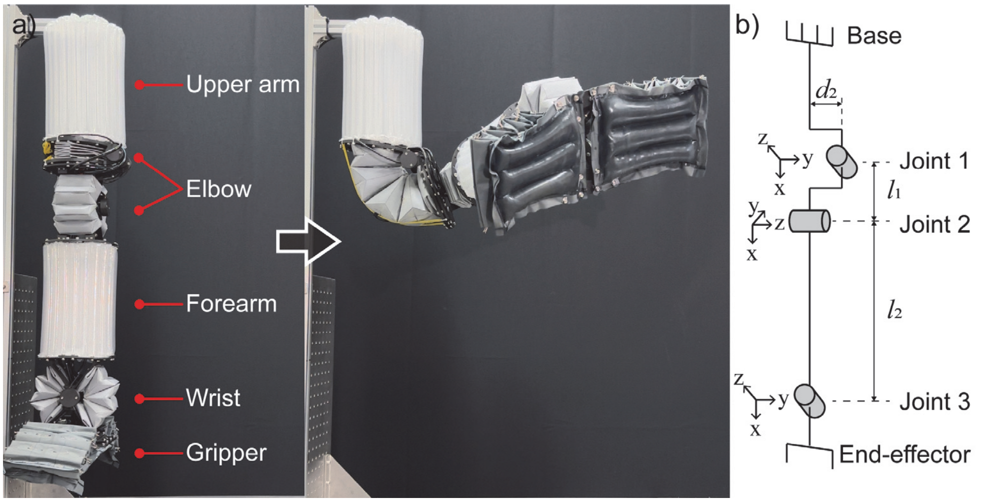

Figure 4-17. (a) Implementation of the proposed joints into the elbow and wrist of a 3DOFs soft robotic manipulator with an inflatable gripper and (b) its schematic diagram.

Kinematic analysis was conducted to track the end-effector position and calculate the desired joint angle of the 3DOFs robot manipulator. The base of the upper arm was considered as the base of the manipulator, and joints 1, 2, and 3 were defined in order of proximity (Fig. 4-17b). The inter-axis distance of the joint was defined with reference to Denavit–Hartenberg parameters. The variable l_i represents the distance in the x-direction between the z-axis of joint i and the z-axis of joint $i+1$, while d_i represents the distance in the z-direction between the x-axis of joint $i-1$ and the x-axis of joint i. As a result, the Cartesian positions x, y, z of joint 3, calculated through the transformation matrix from the base of the robot manipulator to joint 3, are as follows.

$$\begin{aligned} x &= l_2 \cos\theta_1 \cos\theta_2 - d_2 \sin\theta_1 + l_1 \cos\theta_1 \\ y &= l_2 \sin\theta_1 \cos\theta_2 + d_2 \cos\theta_1 + l_1 \sin\theta_1 \\ z &= - l_2 \sin\theta_2 \end{aligned} \tag{4-12}$$

Where θ_1 and θ_2 are the angular positions of joint 1 and joint 2, respectively. Due to hardware limitations of joint actuators, the joint ranges were set as $0^\circ < \theta_1 < 180^\circ$ and $-90^\circ < \theta_2 < 90^\circ$. From (4-12), θ_2 can be rearranged as follows.

$$\theta_2 = \sin^{-1} - \frac{z}{l_2} \tag{4-13}$$

By substituting (4-13) into (4-12), θ_1 can be calculated as follows.

$$\theta_1 = 2\tan^{-1} \frac{\sqrt{d_2^2 + l_1^2 + 2l_1 l_2 \cos\theta_2 + l_2^2 \cos^2\theta_2 - x^2} - d_2}{l_1 + l_2 \cos\theta_2 + x} \tag{4-14}$$

When l_1 is 111.8 mm, l_2 is 419.6 mm, and d_2 is -84.8 mm, the robot arm can reach a range of $l_1 + l_2$ from the elbow.

4.5.2 Performance of 3DOFs robotic manipulator

To measure the positioning accuracy, the robot arm was made to follow a square trajectory with a width and height of 400 mm on the x and z coordinate system within the accessible range. It then performed the task of sequentially moving the joint 3 to eight target points evenly distributed on the path (Fig. 4-18). The position of joint 3 was measured using a motion capture camera (V120:Trio, Optitrack), indicating a maximum position error of 48.6 mm. The primary cause of this error is the deformation of the frame due to the robot arm's weight, particularly due to the weight of the forearm twisting the elbow joints. For joints 1 and 2, the maximum errors were 0.25° and 0.13°, respectively, which are not significant errors in joint angle control, allowing the arm to have good repeatability. However, the combination of a long link, heavy joint, and weak structural rigidity had a significant impact on the end effector position. All joints were individually position controlled by using the PID controllers described previously without significant decrease in performance.

This robotic arm could handle a maximum payload of 2 kg, maintaining 43% of its original range of motion, and it is resilient to unanticipated forces. The arm could also perform tasks such as grasping fruits handed to it from two different designated locations and transferring them to a bowl placed at a designated fixed location (Fig. 4-19). The arm performed the target motion without difficulty regardless of the weight of the fruit from 0.33 kg to 1.2 kg, but it deflected slightly once grasping heavy fruits such as melons to recover subsequently. The kinematic solution was verified by comparing the joint positions between the inputs and the kinematic solutions at various positions, as shown in the demonstration (Table 4-1).

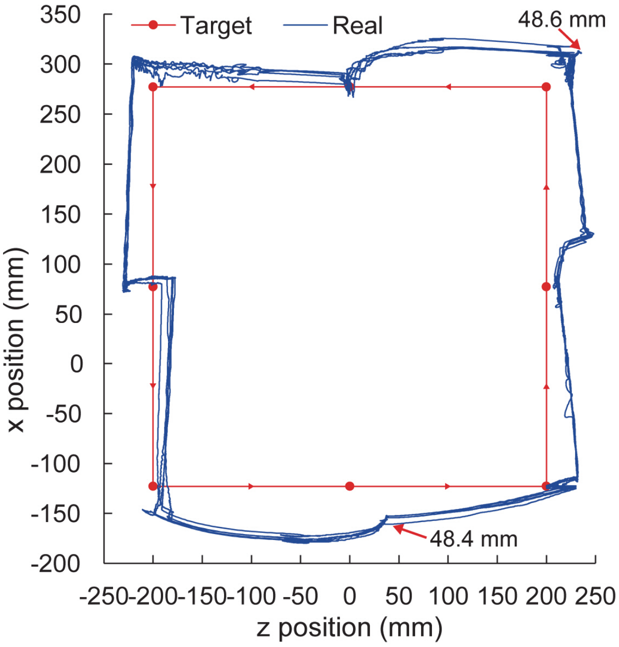

Figure 4-18. Position error of the end effector for eight target points, repeated for five cycles.

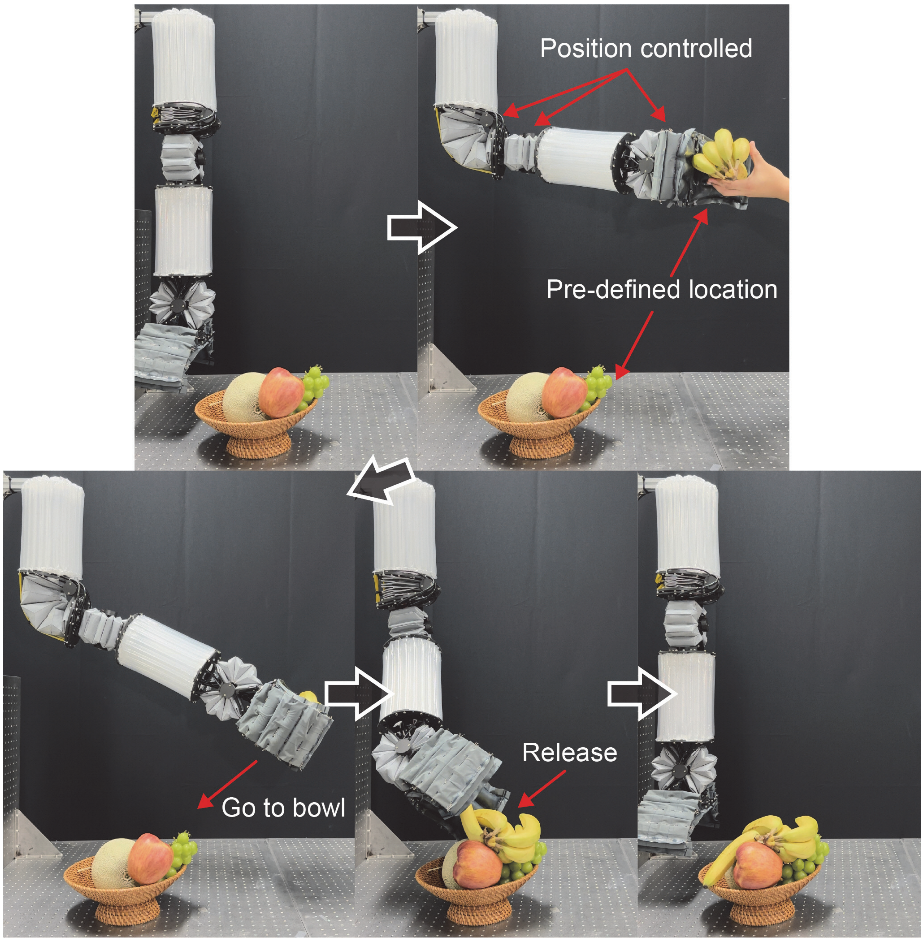

Figure 4-19. The soft robotic manipulator grasping fruits handed to it and transferring them to a fruit bowl.

Position	θ_1 (input)	θ_2 (input)	θ_1 (solved)	θ_2 (solved)
Horizontal straight	90	0	90.000000	0.000000
Fruit grasping	120	-40	120.000000	-40.000000
Bowl	35	-20	35.000000	-20.000000

Chapter 05

Unbuckling inflatable tubes

5.1 Introduction

Like most man-made machines, the behavior of soft pneumatic actuators depends on their design[131-134]. Generally, simple designs result in producing simple behaviors, while imparting complex behaviors usually demand complex design solutions[135, 136]. Examples of desirable complex behaviors in soft pneumatic actuators for robotic systems include stiffening behaviors, bistability, and rapid snapping-like displacements. However, achieving these behaviors often entails adding components with specific properties to the actuating system, implementing carefully engineered structures, or resorting to complex fluidic solutions.

Pneumatic artificial muscles (PAMs)[137-140], having a single polymeric chamber in a cylindrical shape, and pouch motors[10, 116], also having a single chamber but made with thin films in a flat rectangular shape, are the simplest designs producing a linear contraction, achieved through the lateral expansion of their side walls when inflated. Their contractile performances have been improved, such as by reducing nonlinear hysteresis or expanding the range of motion by replacing the material or repeating the structures in the form of seriesPAM[34], fabricPAM[141], and paired pouch motors[142].

As demonstrated in numerous studies, soft actuators exhibit remarkable flexibility in adopting various designs for their structures and materials. This flexibility has enabled further combinations of smooth and compliant deformations useful in applications such as crawling robots[143], aquatic robots[144], soft grippers[145-149], wearable exogloves[15, 150], and structures with tunable wettability[151]. However, despite these actuators being designed to realize various types of deformations such as contraction, extension, bending, rotation, and twisting, the deformation produced by polymeric actuators is not large compared to their initial volume, primarily due to having a significant minimal volume. Meanwhile, film-based actuators can have compact initial position by utilizing the film's inherent thinness and flexibility, unlike polymeric chambers which require a certain thickness to operate. This characteristic offers a potential solution to maximize the range of motion of a given actuator. Origami patterning of film-based chambers has enabled linear pneumatic actuators to produce very large contractions[152], but it is specialized for linear deformations. Inflatable origami mechanisms have been studied for developing structures with initially highly compressed structures[153, 154], but their surfaces need to be made partially from stiff materials and can risk delamination through repeated use. Applying negative and positive pressure inputs to a bi-chamber actuator made from thin plastic film can be used as a lengthening actuator by using the positive pressure chamber for stiffening and antagonistic actuation of the structure[125]. However, these have not been demonstrated for deformations other than linear deformations. While diverse inflatable actuators have been developed with different capabilities, film-based actuators encounter challenges in achieving various actuation types compared to polymeric actuators due to difficulties in programming their deformation and their lack of inherent elasticity. However, integration with a well-designed constraint can overcome this limitation, even with the simplest of inflatable structures. This can be accomplished by the ability of soft actuators to integrate external or embedded elements into their design, allowing them to possess a wide range of physical characteristics and enabling diverse dynamic implementations.

Reconfigurable designs serve as a compelling example, demonstrating the ability to switch the actuation type or function with minimal changes to its components while maintaining their overall shape. Inserting a patterned paper when curing the polymeric chamber of a soft pneumatic actuator can introduce anisotropic properties to the structure, enabling it to perform extension, contraction, bending, or twisting motions based on the pattern of the embedded component[35]. Other methods of inducing programmable anisotropy have been introduced such as using fiber reinforcements with different arrangements[22, 155], using external skeletons with different slit configurations to guide the deformation of the internal bladder[156], and by varying the chamber morphology[157].

Another method for achieving versatility in the deformation of soft pneumatic actuators involves using multimodal designs. This approach integrates multiple actuators into a single system, enabling antagonistic actuation and interaction between actuators. Selectively activating different actuating elements within a single structure allows for antagonistic actuation and interaction between actuators, producing different types of deformations. For example, utilizing three vacuum chambers within a single actuator has enabled bi-directional bending motions which can be used to generate different types of gaits in crawling robots[37]. An axisymmetric configuration comprised of three bellows-like pneumatic actuators, each capable of linear extension when pressurized, can generate vertical extension and three-directional bending[158, 159], as well as bi-directional twisting through the combined actuation of each component within a vertical constraint[160]. A shape-adaptable enveloping gripper capable of grasping various objects by contracting or expanding its diameter through deflation or inflation shows that utilizing different pressure sources can also produce multimodal deformations[161].

Modularization can be considered the final stage in the development of versatile actuators. When designed to enable easy coupling between modules, it becomes possible to expand the range of motion through the connection of similar actuating modules or diversify the types of movements by combining modules with different types of deformations. This has been demonstrated through the magnetic assembly of polymeric blocks driven by shape memory alloys[162, 163], by applying a junction mechanism on both ends of pneumatic actuators[74, 164], and by designing simple rigid structural connections applied to the upper and lower surfaces of actuators[165, 166]. As a result of their capacity for easily expanding their operating range and flexibly reconfiguring their structure, they have contributed to the development of advanced robotic systems with high degrees of freedom. They have been used for applications such as robotic arms[92, 167-170], manipulators[84, 171], continuum robots[172-174], and various other systems[175, 176]. Consequently, the development of modular systems can broaden the range of applications of soft robotic technology, and improvements in their design will ultimately enable their implementation in real-world scenarios.

However, the soft pneumatic actuators still have their distinct limitations and problems to be solved. Most of these soft pneumatic actuators have nonlinear properties resulting from their nonlinear relationship between volumetric deformation and displacement and from the nonlinearities inherent in air-driven deformable structures, but these nonlinear properties are issues to be overcome and do not help these actuators produce complex behaviors. A complex soft actuator behavior which has garnered attention is the stiffening of the actuator which, for example, can help a soft gripper grasp heavier objects than when it can only operate in a soft state. Stiffening behaviors have been added to soft pneumatic actuators by adding particle and layer jamming mechanisms into the structure of the actuator[177-180], through the use of low-melting-point alloy components[181-183], shape memory polymer layers[184, 185], tendon-driven stiffening[186], and through the addition of external rigid locking mechanisms[187]. However, these stiffening behaviors are the result of the behavior of additional non-fluidic components rather than the soft pneumatic actuators themselves and thus increase the complexity of the design.

Another complex behavior which has gained a lot of focus in recent years is the use of instabilities to enhance the capabilities of the device or even gain new functionalities. Such instabilities can be obtained by combining inflatable chambers with soft constraints to produce snap-through motions resulting from nonlinearities in the pressure versus extension response of the structure[188]. Soft bending actuators can be coupled with rigid mechanisms or elastic structures to form instability-driven bistable structure that help in amplifying the speed of deformation through snap-through instabilities[189, 190]. The combination of bistable inflatable origami structures can produce structures capable of localized stiffness control or that can be used as deployable multistable structures[153, 154, 191]. Pre-curved bilayer actuators can use a strain energy storage and release mechanism stemming from their bistability to produce rapid motions[192]. Bi-stable shells can produce a snap-through motion between stable states that can be harnessed to produce fast displacements or jumping motions[193, 194]. Such bi-stable shells can also be used to produce bistable pneumatic valves which can themselves be used to build digital logic devices and embed physical intelligence into robots[195-198].

The buckling of inflatable robots or vine robots consisting of a long inflatable tube that grow through eversion of their structure is generally something that is meant to be avoided[199-202], but it can also be harnessed as a navigation tactic through contacts with the environment[203, 204]. The complex behavior of buckling inflatable tubes exhibits unique mechanical properties that could be harnessed by soft roboticists. The conditions needed to buckle such an inflatable tube are generally derived from the equations for the deflection of an elastic body[205-207], but this does not describe the entire behavior of such buckling tubes which needs to be deformed until this buckling point, can be further deformed after buckling, and can be unbuckled.

This chapter introduces the nonlinear behaviors of a film-based inflated tube, the simplest soft structure, under axial compression, such as snap-through buckling and bistable regions. Additionally, it proposes new designs for inflatable soft robotic systems that harness these nonlinearities to produce unique motions, such as stability-configurable mechanisms, actuation speed-configurable mechanisms, and self-stiffening in bending deformation.

A range of lengths where the tube can remain stable in either the buckled or unbuckled state, which cannot be explained by current models, was investigated. The validity of the existence of this bistable region and the reason why the snap-through buckling must occur at the end of this region were proven through a new geometric modeling of the buckling tube. The numerical model was demonstrated using varied lengths and widths of the tube at different pressures. Subsequently, a pair of inflatable tubes connected in series was integrated with external structures to interact with each other, transitioning between buckled and unbuckled states, and achieving monostable or bistable configurations by regulating the pressure ratio. They ultimately performed rapid motions. Finally, a bundle of multi-segment inflatable tubes was integrated with external structures to develop grippers, utilizing their unbuckling motions to bending deformation. The developed grippers ultimately demonstrated significant ability to withstand high payloads through their self-stiffening behavior, which arises from the significant force required to buckle the tube. In summary, the main objectives of this chapter are:

1) This chapter explores the nonlinear properties of the buckling tube, along with methods to harness them into robotic mechanisms.
2) Suggesting an approximate numerical model through the geometric design of the compressed tube and proposing methods to create new complex behaviors by harnessing nonlinear characteristics.

5.2 Film-based inflatable tubes

5.2.1 Fabrication of the inflatable tube

The inflatable tube, which results in a cylindrical body with tapered ends when inflated, can be simply fabricated from two flat surfaces with bonded edges in a rectangular shape. The surfaces can be polymers, thin thermoplastic films, film coated fabrics, or any other thin materials capable of forming an impermeable bladder. In this work, nylon coated with thermoplastic polyurethane (TPU), which is very flexible but not stretchable so that it can become stiff enough at even low pressure, was used to fabricate all the tubes. The fabrication process involved drawing a pattern on the fabric, cutting the pattern, sealing its lateral edges in a tubular shape using an impulse sealer (SK-150, LOVERO), inserting an air inlet (5116K165, McMaster-Carr), and sealing the ends. Placing a piece of paper between the film and sealer can prevent heat transfer to the film, leaving unbonded areas and resulting in a partition that separates the segment and functions as an air channel (Fig. 5-1).

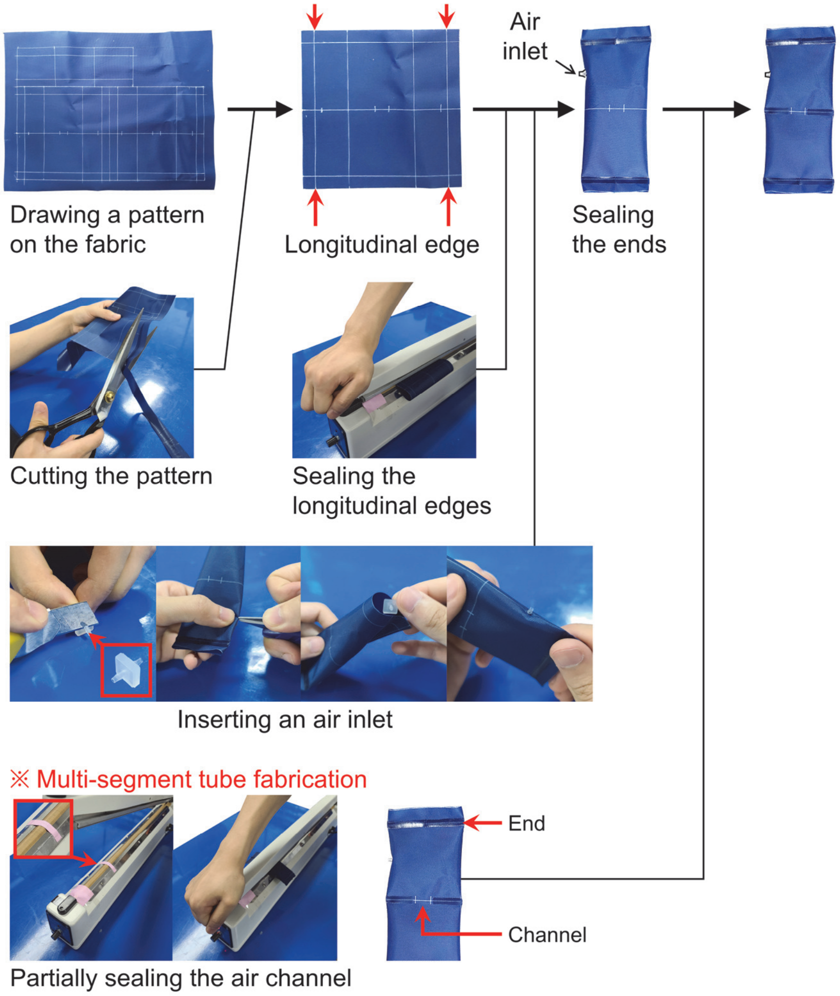

Figure 5-1. Fabrication process of the film-based inflatable tube.

5.2.2 Pneumatic system for inflatable tubes

An inflatable tube is supplied with constant internal pressure from an electro-pneumatic regulator (ITV1030-RC1L-X26, SMC), which receives maximum pressure from a pneumatic compressor (GSAL300-87R-3H50, ACOM) and sets the pressure value by adjusting the voltage through a signal from the analog output module (NI-9263, National Instruments) that transfers the signal using a LabVIEW interface (Fig. 5-2). Additional regulators can receive the same compressed air from the compressor by integrating them at once into a manifold block. A bundle of multiple inflatable tubes can share the same pressure from a single regulator by integrating them using tube connectors, but they can also be independently inflated by using individual regulators. The multi-segment tube, partially sealed in the middle of its entire length, can simultaneously inflate multiple tubes connected in series using one regulator. However, if one of the intersections between two segments is fully sealed, each segment can be independently inflated, requiring an additional regulator. In this study, a two-segment tube, fully sealed in the middle and utilizing two pressure sources, was employed for the bistable structure, and multiple multi-segment tubes, each using individual pressure sources, were employed for the anthropomorphic gripper.

5.3 Tube behaviors under axial compression

5.3.1 Overall behaviors throughout compression

An inflated tube can remain stable in either the buckled or unbuckled state when compressed, and it always generates an extensive force to return to its original uncompressed and unbuckled shape in either state. Despite the inflation of the tube itself being capable of only small contraction or expansion, this unfolding behavior allows for practical motions with larger deformations and better performance by configuring the deflated tube to be pre-folded using interactable systems. In contrast, a buckling occurs when consistent axial compression is applied to the inflated tube until a critical point. Significant interest has been shown in finding this critical point in terms of the maximal force that can be used so as not to overload these inflatable tubes. However, this work studies and uses the complete cycle of buckling and unbuckling behaviors of short inflatable tubes and harnesses these behaviors to produce unique nonlinear functions in soft robotic structures.

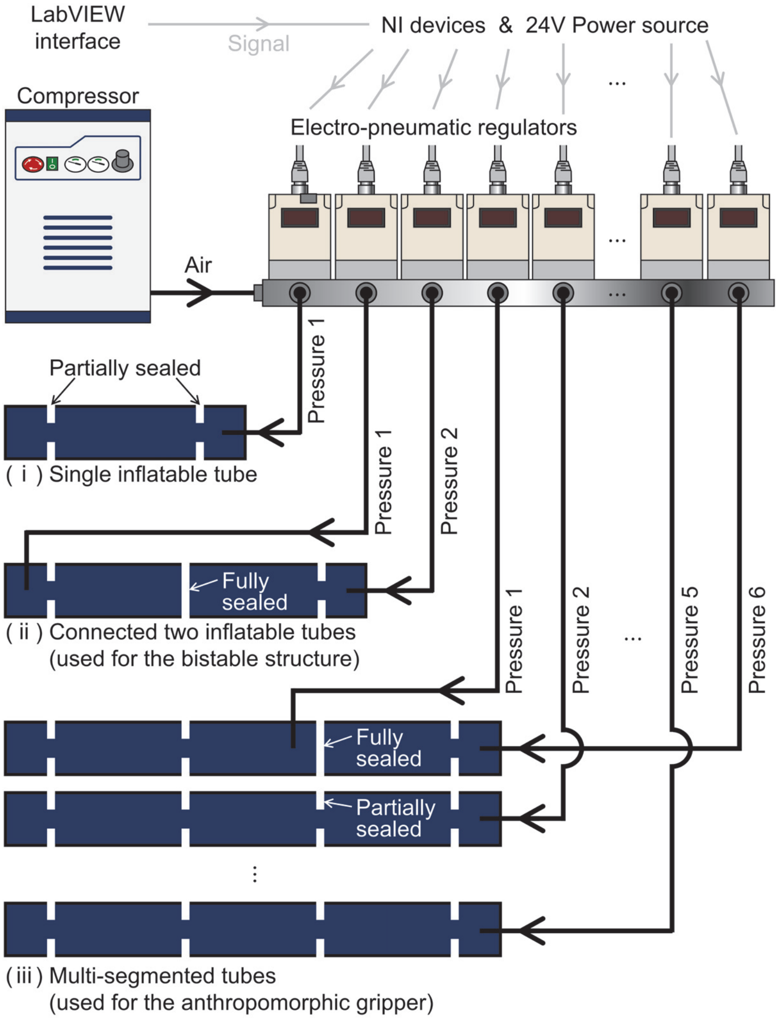

Figure 5-2. Pneumatic system for inflatable tubes.

In the early stage of the compression, the tapered ends of the tube are compressed with the tube remaining in the straight configuration until it reaches a critical amount of compression where the buckling occurs (Fig. 5-3). In the region before this buckling occurs, the tube can be buckled and unbuckled by manually deforming it. Hence, the tube can be said to be bistable within this region. Snap-through buckling of the tube happens at a specific compression point and the transition to the buckled state occurs within a fraction of a second. After the buckling of the tube, it remains stable only in the buckled position and cannot be manually unbuckled. When the tube is allowed to extend again, the tube does not unbuckle by itself at the same point where it buckled and only does so after being allowed to nearly return to its original length. However, it can be unbuckled manually before this if the tube is within the bistable region.

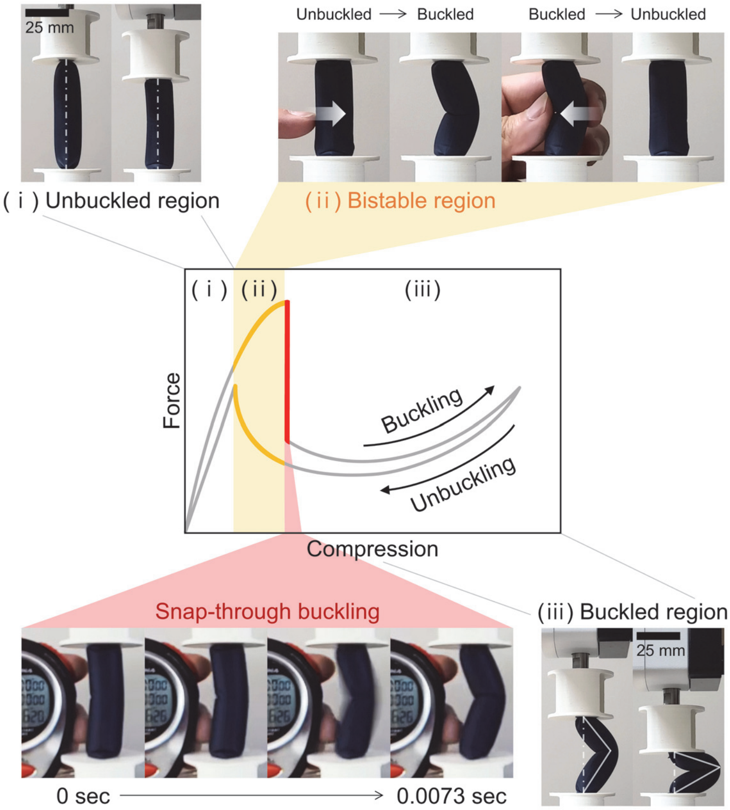

Figure 5-3. Overall behavior of the inflatable tube under axial compression.

In terms of the force, it can be observed that the compression of an unbuckled tube within the bistable region requires more force than for a buckled tube and that the maximum compression force is measured just before buckling occurs. The force drops significantly and instantly as the tube buckles. The force then decreases in the early portion of the buckled state and slowly increases again as the crease in the middle of the buckled tube increases in length due to the folding of the tube. The force first decreases during extension as the crease in the middle of the tube shortens and then increases as the tube gradually returns towards a cylindrical shape. Once unbuckled, the extension force follows the same linear behavior as during the early stage of compression. Some hysteresis between the extension and compression can be observed which is likely due to the energy required for the formation of creases on the surface of the tube and friction between surfaces in contact during the deformation.

5.3.2 Buckling behavior with different length-to-width ratios

The axial compressive force of the inflatable tube was tested at various internal pressures, tube lengths and tube widths. The tubes were attached to the linear tensile testing machine (ESM750, MARK-10) equipped with a force gauge (M5-20, MARK-10) using a 3D-printed jig and tested 5 times for each case with a constant travel speed of 1 mm/s in both directions. The results at pressures of 25, 50, and 100 kPa with a tube having a width and a length of 25 and 75 mm, respectively, show that the magnitude of the force increases proportionally to the pressure and that the pressure does not affect the general behavior of the tube (Fig. 5-4a). Tube lengths of 62.5, 75, 100, and 125 mm with a fixed width of 25 mm were tested at 100 kPa pressurized, and it was found that the tube length affects slightly the location of the snap-through buckling, which causes shorter tubes to have a slightly bigger snap-through buckling behavior than longer ones, and longer tubes can be compressed far more than shorter ones after buckling and require less force to deform (Fig. 5-4b). Tube widths of 30, 25, 18.75, and 15 mm with a fixed length of 75 mm were then tested in the same condition, and it showed that changing the width of the tube significantly affects all aspects of the overall behavior, including the critical force and displacement required to buckle and unbuckle the tube, while the possible displacement remains almost the same since the initial lengths of the tubes are the same (Fig. 5-4c).

It is to be noted that only short tubes with a width-to-length ratio between 2.5 and 5 will be considered in this study as tubes with ratios outside of this range exhibit a slightly different behavior which cannot be used to produce all complex demonstrated behaviors as explained later in this chapter. If the ratio of length-to-width of the tube is too small or too large, then its nonlinear behavior will deviate from that described in the main text. For a small ratio, the tube requires a relatively larger compression displacement to generate the snap-through buckling, and there is an unexpected force drop before the snap-through buckling (Fig. 5-5a, b). However, it maintains the overall expected behavior of buckling inflatable tubes. For a large ratio, the axial compressive force of the tube shows a downward but not vertical slope where buckling and unbuckling occur. This shows that the tube does not produce snap-through buckling, (Fig. 5-5c). The bistable region also disappears, and these long inflatable tubes do not particularly present any nonlinear properties of interest.

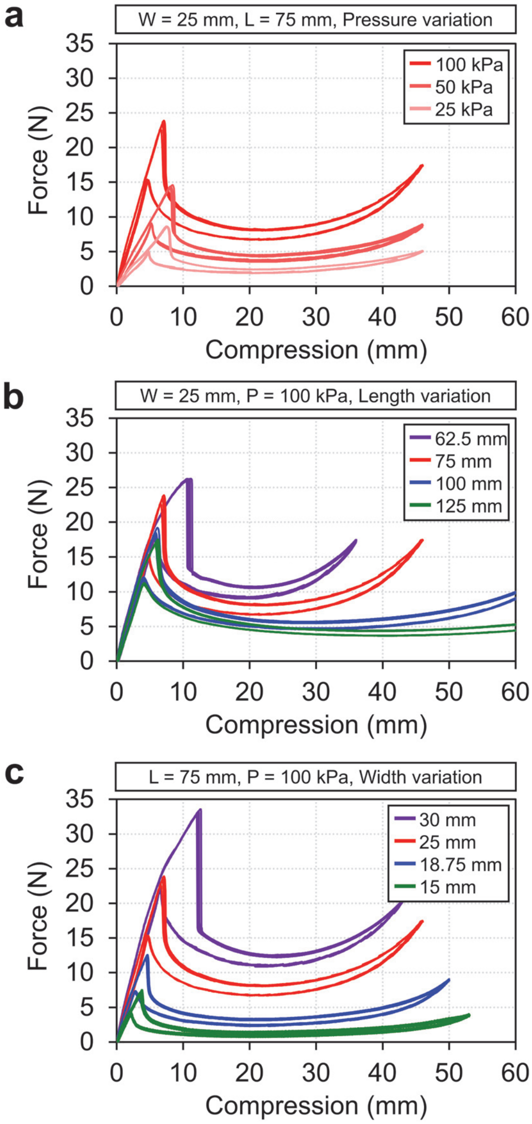

Figure 5-4. Axial compressive force of the inflatable tube with different.

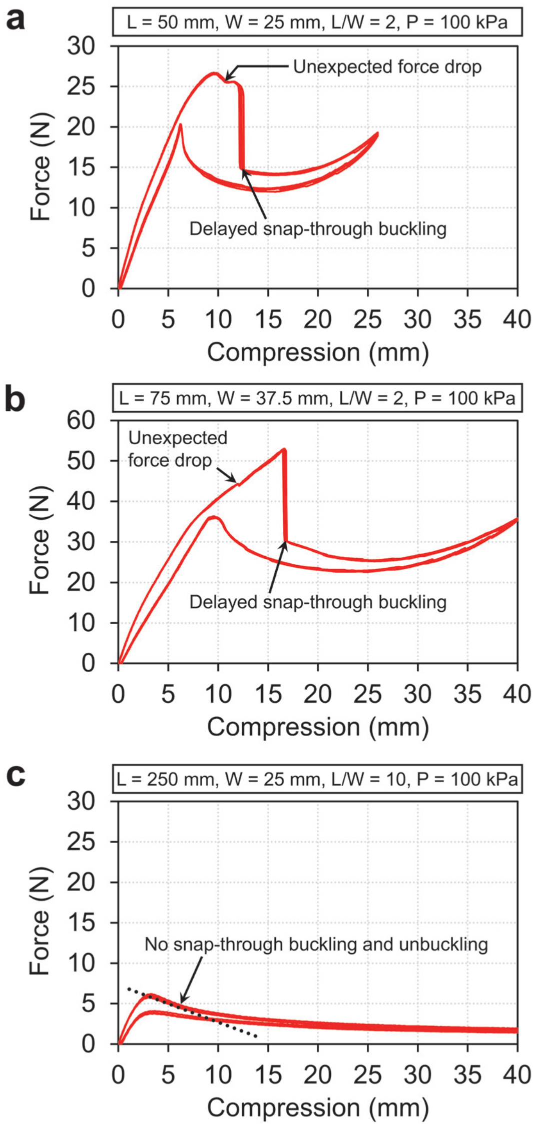

Figure 5-5. Axial compressive force of the inflatable tube with too small and too large length-to-width ratio.

5.3.3 Buckling behavior experiments

The maximum compression displacements shown in the experiments of Figure 3-2 were chosen based on the compression displacement where the proposed model predicts an equal force for a buckled and an unbuckled tube. This was selected in order to take into account the variation in tube length and width in the different experiments. However, any point beyond the snap-through buckling point will show the same general behavior of the tube. A test was conducted where a tube with a length of 75 mm and a width of 25 mm pressurized at 100 kPa was compressed to maximum compression displacements of 10, 20, 30, 40, 50 and 60 mmfor5cycles each (Fig. 5-6a). Results show that the general behavior of the tube is the same regardless of the maximum compression displacement apart from the hysteresis developing gradually upon the start of the extension of the tube. So, the point of extension was set arbitrarily as the point where the proposed numerical model predicts an equal force for a buckled and an unbuckled tube with some given dimensions. Thus, for example, for the experiments shown in Fig. 1c with tube lengths of 62.5, 75, 100 and 125 mm, the maximum compression displacements were set at 36, 46, 67 and 88 mm, respectively (Fig. 5-6b).

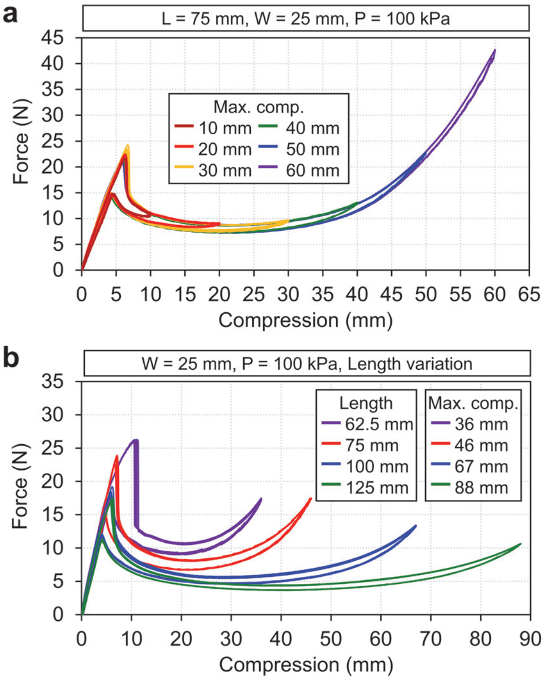

Figure 5-6. Axial compressive force of the inflatable tube with different maximum compression displacements.

All the tubes in this work are supplied with air through the plastic inlet as previously described, and a tiny space between the flat base of the inlet and the sharp surface of a cut air tube generates a small amount of air leakage. Gluing the tube with silicone glue around this interface can entirely prevent air leakage from the system which can be verified by the pneumatic regulators not allowing additional air in the tube to maintain a given pressure. Inserting a manual valve between the tube and the regulator and closing it enables the tube to maintain the amount of air within the tube and thus the pressure to vary through the displacement (Fig. 5-7a). An axial compression test was repeated 5 times with a tube having a length of 70 mm and a width of 25 mm pressurized at 100 kPa for three different cases: opened valve without a glued inlet; opened valve with a glued inlet; and with a closed valve and a glued inlet. By preventing air leakage around the inlet, the tube can increase the amplitude of its overall force compared to the unglued tube potentially due to a delay in adjusting the pressure of the tube during the compression. With a closed valve, the pressure increases throughout the displacement which results in a higher force required to deform the tube with this difference increasing throughout the contraction (Fig. 5-7b). However, this does not affect the overall behavior of the tube and the difference in force is most significant in the buckled section of the deformation.

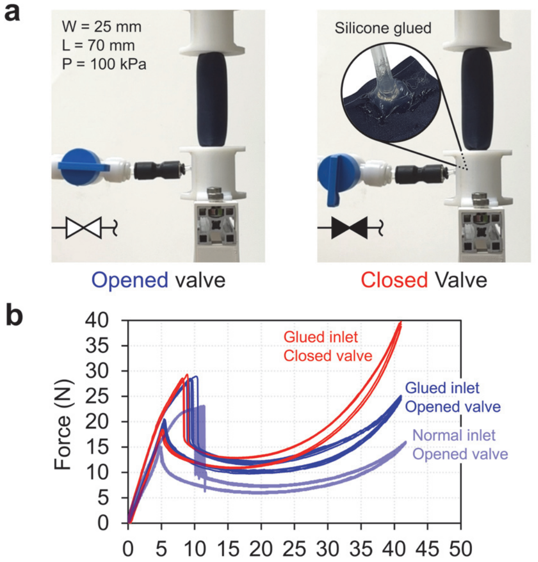

Figure 5-7. Axial compressive force of the inflatable tube with constant pressure and constant amount of air.

The repetition of the buckling and unbuckling behaviors was then tested over 100 cycles with a tube length of 75 mm, a width of 30 mm, and pressurized to 100 kPa (Fig. 5-8a). During the first compression, buckling starts from one end of the tube and gradually moves towards the middle. In subsequent cycles, buckling occurs at the same location. The overall force slightly decreases in the early cycles but eventually stabilizes, consistently producing the same buckling and unbuckling behavior. This initial force decrease is due to the tube becoming slightly curved towards the buckling direction after a few cycles, generating a small pulling force from the initial equilibrium. However, this tendency can be reset by applying an external force in the opposite direction to counteract the tube's curvature from repeated buckling (Fig. 5-8b).

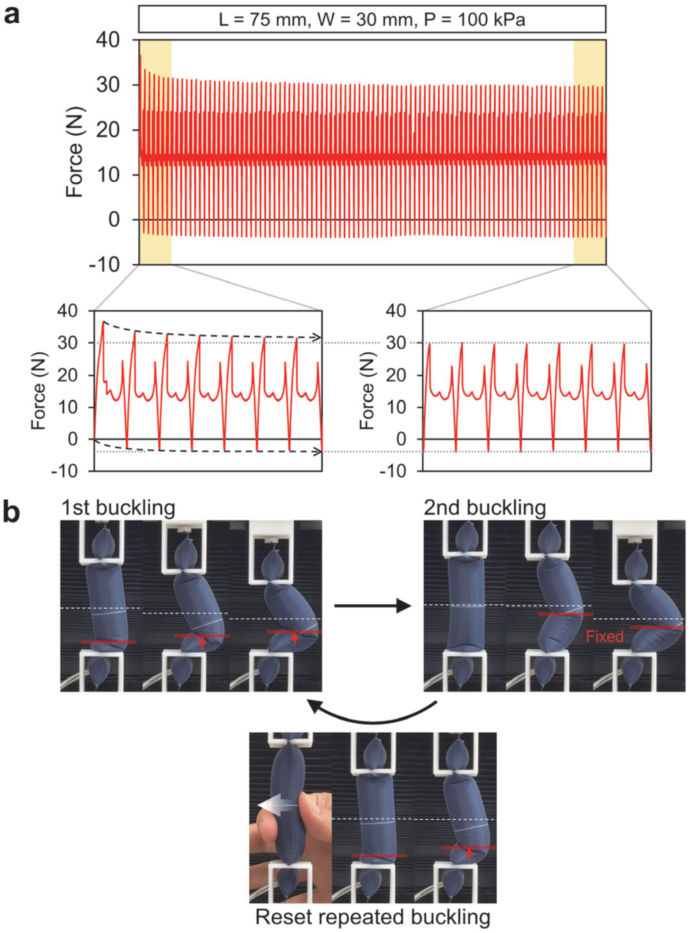

Figure 5-8. Repetition of the inflatable tube buckling.

To prevent the issue at the first buckling and to avoid the tube buckling in random directions, a cover with a hole where the tube will crease, made from the same material, was applied to the inflated tube. Additionally, a small tilt was applied to the fixations at both ends of the tube. When only a tilting angle of 1° was applied without the cover, the issue of the buckling starting from the end of the tube and moving to the middle during the first buckling was not resolved, but it did at least induce the buckling direction opposite to the center of curvature of both fixations (Fig. 5-9a). Applying the cover with the same tilted angle effectively controlled the location of buckling (Fig. 5-9b), even if it was not exactly in the middle of the tube (Fig. 5-9c).

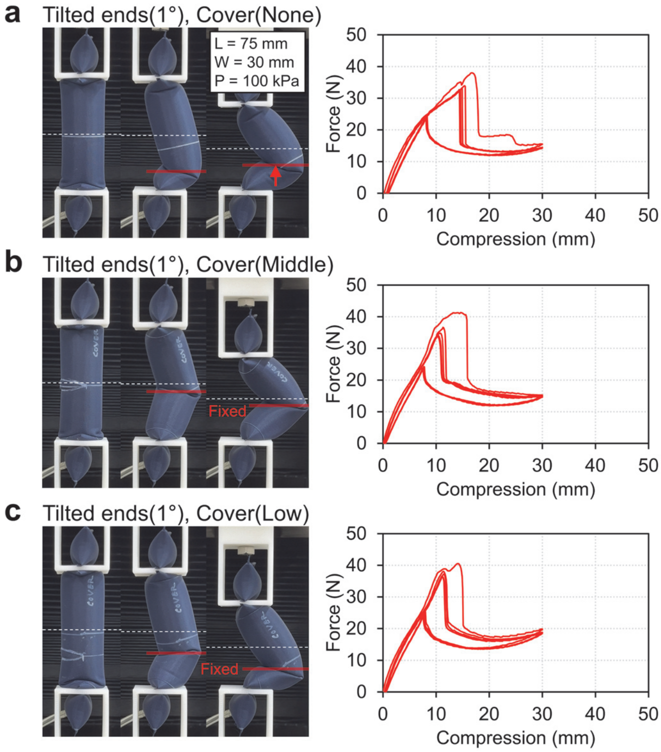

Figure 5-9. Inducing direction and location of the inflatable tube buckling.

5.4 Buckling tube modeling

5.4.1 Basic principles and geometry of the inflated tube

The most common approach to modeling the deformation of a buckling inflatable tube is by approximating it as the elastic deflection of a long elastic beam. This kind of model can be used to find the critical buckling load of a beam undergoing buckling with different loading and support conditions. However, this type of solution does not provide any insight into the behavior of the tube throughout the compression and extension deformations and does not explain the behavior of the tube within the bistable region. The model developed in this work aims to explain the behavior of an inflatable tube throughout both the compression and extension, to explain the transition between states and to explain the presence of the bistable region. The first step of the approach used in this work is to use the conservation of energy for both the buckled and unbuckled states at all lengths where the work of the fluid within the inflatable tube for a given quasistatic displacement corresponds to the mechanical work produced by the tube during this displacement. This can be written as

$$\triangle W = -P\triangle V = F\triangle s \tag{5-1}$$

Where $\triangle W$ is the work produced to the tube, P is the internal pressure of the tube, $\triangle V$ is the volume change of the tube for an axial compressive displacement $\triangle s$, and F is the axial force produced by the tube. The pressure in this model is assumed to be constant as this corresponds to the above experimental conditions. Then, this can be used to determine the axial force generated by the inflatable tube during compression or extension where the work of the fluid within the inflatable tube produces an equivalent mechanical work for a given quasistatic axial displacement (Fig. 5-10a).

In order to use this equation, the volume of the tube is necessary. The Riemann summation method will be used to approximate the volume of the inflatable tube by summing the instantaneous volumes throughout the axis of the tube in both the buckled and unbuckled states (Fig. 5-10b). The volume V_i calculated by the Riemann sum of the quasistatic volume $V_{i,j}$ which has a cross-sectional area $A_{i,j}$ at x_j on the x-axis and a uniform partition size $\triangle x$ from the initial point x_1 to the final point x_n is defined as follows.

$$V_i = \sum_{j=1}^{n} V_{i,j} = \sum_{j=1}^{n} A_{i,j}(x_j)\triangle x \tag{5-2}$$

This volume V_i is one of N elements of volume V and corresponds to the compression element s_i. The volume matrix V throughout the compression s can obtained from arranging all the elements calculated by Riemann's summation. Then, this volume matrix V can produce a new matrix $\triangle V$, which indicates the instantaneous change of the volume throughout the compression by defining each element as the difference between adjacent volume elements as follows.

$$\triangle V_i = V_i - V_{i+1} \tag{5-3}$$

The force matrix F that the tube produces from the axial compression can then be obtained by substituting the internal pressure P, the compression displacement $\triangle s$ corresponding to the volume change $\triangle V$ into Equation 5-1 (Fig. 5-10c). In this work, the uniform interval of the axial displacement $\triangle x$ which is used for applying Reimann's summation was set at 0.001 mm to approximate the volume of the tube with sufficient precision.

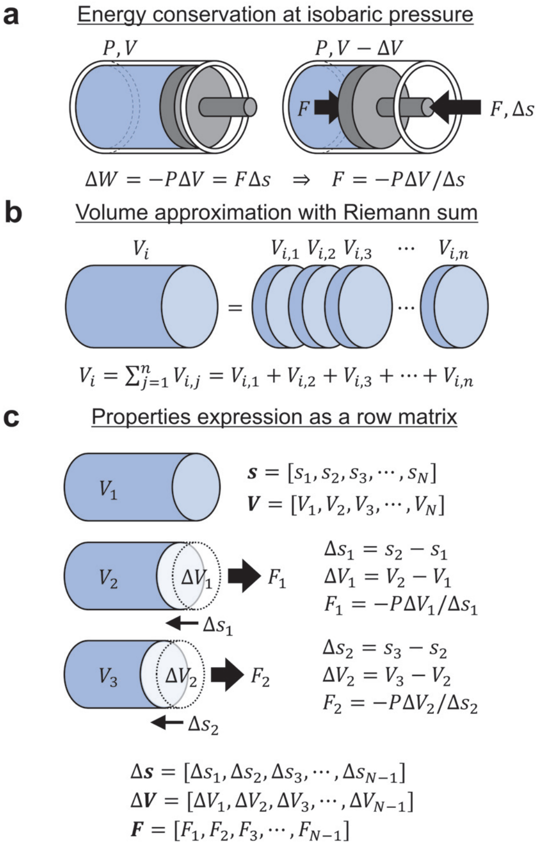

Figure 5-10. Basic mathematical principles for calculating the tube volume and force at every displacement.

To apply these principles, a geometrical model of the inflatable tube throughout the deformation is required. First, a relationship between the uninflated and inflated dimensions of the tube will be established. It can be noticed visually that the uninflated tube has a rectangular shape defined by its length L and width W (Fig. 5-11a), and that the inflated tube has a cylindrical shape with rounded ends with a radius R (Fig. 5-11b). The half-length of the inflated tube is defined as l such that the total length of the inflated tube is $2l$. It is assumed that the cross-section of the inflated tube remains circular throughout with a constant radius (Fig. 5-12a, b). Thus, the cross-section of the inflated tube will have a radius R which is derived from W as

$$R = \frac{2W}{2\pi} = \frac{W}{\pi} \tag{5-4}$$

Assuming that the fabric is not stretchable, it can be assumed that the length of the tube remains constant even as it is deformed during inflation.

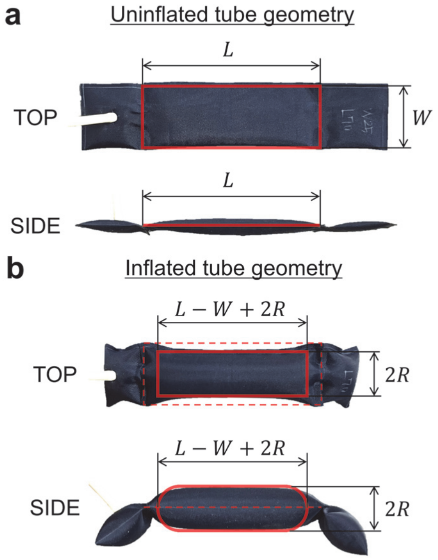

Figure 5-11. Geometry of the uninflated and inflated tubes.

Thus, the length l can be related to L from the geometry. This length l can be obtained as

$$l = \frac{L}{2} - \frac{W}{2} + R \tag{5-5}$$

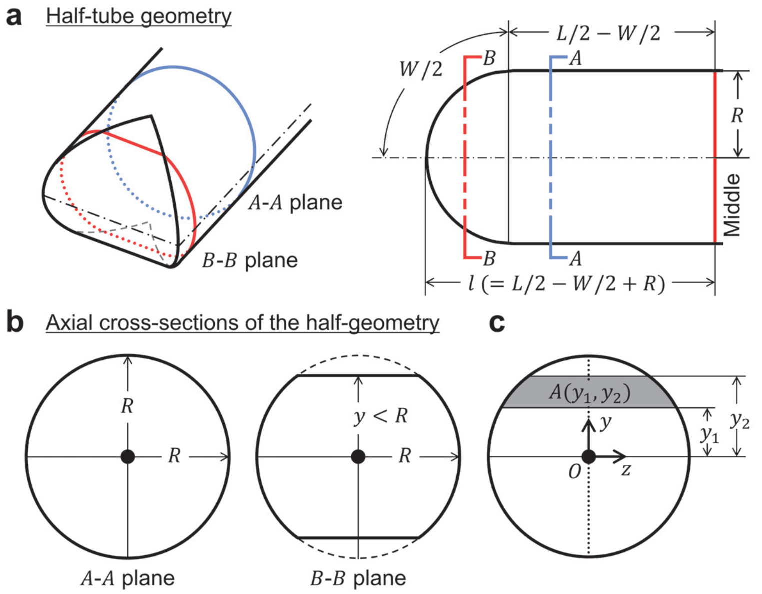

Figure 5-12. Half-geometry of the inflated tube and its circular cross-section.

The shape of the cross-section at the rounded end of the inflatable tube is not constant throughout. So, in order to facilitate the calculation of each area, an equation for a partial area of a circle was defined (Fig. 5-12c). The area $A(y_1, y_2)$ is defined as the area of the circle starting at a height y_1 and ending at a height y_2 on the vertical axis. Let us consider a circle which has a constant radius R, as calculated using Equation 5-4 in the yz-plane, then the partial area $A(y_1, y_2)$ can be obtained as

$$A(y_1, y_2) = R^2\left(\sin^{-1}\frac{y_2}{R} + \frac{1}{2}\sin\left(2\sin^{-1}\frac{y_2}{R}\right) - \sin^{-1}\frac{y_1}{R} - \frac{1}{2}\sin\left(2\sin^{-1}\frac{y_1}{R}\right)\right) \qquad (5\text{-}6)$$

5.4.2 Geometry of the compressed unbuckled tube

The compression of the inflatable tube starts from the undeformed inflated equilibrium position of the tube whose shape is mirrored at each end. As the force is uniformly applied at both ends and the tube is symmetric, half the compression can be applied to the half-segment model (Fig. 5-13a, b). The tapered end of the half-tube compresses first in the early portion of the compression (Fig. 5-13b). This causes some visible creases at the compressed ends of the tube (Fig. 5-13a). In the approximated geometry model, this creasing deformation is neglected, and the end of the tube

1
2
3
4
5
6
7

maintains its tapered boundary with a reduction in volume corresponding to the segment of the tapered end which is outside of the boundary of the wall. Then, all cross-sections throughout the tube can be calculated as in Equation 5-6 by separating the tube into two regions: the cylindrical volume of the body, which has a circular cross-section, and the tapered end region, which has a circular cross-section with a varying partial area (Fig. 5-13c). The two regions can have individual subinterval variables along the axis of the unbuckled tube which will be used for the Riemann summation. The subinterval variable x_b of the circular cylindrical body region can be defined from the middle of the tube until the point where the tapered end starts, and the other variable x_e of the end region can be defined from this point to the wall (Fig. 5-13c). Thus, if the compression s_i is within the portion of the tapered end of the tube such that s_i is smaller than R then the volume of these two regions can be summed to obtain the volume element $V_{UB,\,i}$ of the unbuckled tube. Within this compression range, it can be expressed as follows.

$$V_{UB,\,i} = \sum_{x_b = 0}^{l-R} 2A(0,\ R)\triangle x + \sum_{x_e = 0}^{R-s_i} 2A\left(0,\ \sqrt{R^2 - x_e^2}\right)\triangle x \tag{5-7}$$

As shown in the previous chapter, the unbuckled state of the inflatable tube only occurs in the early portion of the compression. However, this geometrical model can be used to calculate the volume and force produced by a tube that would not buckle throughout the entire compression (Fig. 5-13d). By following a similar process as performed previously, the volume elements $V_{UB,\,i}$ for a displacement where s_i greater than R can be calculated as follows.

$$V_{UB,\,i} = \sum_{x_b = 0}^{l-s_i} 2A(0,\ R)\triangle x \tag{5-8}$$

These volume elements can be added for the entire range of the compression to construct a complete volume matrix V_{UB} as follows.

$$V_{UB} = \left[\, V_{vu,\,1},\ V_{vu,\,2},\ V_{vu,\,3},\ \cdots, V_{vu,\,n} \right] \tag{5-9}$$

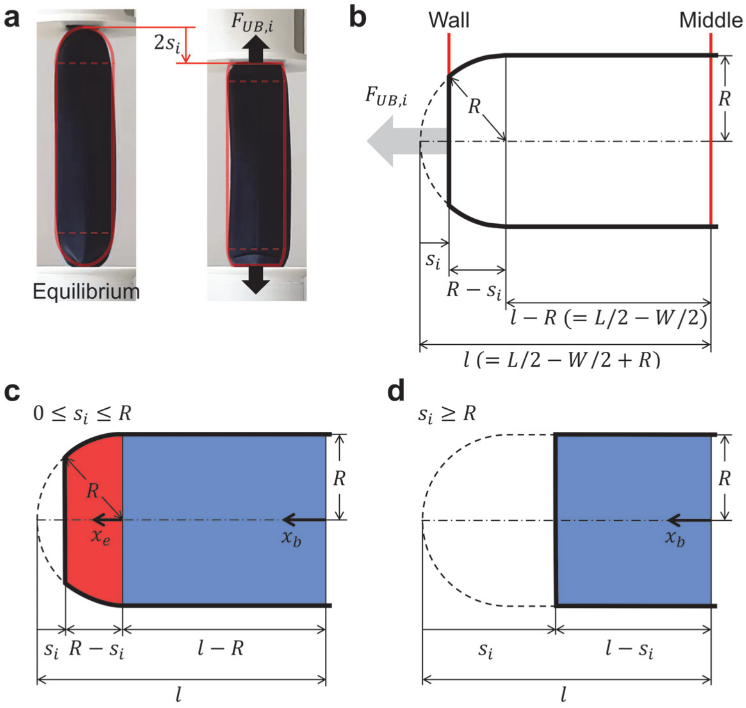

Figure 5-13. Geometry of the compressed unbuckled tube.

Then, the volume change $\triangle V_{UB}$ can be derived to calculate the force F_{UB} that the inflatable tube generates when axially compressed while sustaining the unbuckled state. By using a uniform compression interval $\triangle s$, this force F_{UB} can be calculated as

$$F_{UB} = P \triangle V_{UB} / \triangle s \tag{5-10}$$

For a tube with a length of 75 mm, a width of 30 mm, and pressurized to 100 kPa, the calculated force F_{UB} as a function of the compression s can be plotted as shown in Figure 4-7a.

5.4.3 Geometry of the compressed buckled tube

The buckled state of the inflatable tube happens after snap-through buckling of the tube, is one of two stable states in the bistable region of the deformation and is an unstable state in the early portion of the compression. The geometrical model presented below approximates the geometry of the buckled tube having a crease at its middle throughout the entire compression even when this geometry would not result in a stable state. Due to the buckling, a portion of the boundary in the middle of the tube becomes curved as it transitions into the crease at the center of the tube. The shape of this middle part of the buckled tube was defined using the following assumption: the buckling occurs symmetrically about the middle of the tube and the upper boundary, which is on the opposite side to the creasing, maintains its initial length as defined on the flat uninflated tube. The volume overlapping with the wall and beyond the middle line of the tube where the crease occurs is neglected from the volume of the tube (Fig. 5-14a, b). Two axes are used in the calculations of the volume. The first axis is along the length of the buckled tube which will be used to calculate the quasistatic volumes used for Reimann summation. The second axis is that which corresponds to the quasistatic displacement of the compression (Fig. 5-14b). Here, the length of the upper boundary is assumed to be equal to a half of the initial manufactured length accordingly to the previously defined assumption, so the middle axis of the buckled tube changes at a given angle . Thus, the compression at this angle can be obtained as

$$s_i = l - (1 - R\theta_i) + \cos\theta_i \tag{5-11}$$

Since the boundary curve of the buckled tube changes through the deformation, the geometry should have distinct regions used to define the geometry of the buckled tube throughout the entire deformation. Five regions were defined: upper-end (red), upper-body (green), upper-center (gray), lower-end (yellow), and lower-body (blue) as indicated with different colors in Fig. 5-14c, and their shape and their cross-section type were defined differently for different ranges of values of θ_i. There are four ranges of θ_i that determine the shape and the cross-section type of the upper-end, upper-body, lower-end, lower-body, upper-body, and upper-center. Some regions have the same configuration in different ranges as shown in Fig. 5-15 where the dotted lines indicate when a given region changes segmentation. The four ranges of hi are as follows; Range 1: $0 \le \theta_i \le \phi_1 (= \pi/4)$, Range 2: $\phi_1 \le \theta_i \le \phi_2$, Range 3: $\phi_2 \le \theta_i \le \phi_3$, and Range 4: $\phi_3 \le \theta_i \le \pi/2$ with each breakpoint angle ϕ_1, ϕ_2, and ϕ_3 calculated following the conditions indicated in Figure 5-14d. Within Range 1, the upper-end region (red) has a length variable a_i which is defined as shown in Figure 5-15. To calculate this length variable a_i, the equation identifying the radius R of the circular boundary was built by using the Pythagorean theorem and trigonometric functions as

$$a_i + \sqrt{R^2 - a_i^2}\tan\theta_i = R \tag{5-12}$$

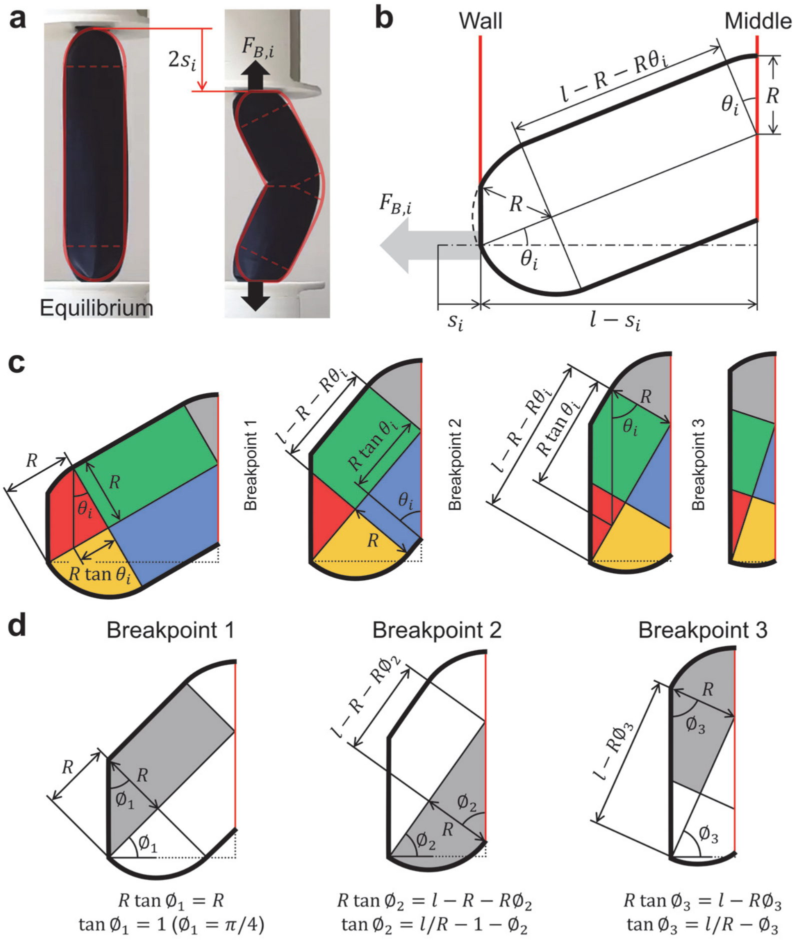

Figure 5-14. Geometry of the compressed buckled tube.

By organizing the left and right sides of this equation and squaring them, the equation can be rewritten into a quadratic equation in terms of as

$$\left(1+\tan^2\theta_i\right)a_i^2 - 2Ra_i + R^2\left(1-\tan^2\theta_i\right) = 0 \tag{5-13}$$

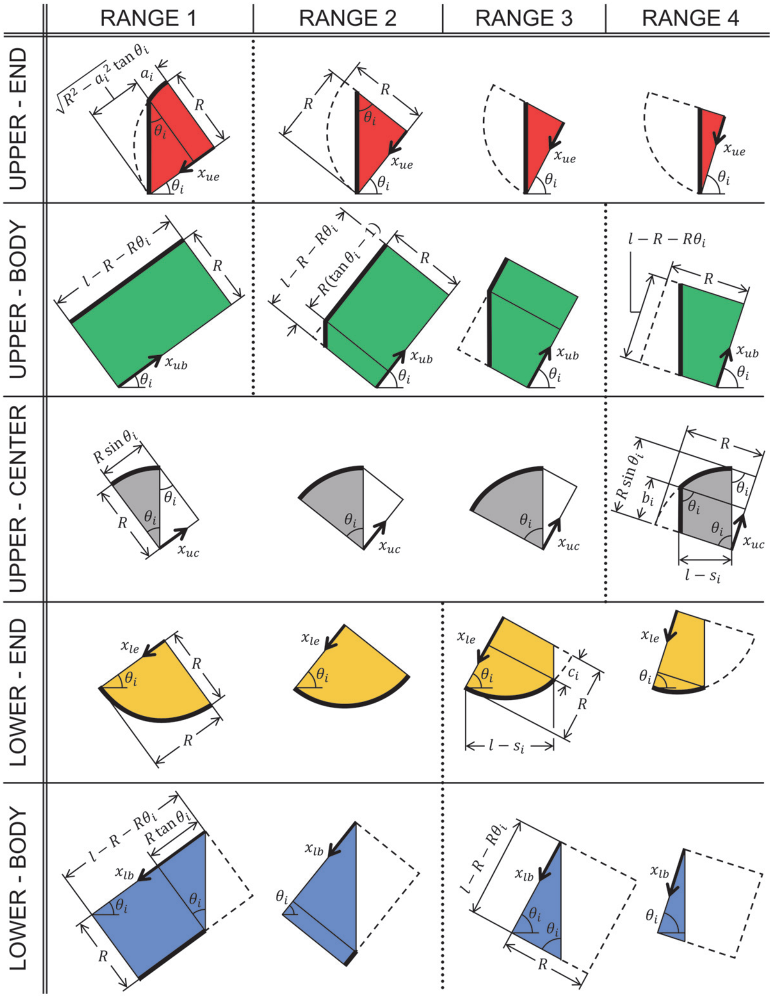

Figure 5-15. Geometry of the compressed buckled tube in detail at different angles.

Thus, the root of this quadratic equation in terms of ai can be expressed as

$$a_i = R\cos 2\theta_i \tag{5-14}$$

The subinterval variable x_{ue} can be separated into two portions where one is the element of length ai and the other is the volume being cut off by the wall. The volume element $V_{B,\,i,\,ue}$ of the upper-end region of the buckled tube can be expressed as follows.

$$V_{B,\,i,\,ue}[\text{Range } 1] = \sum_{x_{ue}=0}^{a_i} A\left(0,\ \sqrt{R^2 - x_{ue}^{\,2}}\right)\triangle x + \sum_{x_{ub}=a_i}^{R} A\left(0,\ \frac{R - x_{ue}}{\tan\theta_i}\right)\triangle x \tag{5-15}$$

Afterwards, the entirety of the volume of the upper-end region is cut off by the wall and the variable ai ceases to be used in defining its geometry. Then, its volume can be calculated similarly to the second term of Equation 5-15 as

$$V_{B,\,i,\,ue}[\text{Range } 2 \sim 4] = \sum_{x_{ue}=0}^{R} A\left(0,\ \frac{R - x_{ue}}{\tan\theta_i}\right)\triangle x \tag{5-16}$$

The upper-body region (green) reduces in length as the curve of the middle of the tube increases, and the total range of its subinterval x_{ub} changes depending on θ_i. The calculation of the volume of this region can be divided into three ranges where the calculation for the volumes within Range 2 and 3 are the same. Within Range 1, the volume is not affected by the wall, but the increase in volume of the upper-center region leads to a decrease in volume of the upper-body region. Thus, the volume element $V_{B,\,i,\,ub}$ of the upper-body region can be expressed as follows.

$$V_{B,\,i,\,ub}\Big[\text{Range } 1] = \sum_{x_{ub}=0}^{l - R - R\theta_i} A(0,\ R)\triangle x \tag{5-17}$$

The volume of the upper-body region starts to be affected by the wall after Range 1, and the volume element $V_{B,\,i,\,ub}$ can be divided with two portions where one is the volume being cut off by the wall and the other is the completely cylindrical part, as follows.

$$\begin{aligned} &V_{B,\,i,\,ub}[\text{Range } 2 \sim 3] \\ &= \sum_{x_{ub}=0}^{R(\tan\theta_i - 1)} A\left(0,\ \frac{R + x_{ub}}{\tan\theta_i}\right)\triangle x + \sum_{x_{ub}=R(\tan\theta_i - 1)}^{l - R - R\theta_i} A(0,\ R)\triangle x \end{aligned} \tag{5-18}$$

As the angle reaches Range 4, the entirety of upper-body region is affected by the wall, and the volume element $V_{B,\,i,\,ub}$ has a single term as follows.

$$V_{B,\,i,\,ub}[\text{Range } 4] = \sum_{x_{ub}=0}^{l - R - R\theta_i} A\left(0,\ \frac{R + x_{ub}}{\tan\theta_i}\right)\triangle x \tag{5-19}$$

The upper-center region (gray) increases its volume as the buckling develops until it contacts with the wall, and its subinterval variable x_{uc} starts from the end of the cylindrical part from the previous region and ends at the orthogonal projection of the radius at the middle of the tube. Thus, from Range 1 to Range 3, the volume element $V_{B,\,i,\,ub}$ of the upper-center region can be obtained as follows.

$$V_{B,\,i,\,uc}[\text{Range } 1 \sim 3] = \sum_{x_{uc}=0}^{R\sin\theta_i} A\left(\frac{x_{uc}}{\tan\theta_i},\ \sqrt{R^2 - x_{uc}^2}\right)\triangle x \tag{5-20}$$

Within Range 4, the upper-center region is partially cut off by the wall and the length variable b_i corresponds to the length of this cut-off amount. To calculate this length variable b_i, the equation for calculating the length $l - s_i$ on the compression axis using the Pythagorean theorem and trigonometric functions can be written as

$$\sqrt{R^2 - b_i^2}\,\sin\theta_i - b_i\cos\theta_i = l - s_i \tag{5-21}$$

By organizing the left and right sides of this equation and squaring them, the equation can be rewritten into a quadratic equation in terms of b_i as

$$b_i^2 + 2(l - s_i)\cos\theta_i b_i + (l - s_i)^2 - R^2\sin^2\theta_i = 0 \tag{5-22}$$

Thus, the root of this quadratic equation in terms of b_i can be expressed as

$$b_i = -(l - s_i)\cos\theta_i + \sqrt{R^2 - (l - s_i)^2}\,\sin\theta_i \tag{5-23}$$

Then, the volume element $V_{B,\,i,\,uc}$ can be expressed as follows.

$$\begin{aligned} &V_{B,\,i,\,uc}[\text{Range } 4] \\ &= \sum_{x_{uc}}^{b_i} A\left(\frac{x_{uc}}{\tan\theta_i},\ \frac{l - R\theta_i + x_{uc}}{\tan\theta_i}\right)\triangle x + \sum_{x_{uc}=b_i}^{R\sin\theta_i} A\left(\frac{x_{uc}}{\tan\theta_i},\ \sqrt{R^2 - x_{uc}^2}\right)\triangle x \end{aligned} \tag{5-24}$$

The lower-end region (yellow) is located where the crease of the buckled tube appears such that it is not directly affected by the wall and maintains its volume in the early portion of the compression, but the crease reduces its volume in the later portion of the compression. The volume element $V_{B,\,i,\,le}$ of the lower-end region of the buckled tube in Range 1 and Range 2 can be calculated as follows.

$$V_{B,i,le}[\mathrm{Range}\ 1\sim 2]=\sum_{x_{le}=0}^{R}A\left(0,\ \sqrt{R^2-{x_{le}}^2}\right)\triangle x \tag{5-25}$$

The crease that occurs in Range 3 and Range 4 decreases the volume of the lower-end region. The volume element $V_{B,i,le}$ has a separate length variable c_i to consider the portion of the volume in the crease. To calculate this length variable c_i, the equation identifying the length $l-s_i$ on the compression axis was developed using the Pythagorean theorem and trigonometric functions as

$$\sqrt{R^2-c_i^2}\sin\theta_i+(R-c_i)\cos\theta_i=l-s_i \tag{5-26}$$

By organizing the left and right sides of this equation and squaring them, the equation can be rewritten into a quadratic equation in terms of c_i as

$$c_i^2+2(l-s_i-R\cos\theta_i)\cos\theta_i c_i+(l-s_i-R\cos\theta_i)^2-R^2\sin^2\theta_i=0 \tag{5-27}$$

Thus, the root of this quadratic equation in terms of ci can be expressed as

$$c_i=-(l-s_i-R\cos\theta_i)\cos\theta_i+\sqrt{R^2-(l-s_i-R\cos\theta_i)^2}\sin\theta_i \tag{5-28}$$

Then, the volume element $V_{B,i,le}$ can be expressed as follows.

$$\begin{aligned}&V_{B,i,le}[\mathrm{Range}\ 3\sim 4]\\&=\sum_{x_{le}=0}^{c_i}A\left(0,\ \frac{l-R-R\theta_i+x_{le}}{\tan\theta_i}\right)\triangle x+\sum_{x_{le}=c_i}^{R}A\left(0,\ \sqrt{R^2-{x_{le}}^2}\right)\triangle x\end{aligned} \tag{5-29}$$

The lower-body region (blue) is also not affected by the wall, but the crease causes a reduction in volume in the later part of the compression. The subinterval variable x_{lb} of the lower-body region starts from the middle of the buckled tube and ends at the point where the lower-end region starts. The volume element $V_{B,i,lb}$ in Range 1 and Range 2, before the crease affects the lower-end region, can be separated into two portions where one is the volume reduced by the overlap between the symmetric half-unit on the other side and the other is the completely cylindrical part, as follows.

$$V_{B,i,lb}[\text{Range } 1 \sim 2] = \sum_{x_{lb}=0}^{R\tan\theta_i} A\left(0,\ \frac{x_{lb}}{\tan\theta_i}\right)\triangle x + \sum_{x_{le}=R\tan\theta_i}^{l-R-R\theta_i} A(0,\ R)\triangle x \tag{5-30}$$

In Range 3 and Range 4, the lower-body region does not contain a completely cylindrical portion, so the volume element $V_{B,i,lb}$ can be expressed as follows.

$$V_{B,i,lb}[\text{Range } 3 \sim 4] = \sum_{x_{lb}=0}^{l-R-R\theta_i} A\left(0,\ \frac{x_{lb}}{\tan\theta_i}\right)\triangle x \tag{5-31}$$

The summation of these five elements becomes a single volume element $V_{B,i}$ of the buckled tube throughout the compression as

$$V_{B,i} = V_{B,i,ue} + V_{B,i,ub} + V_{B,i,uc} + V_{B,i,le} + V_{B,i,lb} \tag{5-32}$$

These volume elements can be gathered to construct a complete volume matrix V_B as follows.

$$V_B = [\ V_{B,1},\ V_{B,2},\ V_{B,3},\ \cdots,\ V_{B,N}] \tag{5-33}$$

Then, the volume change $\triangle V_B$ can be used to calculate the force F_B that the inflatable tube generates when axially compressed in the buckled state. With the compression change $\triangle s$, this force F_B can be calculated as

$$F_B = P\triangle V_B / \triangle s \tag{5-34}$$

For a tube with a length of 75 mm, a width of 30 mm, and pressurized to 100 kPa, the calculated force F_B as a function of the compression s can be plotted as shown in Fig. 4-7a.

5.4.4 Geometry of the transitioning tube

The buckled and unbuckled states represent the two potential stable states of the system and which of these is the stable state depends on the compression deformation. However, knowing the force necessary to compress the inflatable tube in each state is insufficient to predict when the tube changes from a buckled state to an unbuckled state and vice-versa, and does not explain the existence of the bistable behavior within a certain compression range (Fig. 5-16a). Another element is necessary to explain the behavior of the inflatable tube in the bistable region, the snap-through buckling at a specific displacement, and the regions where the tube is only stable in one state (Fig. 5-16b). It will be posited that the inflatable tube tries to maximize its volume towards a local maximum volume rather than a global maximum. The inflatable tube remains at a local maximum volume and transitions between states during compression and extension when the local maximum stops being a local maximum. The bistable state is a result of both states being local maximum volumes.

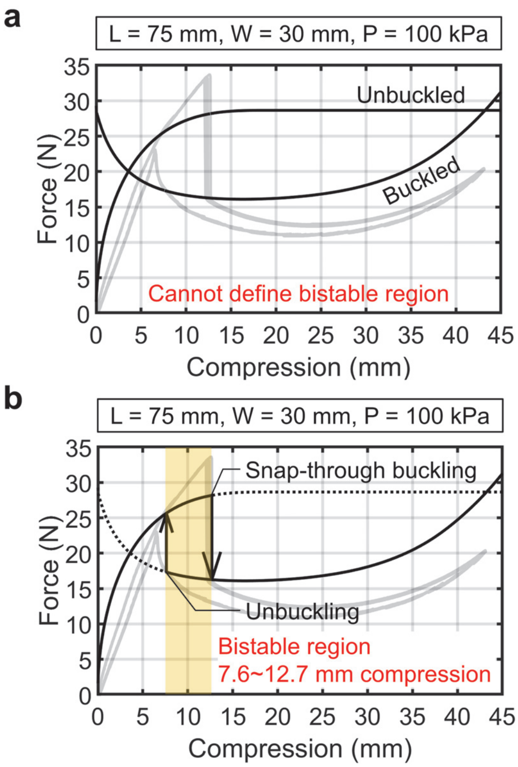

Figure 5-16. Axial compressive force calculated from the model.

The volume throughout the rotation from one state to the other is necessary to determine local and global maximum volumes (Fig. 5-17a). Thus, the volume of the tube for all intermediary tube angles between the unbuckled and buckled states are needed. This will be calculated by modifying the buckled tube model explained in the previous section which produces a geometry for a given displacement s_i with a given tube angle θ_i with respect to the displacement axis. For a given fixed compression displacement s_N of the rotation, all intermediary buckled state tubes ranging from zero displacement to s_N will cover the range of angles from zero to θ_N (Fig. 5-17b).

The geometry of a given buckled tube geometry minus the portion of the geometry outside of the boundary of the given displacement s_N will be considered as the shape of the intermediary geometry. In order to model the geometry for a displacement of s_N, the buckled tube states with displacement s_i ranging from 0 to s_N have to be considered. Thus, the displacement s_i which is dependent on the angle θ_i can be obtained as done previously, and the geometry of the tube during the transition will be separated into five regions to calculate its volume. The upper-end and the lower-end regions have different geometries from the buckled state due to the portion of the geometry outside of the given displacement being removed from the geometry being considered (Fig. 5-17c).

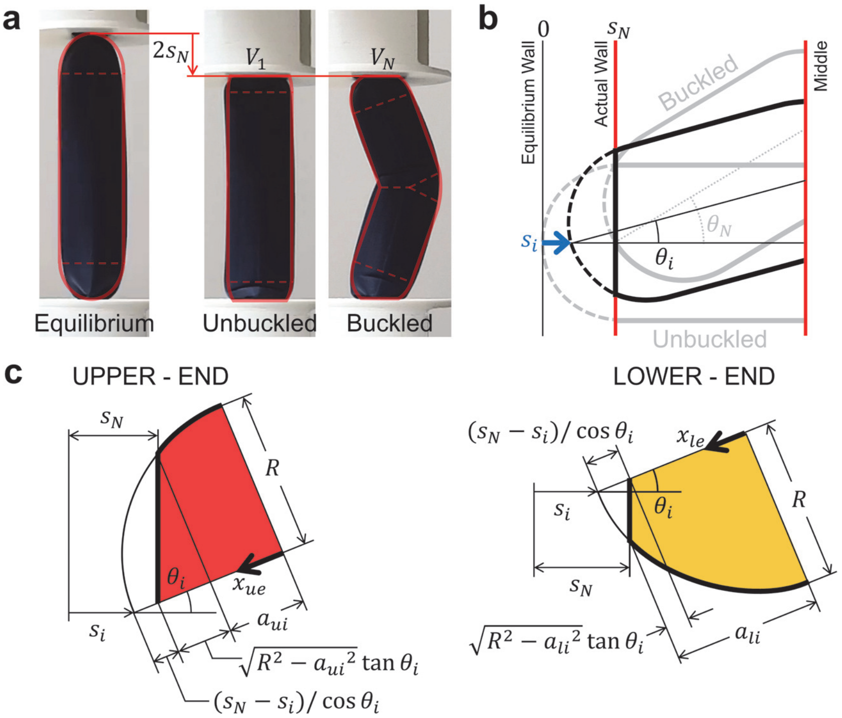

Figure 5-17. Geometry of the transition between buckled and unbuckled states.

The three other regions are the upper-body, upper-center, lower-body region; their dimensions can be calculated as done for buckled tubes using Equation 5-17~19, Equation 5-20~24, Equation 5-30~31 (Fig. 5-15). The upper-end region has a length variable a_{ui} which corresponds to the length of the region which is not cut off by the wall. To define this length variable a_{ui}, the equation identifying the radius R of the circular boundary was defined using the Pythagorean theorem and trigonometric functions as

$$a_{ui} + \sqrt{R^2 - a_{ui}^2}\,\tan\theta_i + (s_N - s_i)/\cos\theta_i = R \qquad (5\text{-}35)$$

By reorganizing the left and right sides of this equation and squaring them, the equation can be rewritten into a quadratic equation of a_{ui} as

$$(1+\tan^2\theta_i)a_{ui}^2 - 2\left(R - \frac{s_N - s_i}{\cos\theta_i}\right)a_{ui} + \left(R - \frac{s_N - s_i}{\cos\theta_i}\right)^2 - R^2 = 0 \qquad (5\text{-}36)$$

The root of this quadratic equation in terms of a_{ui} can be expressed as

$$a_{ui} = \left(R - \frac{s_N - s_i}{\cos\theta_i}\right)\cos^2\theta_i - \sqrt{R^2(1+\tan^2\theta_i) - \left(R - \frac{s_N - s_i}{\cos\theta_i}\right)^2}\,\sin\theta_i\cos\theta_i \qquad (5\text{-}37)$$

The volume element $V_{i,ue}$ of the upper-end region of the tube during the transition can be expressed throughout the displacement x_{ue} as follows.

$$V_{i,ue} = \sum_{x_{ue}=0}^{a_{ui}} A\left(0,\ \sqrt{R^2 - x_{ue}^2}\right)\triangle x + \sum_{x_{ue}=a_{ui}}^{R-\frac{s_N - s_i}{\cos\theta_i}} A\left(0,\ \frac{R - \frac{s_N - s_i}{\cos\theta_i} - x_{ue}}{\tan\theta_i}\right)\triangle x \qquad (5\text{-}38)$$

The length variable a_{li} needs to be calculated to determine the volume of the lower-end region. To define this length variable a_{li}, the equation identifying the radius R of the circular boundary was defined using the Pythagorean theorem and trigonometric functions as

$$a_{li} - \sqrt{R^2 - a_{li}^2}\,\tan\theta_i + (s_N - s_i)/\cos\theta_i = R \qquad (5\text{-}39)$$

By reorganizing the left and right sides of this equation and squaring them, the equation can be rewritten into a quadratic equation of a_{li} as

$$(1+\tan^2\theta_i)a_{li}^2 - 2\left(R - \frac{s_N - s_i}{\cos\theta_i}\right)a_{li} + \left(R - \frac{s_N - s_i}{\cos\theta_i}\right)^2 - R^2\tan^2\theta_i = 0 \tag{5-40}$$

Then, the root of this quadratic polynomial in terms of a_{li} can be expressed as

$$a_{li} = \left(R - \frac{s_N - s_i}{\cos\theta_i}\right)\cos^2\theta_i + \sqrt{R^2(1+\tan^2\theta_i) - \left(R - \frac{s_N - s_i}{\cos\theta_i}\right)^2}\sin\theta_i\cos\theta_i \tag{5-41}$$

The volume element $V_{i,le}$ of the lower-end region of the tube during the transition can be expressed throughout the displacement x_{le} as follows.

$$\begin{aligned} V_{i,le} = & \sum_{x_{le}=0}^{R-\frac{s_N - s_i}{\cos\theta_i}} A\left(0,\ \sqrt{R^2 - x_{le}^2}\right)\triangle x + \\ & \sum_{x_{le}=R-\frac{s_N - s_i}{\cos\theta_i}}^{a_{le}} A\left(\frac{x_{le} - R + \frac{s_N - s_i}{\cos\theta_i}}{\tan\theta_i},\ \sqrt{R^2 - x_{le}^2}\right)\triangle x \end{aligned} \tag{5-42}$$

The volume elements of the circular cylindrical body, upper-central, and lower-central regions are the same as for the buckled tube state shown previously. The volume matrix during the transition can be built by gathering all these elements and can be expressed as

$$V = [\,V_1,\ V_2,\ V_3,\ \cdots,\ V_N] \tag{5-43}$$

This volume matrix V shows how the volume of the inflatable tube changes during the transition between the unbuckled and buckled states for a given displacement. The first element V_1 corresponds to the volume of the unbuckled tube whose axis is aligned to the equilibrium position and the last element V_N corresponds to the volume of the fully buckled tube.

For a tube with a length of 75 mm, a width of 30 mm, and pressurized to 100 kPa, the evolution of the volume throughout the transition between the unbuckled and buckled states at different compression displacements can be plotted as shown in Fig. 5-18 to present each of the unbuckled, bistable, and buckled regions of the compression.

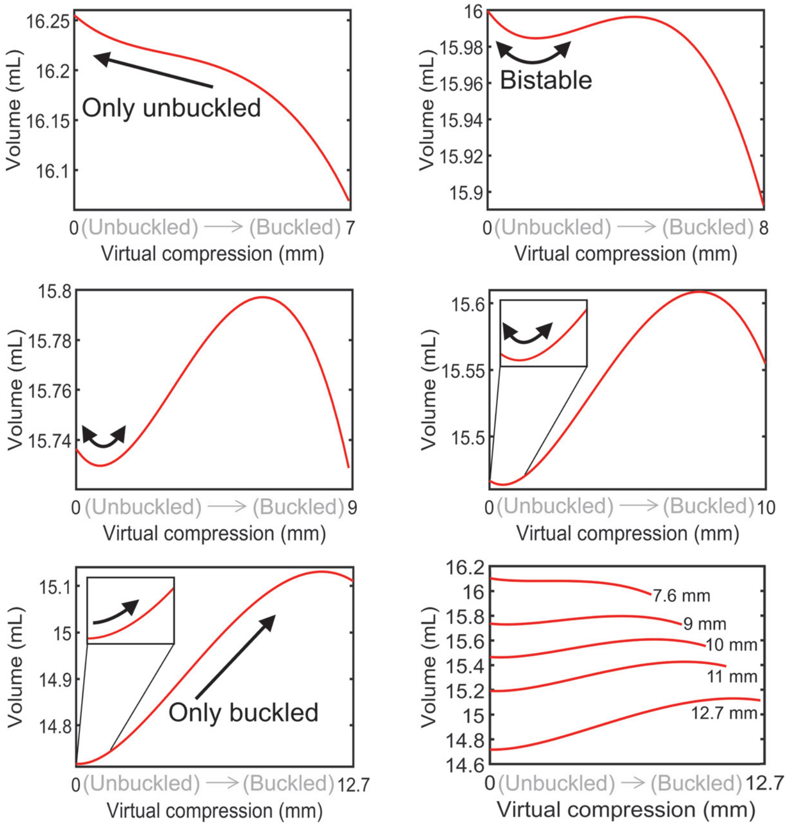

Figure 5-18. Volume change of the transitioning tube calculated from the modeling at different compression displacements.

For a tube length of 75 mm and a width of 30 mm, this volume as a function of the angle was plotted for compression displacements of 7, 8, 9, 10, and 12.7 mm (Fig. 5-18). These compression displacements correspond to the states where the tube is always unbuckled in the case of a displacement of 7 mm, the bistable state in the case of displacements of 8, 9, and 10 mm, and the always buckled state in the case of a displacement of 12.7 mm. In the always unbuckled state, the volume only decreases as it rotates towards the buckled state which results in the tube remaining unbuckled. When the plot enters the bistable region, the shape of the plot becomes convex where the maximum volume is in either the buckled or unbuckled state and the minimum volume is in between these states. This means that the tube will remain in its current state if the tube is either buckled or unbuckled as it is the local maximum volume, but that it can be manually deformed towards the other state which is itself a local maximum volume. This explains the bistable behavior of the tube within this region. As the compression displacement is further increased, the local maximum volume in the unbuckled state ceases to be a local maximum, and the large volume differential between the buckled and unbuckled states results in rapid snap-through buckling of the tube. Afterwards, the only stable state of the tube is the buckled state. The tendency of the tube to remain at the local maximum volume explains why it does not unbuckle during the extension at the same point as it buckles during the compression and why buckling happens at a specific compression point.

5.4.5 Verification for tubes of different dimensions

The proposed model was validated for the different experimental results related to the tube dimensions by calculating and plotting the force generated by each tube and comparing it to the experimental results. The model was first validated for an inflatable tube with different tube lengths. It was applied to tubes with a width of 25 mm and lengths of 62.5, 75, 100, and 125 mm with a pressure of 100 kPa. The buckled and unbuckled force as well as the buckling and unbuckling deformations were calculated

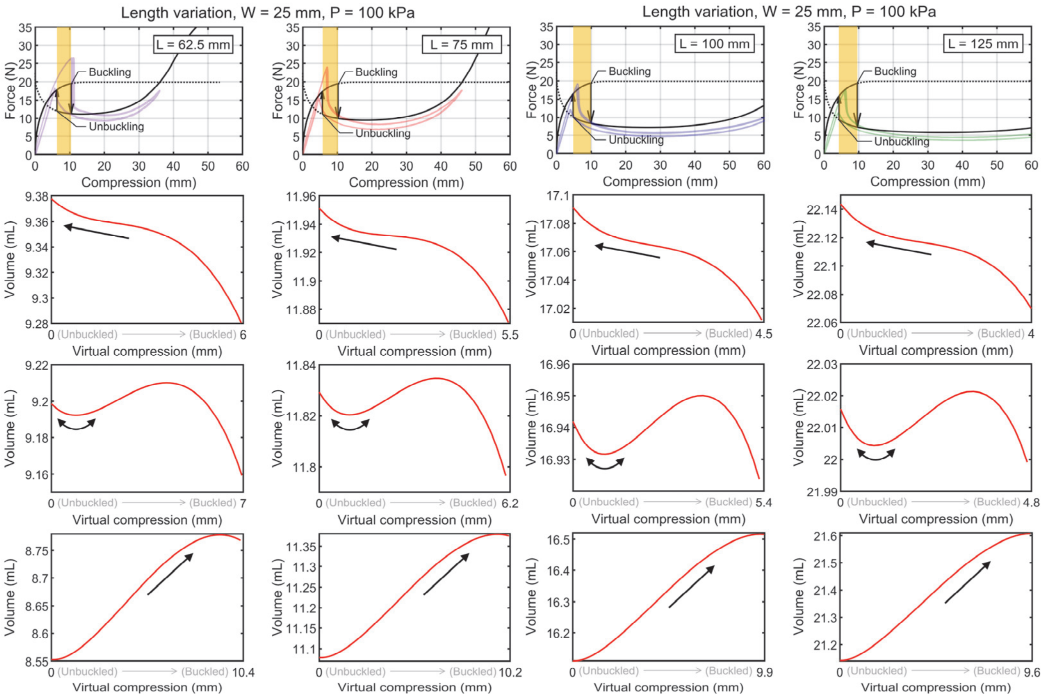

Figure 5-19. Verification for the inflatable tubes with different lengths.

for each tube (Fig. 5-19). The numerical results show that the four tubes with different lengths are predicted to have the same force behavior before buckling but longer displacements required for buckling and unbuckling as the tube length increases, which corresponds well with the behavior observed in the experiment results. Here, each of the buckling and unbuckling points appears at similar displacements as the tube length increases.

The model was then validated for an inflatable tube with different tube widths. It was applied to tubes with a length of 25 mm, widths of 30, 25, 18.75, and 15 mm and with a pressure of 100 kPa. Again, the buckled and unbuckled forces as well as the buckling and unbuckling deformations were calculated for each tube width (Fig. 5-20). The model slightly overpredicts the displacements required for buckling and unbuckling, but it predicts well the effect of the width on the change in displacements required for buckling and unbuckling. It also correctly predicts the change in scaling of forces. Based on these results and that of the length, it can be said that the model is good at predicting the behavior of these inflatable tubes even if there are errors in terms of finding the exact displacement required for buckling and unbuckling.

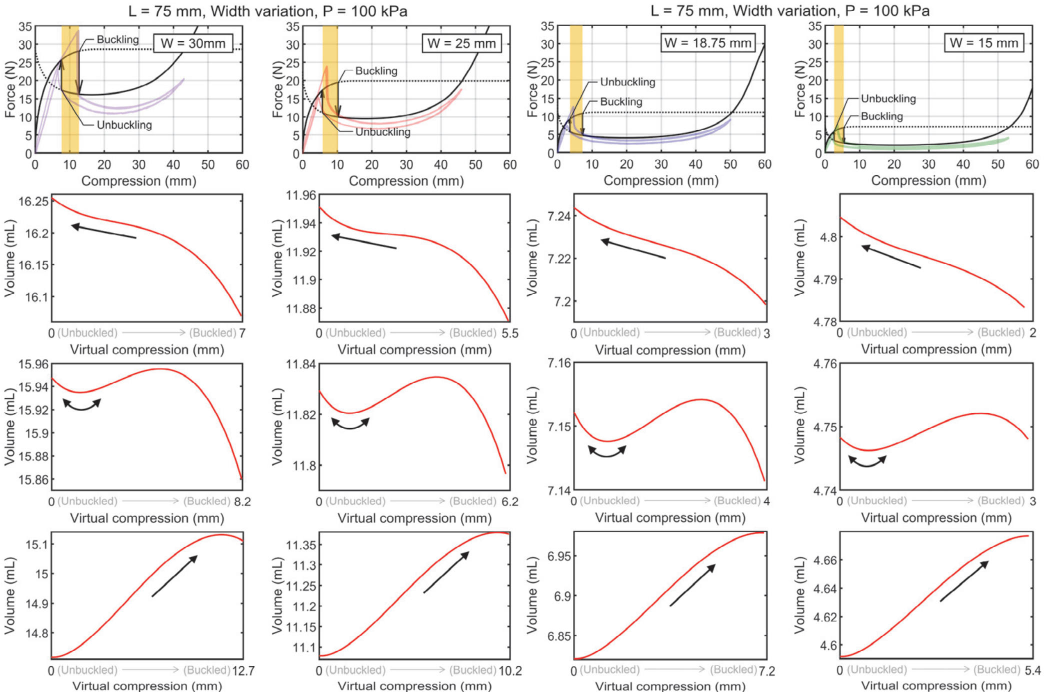

Figure 5-20. Verification for the inflatable tubes with different widths.

5.4.6 Generalization of defining the bistable region

Using the same method proposed above to define the start point of the bistable region where unbuckling occurs and the end point where snap-through buckling occurs, additional data for tubes with different dimensions, having length-to-width ratios of 2.5, 3, 3.5, 4, 4.5, and 5, were calculated to generalize the bistable region based on tube length and width. Surface equations for each start and end point were created using the poly23 type interpolation available in MATLAB software, involving different coefficients (Fig. 5-21). Data with the same length-to-width ratio were aligned along a straight line on the interpolated surface. Since this study focuses on ratios within 2.5 and 5, the outward part of the surface should be neglected, then now the bistable region of the tube with any length and width can be defined within the valid area.

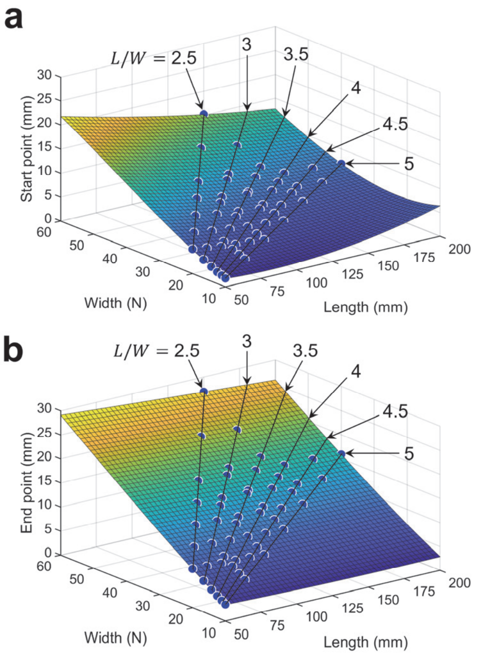

$$\text{Start point}(L, W) = k_0 + k_1L + k_2W + k_3L^2 + k_4LW + k_5W^2 + k_6L^2W + k_7LW^2 + k_8W^3$$

Coefficients (with 95% confidence bounds):
k_0 = 6.826e-02 (-2.439e-01, 3.804e-01)
k_1 = -3.291e-02 (-4.180e-02, -2.403e-02)
k_2 = 3.264e-01 (3.028e-01, 3.501e-01)
k_3 = 4.059e-04 (3.012e-04, 5.107e-04)
k_4 = -2.917e-03 (-3.645e-03, -2.189e-03)
k_5 = 5.021e-03 (3.800e-03, 6.242e-03)
k_6 = -4.600e-06 (-7.426e-06, -1.774e-06)
k_7 = 3.208e-05 (1.399e-05, 5.017e-05)
k_8 = -5.385e-05 (-8.202e-05, -2.567e-05)

$$\text{End point}(L, W) = k_0 + k_1L + k_2W + k_3L^2 + k_4LW + k_5W^2 + k_6L^2W + k_7LW^2 + k_8W^3$$

Coefficients (with 95% confidence bounds):
k_0 = -6.485e-01 (-8.427e-01, -4.542e-01)
k_1 = -9.599e-03 (-1.513e-02, -4.072e-03)
k_2 = 4.408e-01 (4.261e-01, 4.556e-01)
k_3 = 4.659e-05 (-1.858e-05, 1.118e-04)
k_4 = -4.435e-04 (-8.967e-04, 9.613e-06)
k_5 = 1.984e-03 (1.224e-03, 2.744e-03)
k_6 = -5.479e-07 (-2.306e-06, -1.211e-06)
k_7 = 3.126e-06 (8.130e-06, 1.438e-05)
k_8 = -1.214e-05 (-2.967e-05, 5.396e-06)

Figure 5-21. Generalization of defining the bistable region.

5.4.7 Energy storage and conversion of the buckling tube

The snap-through buckling of the inflatable tube represents a form of instantaneous energy conversion due to the volumetric instability of the compressed tube, which accumulates potential energy throughout the compression process. This can be elucidated through the force plot during compression and the volume plot of the

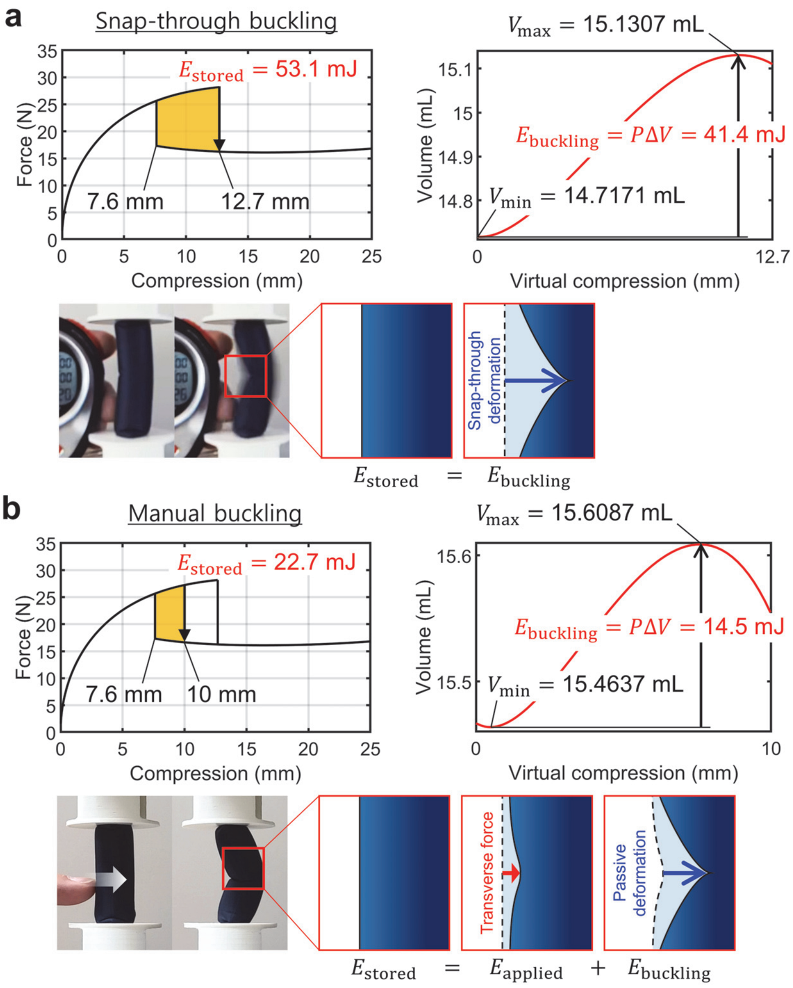

Figure 5-22. Energy storage and conversion of the buckling tube.

transitioning tube at a given compression displacement, as calculated by the suggested model. For instance, at the snap-through buckling of a tube with dimensions of 75 mm in length, 30 mm in width, and pressurized to 100 kPa, the total area between the unbuckled and buckled force plots within the bistable region implies the maximum storable energy. The product of the volume change between the minimum and maximum values of the volume plot and the supplied pressure then represents the total amount of energy converted when the tube undergoes snap-through buckling (Fig. 5-22a). Here, the energy conversion comprises kinetic energy, involving the instant speed, and potential energy used to increase the tube volume created by the buckling motion. Theoretically, each energy calculated from the force and volume plots should be the same, but the suggested model does not produce identical results. This discrepancy is likely because the calculated force of the buckled tube targets the tube state to be fully buckled for every compression displacement, which may not necessarily correspond to the maximum volume that the tube should reach. Additionally, the transitioning tube was interpreted through a virtual axial compression, which does not correspond to the transversal force required to actualize the buckling situation.

Similarly, the case where the tube manually buckles within the bistable region was considered using the same method (Fig. 5-22b). This time, the energy stored in the compressed unbuckled tube can be calculated as the area between the two force plots from the start of the bistable region to the given compression displacement. In this case, the tube needs to be supplied with external energy to deform it sufficiently to enter the phase where the tube can increase its volume and reach the other local maximum volume in the buckled state autonomously. Then, the stored energy should theoretically be the same as the sum of the applied energy and the buckling energy calculated from the volume change plot. However, it also shows non-identical values due to the same issues.

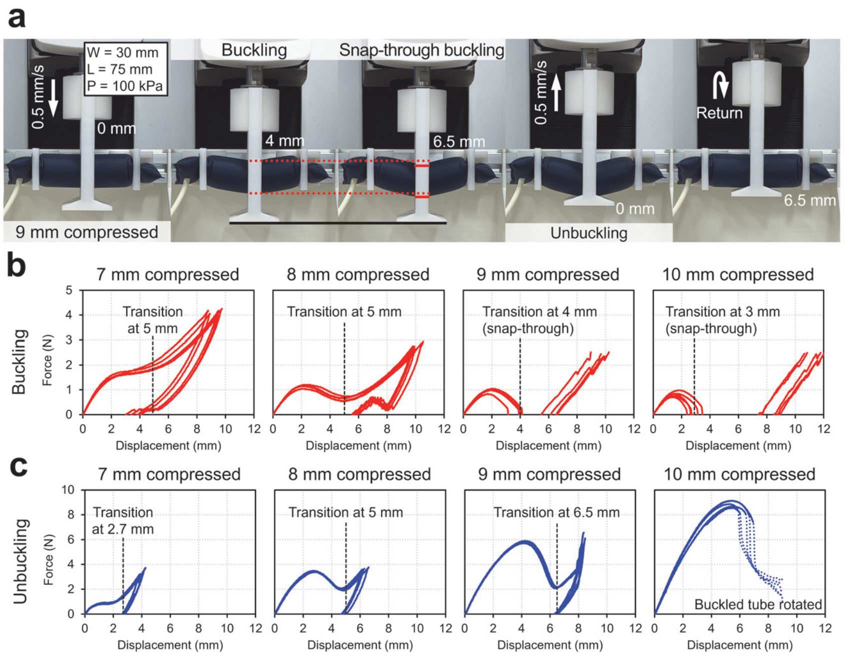

Figure 5-23. Transversal force required for buckling and unbuckling the tube.

The transversal forces required for buckling (Fig. 5-23b) and unbuckling (Fig. 5-23c) the tube at different compression displacements within the bistable region were measured and shows that snap-through buckling happens within the later portion of the bistable region while unbuckling does not produce a snap-through state transition. The test was conducted using a 3D-printed jig, which has a narrow tip to buckle the tube and a wide tip to unbuckle the tube on the opposite side, positioned far enough to avoid contact with the tube during the buckling process and vice versa. The test was performed with a travel speed of 0.5 mm/s (Figure 5-23a). Approaching the early portion of the bistable region, more manual buckling should be applied until the tube buckles and can be easily unbuckled. Conversely, nearing the end portion of the bistable region, less manual buckling is required. The tube naturally reaches the buckled position after a certain point and demands significantly higher force for unbuckling (Fig. 5-23b, c).

5.5 Discussion

The suggested model could explain the force produced by the tube in each state and further how it transitions between these two states by assuming that the tube moves towards a local maximum volume. This is due to the system moving to a lower energy state by the stored energy of the system being converted into kinetic and potential energies of the volume of air in the lateral direction during the transition to the maximum volume. Because the model of the transitioning tube did not account for loading conditions from out-of-plane deformation, it could not predict the transversal forces required for manual buckling and unbuckling. Additionally, due to differences in defining the buckled state of the tube between the force and volume plots, there were minor errors when comparing the energy storage and conversion of the buckling tube.

However, the model successfully explained the behavior of the inflatable tube throughout the compression process and release, including its bistable state and snap-through buckling behavior. It also demonstrated that the transitioning tube within the bistable region can utilize an equivalent amount of stored energy to autonomously increase volume and achieve the buckled stable position. Further improvements to the model will be possible through better approximations of the volume in the different states, of the volume throughout the state transition and by incorporating the effect of the material of the tube into the model.

Chapter 06

Multi-segment inflatable tubes

6.1 Bistable structure design

The buckling and unbuckling behaviors of the inflatable tubes presented in the last chapter can be used to produce a bistable equilibrium as the system alternates between two states where only one segment is unbuckled. This can be achieved by connecting two inflatable tubes in series with a fixed total length D that is shorter than the total length of two inflated tubes $4l$, pressurizing them to similar pressures, and allowing the connection point between the two tubes to slide freely (Fig. 6-1). This sliding connection point allows them to find a stable position with one side tube unbuckled from the unstable equilibrium, while the total compression , which will be the difference between the length of the system and the entire length of two inflated tubes, should ideally be equally distributed to two tubes.

The system length can have a bistable equilibrium within a certain range, which can be viewed from two perspectives: either both tubes are in their bistable region and can be unbuckled when equally compressed, or both tubes are in their buckled region and must be buckled (Fig. 6-1a). In the first case, since one of the unbuckled tubes should be able to contract after its snap-through buckling, the below condition can indicate the minimum compression range for the system to achieve a bistable equilibrium.

$$C > \frac{B_1 + S_1}{2} \tag{6-1}$$

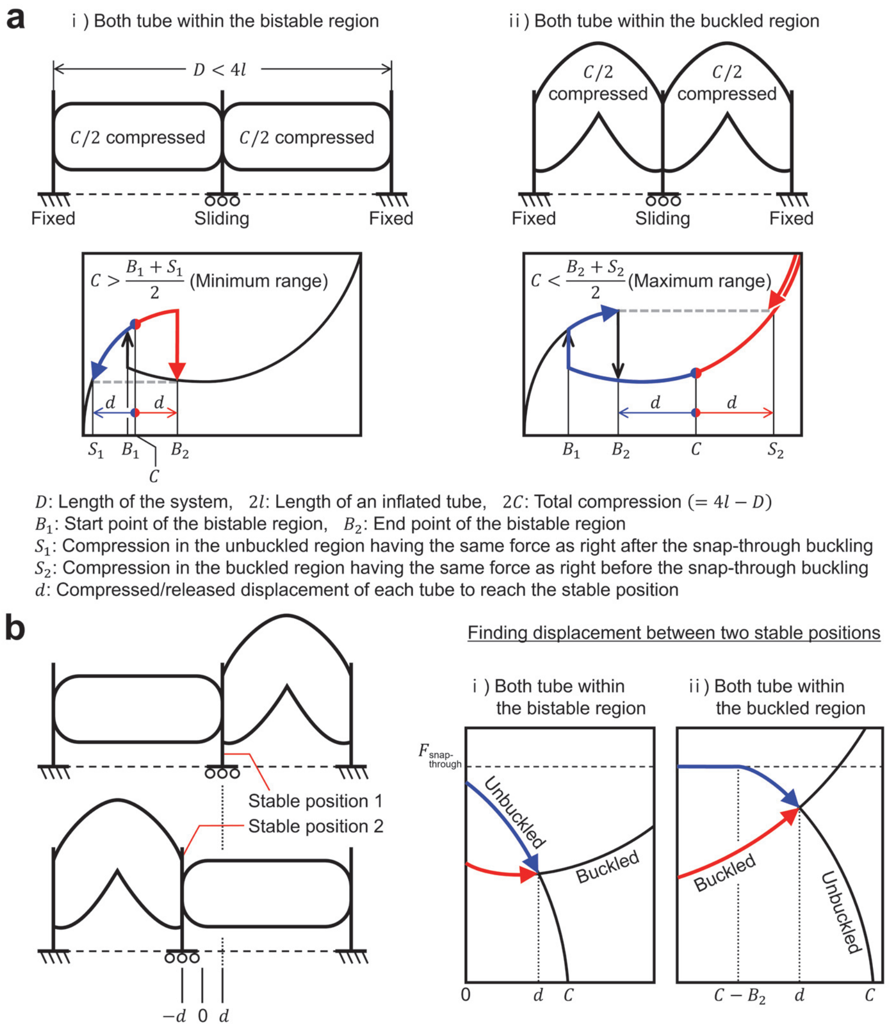

D: Length of the system, $2l$: Length of an inflated tube, $2C$: Total compression $(= 4l - D)$
B_1: Start point of the bistable region, B_2: End point of the bistable region
S_1: Compression in the unbuckled region having the same force as right after the snap-through buckling
S_2: Compression in the buckled region having the same force as right before the snap-through buckling
d: Compressed/released displacement of each tube to reach the stable position

Figure 6-1. Conditions for the bistable structure and its performance.

Where B_1 is the start point of the bistable region, and S_1 is the point within the unbuckled region where the tube produces the same force as right after the snap-through buckling.

In the second case, since the force of the buckled tube cannot be larger than the peak force at the snap-through buckling of the unbuckled tube at the opposite side to maintain their available force equilibrium, the maximum compression range can be indicated by the following condition.

1
2
3
4
5
6
7

$$C < \frac{B_2 + S_2}{2} \tag{6-2}$$

Where B_2 is the end point of the bistable region, and S_2 is the point within the buckled region where the tube produces the same force as right before the snap-through buckling.

The above interpretation took into account a displacement d representing the compressed amount of the tube to be buckled and at the same time the released amounts of the other tube to be unbuckled. This displacement can be found by finding the intersection point of two force plots, one for the unbuckled and one for the buckled tube, for each case where both tubes are compressed within their bistable or buckled region in the structure. Then, the total displacement 2d of both tubes indicates the available displacement of the connection point between two stable positions (Fig. 6-1b).

6.2 Bi-stability configurations

The configuration formed by the pressures of both tubes can be explained by adding the behavior of two individual tubes analyzed in the previous chapter. Each force plot can be offset, reversed, and applied with opposite signs. The first configuration heretofore mentioned having bistability can be accomplished when both tubes are pressurized to the same pressure (Fig. 6-2). In this bistable configuration, the transition between two stable positions can occur through manually pushing on the connection point from one stable state until it moves to the other stable state. Depending on the direction of the compression, one force follows the buckled path of the model until it reaches the unbuckling deformation and the other follows the unbuckled path of the model until it reaches the buckling deformation (Fig. 6-2a). The sum of these two force plots produces a plot that is symmetric throughout the displacement and direction of the compression and implies the system reverses its stable position to the opposite side once it reaches a given point (Fig. 6-2b).

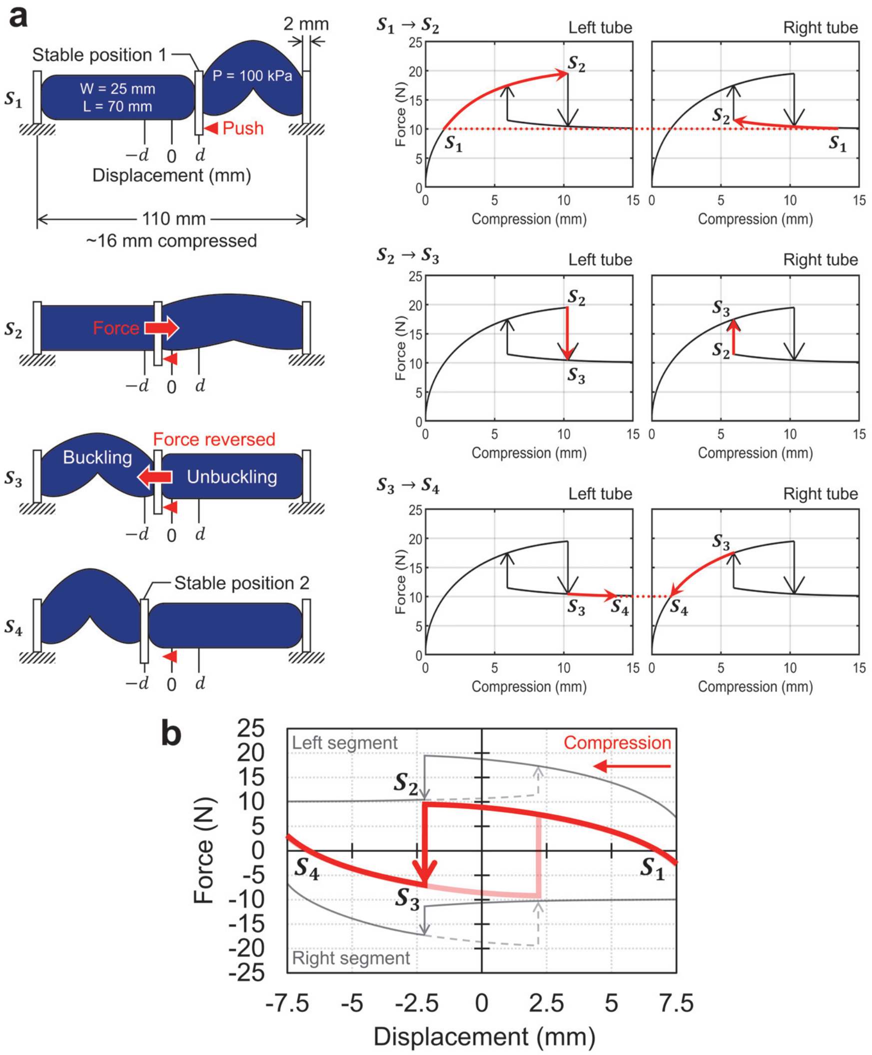

Figure 6-2. Bistable configuration of the bistable structure.

The second configuration results in being monostable when sufficiently increasing the pressure in one of the tubes, and it can move the connection point to the other side without affecting external interaction (Fig. 6-3). This can also be explained in a similar way by using two force plots, but with a plot scaled as the pressure increases (Fig. 6-3a). As the pressure of the buckled tube increases, it produces a higher force while maintaining equilibrium with the unbuckled tube. When the buckled tube is pressurized at even higher pressure to always produce a larger force than the peak force of the unbuckled tube at its snap-through buckling, the system converses into

1
2
3
4
5
6
7

the monostable configuration, and its connection point can only be located in one position. The sum of two force plots produces a plot with a single signed force (Fig. 6-3b). This results in a system that tends to return to a single stable position after being deformed and is thus monostable.

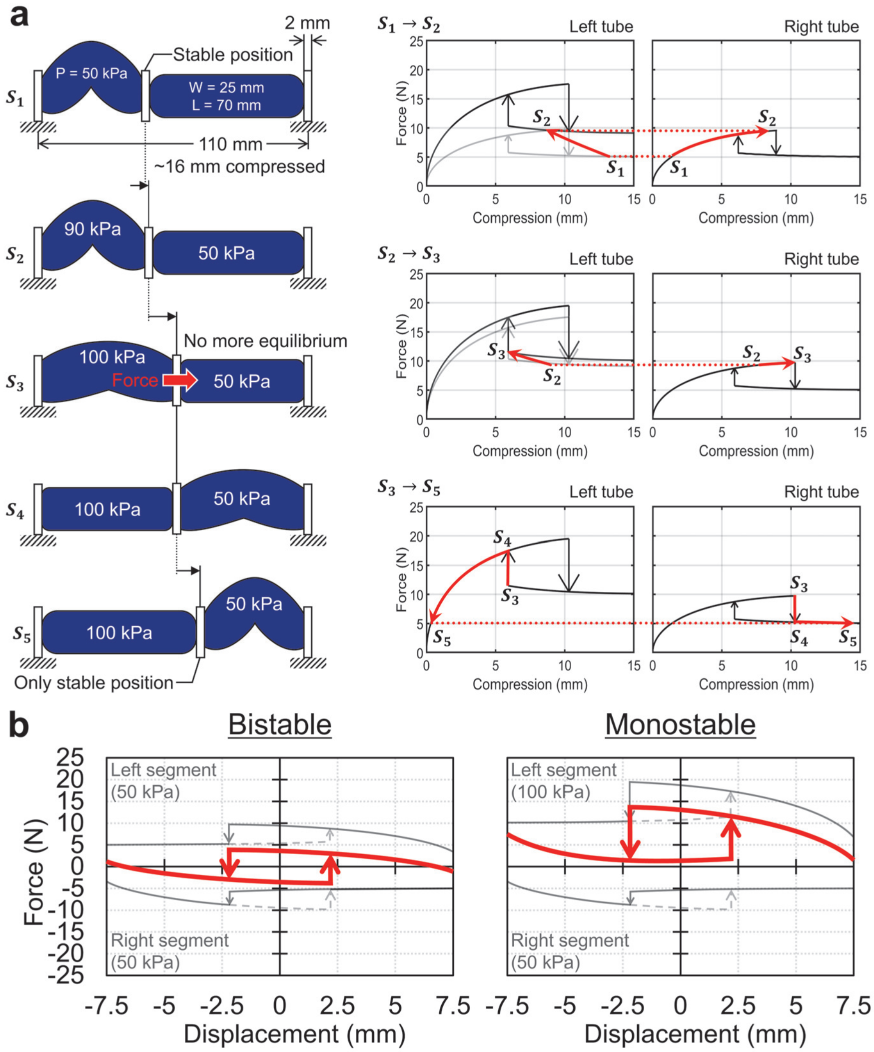

Figure 6-3. Monostable configuration of the bistable structure.

The force required to change between two stable positions of the bistable configuration, where the structure contains a two-segment tube whose segments were completely separated and fully sealed. They were designed with widths of 25 mm and lengths of 70 mm, was evaluated by pushing on the connection point using a 3D-printed tip connected to a force/torque sensor (RFT40, Robotous) (Fig. 6-4a). Three of the 3D-printed partitions to which the tube is connected were fixed onto a speed guide (SSR253A, Slide Korea), where two partitions at both ends are completely fixed not to move and the middle partition on the connection point between two segments can freely slide on the rail. A laser type displacement sensor (LK-G150, Keyence) was used to measure the position, and the speed during transition was approximated from the position measurements as a function of time. Each test was repeated 5 times at each pressure of 25, 50, 100, and 150 kPa (Fig. 6-4b).

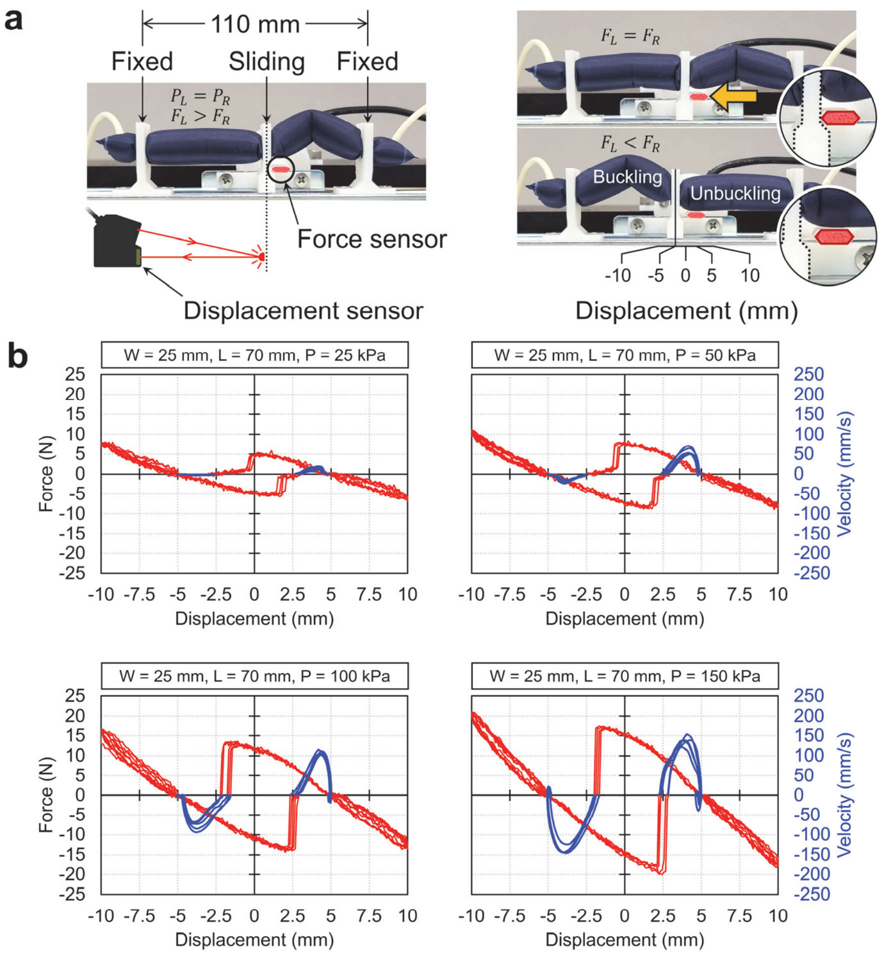

Figure 6-4. Force requirement for the transition of the bistable structure and the speed of the transition.

Pushing from a stable position towards the other stable position requires a gradually increasing force as the unbuckled tube is being compressed which then suddenly drops as the unbuckled tube buckles. After this buckling, the connection point moves to the other stable state. This happens quickly at higher pressures and the maximum speed reached by the connection point is 150 mm/s at a pressure of 150 kPa. However, at lower pressures, small additional forces are required after the unbuckling of the tube being extended to make the connection point to move to the other stable state possibly due to friction in the system. Further increasing the pressure could increase the transition speed between the stable states. When comparing the experimental result to the modeling prediction, there is little error in the location of the equilibrium position and the change in stability.

If the pressure of an initially buckled tube in a bistable system is increased, the current stable state of the system ceases to exist, and a rapid displacement occurs due to the snap-through instability as the bistable system transitions into the monostable system. The predicted pressure required to make the system monostable from the modeling is slightly lower than that verified experimentally, but the model was able to correctly predict that the system can become monostable. Alternatively, the pressure in the unbuckled tube could be reduced to produce a similar instability but with a much slower motion. Starting with equal pressures in both segments, sufficiently lowering the pressure of the unbuckled segment moves the connection point slowly to the other equilibrium towards the deflated segment (Fig. 6-5).

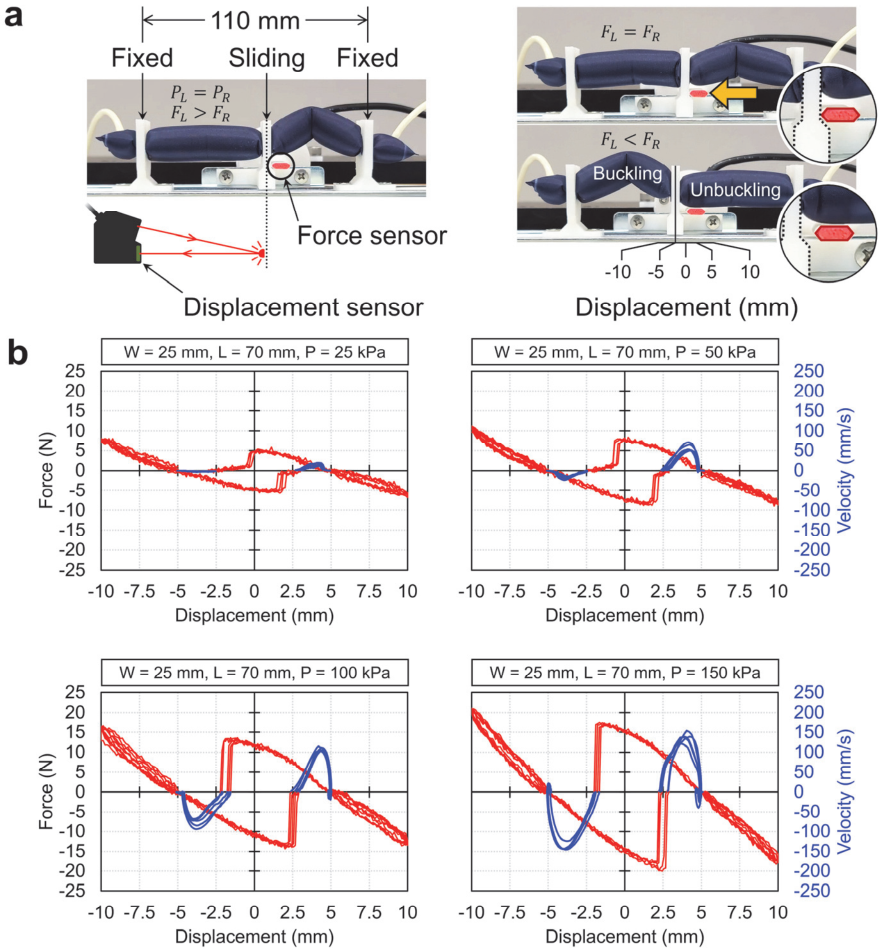

Figure 6-5. High- and low-speed actuation of the bistable structure.

In detail, by starting from an initial pressure of 5 kPa in both chambers and cutting off the pressure in the unbuckled segment, the slowest motion speed of 130 mm/s could be implemented (Fig. 6-6a). Inversely, starting with equal pressures but with a higher level in both segments and making the buckled segment reach a much higher pressure until its force is larger than the unbuckled one can produce a faster motion. It is to be noted that the pressures can be changed simultaneously to change the starting pressures. Starting from equal pressures of 50 kPa and increasing the pressure in the buckled segment to 130 kPa results in a fast motion reaching up to 600 mm/s which oscillates around the equilibrium point (Fig. 6-6e). It can also be seen that the speed is initially slow until the buckling of the unbuckled tube occurs and then accelerates rapidly.

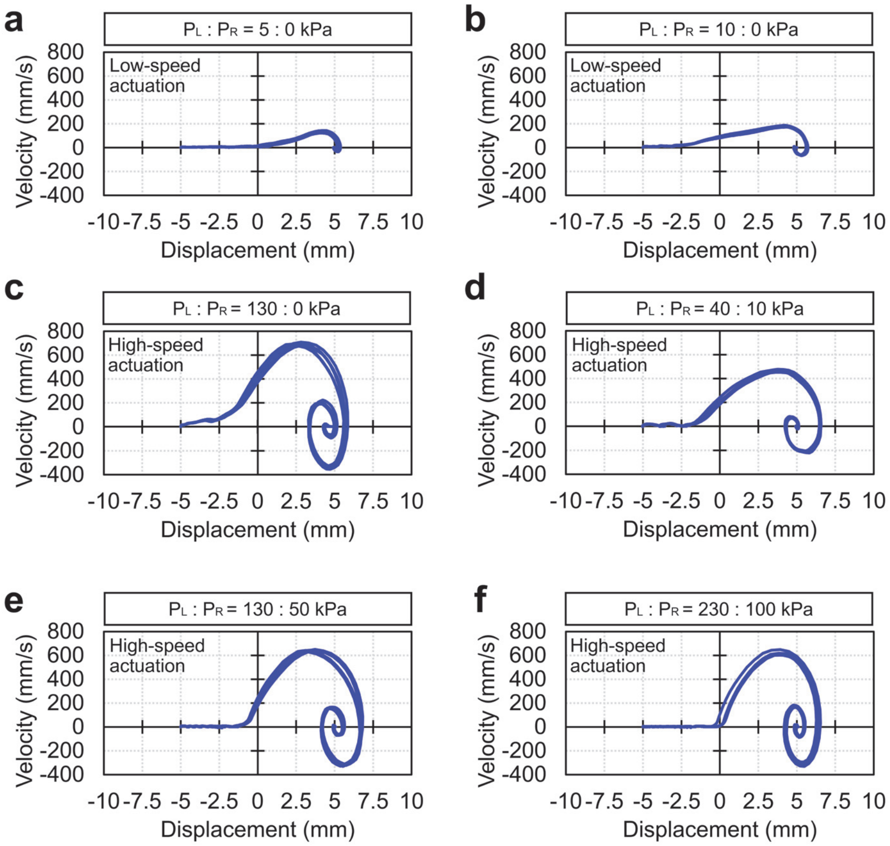

Figure 6-6. Actuation speed variation using different pressure combinations.

There are other pressure combinations to produce intermediate or similar speeds suggested. By starting with initial pressures of 10 kPa, the speed of the actuation can be selected by either cutting off the pressure of the unbuckled segment or increasing the pressure of the buckled segment (Fig. 6-6b, d). The low-speed actuation by cutting off the pressure to the unbuckled tube produces a maximum speed of close to 200 mm/s, slightly faster motion than the case with initial pressures of 5 kPa (Fig. 6-6a) and indicates a slight overshoot of the equilibrium point compared to the slowest motion (Fig. 6-6b). Then, the high-speed actuation by increasing the pressure of the buckled tube up to 40 kPa produces a maximum speed of close to 450 mm/s (Fig. 6-6d). By starting with initial pressures of 130 kPa, cutting off the pressure to the unbuckled tube produces a maximum speed of over 600 mm/s (Fig. 6-6c). It did not show a significant increase compared to the other case of finishing one of the tubes pressurized up to

130 kPa (Fig. 6-6e), but this speed would also depend on how fast air can be taken out of the tube being deflated. The high-speed actuation appears to have a limit in maximum velocity as starting from a higher pressure shortens the time required to reach the maximum velocity but results in a similar maximum velocity and overshoot behavior (Fig. 6-6f).

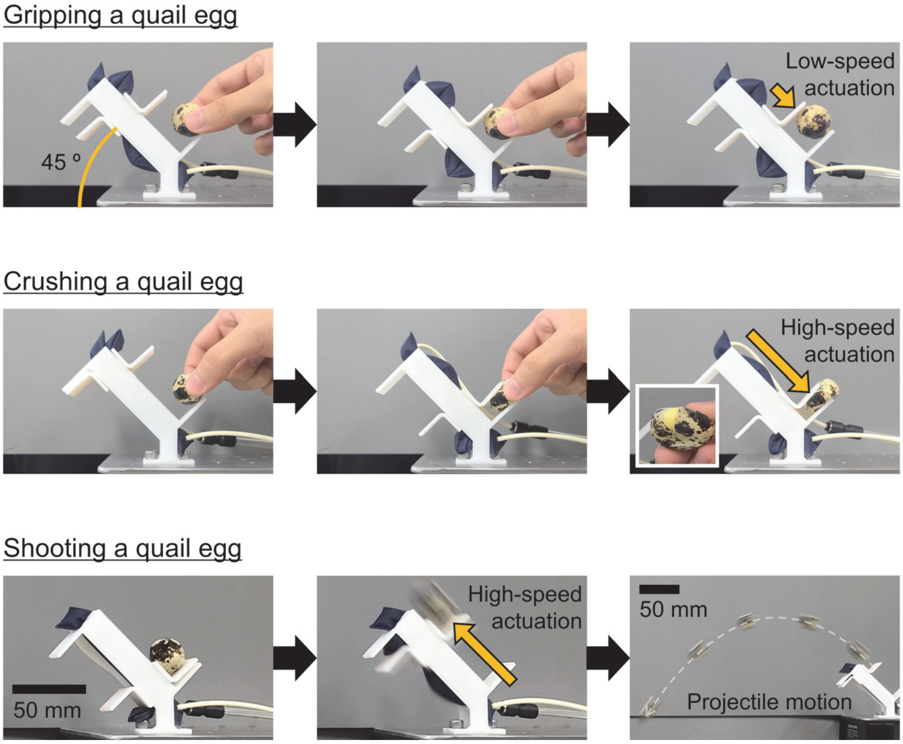

Figure 6-7. Multi-purpose gadget using the speed configuration of the bistable structure.

To visualize what this rapid and slow motions of the bistable structure entail in terms of dynamics, a multi-purpose gadget was built that makes use of this mechanism to control the motion of two jaws that move on a plane angled at an angle of 45° (Fig. 6-7). A cooked 11 g quail egg, which is light and fragile, was used as an object for the gadget to interact with. The effects of slow and fast transitions from the bistable state with the jaws far apart to the closing of the jaws in the monostable state for grasping this egg were tested. First, transitioning from equal pressures of 5 kPa to 0 kPa in the unbuckled segment results in a slow transition and the jaws of the gadget gently grasping the quail egg. Second, transitioning from equal pressures of 50 kPa to 130 kPa in the buckled segment results in the jaw rapidly moving towards the quail egg and crushing it. Third, the egg was set on top of the jaw in the closed position and a rapid transition to the other stable state was done which catapulted it into a parabolic trajectory.

By generalizing the definition of the bistable region of inflatable tubes with given length and width and analyzing the force flow throughout compression in the previous chapter, a bistable structure design, enabling interaction between buckling and unbuckling from two inflatable tubes connected in series, was successfully suggested. However, the presented model could not prove the speed produced by the buckling and unbuckling tubes as the model was designed throughout the compression displacement without any time variables. Though it was possible to validate the ability to convert stability of this bistable structure by adding the behavior of two individual inflatable tubes where one sustains the force plot and the other keeps increasing the force as pressure increases. The pressure only affects proportionally the magnitude of the force of the tube while the general behavior remains the same.

6.3 Bending actuator design

As an inflated tube requires a compressive force to be deformed from its equilibrium point, it follows that the tube can make an extensive force to return to this equilibrium point which can be used for soft actuation if it is coupled with a constraint that produces an antagonistic force. The constraint would then define the shape of the actuator before inflation of the tube and the inflation of the tube would deform the constraint. If this constraint has a flexible but inextensible bottom layer and vertical partitions with holes for integrating the inflatable tube, the height of the tube from the bottom layer H is basically larger than the radius of the inflated tube, and the distance between these partitions D is shorter than the length of the inflated tube , then the bottom layer acts as a strain-limiting layer and forms an arc as the initially buckled tube inflates and pushes the partitions apart, returning to its unbuckled state. This results in the entire system performing a bending actuation (Fig. 6-8a).

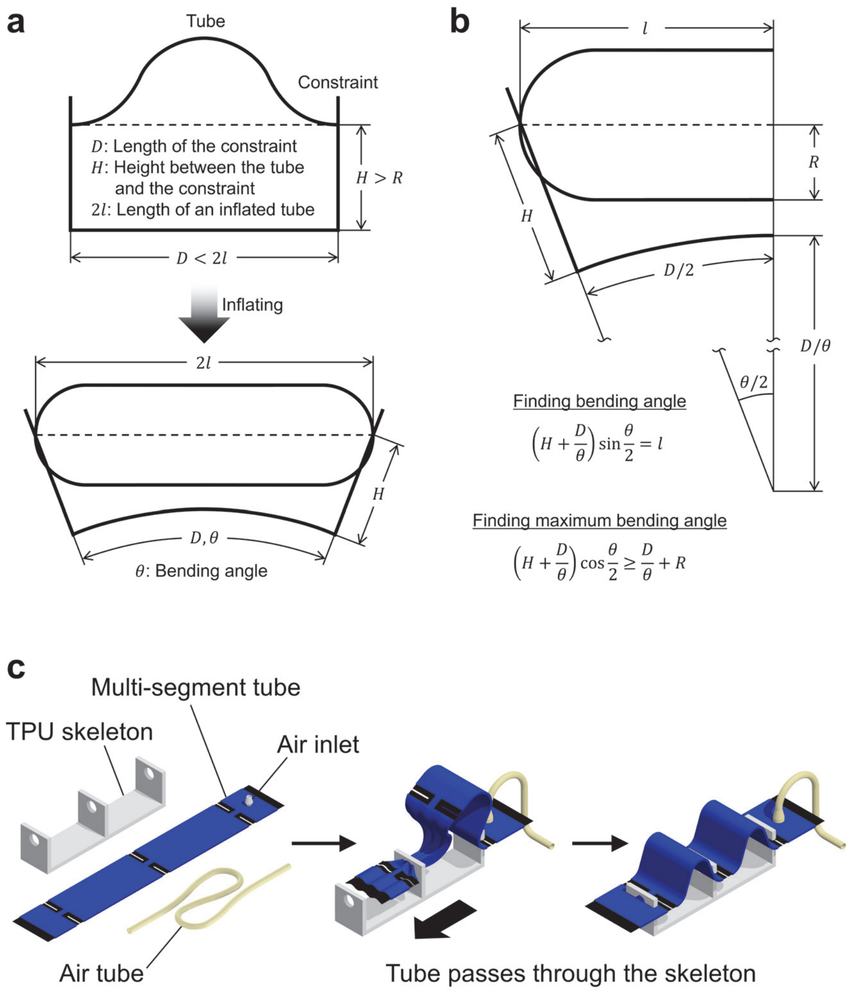

Figure 6-8. Conditions for the bending actuator and its performance.

The length of the structure, the height of the tube from the bottom layer, and the tube's length and width can determine the output bending angle of the entire system θ when the tube is inflated (Fig. 6-8b). Assuming the partitions are perpendicular to the bottom layer and the bottom layer forms a complete arc, the following equation in terms of the length of the inflated tube and the length of the curved constraint can define the output bending angle.

$$\left(H+\frac{D}{\theta}\right)\sin\frac{\theta}{2}=l \tag{6-3}$$

Additionally, the achievable maximum bending angle can be suggested by the following condition, which takes into account the curvature limitation of the constraint where its bottom layer is attached to the surface of the inflated tube.

$$\left(H+\frac{D}{\theta}\right)\cos\frac{\theta}{2}\geq\frac{D}{\theta}+R \tag{6-4}$$

The bending angle calculated above is for a single segment of the tube, thus it can be extended by duplicating the pattern of the constraint in series and integrating it with a multi-segment tube. In this study, the constraint was 3D-printed with TPU filament, and the multi-segment tube was integrated by passing it through the holes on each partition (Fig. 6-8c).

6.4 Multi-segment tube buckling

Connecting multiple inflatable tubes in series can generate interesting nonlinear compressive behaviors. To demonstrate these behaviors, a two-segment tube under axial compression will be analyzed with two force plots based on a model with a tube length of 70 mm, a width of 25 mm, and pressurized to 100 kPa. While the two-segment tube is compressed, both segments initially compress equally and produce an equal force such that the compression displacement of each segment is equal to half of the total compression (Fig. 6-9). When the two-segment tube reaches the force required for buckling of a single-segment, equal forces for each segment are found such that the sum of the lengths of a buckled tube and an unbuckled tube is equal to the corresponding total length. The displacement then increases while finding tube lengths with equal forces such that the sum of their lengths is equal to the current total length. The force then increases with the displacement until the force required to buckle the second segment is reached. Afterwards, both tubes are buckled and have an equal length and force.

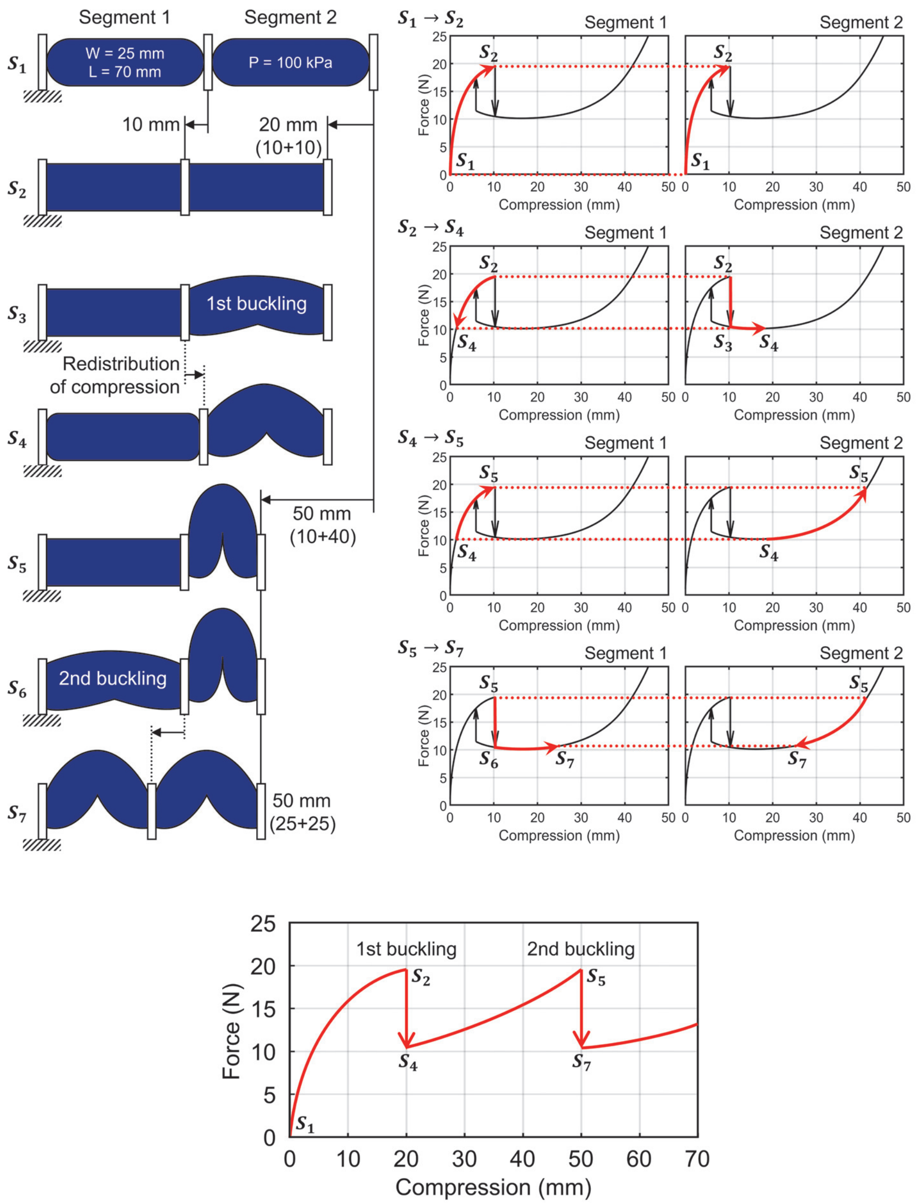

Figure 6-9. Axial compressive force of a two-segment tube during compression progression.

The release of both buckled tubes follows a similar process whereby both tubes have an equal force and length until they reach the point where one tube unbuckles (Fig. 6-10). The other tube remains buckled with an equal force but at a different length until it also unbuckles and both segments again have an equal length.

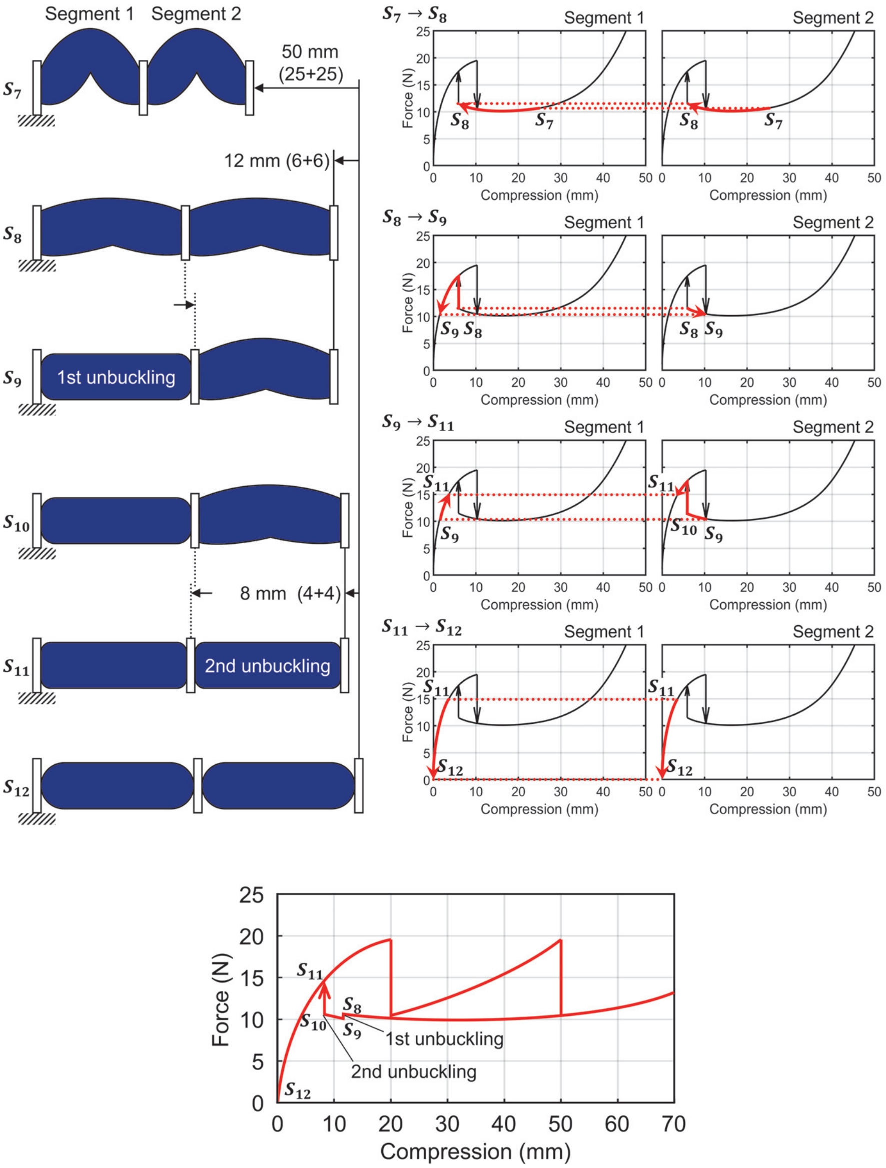

Figure 6-10. Axial compressive force of a two-segment tube during compression release.

In general, serially connected springs distribute the overall displacement uniformly among each spring, and the multi-segment tube also distributes the displacement equally amongst each segment in the early portion of the deformation. However, once a certain displacement is reached, then one of the segments will buckle and compress while the other segments will extend slightly. This is because all segments should produce an equal force to be at equilibrium and that the buckled tubes need to compress significantly more to produce a force equal to that of the unbuckled tubes. These results can be explained by the nonlinear behavior of the buckling tube explained in the previous section where the maximum force required to compress the tube is in the early part of the deformation. Once one of the segment buckles, its length decreases while the length of the other segment increases slightly as the compressive forces even out. Further compression again compresses all the tubes until the buckling force is reached for another tube, and this process repeats until the buckling force is reached for all tubes. While extending, the force gradually decreases with only a very slight peak in force once all segments unbuckle. It can be noticed that the order in which the segments buckle appears randomly and can be attributed to slight errors during manufacturing, but the order remains the same through repeated compression and extension cycles. In theory, simultaneous buckling of all elements should be possible, but is highly unlikely in practice due to slight errors in manufacturing and assembly. This kind of nonlinear behavior is different from other elastic compressive structures and could be engineered to obtain complex engineering behaviors by mixing linear elements such as springs with nonlinear buckling tube elements of different lengths or widths. Another advantage of this concept is that the force during the extension is relatively steady until reaching close to the fully extended point.

A three-segment tube whose segments have 70 mm lengths and 25 mm widths were fabricated and tested to demonstrate the mentioned behaviors (Fig. 6-11). The test was done by using a linear stage on which a force/torque sensor (RFT40, Robotous) was installed, an LM guide rail, and slidable 3D-printed PLA partitions for attaching the tube. The linear stage performs a single-axis movement by using a stepping motor (A16K-M569W, Autonics). The partitions have a hole that enables the connection point between successive segments to be fixed to the apparatus. The sliding partitions can move smoothly along the rail using ball bearings located at their base. A fixed partition is located at one end while the other end has a partition combined with the sensor and fixed to the linear stage. The intermediary partitions are placed on sliding blocks fixed to the LM guide. Each test was repeated 5 times at a pressure of 100 kPa and a linear speed of 1 mm/s. Comparing the modeling result with the experimental result shows almost the same location of the displacements required for buckling and a small difference in the magnitude of the force during the compression release. Therefore, it shows the model can capture the general behavior of the multi-segment tube under compression quite accurately.

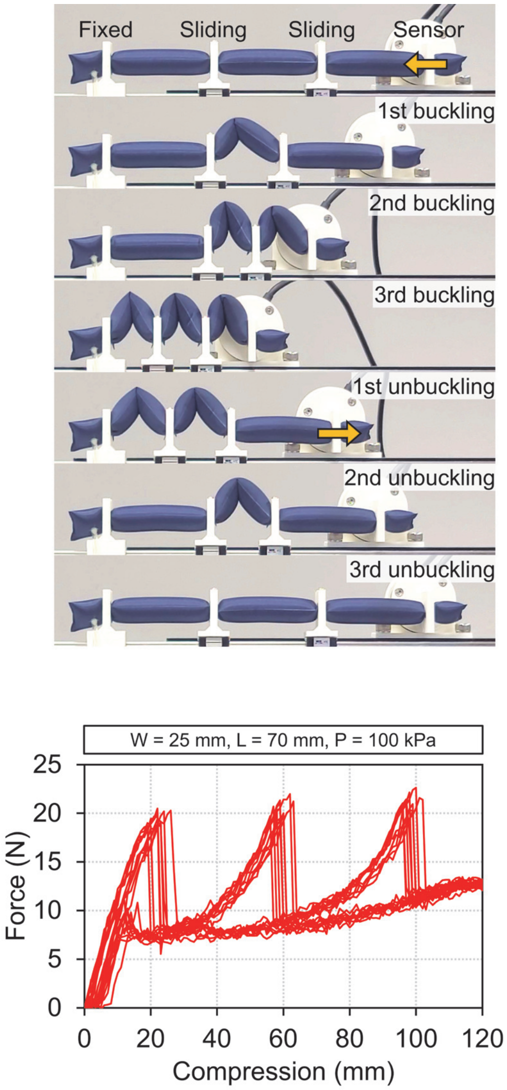

Figure 6-11. Axial compressive force of a three-segment tube.

Since the forces presented above are axial compressive forces, the bending force will not be exactly the same. However, this analysis can still be used to explain how the soft bending actuator stemming the nonlinear behavior of the multi-segment tube exhibits a self-stiffening property. Self-stiffening behavior means that its maximum stiffness occurs when the actuator is allowed to fully bend before loading, as it requires a significantly higher force to buckle the tube than to straighten it. To understand this behavior, two different loading cases with the same payload were compared (Fig. 6-12).

In the first case, an external load is applied to the actuator and the actuator is then pressurized, which results in all inflatable segments being buckled prior to actuation. In the second case, the actuator is inflated without a payload and the external load is then applied at the tip of the actuator, which results in all inflatable segments being unbuckled prior to loading. In the first case, the actuator must generate an extension force towards its unbuckled state but is limited by the force that the buckled tube can produce at a given pressure. In the second case, the actuator is fully unbuckled and can withstand larger forces due to the large force required to reach the buckling point of the unbuckled tube. Compared to general soft bending pneumatic actuators, this type of self-stiffening behavior once fully extended is rather unique and is solely a result of the nonlinear properties of the unbuckling inflatable tubes used to make the actuator.

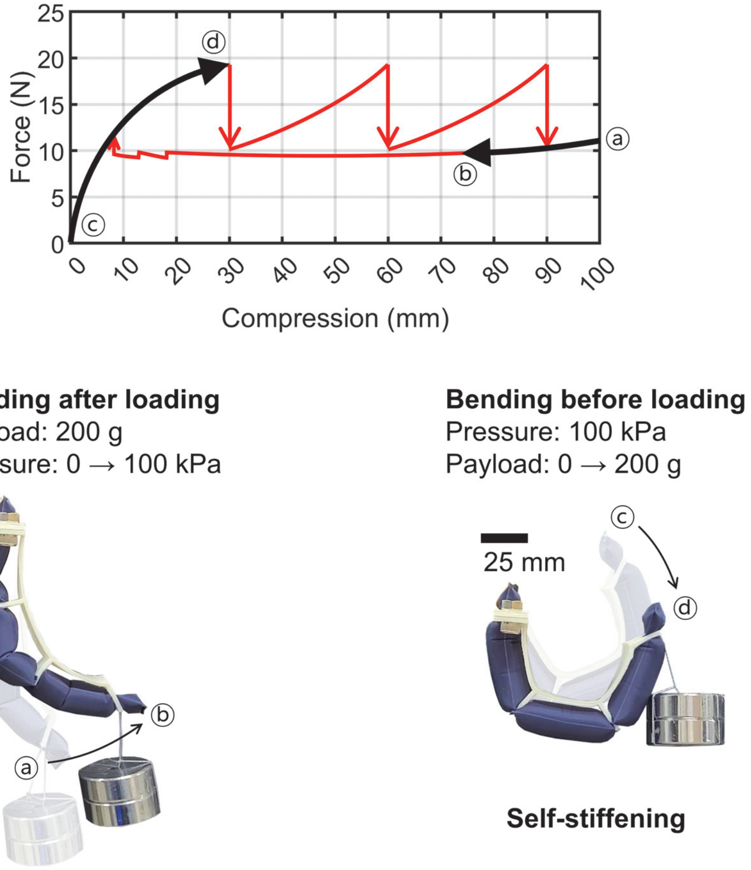

Figure 6-12. Self-stiffening behavior in a multi-segment tube-based bending.

6.5 Inflatable tube grippers

Six of the designed bending actuators were assembled on a 3D-printed rigid palm to form a human-inspired soft robotic hand whose four fingers have three-segment tubes each, and the thumb has a two-segment tube and an additional single-segment tube in the palm. Each finger contains a string tendon that starts with a spring inserted in a 3D-printed forearm frame and passes through the skeleton below the tube to reposition the finger straight after deflating the tubes (Fig. 6-13a). This human-inspired soft robotic hand weighs 68.6 g and can independently control each of its fingers and change its thumb position by varying the pressure of the single-chamber tube at its base, so that the hand can do pinching motions with every finger and also gain the diversity of hand movements (Fig. 6-13b).

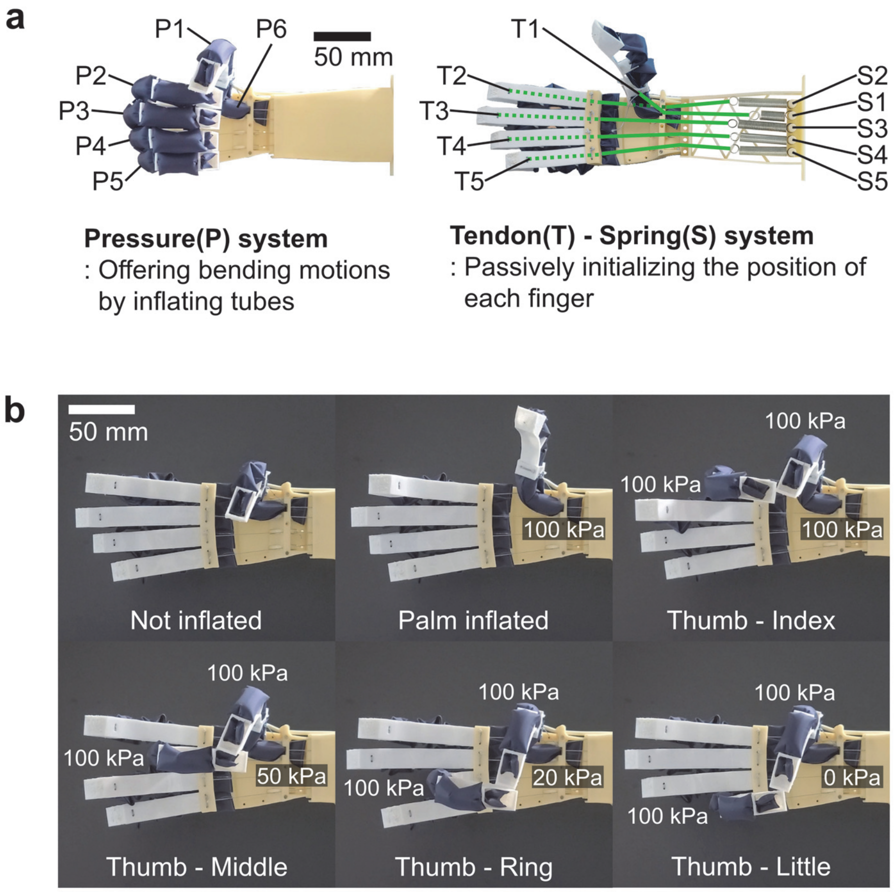

Pressure(P) system
: Offering bending motions by inflating tubes

Tendon(T) - Spring(S) system
: Passively initializing the position of each finger

Figure 6-13. Multi-segment tubes-based anthropomorphic gripper.

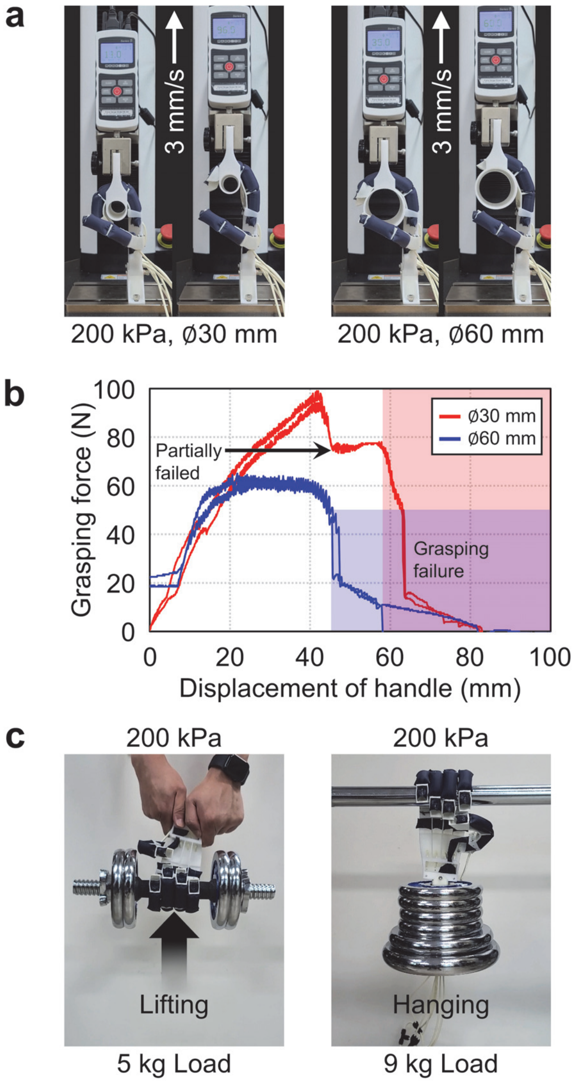

Figure 6-14. Pulling forces of the anthropomorphic gripper to different diameters.

Two characteristics of the finger actuator based on a multi-segment tube make it an interesting choice for a soft robotic hand. First, once allowed to fully unfold, the self-stiffening behavior of the unbuckled tubes allows them to require significant force to deform. Using this property, the soft robotic hand can be used to hold heavy objects. The self-stiffening property of the robotic hand was verified by measuring the grasping force with a pressure of 200 kPa holding a cylindrical handle moving at a rate of 3 mm/s by using a tensile testing machine equipped with a force gauge (M5-300, MARK-10). If the hand holds a handle that is smaller than the maximum curvature of the fingers, then the tubes can fully unbuckle, and the hand would require a large pulling force to buckle the tubes. However, if the handle is larger than the maximum curvature of the fingers then the tubes cannot unbuckle, and the hand requires a smaller force to unbend (Fig. 6-14a, b). With handle diameters of 30 and 60 mm, the maximum pulling force was measured at 99 and 65 N, respectively, which demonstrates the ability of the hand to self-stiffen if able to fully bend before loading. These results were validated by using the hand to lift a dumbbell with a weight of 5 kg and by hanging the hand vertically onto a bar and attaching a payload of 9 kg to the hand (Fig. 6-14c). This kind of stiffening behavior is similar to how humans stiffen their hands when hanging onto bars or holding heavy objects.

Second, the force generated by the buckled inflatable tube throughout its extension does not significantly decrease, such that the force produced by the finger at larger bending angles is similar to that produced in the nearly straight configuration. This allows the robotic hand to interact with various types of objects by adjusting the pressure for producing behaviors such as pinching a thin object like a flower or a sticky note, grasping a baseball, holding a glass that is being filled with juice, pulling the trigger of a water sprayer, or clicking a retractable pen (Fig. 6-15).

The behavior of buckling inflatable tubes presents a few properties which can be useful in robotic applications. They produce a relatively steady force during extension from the buckled state even with multiple inflatable tubes connected in series, which is useful as an extending actuator capable of producing a relatively constant force throughout the entire stroke. Also, the maximum force required to compress the tube occurs close to the fully extended position due to the buckling process and corresponds to the position where the actuator would settle in the absence of an external force. This behavior can be used for producing a self-stiffening behavior where the actuator requires a larger force to be deformed from the fully extended configuration than it can produce to reach the same configuration. The payload-to-weight ratio of the developed soft robotic gripper is 131.2. This value is larger than the highest ratio payload-to-weight ratios of 3.8 and 18.1 for surveyed pneumatic soft robotic anthropomorphic hands.

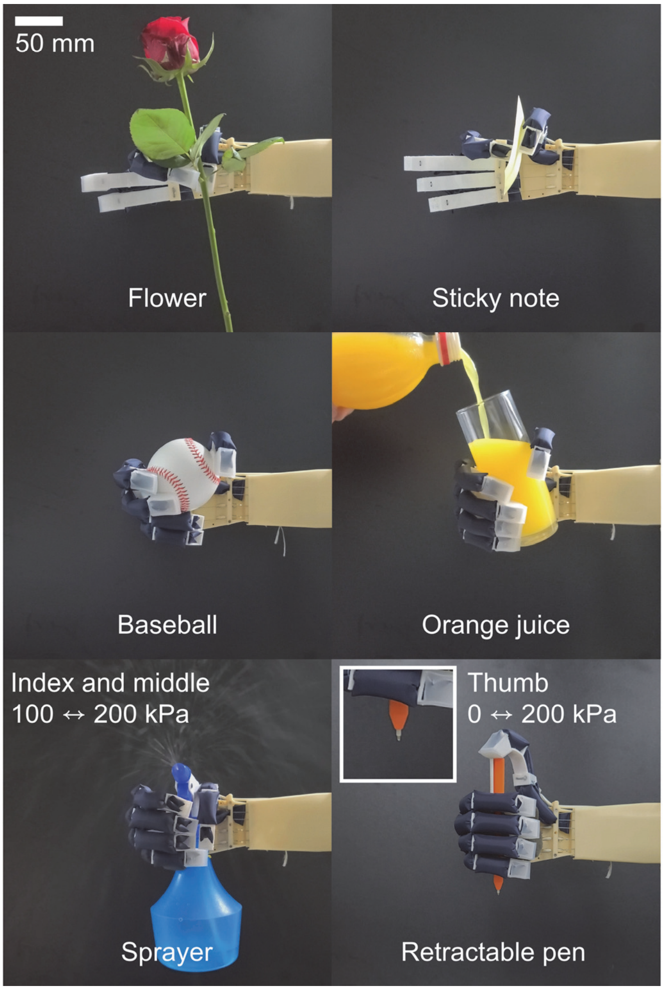

Figure 6-15. Interaction of the anthropomorphic gripper with various objects

Chapter 07

Conclusion

This book explores recent advances in the development of inflatable robots and actuators. Inflatable structures are distinguished by their use of non-stretchable, flexible thin materials that are pressurized. This unique characteristic means their deformation does not depend on material stretching, nor do they possess elastic forces that enable them to naturally return to their original shape. This poses several design constraints that should be considered when designing inflatable actuators and robots.

The first topic covered by this book is the development of vacuum-based actuators relying on a combination of films and rigid elements to guide the deformation through the creation of a negative pressure differential. The combination of flexible and non-stretchable elements which rigid elements allow for a highly engineered structure which produces a highly efficient deformation with nearly a 100% transmission ratio between fluidic and mechanical works. This means that they are highly scalable, can produce a large force throughout their entire range of contraction, and have the highest contraction ratios amongst soft actuators. This demonstrates that the use of inflatable concepts in soft robotics can lead to highly efficient and functional structures.

The second topic covered by this book is the development of inflatable robotic arms. It is demonstrated that multiple inflatable pouches can be maintained in equilibrium by using rigid constraints to form an inflatable robotic joint that can be controller through the balance of pressure in the inflatable chambers. Joints with 1 and 2 DOFs are presented and integrated into a robotic arm with 3 joints and a total of 6 DOFs which are tested in an antagonistic configuration for grasping misaligned boxes by using their natural compliance. This robotic arm was scaled to a length of 5 meters. A bidirectional torsional joint was then developed by using pre-twisted inflatable tubes with different pre-twisting directions assembled around a central shaft. This joint was then added onto the previously developed arm to form a 7 DOFs inflatable robotic arm capable of human-like twisting motions of its wrist. This chapter is a demonstration of how to use the equilibrium between multiple chambers to produce a controllable deformation despite the lack of elasticity of the chambers themselves.

The third topic covered by this book is the development of origami-like chambers for developing controllable robotic joints. These origami-like chambers have a defined deformation which follows a designed trajectory which allows them to be easily paired with a rigid joint to farm a hybrid hard-soft structure which harnesses the compliance of soft robots and the rigidity and precision of rigid robots. Single chamber joints using passive elastic elements to provide a return force and two chamber joints where both are used antagonistically were demonstrated to have a controllable motion, and these were implemented into an easily controllable robotic arm with 3 DOFs. This chapter demonstrates that using origami design can make the deformation of inflatable structures predictable and easier to control.

The fourth topic looks at the behavior of simple inflatable tubes under compression and uses the principle of conservation of energy coupled with the tendency of tubes to go to a local minimum pressure to explain their complex behavior. Predicting the behavior of inflatable tubes is not a new problem but previous solutions only focused on finding the buckling force of the tubes and could not predict their entire range of behavior and the deformation required to buckle and unbuckle them. The proposed numerical model can predict all of these behaviors and gives us a better understanding of the behavior of inflatable structures.

The fifth and last topic covered by this book is the use of serially connected inflatable tubes to produce complex robotic behaviors. The first of these behaviors is to form bistable linear structures by using the bistable buckled-unbuckled behavior of tubes and to trigger fast deformations by changing the system from a bistable system to a monostable system through increasing the pressure in one tube of the bistable system past a point that triggers snapthrough instabilities. The second of these behaviors is the development of bending actuators with a self-stiffening capability triggered when all tubes of the finger are allowed to fully unbuckle and then require a force sufficient to trigger the buckling snapthrough instability to deform. This makes the force required to deform the finger significantly larger when fully deformed than at any other point of the deformation and is in stark contrast with most soft robotic hands that produce

1
2
3
4
5
6
7

their largest force when undeformed and are very easy to deform at their largest deformation configuration. This chapter shows that simple inflatable structures can be used to produce complex robotic behaviors by harnessing their nonlinear behaviors.

This book delves into a comprehensive range of topics concerning inflatable structures, actuators, and robots, offering readers a broad overview of recent advancements in this exciting and rapidly evolving field. It serves as a valuable resource for understanding the key principles behind designing, manufacturing, implementing, and modeling these innovative systems. By addressing both foundational concepts and emerging technologies, this book provides insights that can guide researchers and engineers in overcoming the unique challenges posed by inflatable structures.

Looking ahead, the future of soft inflatable robots appears highly promising. Advancements are expected to enhance their controllability, enabling more precise and versatile motion capabilities. These improvements will allow inflatable robots to leverage their inherent compliance more effectively, particularly in applications requiring safe and adaptive interactions with humans, such as in healthcare, assistive devices, and collaborative workspaces.

Additionally, ongoing developments in pneumatic hardware are poised to significantly improve actuation speed and responsiveness, further expanding the functional potential of these systems. Parallel advancements in manufacturing techniques will likely lead to structures capable of withstanding higher pressures, enabling greater force generation and improved durability. These innovations are expected to increase the reliability and overall performance of inflatable robots, paving the way for broader adoption in diverse applications.

By combining advancements in design, hardware, and manufacturing, the field of inflatable robotics is poised to unlock new possibilities, driving forward the integration of these systems into everyday life.

References

[1] L. A. Geddes, A. G. Moore, W. A. Spencer, and H. E. Hoff, "Electro-pneumatic Control of the McKibben Synthetic Muscle," *J. Prosthet. Orthot.*, vol. 13, no. 1, pp. 33-36, 1959.

[2] B.k Tondu and P. Lopez, "Modeling and Control of McKibben Artificial Muscle Robot Actuators," *IEEE Control Syst.*, vol. 20, no. 2, pp. 15-38, 2000.

[3] K. Suzumori, S. Iikura, and H. Tanaka, "Flexible Microactuator for Miniature Robots," Nara, Japan, January 30 - February 2 1991, pp. 204-209.

[4] F. Ilievski, A. D. Mazzeo, R. F. Shepherd, X. Chen, and G. M. Whitesides, "Soft robotics for chemists," *Angew. Chem.*, vol. 50, no. 8, pp. 1890-1895, Feb. 2011.

[5] R. F. Shepherd *et al.*, "Multigait soft robot," *Proc. Natl. Acad. Sci. U.S.A.*, vol. 108, no. 51, pp. 20400-20403, Dec. 2011.

[6] B. Jamil, N. Oh, J.-G. Lee, H. Lee, and H. Rodrigue, "A Review and Comparison of Linear Pneumatic Artificial Muscles," vol. 11, pp. 277-289, 2024.

[7] J. Shintake, V. Cacucciolo, D. Floreano, and H. Shea, "Soft Robotic Grippers," *Adv. Mater.*, p. 1707035, May 7 2018.

[8] H. Rodrigue and J. Kim, "Soft actuators in surgical robotics: a state-of-the-art review," vol. 17, no. 1, pp. 3-17, 2024.

[9] R. K. Katzschmann, J. DelPreto, R. MacCurdy, and D. Rus, "Exploration of underwater life with an acoustically controlled soft robotic fish," *Sci. Robot.*, vol. 3, p. eaar3449, 2018.

[10] R. Niiyama, X. Sun, C. Sung, B. An, D. Rus, and S. Kim, "Pouch Motors: Printable Soft Actuators Integrated with Computational Design," *Soft Robot.*, vol. 2, no. 2, pp. 59-70, Jun. 2015.

[11] N. Oh, Y. J. Park, S. Lee, H. Lee, and H. Rodrigue, "Design of Paired Pouch Motors for Robotic Applications," *Adv. Mat. Tech.*, vol. 4, no. 1, p. 1800414, Jan. 2019, Art. no. 1800414.

[12] H. Lee, N. Oh, and H. Rodrigue, "Expanding Pouch Motor Patterns for Programmable Soft Bending Actuation: Enabling Soft Robotic System Adaptations," *IEEE Robot. Autom. Mag.*, vol. 27, no. 4, pp. 65-74, Dec. 2020.

[13] J. H. Jang, B. Jamil, Y. Moon, A. Coutinho, G. Park, and H. Rodrigue, "Design of Gusseted Pouch Motors for Improved Soft Pneumatic Actuation," pp. 1-11, 2023.

[14] A. D. Marchese, C. D. Onal, and D. Rus, "Autonomous soft robotic fish capable of escape maneuvers using fluidic elastomer actuators," vol. 1, no. 1, pp. 75-87, 2014.

[15] P. Polygerinos, Z. Wang, K. C. Galloway, R. J. Wood, and C. J. Walsh, "Soft robotic glove for combined assistance and at-home rehabilitation," *Robot. Auton. Syst.*, vol. 73, pp. 135-143, 2015.

[16] G. Udupa, P. Sreedharan, P. Sai Dinesh, and D. Kim, "Asymmetric bellow flexible pneumatic actuator for miniature robotic soft gripper," vol. 2014, 2014.

[17] N. Oh, J.-G. Lee, and H. Rodrigue, "Torsional Pneumatic Actuator Based on Pre-Twisted Pneumatic Tubes for Soft Robotic Manipulators," 2023.

[18] E. Sachyani Keneth *et al.*, "Pre-programmed tri-layer electro-thermal actuators composed of shape memory polymer and carbon nanotubes," vol. 7, no. 2, pp. 123-129, 2020.

[19] C. H. Ahn, W. Wang, J. Jung, and H. Rodrigue, "Pleated film-based soft twisting actuator," vol. 20, pp. 1149-1158, 2019.

[20] E. W. Hawkes, L. H. Blumenschein, J. D. Greer, and A. M. Okamura, "A soft robot that navigates its environment through growth," vol. 2, no. 8, 2017.

[21] G. Singh and G. Krishnan, "Designing fiber-reinforced soft actuators for planar curvilinear shape matching," vol. 7, no. 1, pp. 109-121, 2020.

[22] F. Connolly, P. Polygerinos, C. J. Walsh, and K. Bertoldi, "Mechanical Programming of Soft Actuators by Varying Fiber Angle," vol. 2, no. 1, pp. 26-32, 2015.

[23] H. Lee and H. Rodrigue, "Harnessing the nonlinear properties of buckling inflatable tubes for complex robotic behaviors," 2023.

[24] C. S. Haines *et al.*, "Artificial muscles from fishing line and sewing thread," vol. 343, no. 6173, pp. 868-872, 2014.

[25] R. A. Russell and R. B. Gorbet, "Improving the response of SMA actuators," vol. 3, pp. 2299-2304, 1995.

[26] J.-s. Koh, "Design of shape memory alloy coil spring actuator for improving performance in cyclic actuation," vol. 11, no. 11, p. 2324, 2018.

[27] S. M. Mirvakili *et al.*, "Simple and strong: twisted silver painted nylon artificial muscle actuated by Joule heating," vol. 9056, pp. 77-86, 2014.

[28] G. K. Klute, J. M. Czerniecki, and B. Hannaford, "McKibben artificial muscles: pneumatic actuators with biomechanical intelligence," pp. 221-226, 1999.

[29] T. Szepe and J. Sarosi, "Model based open looped position control of PAM actuator," pp. 607-609, 2010.

[30] X. Liu, A. Rosendo, S. Ikemoto, M. Shimizu, and K. Hosoda, "Robotic investigation on effect of stretch reflex and crossed inhibitory response on bipedal hopping," vol. 15, no. 140, p. 20180024, 2018.

[31] G. Miron and J.-S. Plante, "Design Principles for Improved Fatigue Life of High-Strain Pneumatic Artificial Muscles," vol. 3, no. 4, pp. 177-185, 2016.

[32] F. Daerden and D. Lefeber, "Pneumatic artificial muscles: actuators for robotics and automation," vol. 47, no. 1, pp. 11-22, 2002.

[33] R. Deimel and O. Brock, "A novel type of compliant and underactuated robotic hand for dexterous grasping," *Int. J. Rob. Res.*, vol. 35, no. 1-3, pp. 161-185, 2016.

[34] J. D. Greer, T. K. Morimoto, A. M. Okamura, and E. W. Hawkes, "Series pneumatic artificial muscles (sPAMs) and application to a soft continuum robot," Singapore, May 2017, pp. 5503-5510.

[35] R. V. Martinez, C. R. Fish, X. Chen, and G. M. Whitesides, "Elastomeric Origami: Programmable Paper‐Elastomer Composites as Pneumatic Actuators," vol. 22, no. 7, pp. 1376-1384, 2012.

[36] J. Yi, X. Chen, C. Song, and Z. Wang, "Fiber-reinforced origamic robotic actuator," vol. 5, no. 1, pp. 81-92, February 2018.

[37] M. A. Robertson and J. Paik, "New soft robots really suck: Vacuum-powered systems empower diverse capabilities," vol. 2, no. 9, p. eaan6357, 2017.

[38] M. S. Verma, A. Ainla, D. Yang, D. Harburg, and G. M. Whitesides, "A soft tube-climbing robot," vol. 5, no. 2, pp. 133-137, 2018.

[39] D.-Y. Lee, S.-R. Kim, J.-S. Kim, J.-J. Park, and K.-J. Cho, "Origami wheel transformer: A variable-diameter wheel drive robot using an origami structure," vol. 4, no. 2, pp. 163-180, 2017.

[40] J.-H. Youn *et al.*, "Dielectric elastomer actuator for soft robotics applications and challenges," vol. 10, no. 2, p. 640, 2020.

[41] R. Altmüller, R. Schwödiauer, R. Kaltseis, S. Bauer, and I. M. Graz, "Large area expansion of a soft dielectric membrane triggered by a liquid gaseous phase change," vol. 105, pp. 1-3, 2011.

[42] A. Miriyev, K. Stack, and H. Lipson, "Soft material for soft actuators," vol. 8, no. 1, p. 596, 2017.

[43] S.-W. Kim, J.-G. Lee, S. An, M. Cho, and K.-J. Cho, "A large-stroke shape memory alloy spring actuator using double-coil configuration," *Smart Mater. Struct.*, vol. 24, no. 9, p. 095014, 2015.

[44] S. Ruiz, B. Mead, V. Palmre, K. J. Kim, and W. Yim, "A cylindrical ionic polymer-metal composite-based robotic catheter platform: modeling, design and control," vol. 24, no. 1, p. 015007, 2014.

[45] J. J. Song, H. H. Chang, and H. E. Naguib, "Biocompatible shape memory polymer actuators with high force capabilities," vol. 67, pp. 186-198, 2015.

[46] T. Yukisawa, Y. Ishii, S. Nishikawa, R. Niiyama, and Y. Kuniyoshi, "Modeling of extensible pneumatic actuator with bellows (EPAB) for continuum arm," 2017, pp. 2303-2308.

[47] N. Tsagarakis and D. G. Caldwell, "Improved modelling and assessment of pneumatic muscle actuators," 2000, vol. 4, pp. 3641-3646.

[48] E. W. Hawkes, D. L. Christensen, and A. M. Okamura, "Design and implementation of a 300% strain soft artificial muscle," pp. 4022-4029, 2016.

[49] T. Yukisawa, Y. Ishii, S. Nishikawa, R. Niiyama, and Y. Kuniyoshi, "Modeling of extensible pneumatic actuator with bellows (EPAB) for continuum arm," pp. 2303-2308, 2017.

[50] R. V. Martinez, A. C. Glavan, C. Keplinger, A. I. Oyetibo, and G. M. Whitesides, "Soft actuators and robots that are resistant to mechanical damage," vol. 24, no. 20, pp. 3003-3010, 2014.

[51] K. Han, N.-H. Kim, and D. Shin, "A novel soft pneumatic artificial muscle with high-contraction ratio," vol. 5, no. 5, pp. 554-566, 2018.

[52] S. Li, D. M. Vogt, D. Rus, and R. J. Wood, "Fluid-driven origami-inspired artificial muscles," vol. 114, no. 50, pp. 13132-13137, 2017.

[53] C.-P. Chou and B. Hannaford, "Measurement and modeling of McKibben pneumatic artificial muscles," vol. 12, no. 1, pp. 90-102, 1996.

[54] D. Villegas, M. Van Damme, B. Vanderborght, P. Beyl, and D. Lefeber, "Third–Generation Pleated Pneumatic Artificial Muscles for Robotic Applications: Development and Comparison with McKibben Muscle," *Adv. Robot.*, vol. 26, no. 11-12, pp. 1205-1227, 2012.

[55] H.-C. Fu *et al.*, "Interfacing soft and hard: a spring reinforced actuator," vol. 7, no. 1, pp. 44-58, 2020.

[56] J. Huber, N. Fleck, and M. Ashby, "The selection of mechanical actuators based on performance indices," vol. 453, no. 1965, pp. 2185-2205, 1997.

[57] T. Li *et al.*, "Thermal actuation performance modification of coiled artificial muscle by controlling annealing stress," vol. 56, no. 5, pp. 383-390, 2017.

[58] J. Park *et al.*, "Electrically controllable twisted-coiled artificial muscle actuators using surface-modified polyester fibers," vol. 26, no. 3, p. 035048, 2017.

[59] D. Yang *et al.*, "Buckling pneumatic linear actuators inspired by muscle," vol. 1, no. 3, 2016.

[60] D. Yang *et al.*, "Buckling of elastomeric beams enables actuation of soft machines," 2015.

[61] D. Yang, M. S. Verma, E. G. Lossner, D. B. Stothers, and G. M. Whitesides, "Negative-pressure soft linear actuator with a mechanical advantage," 2016.

[62] C. T. Nguyen, H. Phung, T. D. Nguyen, H. Jung, and H. R. Choi, "Multiple-degrees-of-freedom dielectric elastomer actuators for soft printable hexapod robot," *Sens. Actuators*, A, vol. 267, pp. 505-516, 2017.

[63] F. Carpi, C. Salaris, and D. De Rossi, "Folded dielectric elastomer actuators," vol. 16, no. 2, p. S300, 2007.

[64] Z. Liu and P. Calvert, "Multilayer hydrogels as muscle‐like actuators," vol. 12, no. 4, pp. 288-291, 2000.

[65] L. M. Bellan, M. Pearsall, D. Cropek, and R. Langer, "A 3D interconnected microchannel network formed in gelatin by sacrificial shellac microfibers," vol. 24, no. 38, p. 5187, 2012.

[66] Z.-W. Yang and C.-C. Lan, "An adjustable gravity-balancing mechanism using planar extension and compression springs," vol. 92, pp. 314-329, 2015.

[67] R. Nathan, "A constant force generation mechanism," 1985.

[68] J.-Y. Wang and C.-C. Lan, "A constant-force compliant gripper for handling objects of various sizes," vol. 136, no. 7, p. 071008, 2014.

[69] K. A. Tolman, E. G. Merriam, and L. L. Howell, "Compliant constant-force linear-motion mechanism," vol. 106, pp. 68-79, 2016.

[70] G. Berselli, R. Vertechy, G. Vassura, and V. P. Castelli, "Design of a single-acting constant-force actuator based on dielectric elastomers," 2009.

[71] C. Zhang, P. Zhu, Y. Lin, Z. Jiao, and J. Zou, "Modular soft robotics: Modular units, connection mechanisms, and applications," vol. 2, no. 6, p. 1900166, 2020.

[72] S. Kurumaya *et al.*, "A modular soft robotic wrist for underwater manipulation," vol. 5, no. 4, pp. 399-409, 2018.

[73] J.-Y. Lee, J. Eom, W.-Y. Choi, and K.-J. Cho, "Soft LEGO: bottom-up design platform for soft robotics," pp. 7513-7520, 2018.

[74] J.-Y. Lee, W.-B. Kim, W.-Y. Choi, and K.-J. Cho, "Soft Robotic Blocks: Introducing SoBL, a Fast-Build Modularized Design Block," *IEEE Robot. Autom. Mag.*, vol. 23, no. 3, pp. 30-41, Sept. 2016.

[75] J. Zou, Y. Lin, C. Ji, and H. Yang, "A reconfigurable omnidirectional soft robot based on caterpillar locomotion," vol. 5, no. 2, pp. 164-174, 2018.

[76] J. Ogawa, T. Mori, Y. Watanabe, M. Kawakami, M. N. I. Shiblee, and H. Furukawa, "MORI-A: Soft vacuum-actuated module with 3D-printable deformation structure," vol. 7, no. 2, pp. 2495-2502, 2022.

[77] D. Trivedi, C. D. Rahn, W. M. Kier, and I. D. Walker, "Soft robotics: Biological inspiration, state of the art, and future research," vol. 5, no. 3, pp. 99-117, December 2008.

[78] Q. Guan, F. Stella, C. Della Santina, J. Leng, and J. Hughes, "Trimmed helicoids: an architectured soft structure yielding soft robots with high precision, large workspace, and compliant interactions," vol. 1, no. 4, pp. 1-13, October 2023.

[79] J. Hughes, U. Culha, F. Giardina, F. Guenther, A. Rosendo, and F. Iida, "Soft manipulators and grippers: A review," vol. 3, no. 69, pp. 1-12, November 2016.

[80] T. George Thuruthel, Y. Ansari, E. Falotico, and C. Laschi, "Control strategies for soft robotic manipulators: A survey," vol. 5, no. 2, pp. 149-163, April 2018.

[81] R. Kang, D. T. Branson, T. Zheng, E. Guglielmino, and D. G. Caldwell, "Design, modeling and control of a pneumatically actuated manipulator inspired by biological continuum structures," vol. 8, no. 3, p. 036008, July 2013.

[82] W. McMahan *et al.*, "Field trials and testing of the OctArm continuum manipulator," Orlando, FL, USA, May 2006, pp. 2336-2341.

[83] X. Chen, Y. Guo, D. Duanmu, J. Zhou, W. Zhang, and Z. Wang, "Design and modeling of an extensible soft robotic arm," vol. 4, no. 4, pp. 4208-4215, July 2019.

[84] H. Jiang *et al.*, "Hierarchical control of soft manipulators towards unstructured interactions," vol. 40, no. 1, pp. 411-434, 2021.

[85] C. Meng, W. Xu, H. Li, H. Zhang, and D. Xu, "A new design of cellular soft continuum manipulator based on beehive-inspired modular structure," vol. 14, no. 3, p. 1729881417707380, June 2017.

[86] T. Kalisky *et al.*, "Differential pressure control of 3D printed soft fluidic actuators," Vancouver, BC, Canada, September 2017, pp. 6207-6213.

[87] B. Jamil and Y. Choi, "Modified stiffness-based soft optical waveguide integrated pneumatic artificial muscle (PAM) actuators for contraction and force sensing," vol. 26, no. 6, pp. 3243-3253, February 2021.

[88] S. Kurumaya, H. Nabae, G. Endo, and K. Suzumori, "Exoskeleton inflatable robotic arm with thin McKibben muscle," Livorno, Italy, April 2018, pp. 120-125.

[89] P. Ohta *et al.*, "Design of a lightweight soft robotic arm using pneumatic artificial muscles and inflatable sleeves," vol. 5, no. 2, pp. 204-215, April 2018.

[90] T. Shin and K. Kogiso, "Sensorless angle and stiffness control of antagonistic PAM actuator using reference set," vol. 36, no. 9, pp. 423-437, March 2022.

[91] H.-J. Kim, A. Kawamura, Y. Nishioka, and S. Kawamura, "Mechanical design and control of inflatable robotic arms for high positioning accuracy," vol. 32, no. 2, pp. 89-104, January 2018.

[92] X. Liang, H. Cheong, Y. Sun, J. Guo, C. K. Chui, and C.-H. Yeow, "Design, Characterization, and Implementation of a Two-DOF Fabric-Based Soft Robotic Arm," *IEEE Robot. Autom. Lett.*, vol. 3, no. 3, pp. 2702-2709, 2018.

[93] B. Jamil, G. Yoo, Y. Choi, and H. Rodrigue, "Hybrid Robotic Manipulator using Sensorized Articulated Segment Joints with Soft Inflatable Rubber Bellows," vol. 69, no. 10, pp. 10259 - 10269, October 2022.

[94] M. Hofer and R. D'Andrea, "Design, fabrication, modeling and control of a fabric-based spherical robotic arm," vol. 68, p. 102369, June 2020.

[95] N. Oh and H. Rodrigue, "Toward the Development of Large-scale Inflatable Robotic Arms Using Hot Air Welding," vol. 10, no. 1, February 2023.

[96] B. Gorissen, T. Chishiro, S. Shimomura, D. Reynaerts, M. De Volder, and S. Konishi, "Flexible pneumatic twisting actuators and their application to tilting micromirrors," vol. 216, pp. 426-431, 2014.

[97] F. Connolly, C. J. Walsh, and K. Bertoldi, "Automatic design of fiber-reinforced soft actuators for trajectory matching," vol. 114, no. 1, pp. 51-56, December 2017.

[98] A. Lazarus and P. M. Reis, "Soft actuation of structured cylinders through auxetic behavior," vol. 17, no. 6, pp. 815-820, January 2015.

[99] Z. Jiao, C. Ji, J. Zou, H. Yang, and M. Pan, "Vacuum-powered soft pneumatic twisting actuators to empower new capabilities for soft robots," vol. 4, no. 1, p. 1800429, October 2019.

[100] W. Xiao, X. Du, W. Chen, G. Yang, D. Hu, and X. Han, "Cooperative collapse of helical structure enables the actuation of twisting pneumatic artificial muscle," vol. 201, p. 106483, July 2021.

[101] L. Belding *et al.*, "Slit tubes for semisoft pneumatic actuators," vol. 30, no. 9, p. 1704446, January 2018.

[102] J. Yan, X. Zhang, B. Xu, and J. Zhao, "A new spiral-type inflatable pure torsional soft

actuator," vol. 5, no. 5, pp. 527-540, October 2018.

[103] C. H. Ahn, W. Wang, J. Jung, and H. Rodrigue, "Pleated Film-Based Soft Twisting Actuator," vol. 20, no. 7, pp. 1149-1158, 2019.

[104] S. Sanan, P. S. Lynn, and S. T. Griffith, "Pneumatic torsional actuators for inflatable robots," vol. 6, no. 3, August 2014.

[105] F. Chen, Y. Miao, G. Gu, and X. Zhu, "Soft twisting pneumatic actuators enabled by freeform surface design," vol. 6, no. 3, pp. 5253-5260, April 2021.

[106] R. Balak and Y. C. Mazumdar, "Multi-modal pneumatic actuator for twisting, extension, and bending," Las Vegas, NV, USA, October 2020, pp. 8673-8679.

[107] Y. Fei, J. Wang, and W. Pang, "A novel fabric-based versatile and stiffness-tunable soft gripper integrating soft pneumatic fingers and wrist," *Soft Robot.*, vol. 6, no. 1, pp. 1-20, 2019.

[108] H. D. Yang and A. T. Asbeck, "A layered manufacturing approach for soft and soft-rigid hybrid robots," vol. 7, no. 2, pp. 218-232, April 2020.

[109] M. A. Robertson and J. Paik, "Low-inertia vacuum-powered soft pneumatic actuator coil characterization and design methodology," Livorno, Italy, April 2018, pp. 431-436.

[110] M. Fatahillah, N. Oh, and H. Rodrigue, "A novel soft bending actuator using combined positive and negative pressures," vol. 8, p. 472, May 2020.

[111] C. Tawk, M. In Het Panhuis, G. M. Spinks, and G. Alici, "Bioinspired 3D printable soft vacuum actuators for locomotion robots, grippers and artificial muscles," vol. 5, no. 6, pp. 685-694, 2018.

[112] Z. Wang, Y. Song, Z. Wang, and H. Zhang, "Origami Folding Enhances Modularity and Mechanical Efficiency of Soft Actuators," London, United Kingdom, May 2023, pp. 648-654.

[113] Z. Huang *et al.*, "Fluid-driven hydrogel actuators with an origami structure," vol. 25, no. 7, July 2022.

[114] M. A. Robertson and J. Paik, "New soft robots really suck: Vacuum-powered systems empower diverse capabilities," vol. 2, no. 9, August 2017.

[115] F. Daerden and D. Lefeber, "Pneumatic artificial muscles: actuators for robotics and automation," vol. 47, no. 1, pp. 11-21, 2002.

[116] R. Niiyama, D. Rus, and S. Kim, "Pouch motors: Printable/inflatable soft actuators for robotics," 2014, pp. 6332-6337.

[117] E. W. Hawkes, D. L. Christensen, and A. M. Okamura, "Design and implementation of a 300% strain soft artificial muscle," May 2016, pp. 4022-4029.

[118] D. Yang *et al.*, "Buckling pneumatic linear actuators inspired by muscle," vol. 1, no. 3,

p. 1600055, June 2016.

[119] A. L. Kulasekera, R. B. Arumathanthri, D. S. Chathuranga, T. D. Lalitharatne, and R. C. Gopura, "A low-profile vacuum actuator: Towards a sit-to-stand assist exosuit," New Haven, CT, USA, May 2020, pp. 110-115.

[120] A. L. Kulasekera, R. B. Arumathanthri, D. S. Chathuranga, R. Gopura, and T. D. Lalitharatne, "A thin-walled vacuum actuator (ThinVAc) and the development of multi-filament actuators for soft robotic applications," vol. 332, p. 113088, December 2021.

[121] J.-G. Lee and H. Rodrigue, "Armor-based stable force pneumatic artificial muscles for steady actuation properties," vol. 9, no. 3, pp. 413-424, June 2022.

[122] Z. Zhang *et al.*, "Bioinspired rigid-soft hybrid origami actuator with controllable versatile motion and variable stiffness," vol. 39, no. 6, pp. 4768-4784, December 2023.

[123] Y. Su *et al.*, "A high-payload proprioceptive hybrid robotic gripper with soft origamic actuators," vol. 5, no. 2, pp. 3003-3010, April 2020.

[124] D. Drotman, M. Ishida, S. Jadhav, and M. T. Tolley, "Application-driven design of soft, 3-D printed, pneumatic actuators with bellows," vol. 24, no. 1, pp. 78-87, November 2018.

[125] N. S. Usevitch, A. M. Okamura, and E. W. Hawkes, "APAM: Antagonistic pneumatic artificial muscle," 2018, pp. 1539-1546.

[126] A. Coutinho, J. H. Park, B. Jamil, H. R. Choi, and H. Rodrigue, "Hyperbaric Vacuum-Based Artificial Muscles for High-Performance Actuation," *Adv. Int. Sys.*, vol. 5, no. 1, p. 2200090, 2023.

[127] Y. Liu, W. Shi, P. Chen, Y. Yu, D. Zhang, and D. Wang, "Design and experiment of a novel pneumatic soft arm based on a deployable origami exoskeleton," vol. 18, no. 54, pp. 1-12, January 2024.

[128] C. Zhang *et al.*, "Plug & play origami modules with all-purpose deformation modes," vol. 14, no. 4329, pp. 1-10, 2023.

[129] M. Park *et al.*, "Deployable soft origami modular robotic arm with variable stiffness using facet buckling," vol. 8, no. 2, pp. 864-871, December 2022.

[130] M. Nordin and V. H. Frankel, "Biomechanics of joints," in *Basic Biomechanics of the Musculoskeletal System*4th ed. Philadelphia, PA, USA: Lippincott Williams & Wilkins, 2012, pp. 364-394.

[131] D. Rus and M. T. Tolley, "Design, fabrication and control of soft robots," vol. 521, no. 7553, pp. 467-75, May 28 2015.

[132] C. Laschi, B. Mazzolai, and M. Cianchetti, "Soft robotics: Technologies and systems

pushing the boundaries of robot abilities," vol. 1, no. 1, p. eaah3690, 2016.

[133] C. Tawk and G. Alici, "A Review of 3D-Printable Soft Pneumatic Actuators and Sensors: Research Challenges and Opportunities," vol. 3, no. 6, 2021.

[134] M. Li, A. Pal, A. Aghakhani, A. Pena-Francesch, and M. Sitti, "Soft actuators for real-world applications," vol. 7, pp. 235-249, Mar 2022.

[135] G. Decroly *et al.*, "Programmable Stimuli-Responsive Actuators for Complex Motions in Soft Robotics: Concept, Design and Challenges," vol. 9, no. 4, 2020.

[136] A. Pal, V. Restrepo, D. Goswami, and R. V. Martinez, "Exploiting Mechanical Instabilities in Soft Robotics: Control, Sensing, and Actuation," vol. 33, no. 19, p. e2006939, May 2021.

[137] F. Daerden and D. Lefeber, "The concept and design of pleated pneumatic artificial muscles," vol. 2, no. 3, pp. 41-50, 2001.

[138] E. G. Hocking and N. M. Wereley, "Analysis of nonlinear elastic behavior in miniature pneumatic artificial muscles," vol. 22, no. 1, 2013.

[139] P. Beyl, M. Van Damme, R. Van Ham, B. Vanderborght, and D. Lefeber, "Pleated Pneumatic Artificial Muscle-Based Actuator System as a Torque Source for Compliant Lower Limb Exoskeletons," vol. 19, no. 3, pp. 1046-1056, 2014.

[140] P. Ohta *et al.*, "Design of a Lightweight Soft Robotic Arm Using Pneumatic Artificial Muscles and Inflatable Sleeves," vol. 5, no. 2, pp. 204-215, Apr 2018.

[141] N. D. Naclerio and E. W. Hawkes, "Simple, Low-Hysteresis, Foldable, Fabric Pneumatic Artificial Muscle," vol. 5, no. 2, pp. 3406-3413, 2020.

[142] N. Oh, Y. J. Park, S. Lee, H. Lee, and H. Rodrigue, "Design of Paired Pouch Motors for Robotic Applications," vol. 4, no. 1, 2018.

[143] R. F. Shepherd *et al.*, "Multigait soft robot," vol. 108, no. 51, pp. 20400-3, Dec 20 2011.

[144] R. K. Katzschmann, J. DelPreto, R. MacCurdy, and D. Rus, "Exploration of underwater life with an acoustically controlled soft robotic fish," vol. 3, no. 16, p. eaar3449, 2018.

[145] F. Ilievski, A. D. Mazzeo, R. F. Shepherd, X. Chen, and G. M. Whitesides, "Soft Robotics for Chemists," vol. 123, no. 8, pp. 1930-1935, 2011.

[146] R. Deimel and O. Brock, "A novel type of compliant and underactuated robotic hand for dexterous grasping," vol. 35, no. 1-3, pp. 161-185, 2015.

[147] K. C. Galloway *et al.*, "Soft Robotic Grippers for Biological Sampling on Deep Reefs," (in eng), vol. 3, no. 1, pp. 23-33, Mar 1 2016.

[148] R. L. Truby, R. K. Katzschmann, J. A. Lewis, and D. Rus, "Soft robotic fingers with embedded ionogel sensors and discrete actuation modes for somatosensitive manipulation," 2019, pp. 322-329.

[149] Y. Fei, J. Wang, and W. Pang, "A Novel Fabric-Based Versatile and Stiffness-Tunable Soft Gripper Integrating Soft Pneumatic Fingers and Wrist," vol. 6, no. 1, pp. 1-20, Feb 2019.

[150] H. K. Yap, J. H. Lim, F. Nasrallah, J. C. Goh, and R. C. Yeow, "A soft exoskeleton for hand assistive and rehabilitation application using pneumatic actuators with variable stiffness," 2015, pp. 4967-4972.

[151] J.-N. Wang, Y.-Q. Liu, Y.-L. Zhang, J. Feng, and H.-B. Sun, "Pneumatic smart surfaces with rapidly switchable dominant and latent superhydrophobicity," vol. 10, no. 2, pp. e470-e470, 2018.

[152] J. G. Lee and H. Rodrigue, "Origami-Based Vacuum Pneumatic Artificial Muscles with Large Contraction Ratios," vol. 6, no. 1, pp. 109-117, Feb 2019.

[153] D. Melancon, B. Gorissen, C. J. Garcia-Mora, C. Hoberman, and K. Bertoldi, "Multistable inflatable origami structures at the metre scale," Nature, vol. 592, no. 7855, pp. 545-550, Apr 2021.

[154] D. Melancon, A. E. Forte, L. M. Kamp, B. Gorissen, and K. Bertoldi, "Inflatable Origami: Multimodal Deformation via Multistability," vol. 32, no. 35, 2022.

[155] F. Connolly, C. J. Walsh, and K. Bertoldi, "Automatic design of fiber-reinforced soft actuators for trajectory matching," vol. 114, no. 1, pp. 51-56, Jan 3 2017.

[156] L. Belding *et al.*, "Slit Tubes for Semisoft Pneumatic Actuators," vol. 30, no. 9, Mar 2018.

[157] S. Chen, G. Zhou, D. Li, Z. Song, and F. Chen, "Soft Robotic Joints With Anisotropic Stiffness by Multiobjective Topology Optimization," pp. 1-12, 2024.

[158] H. D. Yang and A. T. Asbeck, "A new manufacturing process for soft robots and soft/rigid hybrid robots," 2018, pp. 8039-8046.

[159] D. Drotman, M. Ishida, S. Jadhav, and M. T. Tolley, "Application-Driven Design of Soft, 3-D Printed, Pneumatic Actuators With Bellows," vol. 24, no. 1, pp. 78-87, 2019.

[160] R. Balak and Y. C. Mazumdar, "Multi-Modal Pneumatic Actuator for Twisting, Extension, and Bending," presented at the 2020 IEEE/RSJ International Conference on Intelligent Robots and Systems (IROS), 2020.

[161] Y. Hao *et al.*, "A Multimodal, Enveloping Soft Gripper: Shape Conformation, Bioinspired Adhesion, and Expansion-Driven Suction," vol. 37, no. 2, pp. 350-362, 2021.

[162] W. Wang, N.-G. Kim, H. Rodrigue, and S.-H. Ahn, "Modular assembly of soft deployable structures and robots," vol. 4, no. 3, pp. 367-376, 2017.

[163] L. Zhao *et al.*, "StarBlocks: Soft Actuated Self-Connecting Blocks for Building Deformable Lattice Structures," vol. 8, no. 8, pp. 4521-4528, 2023.

[164] D. Guo, Z. Kang, Y. Wang, and M. Li, "Design of multi-material soft pneumatic

modules," vol. 30, no. 9, p. 095006, 2021.

[165] C. Meng, W. Xu, H. Li, H. Zhang, and D. Xu, "A new design of cellular soft continuum manipulator based on beehive-inspired modular structure," vol. 14, no. 3, 2017.

[166] M. A. Robertson, O. C. Kara, and J. Paik, "Soft pneumatic actuator-driven origami-inspired modular robotic “pneumagami”," vol. 40, no. 1, pp. 72-85, 2021.

[167] H.-J. Kim, A. Kawamura, Y. Nishioka, and S. Kawamura, "Mechanical design and control of inflatable robotic arms for high positioning accuracy," *Adv. Rob.*, vol. 32, no. 2, pp. 89-104, 2017.

[168] X. J. Chen, Y. X. Guo, D. H. Duanmue, J. S. Zhou, W. Zhang, and Z. Wang, "Design and Modeling of an Extensible Soft Robotic Arm," (in English), *Ieee Robot Autom Let*, vol. 4, no. 4, pp. 4208-4215, Oct 2019.

[169] H. D. Yang and A. T. Asbeck, "Design and Characterization of a Modular Hybrid Continuum Robotic Manipulator," vol. 25, no. 6, pp. 2812-2823, 2020.

[170] M. Hofer and R. D’Andrea, "Design, fabrication, modeling and control of a fabric-based spherical robotic arm," vol. 68, 2020.

[171] W. McMahan *et al.*, "Field trials and testing of the OctArm continuum manipulator," 2006, pp. 2336-2341.

[172] R. Kang, Y. Guo, L. Chen, D. T. Branson, and J. S. Dai, "Design of a Pneumatic Muscle Based Continuum Robot With Embedded Tendons," vol. 22, no. 2, pp. 751-761, 2017.

[173] E. Harsono, J. Yang, S. Bhattacharya, and H. Yu, "Design and analysis of a novel hybrid-driven continuum robot with variable stiffness," vol. 177, p. 105067, 2022.

[174] Q. Guan, F. Stella, C. Della Santina, J. Leng, and J. Hughes, "Trimmed helicoids: an architectured soft structure yielding soft robots with high precision, large workspace, and compliant interactions," vol. 1, no. 1, 2023.

[175] Z. Jiao, C. Ji, J. Zou, H. Yang, and M. Pan, "Vacuum-Powered Soft Pneumatic Twisting Actuators to Empower New Capabilities for Soft Robots," vol. 4, no. 1, 2018.

[176] Z. Jiao, C. Zhang, W. Wang, M. Pan, H. Yang, and J. Zou, "Advanced Artificial Muscle for Flexible Material-Based Reconfigurable Soft Robots," vol. 6, no. 21, p. 1901371, Nov 6 2019.

[177] Y. Wei *et al.*, "A Novel, Variable Stiffness Robotic Gripper Based on Integrated Soft Actuating and Particle Jamming," *Soft Robot.*, vol. 3, no. 3, pp. 134-143, 2016.

[178] Y. Li, Y. Chen, Y. Yang, and Y. Wei, "Passive Particle Jamming and Its Stiffening of Soft Robotic Grippers," *IEEE Trans. Robot.*, vol. 33, no. 2, pp. 446-455, 2017.

[179] Y. S. Narang, J. J. Vlassak, and R. D. Howe, "Mechanically Versatile Soft Machines through Laminar Jamming," vol. 28, no. 17, 2018.

[180] M. Zhu, Y. Mori, T. Wakayama, A. Wada, and S. Kawamura, "A Fully Multi-Material Three-Dimensional Printed Soft Gripper with Variable Stiffness for Robust Grasping," vol. 6, no. 4, pp. 507-519, Aug 2019.

[181] S. Yoshida, Y. Morimoto, L. Zheng, H. Onoe, and S. Takeuchi, "Multipoint Bending and Shape Retention of a Pneumatic Bending Actuator by a Variable Stiffness Endoskeleton," vol. 5, no. 6, pp. 718-725, Dec 2018.

[182] T. L. Buckner, M. C. Yuen, S. Y. Kim, and R. Kramer‐Bottiglio, "Enhanced Variable Stiffness and Variable Stretchability Enabled by Phase‐Changing Particulate Additives," vol. 29, no. 50, 2019.

[183] R. Chellattoan and G. Lubineau, "A Stretchable Fiber with Tunable Stiffness for Programmable Shape Change of Soft Robots," vol. 9, no. 6, pp. 1052-1061, Dec 2022.

[184] Y. Yang, Y. Chen, Y. Li, M. Z. Q. Chen, and Y. Wei, "Bioinspired Robotic Fingers Based on Pneumatic Actuator and 3D Printing of Smart Material," vol. 4, no. 2, pp. 147-162, Jun 2017.

[185] Y. F. Zhang *et al.*, "Fast‐Response, Stiffness‐Tunable Soft Actuator by Hybrid Multimaterial 3D Printing," vol. 29, no. 15, 2019.

[186] Y. Jiang, D. Chen, C. Liu, and J. Li, "Chain-Like Granular Jamming: A Novel Stiffness-Programmable Mechanism for Soft Robotics," vol. 6, no. 1, pp. 118-132, Feb 2019.

[187] X.-Y. Guo, W.-B. Li, Q.-H. Gao, H. Yan, Y.-Q. Fei, and W.-M. Zhang, "Self-locking mechanism for variable stiffness rigid–soft gripper," vol. 29, no. 3, 2020.

[188] J. T. Overvelde, T. Kloek, J. D'Haen J, and K. Bertoldi, "Amplifying the response of soft actuators by harnessing snap-through instabilities," vol. 112, no. 35, pp. 10863-8, Sep 1 2015.

[189] Y. Tang *et al.*, "Leveraging elastic instabilities for amplified performance: Spine-inspired high-speed and high-force soft robots," vol. 6, no. 19, p. eaaz6912, 2020.

[190] Y. Lin *et al.*, "A Bioinspired Stress-Response Strategy for High-Speed Soft Grippers," vol. 8, no. 21, p. e2102539, Nov 2021.

[191] J. Kaufmann, P. Bhovad, and S. Li, "Harnessing the Multistability of Kresling Origami for Reconfigurable Articulation in Soft Robotic Arms," vol. 9, no. 2, pp. 212-223, Apr 2022.

[192] Y. Chi, Y. Tang, H. Liu, and J. Yin, "Leveraging Monostable and Bistable Pre‐Curved Bilayer Actuators for High‐Performance Multitask Soft Robots," vol. 5, no. 9, 2020.

[193] B. Gorissen, D. Melancon, N. Vasios, M. Torbati, and K. Bertoldi, "Inflatable soft jumper inspired by shell snapping," vol. 5, no. 42, p. eabb1967, 2020.

[194] C. Qiao, L. Liu, and D. Pasini, "Bi-Shell Valve for Fast Actuation of Soft Pneumatic Actuators via Shell Snapping Interaction," vol. 8, no. 15, p. e2100445, Aug 2021.

[195] P. Rothemund *et al.*, "A soft, bistable valve for autonomous control of soft actuators," vol. 3, no. 16, p. eaar7986, 2018.

[196] D. J. Preston *et al.*, "Digital logic for soft devices," vol. 116, no. 16, pp. 7750-7759, Apr 16 2019.

[197] L. Jin, A. E. Forte, and K. Bertoldi, "Mechanical Valves for On-Board Flow Control of Inflatable Robots," vol. 8, no. 21, p. e2101941, Nov 2021.

[198] D. Drotman, S. Jadhav, D. Sharp, C. Chan, and M. T. Tolley, "Electronics-free pneumatic circuits for controlling soft-legged robots," vol. 6, no. 51, p. eaay2627, 2021.

[199] E. W. Hawkes, L. H. Blumenschein, J. D. Greer, and A. M. Okamura, "A soft robot that navigates its environment through growth," vol. 2, no. 8, p. eaan3028, 2017.

[200] J. Luong *et al.*, "Eversion and retraction of a soft robot towards the exploration of coral reefs," 2019, pp. 801-807.

[201] N. S. Usevitch, Z. M. Hammond, M. Schwager, A. M. Okamura, E. W. Hawkes, and S. Follmer, "An untethered isoperimetric soft robot," vol. 5, no. 40, p. eaaz0492, 2020.

[202] M. M. Coad, R. P. Thomasson, L. H. Blumenschein, N. S. Usevitch, E. W. Hawkes, and A. M. Okamura, "Retraction of Soft Growing Robots Without Buckling," vol. 5, no. 2, pp. 2115-2122, 2020.

[203] J. D. Greer, L. H. Blumenschein, A. M. Okamura, and E. W. Hawkes, "Obstacle-aided navigation of a soft growing robot," 2018, pp. 4165-4172.

[204] J. D. Greer, L. H. Blumenschein, R. Alterovitz, E. W. Hawkes, and A. M. Okamura, "Robust navigation of a soft growing robot by exploiting contact with the environment," vol. 39, no. 14, pp. 1724-1738, 2020.

[205] W. Fichter, *A theory for inflated thin-wall cylindrical beams*. National Aeronautics and Space Administration, 1966.

[206] J. C. Thomas and A. Le Van, "Deflections of pneumatic masts and columns," *Archit. Eng. Des. Manag.*, vol. 17, no. 3-4, pp. 299-315, 2020.

[207] J. Y. Kim, N. Mazzoleni, and M. Bryant, "Modeling of Resistive Forces and Buckling Behavior in Variable Recruitment Fluidic Artificial Muscle Bundles," vol. 10, no. 3, 2021.